Micro- and Nano-scale Colloidal Dynamics Near Surfaces

by

Jeffrey S. Guasto

B.S., Mechanical Engineering, Lehigh University, 2003
B.S., Physics, Lehigh University, 2003
Sc.M., Engineering, Brown University, 2004

Thesis

Submitted in partial fulfillment of the requirements for
the Degree of Doctor of Philosophy
in the Division of Engineering at Brown University

May 2009

Abstract of "Micro- and Nano-scale Colloidal Dynamics Near Surfaces," by Jeffrey S. Guasto, Ph.D., Brown University, May 2009

We present an examination of near-wall colloidal particle dynamics, their associated measurement techniques and applications to micro- and nano-scale fluid flows. The dynamics of small particles in solution exhibit interesting and useful properties. The most popular measurement methods for characterizing their motion are imaging techniques based on evanescent wave illumination, namely total internal reflection fluorescence (TIRF) microscopy, which allows the imaging of small, fluorescent particles (10 nanometer to 10 micron) within a few hundred nanometers of a fluid-solid interface. In some instances, the particle intensity may be used to determine particle's distance from the wall, and thus, the three-dimensional particle motion. In the presence of a solid boundary, the random, Brownian motion and the convective motion of the particles is modified due to interactions between the particle and wall. Some examples of these effects are hindered diffusion, shear-induced rolling, electrostatic repulsion and van der Waals attractive forces. This has immense consequences for fluid velocity measurement techniques that infer fluid motion from the measured particle motion. Evanescent wave illumination was applied to measure single particle dynamics and also to infer the fluid motion in several fluid systems. The dynamics of semiconductor nanocrystals or quantum dots (QDs) and single molecules were examined and applied as tracer particles, extending the resolution of particle velocimetry probes down to about 10 nm. Additionally, the inherent intensity variation of QDs with temperature was used to measure the local fluid temperature within the evanescent field. QDs were also applied to measure high speed micro-flows (near 1 cm/s) within about 200 nm of the fluid-solid interface. A three-dimensional TIRF velocimetry (3D-TIRV) technique was developed to measure slip velocities at microchannel walls with tracer particles on the

order of 100 nm. The three-dimensional adhesion dynamics of large (6 micron diameter) particles were examined to determine the kinetics of adhesion ligands and receptors for applications to leukocyte dynamics. Finally, the techniques of fluorescence microscopy and in-line holographic imaging were applied to characterized the structure and dynamics of electrospray droplets.

This dissertation by Jeffrey S. Guasto is accepted in its present form by
the Division of Engineering as satisfying the dissertation requirement
for the degree of Doctor of Philosophy.

Date. . . . .
                                            Kenneth S. Breuer, Advisor

Recommended to the Graduate Council

Date. . . . .
                                            Derek Stein, Reader

Date. . . . .
                                            Anubhav Tripathi, Reader

Date. . . . .
                                            Rashid Zia, Reader

Approved by the Graduate Council

Date. . . . .
                                            Sheila Bonde
                                            Dean of Graduate School

The Vita of Jeffrey S. Guasto

Jeffrey S. Guasto was born on February 24, 1981 in Pittston, Pennsylvania where he resided until graduating from Pittston Area High School in 1999. Upon graduation, he attended Lehigh University in Bethlehem, Pennsylvania and received Bachelor of Science degrees in both Mechanical Engineering and Physics in 2003. Immediately following his undergraduate work, Mr. Guasto began pursuing graduate studies at Brown University in Providence, Rhode Island. There, he earned a Master of Science in Engineering with a concentration in fluid mechanics and transport processes in 2004, and he continued on toward a Doctor of Philosophy in Engineering investigating micro- and nano-scale colloidal dynamics. Subsequently, he published several peer reviewed journal articles on his work and was awarded the Simon Ostrach Fellowship in 2006. Upon completion of his graduate studies, Mr. Guasto plans to begin a postdoctoral appointment at Haverford College in Haverford, Pennsylvania. In the future, he anticipates pursuing a career in academic research with an emphasis on fluid mechanics, transport phenomena and soft condensed matter physics.

Preface

This dissertation contains experimental studies of colloidal particle dynamics near solid surfaces with an emphasis on micro- and nano-scale fluid mechanics and diagnostic applications. The content and relevant contributions are as follows:

Chapter 1. Introduction. A description of fundamental phenomena and measurement techniques associated with near-wall colloidal dynamics is discussed along with applications.

Chapter 2. "Statistical particle tracking velocimetry using molecular and quantum dot tracer particles" by Jeffrey S. Guasto, Peter Huang and Kenneth S. Breuer. *Experiments in Fluids*, Vol. 41, pp. 869-880, 2006. Experiments were conceived by Guasto, Huang and Breuer, with J.S. Guasto and P Huang executing the experiments and J.S. Guasto performing the analyses. The summary of results was composed by Guasto and Breuer.

Chapter 3. "Simultaneous, ensemble-averaged measurement of near-wall temperature and velocity in steady micro-flows using single quantum dot -tracking" by Jeffrey S. Guasto and Kenneth S. Breuer. *Experiments in Fluids*, Vol. 45, pp. 157-166, 2008. Experiments were conceived and summarized by both Guasto and Breuer with J.S. Guasto being solely responsible for the experiment execution and data analyses.

Chapter 4. "Direct measurement of slip velocies using three-dimensional total internal reflection velocimetry" by Peter Huang, Jeffrey S. Guasto and Kenneth S. Breuer. *Journal of Fluid Mechanics*, Vol. 566, pp. 447-464, 2006. Experiments were conceived and summarized by Huang and Breuer, with P. Huang performing the experiments and data analysis. J.S. Guasto contributed to the development of the calibration methods, nanoparticle intensity variation model and statistical analysis of intensity distributions to interpret the *measured* particle concentration profiles.

Chapter 5. "Measurement bias in evanescent fields due to particle size variations and force interactions" by Jeffrey S. Guasto and Kenneth S. Breuer. *Measurement Science and Technology*, in review, 2008. The analyses were conceived, developed and written by J.S. Guasto with K.S. Breuer assisting in interpretation and writing.

Chapter 6. "Hindered Brownian motion and depletion layer of particles in shear flow and their implications for near-wall velocimetry" by Peter Huang, Jeffrey S. Guasto and Kenneth S. Breuer. In preparation for *Journal of Fluid Mechanics*, 2008. Numerical simulations were conceived by Huang and Breuer with P. Huang being primarily responsible for execution of the simulations and results summary. Experiments were conceived by Guasto, Huang and Breuer, where J.S. Guasto performed the experimental measurements and data analysis of diffusion-induced velocity bias.

Chapter 7. "High-speed quantum dot tracking using evanescent wave illumination" by Jeffrey S. Guasto and Kenneth S. Breuer. In preparation for *Experiments in Fluids*, 2008. The experiments were conceived, executed and analyzed by J.S. Guasto with assistance in interpretation and summary by K.S. Breuer.

Chapter 8. "Evanescent wave imaging of particle adhesion dynamics near solid surfaces" by Jeffrey S. Guasto, Brian J. Schmidt, Michael B. Lawrence and Kenneth S. Breuer. In preparation for *Biophysical Journal*, 2008. Experiments were conceived by Guasto, Schmidt, Lawrence and Breuer. Experimental execution and data analysis was performed by J.S. Guasto. Results were interpreted and summarized by Breuer and Guasto.

Chapter 9. "Visualization and tracking of electrospray droplet emissions using fluorescence and holographic techniques" by Anthony N. Zorzos, Jeffrey S. Guasto and Kenneth S. Breuer. In preparation for *Journal of Colloid and Interface Science*, 2008. Experiments were conceived and summarized by Zorzos and Breuer with A.N. Zorzos performing all

experiments and fluorescence imaging data analyses. J.S. Guasto contributed the development of both the fluorescence and holographic imaging systems and is responsible for the implementation of the holographic imaging data analysis.

Chapter 10. Conclusion. Final remarks and recommendations for future work.

Acknowledgments

This thesis is the culmination of several years of detailed thought and experimental research, which was made possible by the support and devotion of many individuals.

First and foremost, I owe a debt of gratitude to my advisor and mentor, Professor Kenneth S. Breuer. Aside from providing world-class equipment, facilities and financial support, he is responsible for the development of my professional academic career. He allowed room for me to explore new avenues of research, while continually motivating me to stay focussed on fundamental science. Through him, I learned not only to scrutinize and dissect experimental details, but also to consider the broader impact of our scientific research.

I would like to thank all of my reviewers for providing detailed analyses and suggestions on all aspects of this thesis. The insight of Professors David Erickson and Derek Stein has surely made this research much stronger. In addition to my advisor, Professors Anubhav Tripathi and Rashid Zia have helped to guide me both professionally and scientifically, which lead directly to a portion of the work contained in this thesis on microfluidics and holography, respectively.

I have been privileged to work with many gifted graduate and undergraduate students during my time at Brown University, all of whom contributed in part to further this research: Professor Minjun Kim, Jahn Torres, Qian Bian, Arnold Song, Charles Peguero, Alexandre de Chaumont Quitry, Doctor Matthew Kirby and Doctor Jinkee Lee. A special thanks is due to two of my former labmates including my coauthor, colleague and good friend, Professor Peter Huang. He is an outstanding teacher and insightful experimentalist. He patiently introduced me to the intricacies of microscale experimentation and endured

countless conversations, which ultimately produced a large portion of the manuscript presented here. I also had the pleasure to work closely with Anthony Zorzos, who I watched develop from a young undergraduate student into a bright experimentalist with a rewarding scientific career ahead of him.

I would also like to acknowledge several outside collaborators, namely Doctor Joel Hensley from Physical Sciences Incorporated for assistance on quantum dot studies and Professor Michael B. Lawrence and Brian J. Schmidt of the University of Virginia for assistance with leukocyte adhesion studies. Additional thanks are necessary for the support from Michael Jibitsky of the Brown University Microelectronics Facility, Charles Vickers of the Joint Engineering Physics Instrument Shop and especially our administrative assistant, Jeff Brown.

I must acknowledge the support of my friends from my home of Pittston, Pennsylvania that never allow me to forget my roots and my friends from Brown University, who made my time in graduate school an education in more than just science.

To my parents, grandparents and family, I am forever grateful for their support and sacrifice throughout my education. They instilled in me the importance of education and encouraged me to pursue it to the highest level.

Finally, to my soon to be wife, Nadine Palermo, I am indebted the most. Her patience, understanding and love for me has been constant and unwaivering. Without her in my life, none of this would have been possible.

Dedication

To my father, Frank A. Guasto, and grandfather, Salvatore J. Guasto.

Contents

List of Tables

List of Figures

xix

Chapter 1

Introduction

The advent of microfluidics in the late 1990's brought about a new frontier in fluid mechanics. The fabrication of small scale fluid devices and application of microscopy techniques to fluid mechanics allowed us to probe new and interesting physical phenomena. The idea of a lab-on-a-chip spawned an industry that strives to miniaturize and popularize the ability to detect, process and analyze biological and chemical specimens on small, inexpensive microfluidics-based platforms. Many of the processes need to be quantitatively characterized with accurate diagnostic techniques. As the device dimension shrinks, bulk properties of the fluid medium become less important and understanding interfacial and near-wall fluid-solid interactions become vital to the advancement of these technologies. Additionally, the use of colloids for self-assembly processes [1] and the medical application of nanoparticles has recently become of interest [2].

Microfluidics presents an interesting advantage to researchers, who are now able to probe new and exciting effects in capillary and low Reynolds number flows, where the small dimension of these devices enables the necessary length scales for these phenomena to dominate. Colloidal dynamics also exhibit interesting particle-particle and particle-wall

interactions that were previously not observable in the conventional realm of fluid mechanics and soft condensed matter physics. The observations of wall interactions are critical to understanding these phenomena. More recently, advanced fabrication techniques are allowing fluid handling structures with feature sizes less than one micron, ushering in a new wave of nanofluidic technologies [3]. This will allow us to approach the molecular scale and breakdown of the continuum limit, where newer, stranger effects take place.

This thesis examines several different aspects of near-wall colloidal physics and fluid mechanics. The near-wall physical phenomona, application of new types of particles, experimental measurement techniques and associated measurement biases are all addressed. We begin with the application of quantum dots (QDs) as fluorescent tracer particles in near-wall colloidal dynamics studies. The particle motion is measured within several hundred nanometers of the fluid-solid interface of a microchannel wall for application to velocity and temperature measurements. The technique of total internal reflection fluorescence (TIRF) microscopy is applied to measure slip velocities and the three-dimensional motion of large particles for applications to leukocyte dynamics in blood flow. We discuss some of the typical colloidal dynamics and particle-wall interactions that are prominent in near-wall colloidal physics. These interactions can lead to bias errors in the interpretation of velocity measurement data produced from TIRF velocity measurement techniques. Finally, we explore related microscale diagnostic techniques for applications to electrospray aerosol droplet dynamics. Two-dimensional droplet dynamics are examined using fluorescence microscopy and three-dimensional spray structures are examined using in-line holographic microscopy.

1.1 QUANTUM DOT TRACER PARTICLES

1.1.1 Velocity Measurements

Particle Image Velocimetry (PIV) and Particle Tracking Velocimetry (PTV) have become integral techniques in experimental fluid mechanics. Originally developed for macro-scale measurements [4], these velocimetry methods have evolved to suit applications in micro-scale [5] and nano-scale [6] fluid mechanics. Both techniques employ the use of tracer particles suspended in a fluid of interest along with digital cameras to capture successive images of particle position in the fluid through time. PIV uses cross-correlation algorithms to determine the most probable displacement for a given region in two successive images. High density particle seeding and low diffusivity is preferable to increase accuracy. PTV methods, on the other hand, typically track single particles and use particle center detection with nearest-neighbor matching to determine the most probable single particle displacement [7]. For PTV, low particle seeding density is typically necessary to prevent particle misidentification.

Recently, interest has peaked in the use of semiconductor nanocrystals or quantum dots (QDs) as truly nanometer-sized flow tracer particles for micro- and nano-fluidic diagnostics [8, 9, 10, 11, 12, 13, 14]. QDs are single crystals that are self assembled from semiconductor materials, and they are similar in many ways to single fluorophore molecules with comparable fluorescence lifetimes ($\approx$10 ns). As the length scales of microfluidic devices decrease, it is advantageous to probe these flows with smaller diameter tracer particles for improved resolution. QDs are available in diameters ranging from 3 to 25 nm in diameter, which is an order of magnitude smaller than typical tracer particles (100 nm to 1 μm). Furthermore, they have several other advantages over typical tracer particles and are

now commercially available to researchers. The fluorescence emission wavelength is tunable using the diameter of the QD and can range from the visible to the near infrared. Their quantum efficiency is comparable to typical fluorescent molecules, and they are considerably more resistant to photobleaching [15]. QDs have also been integrated into nanoparticles to produce ultra-bright, small, fluorescent tracer particles [11]. Additionally, QDs exhibit an inherent temperature sensitivity that has been exploited as a temperature measurement technique [12].

In spite of the many advantageous characteristics listed above, there were several features of QDs that required special treatment before applying them to micro-scale fluid mechanics measurements. Although they are as bright and more stable than other single fluorophores, their small size means that QDs are significantly less intense than tracer particles that are several hundred nanometers in diameter containing thousands of fluorescent molecules. Further complicating this issue, their small diameters yield high diffusivity, and it is desirable to have the capability to measure fast moving flows, both of which require short imaging times to accurately measure particle positions. In the past, QD motion has been either hindered by elevating the fluid viscosity [8] or by using highly sensitive imaging techniques [9] (see figure 1.1). To capture their motion in low viscosity, aqueous flow, highly sensitive intensified cameras are required, which are known to produce imaging artifacts that can appear similar in size and shape to the diffraction limited image of a QD [16]. For flow tracing application in fluid mechanics, it is preferable to have dense seeding concentrations of tracer particles in the fluid for efficient and accurate data collection. This, combined with the high diffusivity of the particles results in misidentification in tracking [17]. Diffusion of particles perpendicular to the imaging plane also presents a problem where particles will diffuse out of the focal plane ("drop-out"). Like other single fluorophores, QDs also exhibit
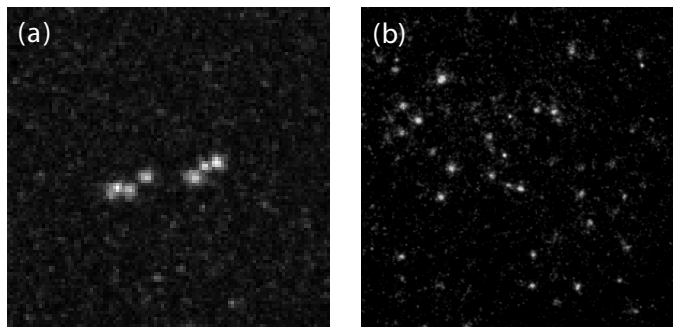
Figure 1.1: Quantum dot images: (a) a composite time series of 7 frames with equal time spacing for an organic soluble QD diffusing and blinking in a slight convective flow in PDMS and hexane (6.5 μm $\times$ 6.5 μm field of view) and (b) typical image of QDs in water illuminated by an evanescent field (19.3 μm $\times$ 19.3 μm field of view).

fluorescence intermittency or "blinking" [18], where under continuous illumination, they will cease to emit photons for random periods of time as shown in the single QD intensity time trace of figure 1.2. In *Statistical particle tracking velocimetry using molecular and quantum dot tracer particles* (chapter 2), we address each of these issues in turn. A novel yet simple particle tracking method is introduced to alleviate these problems based on the statistical nature of diffusion, blinking and drop-out. In *High-speed quantum dot tracking using evanescent wave illumination* (chapter 7), we further extend the capabilities of QD velocimetry to real-time particle imaging using a high-speed intensified camera to resolve QD trajectories at velocities near 1 cm/s.

1.1.2 Temperature Measurements

There also exists a demand in microfluidics for non-invasive thermal diagnostic methods with applications such as DNA amplification (PCR) [19, 20] and heat transfer in micro-electro-mechanical systems (MEMS) [21, 22]. Additionally, it is a natural progression to integrate both temperature and velocity measurement, since thermal and fluid problems
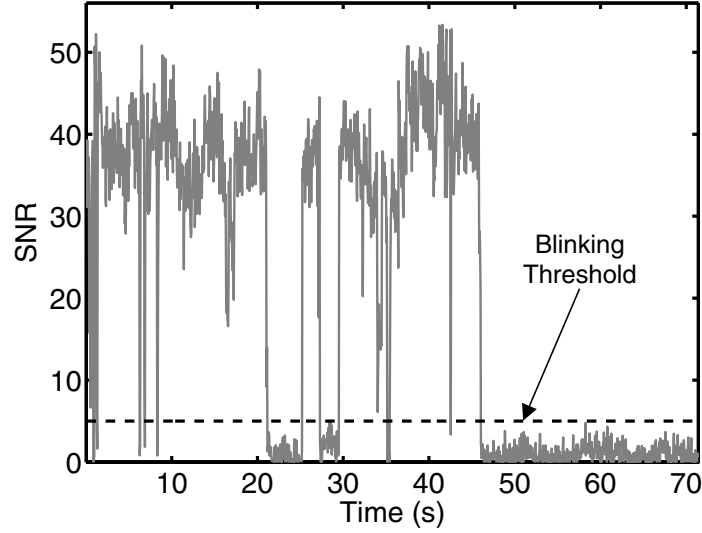
Figure 1.2: Sample intensity time trace for a single, immobilized quantum dot under continuous illumination. An intensity greater than the threshold of SNR=5 designates blinking on-times from off-times.

are often coupled. Two viable methods of optical temperature measurement have been successfully demonstrated including laser induced fluorescence (LIF) thermometry [23, 24] and PIV thermometry [25, 26, 27].

The first technique, LIF thermometry, uses the variation in emission intensity with temperature of fluorescent material in solution due to changes in quantum efficiency:

$$I = I_0 c \epsilon \phi (T) , \tag{1.1}$$

where I_0 is the intensity of the incident excitation light of wavelength λ_0, c is the concentration of the fluorescent dye, ϵ is the molar absorption coefficient and $\phi (T)$ is the quantum efficiency at temperature, T. These methods typically image high concentration fluorescent dye solutions and relate the local intensity to temperature through careful calibration [23].

Since the excitation light intensity can vary in both space and time, it advantageous to normalize the temperature sensitive dye intensity by dispersing and simultaneously measuring the intensity of a temperature *insensitive* dye in the same working fluid [24]. Both one- and two-color LIF thermometry have been applied simultaneously with particle velocimetry measurements. More recently, LIF thermometry has been applied to micro-flows to measure viscous heating, electrokinetic flows and thermally driven buoyant flows [28, 29, 30].

The second technique, PIV thermometry, exploits the Brownian motion of tracer particles to estimate fluid temperatures through the diffusion coefficient. In free solution,the mean square tracer particle displacement due to diffusion is $s^2 = 2D\Delta t$, where Δt is the time allowed for diffusion. The diffusion coefficient, D, for a particle of radius, a, is well approximated by the Stokes-Einstein relation when the particle radius is significantly larger than the solvent molecules:

$$D_{se} = \frac{k_b T}{6\pi\mu(T)a},$$
(1.2)

where k_b is Boltzmann's constant, T is absolute temperature and $\mu(T)$ is the temperature dependent viscosity. The details of this technique have been outlined and demonstrated experimentally [25, 26, 27] by relating the diffusion length to the spatial cross-correlation obtained from PIV data. One advantage of PIV thermometry, is that the same tracer particles used to measure the fluid velocity are used to measure temperature simultaneously (provided the temperature dependence of viscosity is known).

QDs have a unique advantage as thermal-fluid tracer particles since they exhibit inherent optical temperature sensitivity, and the thermo-optical properties of bulk QDs in solution as well as immobilized single QDs are well documented. QDs exhibit a small red shift (~ 0.11 nm K^{-1}) in emission wavelength with increasing temperature near room temperature [31], but the decrease in emission intensity with increasing temperature is much more significant

as shown in figure 1.3). Several researchers have measured the temperature sensitivity of QD emission intensity near room temperature. In particular, Walker *et al.* proposed the use of (CdSe)ZnS core-shell QDs for temperature sensitive coatings [32]. Organic soluble QDs were suspended in a solid, poly(lauryl methacrylate) (PLMA) matrix, and the temperature variation for the bulk emission intensity of the QD/PLMA composite was -1.3% K^{-1} between 278 K and 313 K. Liu *et al.* measured a similar temperature sensitivity of -1.1% K^{-1} between 280 K and 350 K for bulk emission water-soluble CdSe/ZnS core-shell QDs in a phosphate buffered saline (PBS) solution for use as a bio-probe [31]. Koochesfahani *et al.* also investigated the bulk photophysical properties of CdSe/ZnS quantum dots and were among the first to propose their use as a temperature sensitive dye for LIF thermofluid diagnostics [33]. Lastly, Banin *et al.* studied the effects of temperature and illumination intensity on fluorescence intermittency in single QDs immobilized in thin films of poly(methyl methacrylate) (PMMA) for temperatures between 15 K and 300 K [34]. They statistically investigated the intermittency behavior by building ensemble distributions from single QD measurements, but they did not comment directly on the link between temperature and emission intensity. In *Simultaneous, ensemble-averaged measurement of near-wall temperature and velocity in steady micro-flows using single quantum dot tracking* (chapter 3), we demonstrate a simultaneous temperature and velocity measurement system based on TIRF illumination of single QDs within 200 nm of a liquid-solid interface.
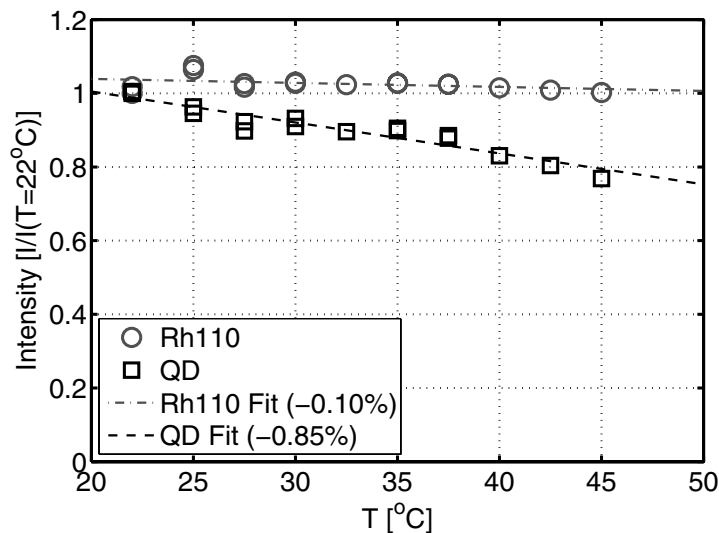
Figure 1.3: Intensity variation with temperature for bulk quantum dots and rhodamine 110 dye solutions.

1.2 TOTAL INTERNAL REFLECTION VELOCIMETRY

1.2.1 Advantages and Applications

As fluid mechanics reaches into the micro- and nano-scale, interfacial phenomena become increasingly important. An important technique for fluid-solid interfacial studies is evanescent wave microscopy or, when combined with fluorescence microscopy, total internal reflection fluorescence (TIRF) microscopy. Evanescent wave microscopy has been employed by biophysics researchers since the 1970's [35]. The technique has been used to measure chemical kinetics and surface diffusion, molecular conformation of adsorbates, cell development during culturing, visualization of cell structures and dynamics, and single molecule visualization and spectroscopy [36]. During the 1990's, several groups began studying near-wall colloidal dynamics by observing the light scattered by micron-sized particles in the evanescent field. In particular, they successfully and accurately measured gravitational attraction,
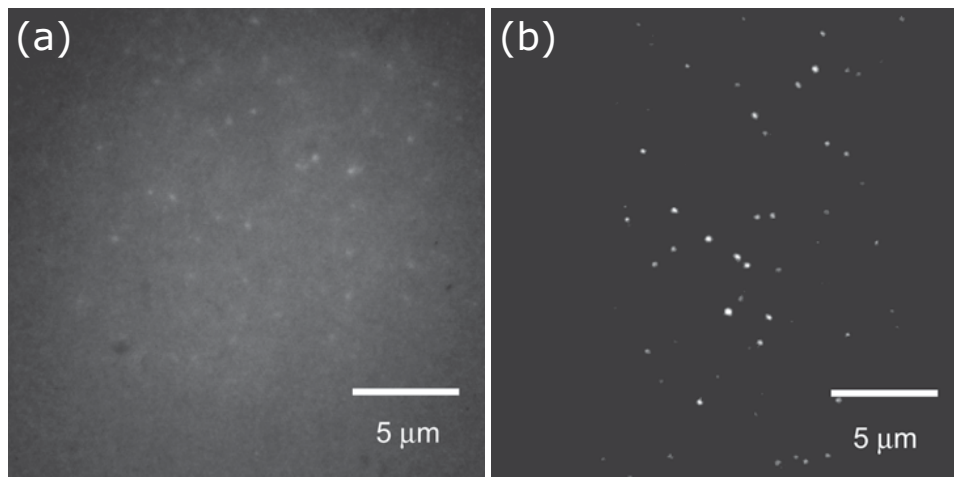
Figure 1.4: Sample images of (a) conventional versus (b) TIRF illumination for 200 nm particles.

double layer repulsion, hindered diffusion, van der Waals forces, optical forces, depletion and steric interactions, and receptor-ligand pair interactions [37, 38]. However, scattering by nanometer-sized particles is weak and thus limited the minimum particle size to about one micron.

The advantage of the TIRF technique lies in its ability to produce extremely confined illumination at a dielectric interface by reflecting an electromagnetic wave off of the interface. An extremely high sensitivity is achieved by imaging fluorescent dyes or particles and illuminating only those fluorophores within $\sim$200 nm of the interface. Since no extraneous, out-of-focus fluorescence is excited, there is little background noise as shown in the TIRF image of 200 nm diameter colloidal particles in figure 1.4. Additionally, since the illumination intensity decreases monotonically away from the interface, it is possible to infer an object's distance from the interface through intensity. More recently, the TIRF technique was adopted by the microfluidics community, integrated into well established particle velocimetry techniques and called Total Internal Reflection Velocimetry (TIRV) [39] or

nano-PIV (nPIV) [6]. Typically, the method has been used to measure the dynamics of significantly smaller colloidal particles (10 nm to 300 nm) and applications have included the characterization of electro-osmotic flows [40], slip flows [41, 42], hindered diffusion [43, 44], near-wall shear flows [45, 46, 13, 47, 48] and quantum dot tracer particles [9, 10, 12, 13, 14].

In *Direct measurement of slip velocities using three-dimensional total internal reflection velocimetry* (chapter 4), we demonstrate the 3D-TIRV technique by quantifying fluid slip at the fluid-solid interface of a microchannel (verification of the no-slip boundary condition). The high resolution of TIRV provided a vehicle to estimate the slip length at about 50 nm. Another application of 3D-TIRV is provided in *Evanescent wave imaging of particle adhesion dynamics near solid surfaces* (chapter 8). We present results on the three-dimensional adhesion dynamics of micron-sized particles in shear tethered to microchannel substrates with applications to leukocyte rolling and adhesion to blood vessel walls, which are important functions for immune system surveillance and response.

1.2.2 Theory of Evanescent Wave Illumination

When an electromagnetic plane wave (light) in a dielectric medium of index, n_1, is incident upon an interface of a different dielectric material with a lower optical density, n_2, at an angle, θ, greater than the critical angle predicted by Snell's law, $\theta > \theta_{cr} = \sin^{-1}(n_2/n_1)$, total internal reflection occurs as illustrated in figure 1.5. Although all of the incident energy is reflected, the full solution of Maxwell's equations predicts the existence of an electromagnetic field in the less dense medium with intensity decaying exponentially away from the interface. This evanescent wave propagates parallel to the interface and has a decay length, δ, on the order of the wavelength of the illuminating light, λ_0. However, photons are not actually reflected at the interface, but rather tunnel into the low index material (a
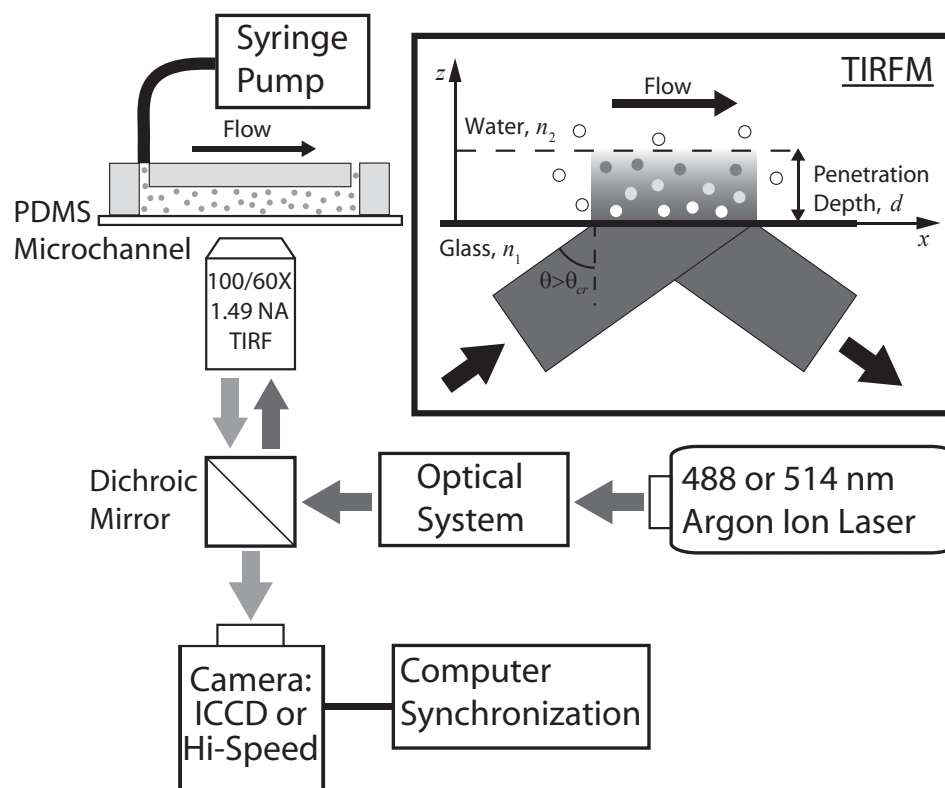
Figure 1.5: Typical TIRF imaging setup for measuring near-wall colloidal dynamics.

process called optical tunneling). As a result, the reflected beam of light is shifted along the interface by a small amount ($\Delta x \approx 2\delta \tan \theta$), which is known as the Goos-Haenchen shift [49].

The full details to this solution of Maxwell's equations are outlined elsewhere [35]. Only the basic results relevant to evanescent wave microscopy are presented below, specifically the intensity distribution in the lower optical density material. The solution presented here assumes an infinite plane wave incident on the interface, which is a good approximation to a Gaussian laser beam typically used in practice. The intensity has the exponential form

$$I\left(z\right) = I_0 e^{-z/\delta}, \tag{1.3}$$

where z is the coordinate normal to the interface into the low index medium, I_0 is the wall intensity and the decay length, δ, is given by

$$\delta = \frac{\lambda_0}{4\pi n_1} \left[\sin^2 \theta - n^2\right]^{-1/2}, \tag{1.4}$$

and $n = n_2/n_1 < 1$. In a typical system with a glass substrate ($n_1 = 1.515$), water as the working fluid ($n_2 = 1.33$) and an Argon Ion laser for illumination ($\lambda_0 = 514$ nm), a penetration depth of about $\delta = 140$ nm can be produced with an incident angle of $\theta = 64.0^o$. The polarization of the incident beam does not affect the penetration depth, but it does affect the amplitude of the evanescent field. For plane waves incident on the interface with intensity, I_1, in the dense medium, the amplitude of the field in the less dense medium, I_0
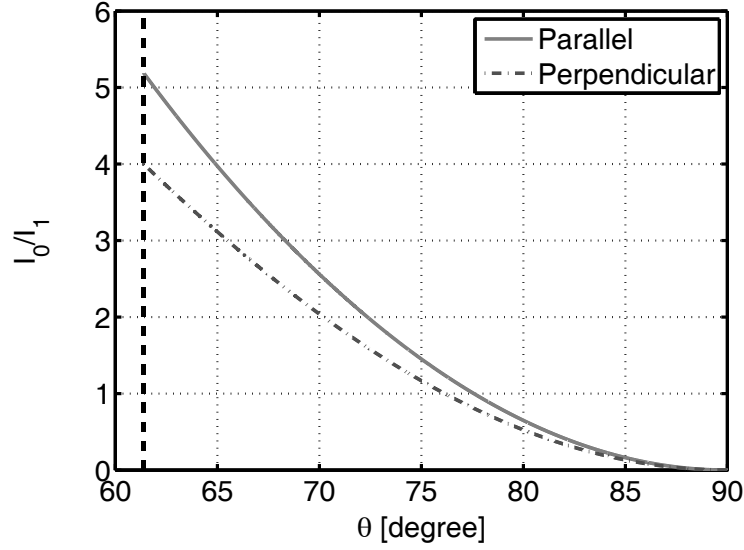
Figure 1.6: Evanescent field wall intensity as a function of incident angle for both parallel and perpendicular polarizations at a typical glass-water interface.

is given by

$$I_0^{\parallel} = I_1^{\parallel} \frac{4 \cos^2 \theta \left(2 \sin^2 \theta - n^2\right)}{n^4 \cos^2 \theta + \sin^2 \theta - n^2}, \tag{1.5}$$

$$I_0^{\perp} = I_1^{\perp} \frac{4 \cos^2 \theta}{1 - n^2}, \tag{1.6}$$

for incident waves parallel and perpendicular to the plane of incidence, respectively, as shown in figure 1.6. Both polarizations yield a wall intensity significantly greater than the incident radiation, with the parallel polarization being 25% greater than the perpendicular polarization.

1.2.3 Implementation and Particle Tracking

The basic components of a TIRF imaging system include: light source, conditioning optics, specimen or microfluidic device, fluorescence emission imaging optics and a camera. An

example of such a system is shown in figure 1.5. In past studies, light sources have included both continuous-wave (CW) lasers (argon-ion, helium-neon) and pulsed lasers (Nd:YAG) since they are collimated, narrow wavelength excitation sources. Non-coherent sources (arc-lamps) are not as common in typical homemade systems, but commercial versions are available. Conditioning optics are used to create the angle of incidence necessary for TIR and are of two types: prism-based and objective-based [36]. Prism-based TIRF systems are typically home-built and low cost. A prism is placed in contact with the sample substrate and coupled using an immersion medium. The laser beam is focused through the prism onto the substrate at an angle greater than the critical angle. Air immersion objectives are often used for imaging to prevent decoupling of the guided wave from the substrate into the imaging optics. In contrast, objective-based TIRF requires high numerical aperture objectives ($NA > 1.4$) to achieve the large incident angles required for total internal reflection. These objectives are usually high magnification ($60\times \leq M \leq 100\times$) immersion objectives. In this method, a collimated light source is focused onto the back focal plane of the objective, then shifted off axis to create the large incident angle. The fluorescence emission is then collected by the objective as in typical fluorescence microscopy, and the excitation light is rejected by spectral filtering with dichroic mirrors and filters. Another advantage to note is that the imaging depth in TIRF provides significantly greater resolution than the typical depth of field, DOF, of the objective given by:

$$DOF = \frac{\lambda_0 n_1}{NA^2} + \frac{n_1}{M \cdot NA} e,$$

(1.7)

where e is the smallest distance that can be resolved by the detector [50]. Even for a high magnification and large numerical aperture objective the DOF can be 600 nm or more.

With a TIRF microscopy system and microfluidics in place, quantitative images of particles in near-wall microflows are examined using one of several methods. μPIV [5] and nPIV [6] infer the most probable displacement of a fluid element from the cross-correlation peak between to sequential image segments taken in time. There are several shortcomings to this approach in near-wall studies. The high velocity gradient near the wall cannot be resolved directly. Additionally, since particles near the wall are brighter due to the evanescent field gradient, the cross-correlation method weights slower moving particles close to the wall more heavily, thus biasing the mean velocity. Small, Brownian particles in low Reynolds number flows typically have Peclet numbers of order unity. The Reynolds number, Re, is defined by

$$Re \equiv \frac{\rho V a}{\mu}, \tag{1.8}$$

and the Peclet number, Pe, by

$$Pe \equiv \frac{V a}{D_0}, \tag{1.9}$$

where a is the particle radius, V is the mean local velocity and ρ is the fluid density. These high levels of diffusion tend to degrade the sharpness of the cross-correlation peak and introduce additional uncertainty. Finally, no particle depth information is provided by PIV methods, and one typically assumed a uniform particle concentration near the wall, which is unlikely to occur. Several groups have demonstrated that the intensities of a wide range of particles diameters decay exponentially away from the fluid-solid interface with similar decay lengths to the penetration depth [51, 41, 47]. This makes it possible to discern the height of a particle from the wall, based on its intensity. Although there have been some attempts to evaluate cross-correlations over multiple particle layers [52] within the evanescent field, many difficulties still remain. Tracking individual particles near the wall

to resolve velocities is a much more direct method to measure their dynamics [39].

The statistical nature of colloidal dynamics makes particle tracking a natural fit [53]. In PTV, all particle locations from two or more successive video frames can be identified to good accuracy using their intensity centroids for large particles or by fitting a two dimensional Gaussian distribution to the diffraction limited spot for sub-wavelength particles [54, 55]. Next, particles are matched to one another between frames to track their trajectories. In some cases (for example, in fast moving flows), only two frames may be available at a time for matching (image pairs) due to limits in camera acquisition speed. If the tracer concentration is dilute, then nearest neighbor matching is simple and effective [13], and for large Peclet numbers, a multiple matching method may be useful [56]. However, for small Peclet numbers or highly concentrated particle solutions, a statistical tracking method [10] is advantageous, or possibly, a neural network matching algorithm [43, 17]. In the case that a multiple-frame image sequence is available, there is some benefit to using window shifting and predictor corrector methods [17], but only for large Peclet number. Once the ensemble particle displacements are measured, the individual intensities of matched particles can provide information about the particle distance to the wall as mentioned above. Colloidal particles typically have a large diameter size variation (3% to 20%), that can bias the interpretation of intensity to distance. Since particle intensity can also be a function of particle size [57, 58, 59], a large particle far from the wall can appear to have the same intensity as a small particle near the wall [41, 48]. Caution must be exercised when using these techniques as is outlined in *Measurement bias in evanescent fields due to particle size variations and force interactions* (chapter 5).

1.3 PARTICLE MOTION AND FLUID MEASUREMENTS

The dynamics of colloidal particles near fluid-solid interfaces provide a rich variety of interesting physical phenomena that are emphasized by the small length scales involved (less than one micron). Under shear flow, several additional forces, induced by the presence of the wall, may act upon the particles. The diffusion of particles as large as several microns is noticeable under high magnification, and small, nanometer-sized particles are highly Brownian. Hydrodynamic interactions between the particles and solid boundary suppress their diffusivity in an anisotropic manner. Spherical particles in shear flows are known to rotate with the flow and larger particle can experience lift forces. Buoyancy effects are also noticeable for non-Brownian particles or particle-fluid systems with a severe density mismatch. Electrostatic interactions can attract or repel charged particles and surfaces, and van der Waals attractive forces may be observed for even smaller separation distances. Finally, through observing particles in a microscopic environment, optical forces may be imparted to the particles due to either scattering or large electric field gradients.

Many of these individual effects have been studied in detail using evanescent wave microscopy, and the sum of their effects can have severe consequences on the interpretation of near-wall fluid velocity measurements. There are several important results. The wall-normal forces result in a non-uniform distribution of particles and may lead to a depletion layer near the wall. This concentration gradient causes a mis-weighting of the velocity profile. Rolling particles travel at a slower speed than the local fluid velocity, and dispersion effects, resulting from particle diffusion in the velocity gradient direction, also lead to misinterpretation of instantaneous particle velocity measurements. Below, we discuss some of the relevant physical interactions between colloidal particles an solid boundaries and summarize theoretical and experimental results in the dilute limit (we are not considering

particle-particle interactions). Additionally, we provide a synopsis of their effects on fluid velocity measurements in the near-wall region.

1.3.1   Near-wall Particle Dynamics

Hindered Brownian Motion

In the time since the original observations of Brownian motion in 1828 [60], the motion of small particles due to molecular fluctuations has become well-understood. The random forcing of small particles is damped by hydrodynamic drag resulting in an overall mobility, and the particle's motion can be described as a diffusion process [61] with diffusion coefficient, D_0, in an infinite quiescent fluid. For a spherical particle that is significantly larger than the surrounding solvent molecules, the mobility is described by the denominator in equation 1.2 [62]. When an neutrally buoyant, isolated particle is in the vicinity of a solid boundary, its Brownian motion is hindered anisotropically due to an increase in hydrodynamic drag. Several theoretical studies have accurately captured this effect for various regimes of particle-wall separation distance [63, 64, 65, 66]. In particular, the "method of reflections" approach is typically employed to estimate the wall-parallel drag force on a moving particle near a stationary wall in a quiescent fluid when the particle radius, a, is small compared to the separation distance to the wall, $z/a > 2$ [67]. Goldman *et al.* proposed an asymptotic solution based on lubrication theory for the drag force on a particle when the particle-wall separation distance is small, $z/a < 2$ [65]. Brenner, on the other hand, found an exact solution for the drag force on a particle in the wall-normal direction [64]. From these results, the anisotropic particle mobility is obtained. This specifies the spatially varying diffusion coefficients in the wall-parallel direction, D_x, and wall-normal direction, D_z, which are plotted in figure 1.7. These theoretical results have been verified
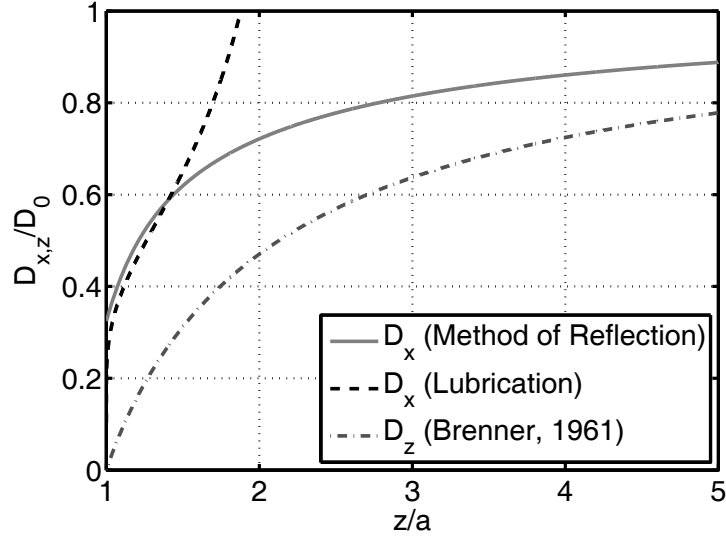
Figure 1.7: Hindered diffusion coefficients in the wall-parallel, D_x, and wall-normal, D_z, directions for a neutrally buoyant, spherical particle near a solid boundary.

over different length scales by various researchers including several evanescent wave illumination studies [68, 37, 69, 70, 71, 72, 44]. Both components of the hindered diffusivity become noticeable for particle-wall separation distances of order one (see appendix A).

Near-wall Shear Effects

It is well known that rigid particles tend to rotate in shear, and in the special case of a sphere near a planar wall, additional hydrodynamic drag slows the particle's velocity below that of the local fluid velocity [63, 66]. Goldman *et al.* showed that the velocity, v, of neutrally buoyant particle with radius, a, that is free to move in a near-wall shear flow with shear rate, S, is given again by the "method of reflections" for large z/a, and by an asymptotic solution based on lubrication theory for small z/a [66] as shown in figure 1.8 (see appendix A). As we will discuss later, this effect has major implications for the interpretation of the fluid velocity from the measured particle motion. Particle rotation also induces a lifting
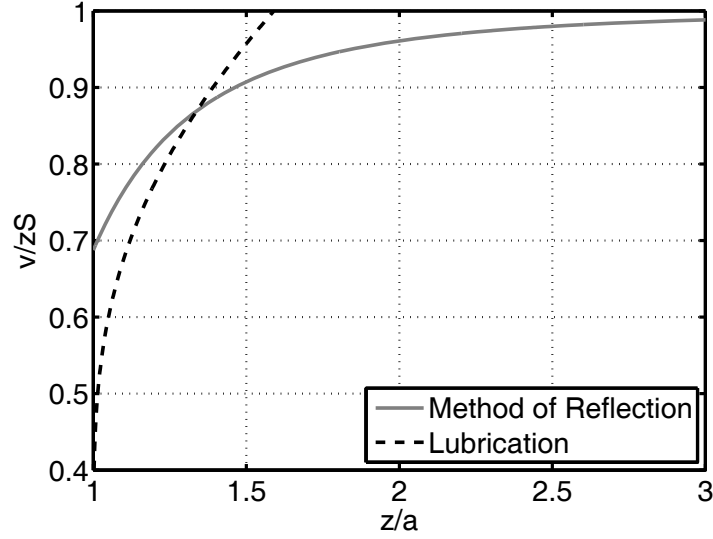
Figure 1.8: Particle velocity relative to the local fluid velocity in a near-wall shear flow given by the method of reflection and asymptotic solutions from Goldman *et al.*, 1967b.

force, which tends to make the particles migrate away from the wall [73]. The magnitude of this force depends upon the Reynolds number near the wall, where the velocity scale is based on the shear rate and particle distance from the wall, and the particle Reynolds number with the velocity scale being the relative velocity of the particle to the local fluid velocity [74]. For nano-particles within several radii away from the wall at moderate shear rates in microchannels, these lifting forces are negligible [75].

Electrostatic and van der Waals Forces

Electrostatic forces arise from the Coulombic interactions between charged bodies. When immersed in an ionic solution, these forces are moderated by the formation of an ionic double layer on the surfaces of the bodies, which screens the charge. The characteristic length scale of these forces is given by the Debye length, κ^{-1}, which is inversely proportional to the square root of the ionic concentration, $\kappa^{-1} \propto c^{-1/2}$, [76]. For a plane-sphere geometry,

the potential energy of the interaction decays exponentially:

$$\frac{U^{el}(z)}{k_b T} = \hat{B}_{ps} e^{-\kappa(z-a)}, \tag{1.10}$$

where $\hat{B}_{ps}$ is the non-dimensional magnitude of the electrostatic potential energy [77] given in appendix B. Several experimental studies have accurately measured electrostatic forces between colloidal particles and surfaces through evanescent wave microscopy [78, 37]. When considering particle dynamics over length scales on the order of nanoparticle radii, contributions from attractive, short-ranged van der Waals forces should be considered. However, evanescent wave imaging experiments have been unsuccessful in a definitive measurement of van der Waals forces. These forces originate from multipole dispersion interactions [79], and the typical length scale over which they act is on the order of 10 nm. The potential associated with the van der Waals interactions for a plane-sphere geometry is given by

$$\frac{U^{vdw}(z)}{k_b T} = -\frac{A_{ps}}{6 k_b T} \left[\frac{a}{z-a} + \frac{a}{z+a} + \ln\left(\frac{z-a}{z+a}\right) \right], \tag{1.11}$$

where A_{ps} is the Hamaker constant for the system [80, 81].

Other Forces

In specific situations, several other forces may also be relevant to the near-wall dynamics of colloidal nanoparticles. Particle-particle interactions (including hydrodynamic effects, electrostatic, van der Waals, etc.) become important for high particle concentrations, but are generally negligible when particles are used as fluid tracers with small volume fractions ($< 0.1\%$). The gravitational forces for nearly density-matched, nanometer-sized particles are also small when compared to the thermal energy ($U^g/k_b T \sim 10^{-5}$) and may be neglected.

However, for micron-sized particles, this effect can have a strong contribution. Finally, optical forces from the illuminating light can trap or push colloidal particles [82]. In many experiments, this force is exploited to manipulate small objects by conventional optical tweezers [83] and has also been demonstrated using evanescent waves [84]. When the particles are used as fluid tracers, illumination power is typically minimized ($U^{opt}/k_b T \sim 10^{-3}$) in order to prevent optical trapping effects (see appendix B). However, further studies should be conducted to determine the forces on strongly absorbing particles, which can be repulsive (for example the semiconductor materials found in quantum dots).

1.3.2   Velocity Measurement Accuracy

As we have shown in the previous section, several competing effects can influence the motion of colloidal nanoparticles near solid surfaces. Evanescent wave imaging (with and without fluorescence) has been applied to verify many of these effects. However, they pose a problem for colloidal particle image-base velocity measurement techniques at the microscale [5] and nano-scale [6, 39, 41, 10]. There are several obvious consequences, which result directly from the particle dynamics discussed above. First and foremost, the tracer particles are convected along at a speed slower than the local fluid velocity due to an additional hydrodynamic drag imposed by the wall. This effect has been addressed in several studies [41, 47] including *Direct measurement of slip velocities using three-dimensional total internal reflection velocimetry* (chapter 4).

When attempting to measure the mean velocity or velocity profile near a solid boundary through particle-based imaging, the concentration distribution of particles in the wall-normal direction must be established to properly weight the spatially varying velocity. In many previous studies, the concentration distribution has been assumed to be uniform,

which is almost never the case [6, 39]. The equilibrium concentration of colloidal particles in the wall-normal direction from a liquid-solid interface is given by the Boltzmann distribution

$$p(z) = p_0 \exp\left[-U(z)/k_bT\right], \tag{1.12}$$

where p_0 is a normalization constant [37] and U is the total potential energy of a particle. In the absence of any forces between particles and the surface, the potential energy is zero, leading to a uniform particle concentration distribution. However, electrostatic, van der Waals, optical and gravitational forces can create non-uniform potentials between the particle and wall, thus leading to non-uniform concentration distributions as shown in figure 1.9 for a 500 nm diameter polystyrene particle in water near a glass substrate with a 10 nm Debye length.. The formation of a depletion layer near the wall can thus skew the inferred mean fluid velocity to higher values [37, 47, 48, 46]. We address these issues in *Hindered Brownian motion and depletion layer of particles in shear flow and their implications for near-wall velocimetry* (chapter 6). In a related matter, for the case of TIRF imaging of nanoparticles, particle size non-uniformity and the decaying evanescent intensity field further modify the *measured* particle concentration distribution. We discuss in detail these phenomena and their effects on particle velocimetry with TIRF in *Measurement bias in evanescent fields due to particle size variations and force interactions* (chapter 5).

Recently, much attention has been devoted to quantifying the accuracy of near-wall velocimetry measurements in TIRV and other such methods due to dispersion effects [45, 46, 13]. The spatial variation in diffusivity due to hindered Brownian motion normal to the wall is a major cause of measurement bias for long inter-frame time intervals between two successive particle images. However, the shear-induced velocity lag of particles causes a more significant bias if the time interval between image acquisitions is short. This effect is shown
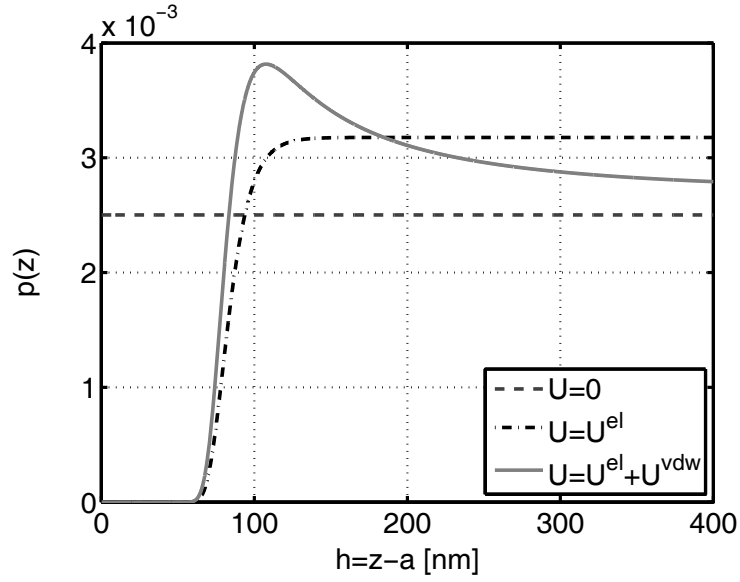
Figure 1.9: Near-wall particle concentration profiles for a 500 nm diameter polystyrene particle in water near a glass substrate with a 10 nm Debye length.

in figure 1.10 where ΔT is the non-dimensional inter-frame time appropriately normalized by the characteristic diffusion time given by the particle radius and diffusion coefficient, $\Delta T = \Delta t a^2 / D_0$ and $\langle V_p \rangle / \langle V_f \rangle$ is the ensemble averaged particle velocity normalized by the mean fluid velocity. In *Hindered Brownian motion and depletion layer of particles in shear flow and their implications for near-wall velocimetry* (chapter 6), we address many of these issues and use a Langevin simulation along with experiments to confirm the results velocimetry to measure fluid velocities. Additionally, in *High-speed quantum dot tracking using evanescent wave illumination* (chapter), we apply high-speed quantum dot tracking to near-wall velocimetry as additional confirmation of this effect at smaller particle length scales.
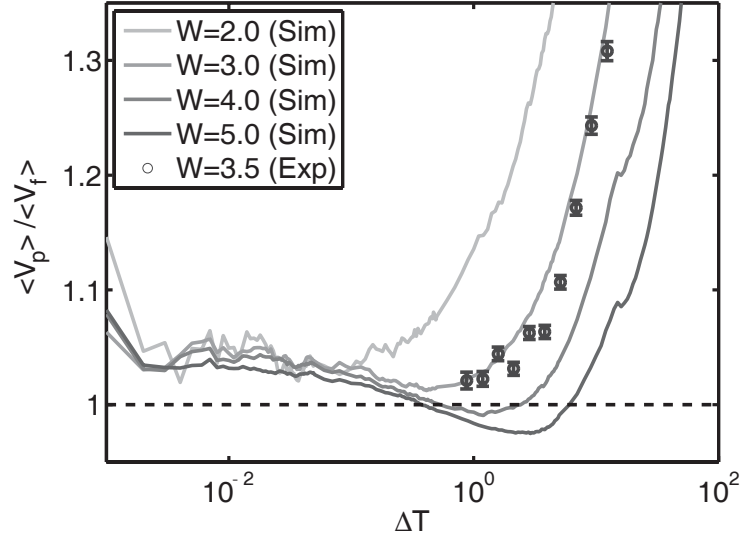
Figure 1.10: Numerical simulation and experimental verification of mean particle velocity normalized by the mean fluid velocity within a finite region of a near-wall shear flow for various inter-frame times, ΔT, which are appropriately normalized by the characteristic diffusion time given by the particle radius and diffusion coefficient, $\Delta T = \Delta t a^2 / D_0$.

1.4 ELECTROSPRAY DIAGNOSTICS

When a Taylor cone is formed in a an electric field by the free surface of conducting fluid contained at the end of a capillary tube, a microscale, high-speed liquid jet emanates from the apex of the Taylor cone [85]. Due to the small diameter of the jet (several microns), surface tension forces dominate eventually necking it into droplets. The like-charged droplets exert a Coulombic repulsion forces on one another, causing the linear droplet stream to diverge into an electrospray. This process of electrospray atomization produces mono-disperse droplets at high velocities and has found many applications in space propulsion [86, 87, 88, 89], mass spectrometry [90], aerosol science [91], and combustion technology [92]. Many different emission modes of electrosprays have been described in the past [93, 94], but one of the simplest and most useful is the stable cone-jet mode [95, 96].

Several studies have been conducted to characterize different aspects of both the Taylor cone and it's emissions. Ganan-Calvo studied droplet size and velocity dependence on axial and radial position [97]. Later, they examined emission current and droplet size for various fluids and conductivities using phase Doppler anemometry (PDA) and developed scaling laws [98]. Cloupeau and Prunet-Foch used a laser granulometer to measure droplet diameter and emission frequency [96]. Tang and Gomez also used a PDA to study droplet size, axial velocity, droplet concentration and field strengths. Additionally, they quantified the relative importance of the external field and the Coulomb interaction among the charged droplets [99]. Gamero-Castano and Hruby used time-of-flight and energy analysis techniques to measure the voltage difference, velocity, and natural wavelength for varicose breakup of the jet [86]. However, their study was inconclusive in determining if the droplet diameter scaling with flow rate is of the Ganan-Calvo form [98] or Fernandez de la Mora [100]. Fernandez de la Mora presented results on the current and droplet size emitted from highly conducting Taylor cones, and put forth scaling laws for both current and droplet size relative to flow rate [101]. de Juan and Fernandez de la Mora investigated droplet charge and diameter using a differential mobility analyzer (DMA) [100].

Many indirect methods for electrospray diagnostics exist (listed above), but direct imaging of electrosprays has not been exploited to its fullest. Both standard fluorescence microscopy and digital in-line holography are powerful, quantitative imaging techniques applicable to electrosprays to quantify droplet size, structure and dynamics. Holographic image reconstruction has been used to measure the position, size and motion of micron-sized particles and microorganisms suspended in both fluids and solids [102, 103, 104, 105, 106]. In in-line holographic microscopy, coherent laser light is scattered by an object (electrospray droplets), which interferences with the unperturbed laser light (reference beam) creating a
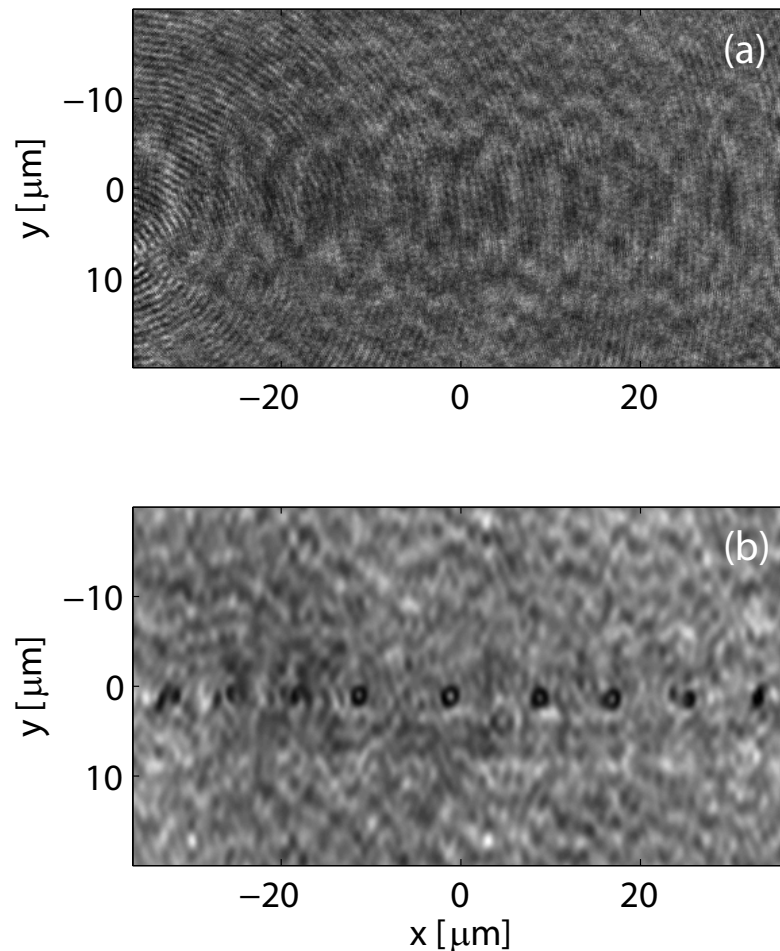
Figure 1.11: Sample holographic reconstruction where (a) is the original hologram image at 75 μm out of focus and (b) is the mathematical image reconstruction at 75 μm from the hologram plane.

hologram, $I_h(x, y)$, on a CCD detector [107] as shown in figure 1.11a. The three-dimensional field, $f(x, y, z)$, is mathematically reconstructed from a single hologram image [104]. Once the intensity volume is reconstructed, particles are located by searching for dark regions within the volume shown in figure 1.11b. Holography is a powerful technique that can be used to extract detailed, three-dimensional information from the complex dynamics of electrospray droplet distributions. In *Visualization and tracking of electrospray droplet emissions using fluorescence and holographic techniques* (chapter 9), we demonstrate the use of

both fluorescence microscopy and in-line holographic microscopy for electrospray droplet measurements.

1.5 SUMMARY

The dynamics of colloidal particles near solid surfaces represents an important branch microscale science. In addition to pure science and colloidal physics, near-wall particle dynamics are also important to medicine, biology, biophysics and engineering. Colloids play an important role as diagnostic tools in microscale fluid mechanics, and understanding their behavior will improve measurement accuracy and bring about new applications. As microfabrication techniques improve, the nominal dimensions of microfludic devices continue to decrease down to nanometer scales, where wall effects are increasingly important. Quantum dots (QDs) are proven to be viable colloidal particles for studying both particle and fluid dynamics. As fluid tracers, they are among the most robust nanometer-sized particles to date and have been used to measure both fluid velocity and temperature. As the technology develops, the quantum efficiency and brightness of QDs is sure to improve as will their temperature sensitivity.

Evanescent wave microscopy is an invaluable tool for studying near-wall colloidal dynamics and in addition to biophysics, it has yielded a number of contributions to the fields of micro- and nano-scale fluid mechanics and mass transport. These applications include investigation of the no-slip boundary condition, applications to electrokinetic flows, measurement of electrostatic forces and verification of hindered diffusion. As the resolution of evanescent wave microscopy improves, robust three-dimensional tracking of small particles and QDs will follow. Extremely high numerical aperture imaging optics, low noise/high sensitivity camera systems, control over smaller evanescent field penetration depths and on-

chip evanescent wave illumination will all contribute to facilitate these advances. Although evanescent wave microscopy is a well-established technique, it's application to microscale fluid mechanics and nanoparticle colloidal dynamics is relatively new. There are vast new areas for the expansion of this technology including application to nanochannels and micro-patterened substrates.

Similarly, electrospray technology is also well-established. However, the application of new diagnostic techniques can bring about a deeper understanding of the complex under-lying physics. With standard fluorescence microscopy, direct imaging of droplet sprays in two dimensions can be achieved. Although somewhat computationally expensive, in-line holographic microscopy can easily extract three-dimensional droplet spray structure and eventually droplet dynamics.

Chapter 2

Statistical particle tracking velocimetry using molecular and quantum dot tracer particles

J.S. Guasto, P. Huang and K.S. Breuer. *Experiments in Fluids*, Vol. 41, pp. 869-880, 2006.

We present a statistical approach to particle tracking velocimetry developed to treat the issues associated with nanometer-sized tracer particles such as fluorescent molecules and quantum dots (QDs) along with theory and experimental results. Extremely small tracers pose problems to traditional tracking methods due to high levels of thermal motion, high levels of intensified camera noise, high drop-in/drop-out rates and, in the case of quantum dots, fluorescence intermittency ("blinking"). The algorithm presented here compensates for these problems in a statistical manner and determines the physical velocity distributions from measured particle displacement distributions by statistically removing randomly distributed,

non-physical tracking events. The algorithm is verified with both numerically simulated particle trackings and experiments using 54 nm diameter fluorescent dextran molecules and 6 nm and 16 nm diameter QDs.

2.1 INTRODUCTION

Particle Image Velocimetry (PIV) and Particle Tracking Velocimetry (PTV) have become integral techniques in experimental fluid mechanics. Originally developed for macroscale measurements, these velocimetry methods have evolved to suit applications in microscale fluid mechanics (μPIV and μPTV). Both techniques employ the use of tracer particles suspended in a fluid of interest along with digital cameras to capture successive images of particle position in the fluid through time. PIV uses cross-correlation algorithms to determine the most probable spatial displacement for an interrogation region (IR) within an image pair [4]. High density particle seeding and low diffusivity is preferable to increase accuracy. PTV methods, on the other hand, typically track single particles and use particle center detection with nearest-neighbor matching to determine the most probable single particle displacement [7]. For PTV, low particle seeding density is necessary to ensure one-to-one tracking between IRs.

As we approach the nanoscale in fluid mechanics, Brownian motion, camera noise and the desire for higher tracer particle seeding make traditional PTV methods difficult to implement. Brownian motion increases as tracer particle diameter decreases, resulting in large variations in the measured velocity, even for a "steady" flow. In addition, thermal motion leads to high particle drop-out, in which particles observed in the first IR of an image pair are lost from the subsequent IR. Since CCD cameras are limited by a finite exposure time and image pair separation time, IRs must be chosen to cover a relatively large image

area to adequately capture a significant number of tracer particles that would otherwise drop-out within that time. Large IRs and/or dense tracer particle concentrations result in the gross mismatching of tracer particles, which is a major problem for PTV methods that rely on one-to-one tracking.

Nanometer-sized tracers also have a significantly lower image intensity than tracer particles measuring several hundred nanometers, which requires experiments to push the detection limits of intensified CCD (ICCD) cameras. High intensifier gain produces significant shot noise and intensifier noise, much of which is easily rejected through imaging optimization and image processing. However, at high intensifier gain, ICCD cameras can produce noisy artifacts due to effects like blooming and cross-talk [16], which can appear similar in shape, size and intensity profile to real tracer particles. This intensifier noise is often indistinguishable from a tracer particle's diffraction-limited spot, and consequently, may be misconstrued as a real particle by a PIV/PTV algorithm. This leads to another source of tracking error - false particle images.

Nanoparticles themselves also introduce unique problems for tracking algorithms. Semiconductor nanocrystals or quantum dots (QDs) are promising new nanofluidic tracer particles [8, 9]. Although, they exhibit several qualities beneficial for nano-velocimetry (small diameter, tunable wavelength, variable surface coating), their high diffusivity makes them difficult to track. Also, they experience fluorescence intermittency or "blinking," which results in periods of fluorescence and dormancy on time scales ranging from sub-milliseconds to hours [18]. We discuss the effects of this phenomena on tracking algorithms and show that it can be interpreted as an additional optical drop-in/drop-out.

In order to address these issues, we present a statistical particle tracking method, which is similar in principle to traditional PTV algorithms, but resolves all of the above-mentioned

problems. The technique deliberately measures velocity distributions (rather than a single velocity), and utilizes a large search window to purposely include multiple tracer particles. Drop-in/drop-out particles, blinking particles and extraneous intensifier noise signals are all included in the tracking, and later eliminated from the velocity distribution by exploiting their statistical nature. The algorithm is validated both experimentally, by tracking single molecules and QDs, and with a particle tracking simulation. The remainder of the paper is organized as follows: The next section discusses the statistical tracking algorithm, including a theory for particle drop-out, proposed statistical techniques for removal of spurious tracking due to intensifier noise, drop-in/out and QD blinking, and numerical validation. Lastly, experimental validation is presented using both molecular and quantum-dot tracer particles.

2.2 THEORETICAL CONSIDERATIONS

2.2.1 Principles of Statistical Tracking

Single particle tracking is difficult with high tracer particle concentrations, or analogously, highly diffusive tracer particles, because during any reasonable time delay, each particle can move a large enough distance (due to diffusion and/or convection) to infringe on the IR of another particle. Nearest-neighbor matching does not guarantee a correct match, and one-to-one tracking may not be possible given the need for a large IR to catch large particle displacements, which will undoubtedly include spurious particles. Consider an ideal image pair with particles in motion but no noise, no drop-in/drop-out and no blinking. In a typical PTV algorithm, the sub-pixel center locations of all individual particles are found using a thresholding and center detection scheme in both images. Next, an IR (usually square or

circular) of predetermined size is centered on each individual particle in the first image and tracked to a *single* particle in the second frame, which falls within that IR. If more than one particle (or zero) is detected in the IR of the second frame, then those possible trackings must be omitted due to uncertainty. The IR size and particle seeding density must be carefully selected in conjunction with the diffusion and convection in the system to ensure one-to-one tracking, and this generally requires low seeding densities.

In the Statistical Particle Tracking Velocimetry (SPTV) algorithm, we implement a similar approach, but allow multiple particle trackings for each IR, which allows for larger IRs and higher seeding densities. A rectangular IR is constructed around each particle in the first image. The IRs need not be centered around each particle, but they should have the same orientation with respect to each particle. Next, we compute displacement vectors from the single original particle location to every particle detected within that IR in the second image. Over a given spatial region of the image where the diffusion and convection are approximately constant, we repeat this procedure for all particles and many images (several hundred), building a large distribution of particle displacements. Again, for ideal images and a sufficiently large IR, we guarantee that one displacement vector of the multiple trackings for each IR is correctly matched. All other trackings are computed from uncorrelated positions due to mismatching. Because of the manner in which we produce the IRs, the displacement distribution of the mismatched particles form a random, uniform distribution. By estimating the size of the random distribution it can be statistically subtracted from the total displacement distribution to reveal the physical displacement distribution (a similar method was first proposed by [56]).

In practice, we must consider the effects of tracking particles which physically drop-in and drop-out of the image due to diffusion and convection, and optically drop-in and

drop-out due to blinking in particles such as QDs. We will show later that these two phenomena can be treated identically. Additionally, small, low intensity tracer particles require the use of high gain ICCD cameras, which can produce random intensifier noise signals that can appear identical to tracer particles in size, shape and intensity. These intensifier noise signals can meet the detection criteria for real particle signals and are often tracked mistakenly. Thus, when we track a signal (real particle or noise) from the first image to a signal from the corresponding IR of the second image, the tracking has one of five possible meanings: (1) particle to particle (physical), (2) particle to particle (mismatch), (3) noise to particle, (4) particle to noise and (5) noise to noise tracking. Each of these phenomena make single particle tracking, and possibly PIV ensemble particle tracking less accurate due to the presence of random statistical contamination. We can easily rationalize that for a large ensemble of trackings, all non-physical trackings contribute to a random, uniform displacement distribution just as the mismatched particles in the ideal case. The reason is that at least one of the two signals is randomly located in its image with respect to the other, and thus there is no correlation between the positions of the two signals.

The SPTV technique is comparable to a method developed by Breedveld et al [56], who presented an algorithm that is based on the spatial correlation of all particle locations over a single IR with diffusion and convection for the purpose of measuring self-diffusion in suspensions. The method can account for physical drop-out and if it were applicable at the time, optical drop-out (blinking). However, the algorithm does not take into account random detectable signals such as those due to ICCD camera noise, which was not applicable for their experiments with large particles (tens of microns) in direct illumination. Additionally, complicated displacement distributions resulted from the choice of IR, which requires an assumed velocity profile and could not be evaluated due to dependence on other

unknown functions. In practice, the authors were able to determine the shape of the particle displacement distribution through a clever symmetry argument, then extract the diffusion dynamics through a Gaussian fit of the particle displacements.

The strength of the SPTV algorithm is in considering the contributions of random noise signals and the choice of IR such that the uncorrelated trackings always form a simple random, uniform distribution. Additionally, the individually tracked particles can easily be re-binned across different regions of the image to resolve non-uniform velocities. This technique can in principle be used in systems with high particle seeding as long as individual particles are discernible for proper center detection. The average velocity and thermal motion can be extracted from the total displacement distribution function by fitting a distribution (Gaussian or otherwise). This can be done more generally through estimating the height of the random displacement distribution and subtracting the contributions of its moments from the total distribution. For this procedure, the drop-out and number of real particle signals must be estimated. A general method is critical in nanoscale systems where non-Gaussian particle motions are common (for example close to walls where hindered diffusion and shear generate asymmetric particle displacement distributions [39, 41]).

2.2.2 Tracer Particle Diffusion and Drop-out Estimation

As tracer particle size decreases, the contribution of diffusion to velocity measurements becomes considerable and cannot be ignored. Here we present estimations for tracer particle diffusion and drop-out. In the fluid bulk, diffusion is isotropic and can be decoupled in all three dimensions. Additionally, we do not include coupling of convection and diffusion, since Peclet numbers tend to be quite small (less than 0.04 for our experiments). The probability that a single particle will displace a distance Δz during a time interval Δt typically follows

a Gaussian distribution and, in one dimension, is described by

$$P(z) = \frac{1}{\sqrt{2\pi}d} \exp\left[-\frac{\Delta z^2}{2d^2}\right], \text{ with } d = \sqrt{2D\Delta t}, \tag{2.1}$$

where d is the characteristic diffusion length (and the standard deviation of the probability distribution $P(z)$) and D is the diffusivity. For Newtonian fluids, D is accurately approximated by the Stokes-Einstein equation

$$D = \frac{k_B T}{6\pi\mu a}, \tag{2.2}$$

where k_B is Boltzmann's constant, T is the absolute temperature of the fluid, μ is the dynamic viscosity of the fluid and a is the radius of the tracer particle.

A particle experiences out-of-plane drop-out when it diffuses along the optical axis z, perpendicular to the focal plane and out of the finite effective depth of field, $2h$, described by

$$h = \left[\left(\frac{1-\sqrt{\epsilon}}{\sqrt{\epsilon}}\right)\left[a^2\left[(n/NA)^2 - 1\right] + \frac{1.49\left(M+1\right)^2 \lambda_{em}^2 \left[(n/NA)^2 - 1\right]^2}{4M^2}\right]\right]^{\frac{1}{2}}, \tag{2.3}$$

where λ_{em} is the emission wavelength of the particle, n is the index of refraction of the immersion medium, M is the lateral magnification, NA is the numerical aperture and ϵ is chosen to be 0.1 [108, 27]. Estimates for the region of particle detectability (table 7.1) are comparable in magnitude to the depth of field of the objective [50].

The probability distribution for the initial position z_0 of any particle (measured from the center of the focal plane) is given by $P(z_0) = 1/2h$ assuming uniform detectability, while the final position, $P(z|z_0)$, after a time Δt is given by equation 2.1 (see figure 2.1).

Particle	Fluid	λ_{em} (nm)	$2a$ (nm)	μ (cP)	d (nm)	$2h$ (nm)	h/d
Microsphere	Water	612	500	0.9	87	630	3.60
Microsphere	Water	612	200	0.9	138	469	1.70
FITC-Dextran	Glycerol & Water	525	54	24.3	115	177	0.77
Quantum Dot	Toluene	614	6.1	0.6	2,150	130	0.03
Quantum Dot	Hexane & PDMS	614	6.1	413	83	292	1.77
Quantum Dot	Water	606	16	0.9	489	427	0.44
Quantum Dot	Glycerol & Water	606	16	50	147	201	0.69

Table 2.1: Properties for typical tracer particle/fluid systems.

The final positions of particles detected within the focal plane is

$$P(z, z_0) = P(z_0)P(z|z_0) = \frac{1}{2h\sqrt{2\pi}d} \exp\left[-\frac{(z-z_0)^2}{2d^2}\right]. \qquad (2.4)$$

Integrating over the effective depth of field yields the probability, $P_{\perp,i}$, that a tracer particle initially in the depth of field will remain there after time Δt, while the out-of-plane drop-out probability is $P_{\perp,o} = 1 - P_{\perp,i}$. This can be expressed by the ratio between the focal plane depth and the diffusion length, h/d, and is shown in figure 2.2. Also shown are two typical μPIV operating conditions: a 300 nm particle in water imaged with a 60$\times$ objective, and a 6 nm QD with a 100$\times$ objective and fluid viscosity of water.

We can perform a similar analysis for the in-plane drop-out. For an asymmetric displacement distribution the most probable displacement is not necessarily the mean displacement, therefore, the distribution tails must be captured to completely quantify the distribution. In the case of pure diffusion, a square IR of side length $2l$ is constructed around the center of every particle in the first frame of an image pair. However, if a mean local velocity $\bar{u}$ is present, we assume that the IR is chosen sufficiently large to capture the tails of the distribution or appropriately shifted in the direction of the local velocity by an amount
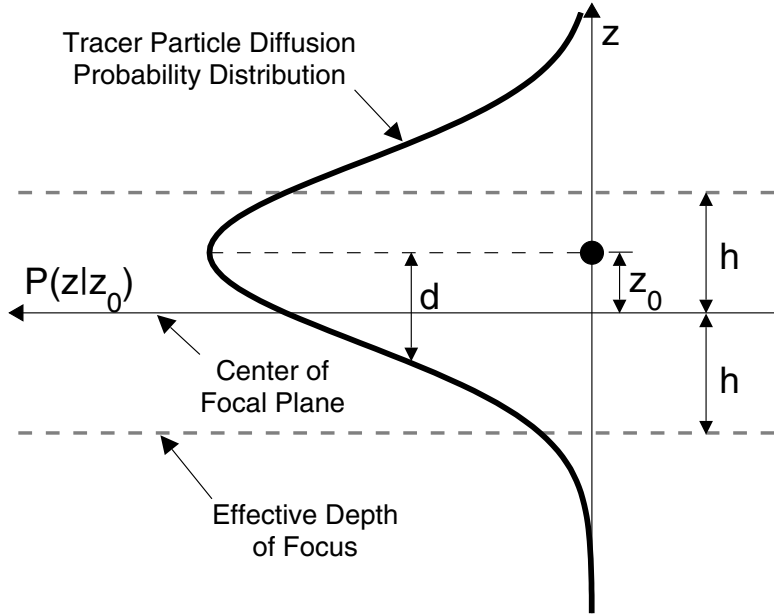
Figure 2.1: Diagram illustrating tracer particle diffusion along the optical axis, relative to the depth of field from an initial position z_0 to a final position z after a time Δt. Out-of-plane drop-out results when the final position of a tracer is outside of the depth of field, $2h$.

$\bar{u}\Delta t$, neither of which affect the shape of the spurious tracking distribution. For diffusion, the in-plane particle displacement is given by

$$P(x,y) = P(x)P(y) = \frac{1}{2\pi d^2} \exp\left[-\frac{x^2 + y^2}{2d^2}\right].\qquad(2.5)$$

Equation (2.5) is integrated over the IR to yield the probability, $P_{\parallel,i}$, that a given particle will stay within the IR. Thus, the in-plane drop-out probability is $P_{\parallel,o} = 1 - P_{\parallel,i}$, which is shown in figure 2.3. We can choose $l/d \gg 1$ so that the in-plane drop-out probability is effectively zero. In practice, if we choose l/d over 3, $P_{\parallel,o}$ will be less than 1% for diffusion and/or convection, when the tails of the displacement distribution are included, effectively eliminating in-plane drop-out. We point out that a 6 nm QD requires an IR side length
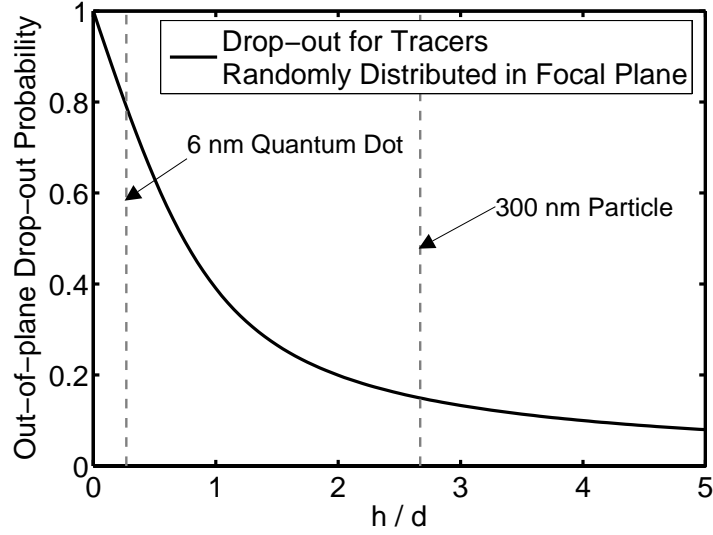
Figure 2.2: Out-of-plane tracer particle drop-out probability, where h is the half-depth of the focal plane and d is the diffusion length of the tracer particle. Also shown are two typical cases for h/d: a 300 nm particle in water imaged with a $60\times$ objective, and a 6 nm quantum dot in water imaged with a $100\times$ objective.

7 times greater than a 300 nm particle for the same fluid conditions and exposure time.

Combining the in-plane and out-of-plane drop-out, the total drop-out probability, P_{drop}, is

$$P_{drop} = 1 - P_{\perp,i}P_{\parallel,i}. \tag{2.6}$$

2.2.3   Statistical Particle Tracking Procedure

Next, we describe the SPTV algorithm procedure and theory to predict contributions of spurious trackings. An image pair consists of two sequential CCD images (image A and image B with area A_{image}). For each image pair, basic image processing techniques are first applied to eliminate defective pixels and other obvious noise signals. Following this, "signals" (i.e. potential particles) are identified through intensity thresholding. Next, the
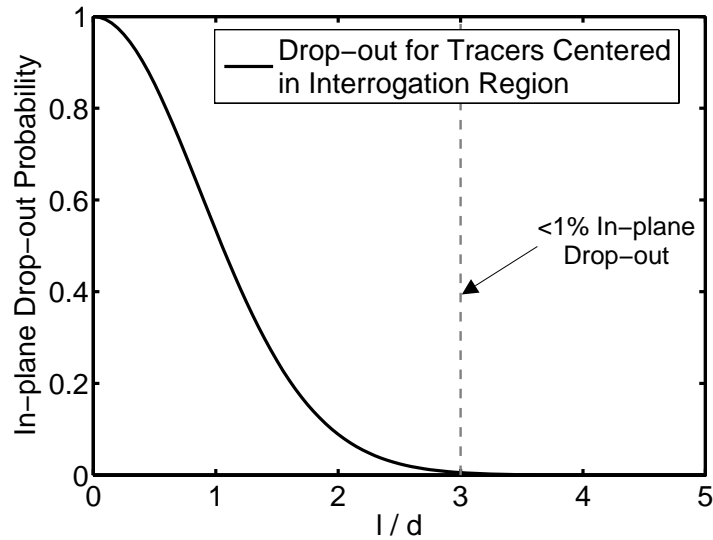
Figure 2.3: In-plane tracer particle drop-out probability where l is the half-width of the interrogation region (IR) and d is the diffusion length of the tracer particle. Choosing an IR greater than 3 times the particle diffusion length ensures to 99.5% probability that a particle originally centered in the IR will not drop out of the IR within the focal plane.

sub-pixel center locations of each signal are found through a 3×3 pixel, two-dimensional Gaussian fit. The Gaussian fit is used to approximate the diffraction limited spot produced by the sub-wavelength diameter particles and has been shown to be more accurate in determining particle displacements than correlation methods for single sub-wavelength particles [54]. However, with the long exposure times typically used for low intensity probes, significant tracer motion can affect the accuracy of the Gaussian center detection method at low viscosities. An IR is defined around a single signal in image A according to the criteria set by section 2.2.2. Displacements in x and y are computed from that single signal location in image A to any signal location in image B that falls into that IR. This process is repeated for each signal identified in image A, then a displacement distribution is constructed from the cumulative data. Additionally, displacements may be binned together for smaller sections

of each image to resolve velocity gradients. However, the bins should be small enough so that the velocity is approximately constant in that region and several hundred images are typically needed to achieve proper statistical averaging. Finally, the spurious, uncorrelated trackings must be removed from the total displacement distribution. For the purposes of this paper, a Gaussian distribution was fitted to the distribution lineshape to extract the random, uniform distribution due to uncorrelated trackings.

In theory, the size of the uncorrelated tracking distribution can be determined if we know the both the drop-out probability and the number of real particles per image. The drop-out can be calculated from the theory outlined in section 2.2.2. The number of real particles per image can be determined by carefully seeding the fluid, which is characterized by an area concentration, c_P, due to the integration of the camera through the focal plane. For an image with area A_{image}, the number of physical particle trackings is

$$N_{PP,phys} = A_{image} c_P \left(1 - P_{drop}\right), \tag{2.7}$$

where P_{drop} is the total drop-out probability, estimated from the system properties (equations 2.1-2.6). The number of spurious trackings is given by $(N_{total} - N_{PP,real})$, where N_{total} is the total number of tracking found from the SPTV algorithm, which can now be subtracted from the total displacement distribution.

Furthermore, we can estimate the number of particle-noise, noise-particle and noise-noise trackings. The number of each contributing to the random displacement distribution is simply the number of one type of signal (particle or noise) found in image A multiplied by the expected number of another signal type found in an IR of image B. The resulting

number of trackings are as follows:

$$N_{NP} = A_{IR} c_P c_N A_{image}, \tag{2.8a}$$

$$N_{PN} = A_{IR} c_N c_P A_{image}, \tag{2.8b}$$

$$N_{NN} = A_{IR} c_N^2 A_{image}, \tag{2.8c}$$

where A_{IR} is the area of the IR typically equal to $(2l)^2$. However, as mentioned in section 2.2.2, the IR may be asymmetric and/or shifted without affecting the random, uniform distribution due to spurious trackings, as long as the shape and relative position is constant for an ensemble of trackings. The number of uncorrelated particle-particle trackings is calculated by subtracting the sum of these contributions from the total number of particle trackings

$$N_{PP,random} = N_{total} - (N_{PP,phys} + N_{PN} + N_{NP} + N_{NN}). \tag{2.9}$$

Estimations for the accuracy of the mean displacement (velocity) and diffusion length measurements are also derived from the statistics of the system. The standard error of the mean physical displacement is related to the standard deviation of the distribution, which is simply the diffusion length. For any displacement distribution, the true mean is contained within the 95% confidence interval of the measured mean with the well known factor $\pm 2d/\sqrt{N_{PP,phys}}$. The standard error of the diffusion length measurement is more complex and for the general case depends on the fourth and second moments of the displacement distribution [109]. However, for a normal distribution, the 95% confidence interval for the standard error of the diffusion length reduces to $\pm d\sqrt{2/N_{PP,phys}}$. A total of 1,000 physical trackings results in an error of approximately $\pm 6.3\% d$ for the mean displacement and $\pm 4.5\% d$ for the diffusion length.

2.2.4 Numerical Validation

The SPTV algorithm was validated numerically using MATLAB to simulate particle and noise signal locations for particle diffusion. Random particle and noise signal locations were produced on a 2-D domain corresponding to an area several IRs larger than a typical image to allow for in-plane drop-in on the actual image domain. For a second domain, a fraction of the particle signals, proportional to $P_{\perp,i}$, were perturbed in the x and y direction according to a random, normal distribution with standard deviation d. For the remaining number of particles and noise signals, random signal locations were produced to emulate out-of-plane drop-in/drop-out and random generation of noise. Again, we assume that the probability of drop-out is the same as the drop-in. All signals were tracked using the SPTV algorithm described above in equations(2.7-2.9) for approximately 200 image pairs. Additionally, the exact contributions from tracer mismatching and random signal cross tracking were computed with the knowledge of the simulated signal origins. Cumulative contributions to the PDF from each type of tracking calculated by equations (2.7-2.9), which correspond closely to the exact values. A typical displacement distribution is shown in figure 2.4 for 50,000 total trackings resulting from 60% drop-out, 50% noise signals and a total signal concentration corresponding to an inter-signal distance of 15 diffusion lengths. The ability of the equations to accurately predict the height of the uncorrelated floor is good confirmation that the basis of technique is sound.

2.3 EXPERIMENTAL VALIDATION

The tracking algorithm was also validated using three physical experiments. The experiments measured the diffusion and/or convection of three different tracer particles: 54 nm
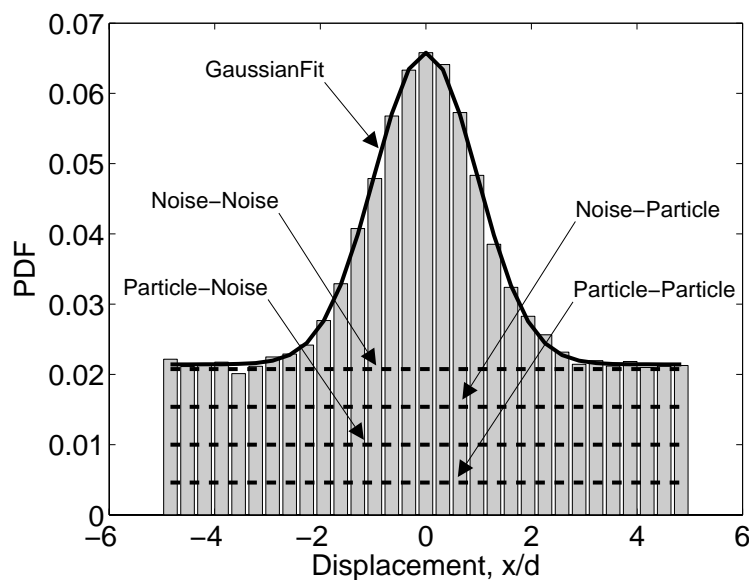
Figure 2.4: Displacement distribution for simulated diffusion data with intensifier noise and drop-in/drop-out. The cumulative contributions to the random distribution due to tracking noise and drop-out particles were calculated from the statistical tracking algorithm.

diameter FITC-Dextran molecules, 6 nm diameter organic-soluble quantum dots and 16 nm diameter water-soluble quantum dots. The images were acquired using a Nikon Eclipse TE2000-U inverted microscope with a Nikon PL Apo NA 1.45 100× TIRF oil immersion objective and an intensified CCD (ICCD) camera (Q-Imaging Intensified Retiga) capable of 1,360 pixels by 1,036 pixels 12-bit images with an effective pixel size of 64.3 nm at 100×. Tracers were illuminated using a mercury lamp 3-5 μm above the lower glass surface or through-the-objective total internal reflection fluorescence (TIRF) [41] with the 514.5 nm line of an argon ion laser (Coherent) within about 135 nm of the lower glass surface. The camera's intensifier gate was used to control the image exposure and a syringe pump (Harvard Apparatus) was used to charge the channels. Solvent viscosities were found using a TA Instruments AR-2000 Rheometer or specified tables. In-house MATLAB software was used for data acquisition and particle tracking.

2.3.1 SPTV Using Single Molecule Tracers

Free diffusion of fluorescein isothiocyanate-dextran (FITC-Dextran, 2,000,000 MW, Sigma-Aldrich) molecules in solution was observed between two cover glasses separated by 10 μm. The molecules have a hydrodynamic radius of 27 nm specified by manufacturer and peak absorption and emission wavelengths of 490 nm and 525 nm respectively. The FITC-Dextran molecules were dissolved into a solvent of 33% pure water (Fluka) and 66% glycerol (99.5+%, Sigma-Aldrich) by volume with a dynamic viscosity of 24.3 cP at room temperature. Images were acquired with a 10 ms integration time and a 20 ms separation time between the frames of each image pair.

After measuring the total displacement distribution, the spurious displacements were estimated by fitting a Gaussian profile to the data. Figure 2.5 confirms this, and shows the Gaussian displacement distribution due to isotropic Brownian motion, sitting atop the random, uniform distribution resulting from spurious trackings as determined by our analysis. For these particles and imaging system, the drop-out probability was about 50% and the ratio of physical trackings to spurious trackings was about 2 to 1 for about 5,000 trackings, which is mostly due to high levels of detectable noise signals. The measured diffusion length was $d_{PTV} = 133$ nm, which compares well to the predicted Stokes-Einstein model of $d_{SE} = 115$ nm with error possibly resulting from the high sensitivity of glycerol solutions to concentration and especially temperature.

2.3.2 SPTV Using Quantum Dots

A more challenging application of the SPTV technique is found when using very small tracer particles. Quantum dots (QDs) are semiconductor nanocrystals with monodispersed size, narrow emission spectra and broad absorption spectra. They show great promise for use as
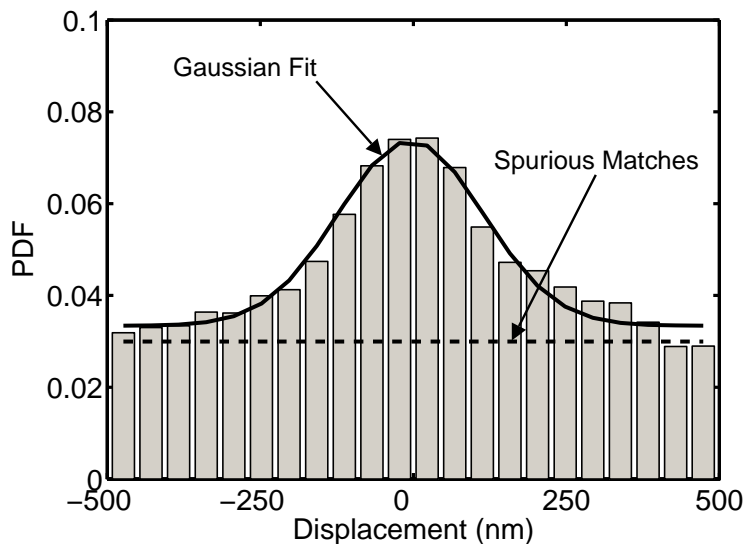
Figure 2.5: Measured displacement distribution for the free diffusion of 54 nm FITC-Dextran molecules in a glycerol/water solution with a viscosity of 24.3 cP.

tracer particles in nanofluidic systems [8, 9]. However, QDs add another complication to the SPTV analysis. QDs exhibit well-known fluorescence intermittency or "blinking" [18, 110] where, under continuous illumination, QDs cycle through states of nearly continuous emission and darkness. Within the context of particle tracking, blinking can be treated in a similar manner to drop-in/drop-out, although the statistics of this optical drop-out must be characterized experimentally. Methods for blinking suppression have been demonstrated [111], but blinking is actually a useful feature to differentiate single QDs from groups of aggregated QDs, if necessary. Pure (core or core-shell) QDs can only be used in organic solvents. Water-soluble QDs have an additional ligand coating, which increases their diameter and can decreases their emission intensity. The organic-soluble QDs used in this study were CdSe/ZnS core-shell QDs with a diameter of 6.1 nm (Evident Technologies, diameter determined by TEM) and a peak emission wavelength of 614 nm. The water-soluble QDs

(Quantum Dot Corporation, diameter determined by a HPLC method) were also CdSe/ZnS core-shell QDs with a core diameter of about 6 nm and an overall hydrodynamic diameter of about 16 nm due to a carboxyl or amine coating to make them water-soluble and a peak emission wavelength of 606 nm.

Quantum dot blinking characteristics

To quantify the nature of blinking, organic-soluble QDs in toluene were immobilized by drying a dilute solution on a glass coverslip, then covering them with another coverslip to minimize the effects of oxidation. The blinking of several hundred single QDs was observed under continuous mercury lamp illumination for a period of 10 minutes. Images were recorded using an ICCD camera and locations of the QDs were identified and monitored in time. The signals were scaled by the background noise, which was normalized to have a mean and standard deviation of one. By defining an intensity threshold based on a signal to noise ratio (SNR) of about 5, we were able to designate on-times and off-times. A sample intensity time trace of a single blinking QD is shown in figure 2.6. The on-time and off-time blinking statistics were verified as previously reported by [110] as an initial test for single QD detection. Histograms for the length of consecutive off-times and on-times (not shown here) exhibited the characteristic power law slope of -1.5 in excellent agreement with the results reported by Shimizu *et al.* The on-times also showed strong for deviation from the power law for long on-times.

For PTV applications, blinking characteristics are similar to drop-in and drop-out. If we assume that the QD is physically present in both frames of an image pair, then it is important to know if it will be optically "on" in both frames. This is a slightly different reading of the raw blinking statistics measured above. Single QD blinking was observed for
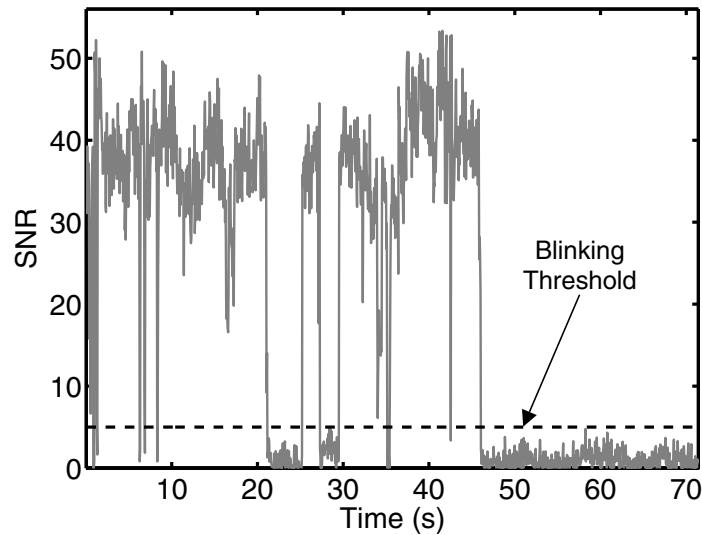
Figure 2.6: Sample intensity time trace for single, immobilized quantum dots under continuous illumination. An intensity greater than the threshold of SNR=5 designates blinking on-times from off-times.

different exposure times and inter-frame times in order to determine the blinking probability. Image pairs of immobilized QDs were recorded for exposure times varying from 1-50 ms and inter-frame times varying from 2-51 ms according to the same procedure outlined above. "On-states" and "off-states" were identified for each frame within an image pair. Both on- and off-times with time scales less than the camera exposure time can occur within a single exposure. The sensitivity of the detector and the SNR determine the ability to designate an on-state (or off-state) for a given frame. The probabilities for a single QD to be on in both frames (on-on), off in both frames (off-off), on in the first frame and off in the second (on-off) and off in the first frame and on in the second (off-on) were determined (figure 2.7). This data indicates that the image pair blinking probabilities are approximately invariant for exposure time and separation time under continuous illumination (not surprising given the low SNR chosen). Notice that about 70% of the QDs are in off-states during both frames

of an image pair. This result is most likely due to the decay of QD emission intensity for prolonged exposure to illumination [112]. This result may change if pulsed or gated illumination is used, as is common in PTV systems, which use Q-switched or shuttered laser systems. Since these QDs are effectively invisible to a real PTV analysis, they have no effect on the blinking drop-out/drop-in probabilities. Of the detectable QDs, only those which remain on for two consecutive frames and remain within the interrogation volume will contribute to the physical tracer particle displacement distribution. From this data, the blinking drop-out and drop-in probability is calculated by

$$P_{drop-out,blink} = \frac{P_{on-off}}{P_{on-off} + P_{on-on}}, \tag{2.10a}$$

$$P_{drop-in,blink} = \frac{P_{off-on}}{P_{off-on} + P_{on-on}} \tag{2.10b}$$

where $P_{drop-out,blink} \approx P_{drop-in,blink}$ as expected. Physically, these quantities represent the probability of observing the transition of a QD from an on-state to an off-state within an image pair, which is about 12%. We should note that the optical drop-out is much less than the physical drop-out of a QD in a water-like substance ($\approx$80%). The blinking drop-out probability is combined with the diffusion drop-out to yield the total drop-out probability. So, we see that the for tracer particles with high drop-out, the effects of blinking on tracer particle detectability diminish.

Diffusion measurements using organic-soluble quantum dots

Free diffusion of 6.1 nm organic-soluble QDs was observed with mercury lamp illumination in a sealed Poly(dimethylsiloxane) (PDMS) microchannel. For this demonstration, the solvent viscosity and exposure time was chosen to ensure that single quantum dots were
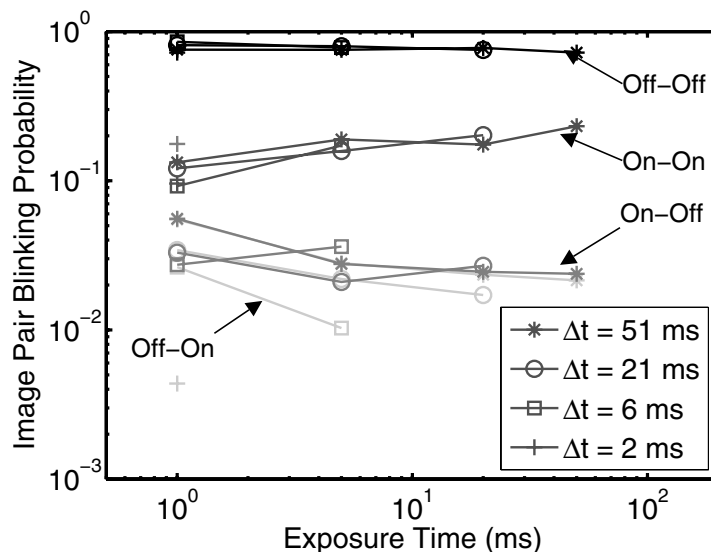
Figure 2.7: Quantum dot blinking probability for two successive images with varying exposure time and inter-frame time. Only QDs that are "on" in both frames are trackable, while QDs that are "on" in only one frame optically drop-in or drop-out with a probability of about 12%. The QDs that are "off" in both frames of an image pair are essentially invisible and untrackable.

captured both blinking and diffusing. The QDs were re-suspended in 13% hexane and 87% 1,000 cSt PDMS 200 fluid (Sigma-Aldrich) with a viscosity of 413 cP at room temperature. The camera exposure was set to a 15 ms integration time with a separation time of 20 ms between the frames of each image pair. A sample time sequence of evenly spaced images for a single, blinking QD is shown in figure 2.8.

The distribution of the QD displacements is shown in figure 2.9 and reveal some interesting characteristics. Firstly, the general character of the distribution is similar to that found in the FITC-Dextran tracers. The characteristic uncorrelated tracking floor was also predicted as before and was quantified by fitting a Gaussian distribution to the data of 3,000 total trackings. However, on close examination, the width of the diffusion distribution ($d_{PTV} = 42$ nm) is smaller than would be predicted using the idealized Stokes-Einstein
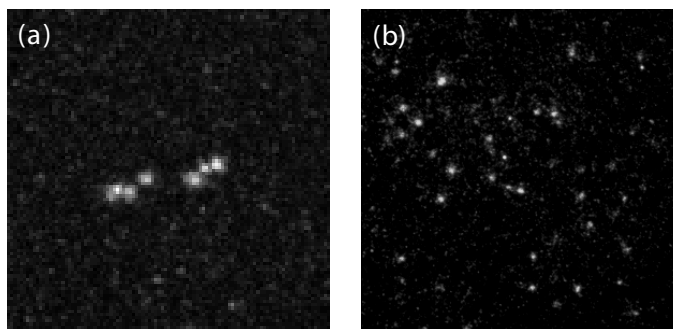
Figure 2.8: Quantum dot images: (a) a composite time series of 7 frames with equal time spacing for an organic soluble QD diffusing and blinking in a slight convective flow in PDMS and hexane (6.5 μm $\times$ 6.5 μm field of view) and (b) typical image of QDs in water illuminated by an evanescent field (19.3 μm $\times$ 19.3 μm field of view).

model (d_{SE} = 83 nm) with the known QD diameter and the measured viscosity of the solvent. Although we do not know the source of this reduced diffusion, there are two possibilities. The first is that the QDs were not single dots, but agggregations with larger effective radii. However, since blinking was observed, this is considered an unlikely explanation. A second possibility is that the QDs are diffusing through a network of long-chain PDMS molecules whose average chain length (121 nm) is significantly larger than the QD diameter (6 nm). This larger-scale network likely leads to non-Brownian diffusion [113, 114] although detailed study of this is beyond the scope of the current manuscript which focuses solely on the particle tracking demonstration and use of nanometer-sized tracers.

Velocity measurements using water-soluble quantum dots

Carboxyl coated water-soluble QDs in a water-based buffer with a 16 nm hydrodynamic diameter were imaged flowing in a rectangular 75 μm by 600 μm PDMS micro-channel within 135 nm of the surface using the TIRF method described above. The high SNR of the TIRF method along with a high power argon ion laser and ICCD camera allowed for
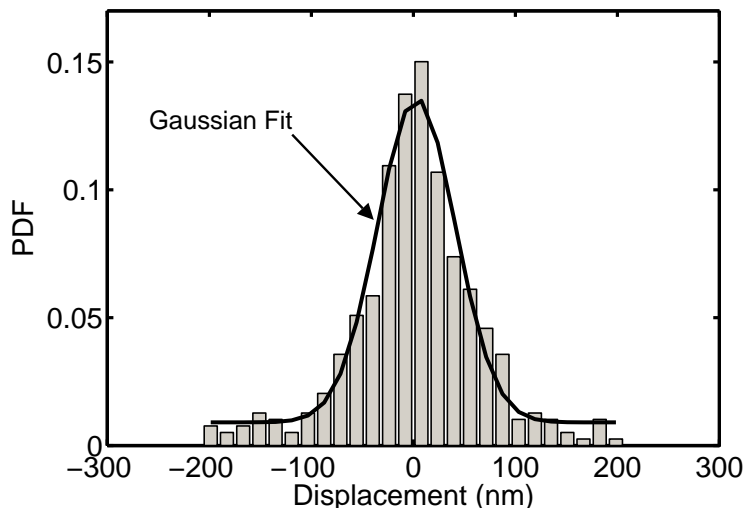
Figure 2.9: Measured displacement distribution for the free diffusion of 6 nm quantum dots in a hexane/PDMS solution with a viscosity of 413 cP.

camera exposures as low as 1 ms. A typical TIRF image of the QDs in buffer is shown in figure 2.8. Diffusion measurements using the SPTV method at inter-frame times of 3 ms and 7 ms showed a mean diffusivity of 16.7 μm^2/s.

The QDs were also tracked in both the streamwise and cross-stream directions for various flow rates using the SPTV algorithm with an inter-frame time of 4 ms. An example is shown in figure 2.10. The data again shows diffusion dynamics atop a random, uniform distribution with over 140,000 total trackings and a ratio of physical trackings to spurious trackings of about 1 to 10 resulting from 900 image pairs. The high diffusivity and shallow imaging depth contribute to the significant drop-out and particle mismatching. A mean displacement shift in the streamwise direction corresponds to measured mean velocities, v_{mean}, of 34.8, 79.1 and 139.1 μm/s for flow rates of 10, 20 and 40 μL/min, respectively, and less than 5 μm/s cross-stream velocity, u_{mean}. An increasing standard deviation of velocity in the streamwise direction, v_{std}, of 90.6, 100.7 and 110.9 μm/s was observed with increasing flow
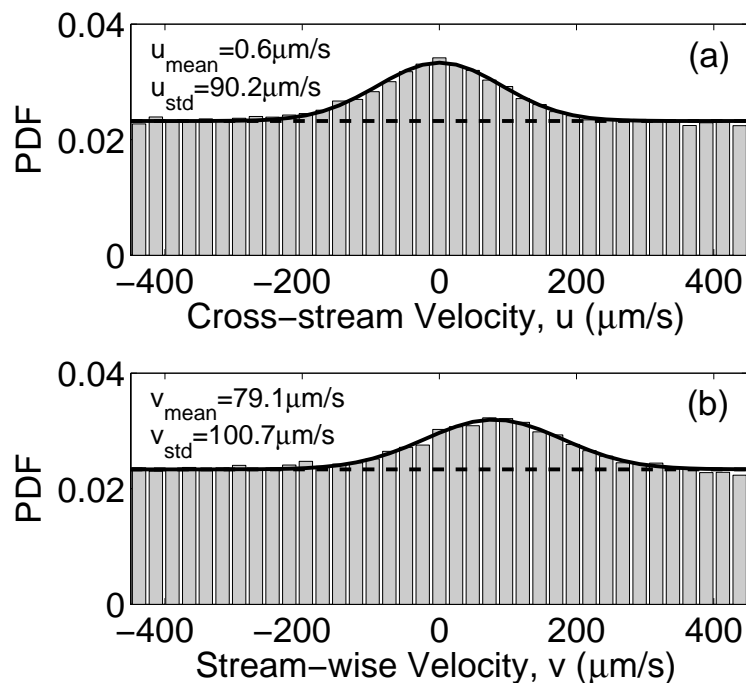
Figure 2.10: Measured velocity distributions for 16 nm carboxyl conjugated water-soluble quantum dots in a water-based buffer solution in the (a) cross-stream and (b) streamwise directions for a PDMS microchannel using TIRF with the SPTV algorithm for 900 image pairs.

rate, while the standard deviation of velocity in the cross-stream direction, u_{std}, remained

nearly constant with a mean of 91.7 μm/s (consistent with the diffusivity measured above).

This is attributed to sampling different shear planes within the evanescent field where the

streamwise velocity varies away from the wall [41]. Finally, hydrodynamic interactions

between the particle and wall hinder the 118.7 μm/s standard deviation predicted by the

Stokes-Einstein model to 111.0 μm/s [70], which is consistent with a slightly larger nominal

tracer diameter than the hydrodynamic diameter specified by the manufacturer.

To resolve velocity fields with the SPTV technique, particle trackings are binned together

within an image and the analysis is performed as described earlier. In figure 2.11, we

show an example of a flow near a corner in a 10 μm deep PDMS micro-channel for amine
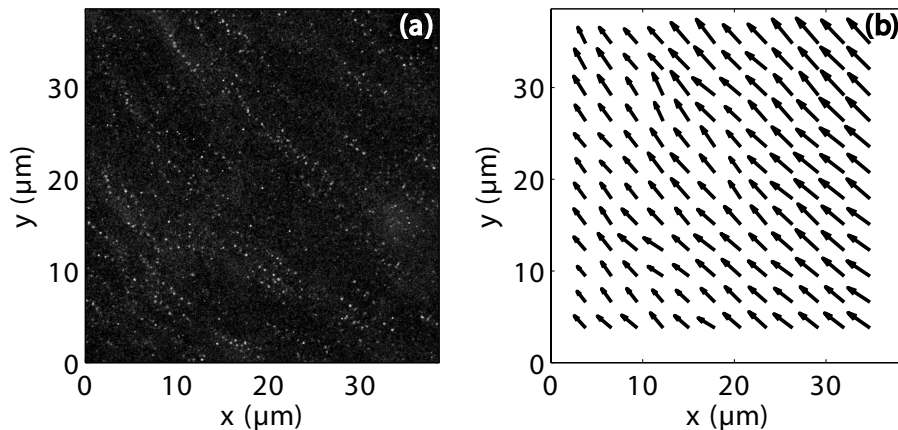
Figure 2.11: Amine conjugated water-soluble quantum dot seeded flow near a corner in a micro-channel: (a) composite of 10 equally spaced images and (b) the corresponding vector field computed with the SPTV method. The vectors are the result of binning particle displacements over a 5.7 μm (88 pixels) square window with 50% overlap for 800 image pairs.

coated water-soluble QDs in a 50 cP glycerol solution [115]. Each vector is the result of approximately 7,500 trackings over a 5.7 μm (88 pixel) square window with 50% overlap and a ratio of physical to random trackings of 1 to 3. To achieve a sufficient number of physical trackings, 800 image pairs were needed for proper averaging, which yielded a mean velocity of 4.4 μm/s over the domain. We do note that aggregations can occur in systems with high concentrations of QDs and glycerol, however, this does not affect our ability to measure mean velocities.

2.4   CONCLUSIONS

We have identified several shortcomings of traditional particle tracking techniques that become important as the tracer particles become smaller. The statistical particle tracking

velocimetry (SPTV) algorithm presented here addresses many problems associated with small tracers, including the desire to use higher tracer seeding densities, large drop-out rates and the fluorescence intermittency behavior of quantum dots. However, effects of fluorescence intermittency are diminished in comparison to physical drop-out in highly diffusive systems. The essential approach of the SPTV algorithm is to measure displacement distributions, rather than single displacements, and to use the known statistics of the system to eliminate random signal trackings due to trackable intensifier noise signals, tracer mismatching and drop-in/drop-out.

The algorithm has been verified using both simulations and experiments and shows great promise as a velocimetry technique for nanometer-sized tracer particles in systems with significant intensifier noise and with large tracer particle diffusivities and concentrations. In the present paper, we have validated the SPTV algorithm for several systems employing innovative tracer particles: single molecules and quantum dots, but the technique is also applicable over the full range of tracer particle length scales where traditional μPIV and μPTV methods are typically used. By treating all detectable signals within an image equally, the underlying physics of the system is allowed to present itself, while the uncorrelated information is easily removed through simple statistics. It is this simplicity that makes the statistical tracking algorithm attractive for smaller length scales. However, there is still much room for improvement in nano-PIV/PTV systems.

Lastly, we have observed a smaller measured diffusion length as compared to the expected Stokes-Einstein prediction for both the organic and inorganic QDs. In the case of the organic QDs, the smaller diffusion dynamics may be the result of diffusion in a long-chain liquid polymer. However, the similar discrepancy, to a lesser extent for the water-soluble QDs suggests that the small size of the tracers may not be accurately described by the

Stokes-Einstein relation, even when taking into account hindered diffusion where applicable, but we cannot completely explain this phenomenon. The unexpected width of the diffusion peak has no impact on the ability of the SPTV technique to measure mean velocities in micro- and nano-fluidic systems, but only on the interpretation of the distribution shape. For example, it has been proposed [116] that the width of the distribution could be used to measure local fluid temperature. Although this is an appealing idea, it is fraught with complexities of the type revealed here, since complex fluids and small tracer particles are not guaranteed to observe the Stokes-Einstein relation. Similarly, in shear flows, the displacement (and hence velocity) distributions can be non-Gaussian [41] and so it becomes critical to measure the distributions and not to assume any particular shape.

ACKNOWLEGMENT

Chapter 3

Simultaneous, ensemble-averaged measurement of near-wall temperature and velocity in steady micro-flows using single quantum dot tracking

We present results from a series of experiments demonstrating the use of single quantum dots (QDs) as simultaneous temperature and velocity probes at the micro-scale. The fluorescence intensity of QDs varies predictably with temperature due to changes in quantum efficiency. We use Total Internal Reflection Fluorescence Microscopy (TIRFM) to study

the region within 200 nm of a fluid-solid interface. A two-color, time-averaged temperature sensing technique based on the ensemble intensity changes of single QDs as compared to a reference dye (rhodamine 110) is presented. Many single QD intensity measurements are used to build intensity distributions which can be mapped to fluid temperature. Simultaneously, we track the motion of individual QDs, building a distribution of particle displacements, where the mean displacement yields the local fluid velocity. We also show that the width of the displacement distribution (or the diffusion coefficient) captures the scaling of the temperature to viscosity ratio, which may allow for independent viscosity measurement.

3.1 INTRODUCTION

In the rapidly developing field of micro-fluidics, there is a growing need for thermal-fluid diagnostic methods at small length scales. For example, temperature control is critical for DNA amplification in polymerase chain reaction (PCR) [19, 20]; boiling and heat transfer are becoming more common in micro-electro-mechanical systems (MEMS) devices [21, 22] and accompanying diagnostic techniques are required to determine device performance. The small length scales involved in these applications require non-invasive diagnostic methods for temperature, velocity and viscosity measurements. Among the most successful non-invasive velocity measurement techniques are particle image velocimetry (PIV) and particle tracking velocimetry (PTV). They are well-established fluid velocimetry techniques for macro-scale, micro-scale and nano-scale diagnostics [4, 5, 6]. Several viable methods of optical temperature measurement have been proposed that use digital imaging of a temperature field for quantitative measurements. These methods include laser induced fluorescence (LIF) thermometry [23, 24] and PIV thermometry [25, 26, 27].

3.1.1 Optical Thermometry

The emission intensity of most organic, fluorescent dyes (rhodamines, fluorescein, etc.) in solution varies with temperature due to changes in quantum efficiency. Laser induced fluorescence (LIF) thermometry uses CCD cameras to quantitatively capture the spatial intensity variations in solutions of temperature sensitive dyes and map them to temperature fields through careful calibration [23]. These methods use relatively high concentration solutions of organic dyes under low magnification ($<10\times$). The emission intensity per unit volume of dye solution is described by

$$I = I_0 c \epsilon \phi, \tag{3.1}$$

where I_0 is the intensity of the incident excitation light of wavelength λ_0, c is the concentration of the fluorescent dye, ϵ is the molar absorption coefficient and ϕ is the quantum efficiency. The intensity of the excitation light is independent of temperature T, but it can vary in space and time. The change in concentration and molar absorption with temperature is typically insignificant, while the change in quantum efficiency can vary strongly between dyes. For instance, the emission intensity of Rhodamine 110 (Rh110) decreases about -0.13% K^{-1} whereas Rhodamine B (RhB) shows a much stronger temperature dependence with a decrease of -2.3% K^{-1} [24].

Two-color LIF systems eliminate the spatial dependence on I_0 by comparing the intensity of the temperature sensitive dye to the fluorescence intensity of a temperature independent reference dye. By suspending two dyes of different temperature dependence (for example RhB and Rh110) in one solvent, the intensities of both dyes are measured independently at any given location through spectral filtering. The ratio of the two emission intensities will

also be temperature dependent, but spatially invariant:

$$\frac{I_a}{I_b} = \frac{c_a \phi_a \epsilon_a}{c_b \phi_b \epsilon_b}, \tag{3.2}$$

where the subscripts a and b denote two different dye species presumably with different emission maxima at λ_a and λ_b, respectively. Since the emission spectrum of each species has a finite width and optical filters are not perfect, some of the light of wavelength λ_a will inevitably leak onto the detector region for λ_b and vice versa, which is accounted for using an excellent analysis found in [24]. Both one- and two-color LIF techniques have been combined with velocimetry methods using at least two cameras to capture both velocity and temperature information. More recently, LIF has been applied using microscope optics to measure micro-scale applications including viscous heating, electrokinetic flows and thermally driven buoyant flows [28, 29]. Two-color, micro-scale LIF thermometry has been demonstrated using a single camera (without velocity measurement) and not accounting for temporal fluctuations as many micro-scale effects are measured in the steady-state [29].

PIV Thermometry exploits the Brownian motion of tracer particles to estimate the local fluid temperature. The diffusion length, s, is the expectation value of the mean square particle displacements due to Brownian motion. In general, the diffusion length can be characterized by a diffusion coefficient D and the sampling time Δt, which in our case is the inter-frame time of an image pair. In one dimension, the diffusion length is given by

$$s = \sqrt{\langle \Delta x^2 \rangle - \langle \Delta x \rangle^2} = \sqrt{2D\Delta t}, \tag{3.3}$$

where Δx is the particle displacement and the angled brackets denote the ensemble-average. The diffusion coefficient is dependent on the absolute temperature T, the particle radius

a and the dynamic viscosity μ, which can be a strong function of temperature $\mu(T)$. The Stokes-Einstein diffusion coefficient D_{se} is a reasonable estimate for the diffusion coefficient of a spherical particle in an infinite (bulk) liquid solvent with the particle diameter being sufficiently larger than the surrounding solvent molecules

$$D_{se} = \frac{k_B T}{6\pi\mu(T)a}, \tag{3.4}$$

where k_B is Boltzmann's constant. The temperature of a system can be inferred by quantifying the diffusion length from the random motions of tracer particles. The details of this technique have been outlined and demonstrated experimentally [25, 26] by relating the diffusion length to the spatial cross-correlation obtained from PIV data. Using this, the temperature can be inferred using equations (3.3) and (3.4), but only if the temperature dependence of the fluid viscosity is known [27]. The advantage of PIV Thermometry, is that the same tracer particles used to measure the fluid velocity are used to measure temperature simultaneously.

3.1.2 Quantum Dots

Recently, interest has peaked in the use of semiconductor nanocrystals or (QDs) as truly nanometer-sized tracer particles. QDs are single fluorophores, with fluorescence lifetimes similar to conventional fluorophores, but with significantly higher quantum efficiency and resistance to photo-bleaching. They exhibit several qualities beneficial to nano-scale velocimetry including small diameters ranging from 5 nm to 25 nm, tunable emission wavelength, and controllable surface coatings for solubility in either organic or inorganic solvents. Since they are nanometer-sized, single fluorophores, individual QDs have a low signal-to-noise-ratio (SNR) due to high diffusivity and low emission intensity. However, nano-scale

velocity measurements in aqueous solutions have been achieved using single QDs with the high SNR detection method of total internal reflection fluorescence microscopy (TIRFM) [35] combined with particle velocimetry techniques [9, 10].

QDs exhibit a small red shift (~ 0.11 nm K^{-1}) in emission wavelength near room temperature [31], but the decrease in emission intensity with increasing temperature is much more significant. Several authors have measured the temperature sensitivity of QD emission intensity near room temperature. In particular, [32] proposed the use of (CdSe)ZnS core-shell QDs for temperature sensitive coatings. Organic soluble QDs were suspended in a solid, poly(lauryl methacrylate) (PLMA) matrix, and the temperature variation for the bulk emission intensity of the QD/PLMA composite was -1.3% K^{-1} between 278 K and 313 K. [31] measured a similar temperature sensitivity of -1.1% K^{-1} between 280 K and 350 K for bulk emission water-soluble CdSe/ZnS core-shell QDs in a phosphate buffered saline (PBS) solution for use as a bio-probe. Koochesfahani and co-workers (personal communication, 2005) also investigated the bulk photophysical properties of CdSe/ZnS quantum dots and were the first to propose their use as a temperature sensitive dye for LIF thermofluid diagnostics. Lastly, [34] studied the effects of temperature and illumination intensity on fluorescence intermittency in single QDs immobilized in thin films of poly(methyl methacrylate) (PMMA) for temperatures between 15 K and 300 K. They statistically investigated the intermittency behavior by building ensemble distributions from single QD measurements, but they did not comment directly on link between temperature and emission intensity.

In this paper, we demonstrate an ensemble-averaged, simultaneous temperature and velocity measurement system based on TIRF illumination of single QDs within 200 nm of a liquid-solid interface. First, we verified the thermo-optical properties of the bulk QD solutions used in our system against previous studies under low magnification. Next, we per-

formed temperature and velocity measurements by building statistical ensembles from the intensities and displacements of single QDs measured under high magnification ($100\times$) using TIRFM. Measurements were performed in rectangular PDMS micro-channels using aqueous solutions of QDs ($\lambda_a = 606$ nm) and Rh110 ($\lambda_b = 520$ nm). Simultaneous measurements of steady flows are achieved by separating the dual emission image by wavelength using an image splitter, then projecting the QD and reference dye images onto a single, intensified CCD (ICCD) camera. The positions of single QDs are tracked to build a displacement distribution from which fluid velocity and QD diffusion dynamics are obtained. In a similar manner, the intensities of single QDs are normalized by the nearly temperature-independent reference dye, and intensity distributions are built from which the fluid temperature can be inferred from the ensemble-averaged behavior. Finally, we will show that the width of the displacement distribution provides additional information about the temperature to viscosity ratio, which may provide viscosity measurements in the future. This technique differs from traditional LIF thermometry in that our temperature probes are discrete, resolved, single particles as opposed to continuous dye solutions and can thus double as velocity tracers. At high magnification ($100\times$), our aim is to measure averaged fluid properties over our small field of view in the very near-wall region of micro- and nano-channels, as opposed to the whole-field, spatially resolved data obtained from LIF. We use ensemble-averaged properties of displacement and intensity distributions, since the variance of a single quantum dot intensity or displacement realization is large due to quantum optical effects and diffusivity, respectively.

3.2   EXPERIMENTAL METHODS

3.2.1   Experimental Setup and Materials

The imaging system for this two-color, simultaneous temperature and velocity measurement technique is built around a Nikon Eclipse TE2000-U inverted fluorescence microscope with the 488 nm line of an Argon-ion CW laser (Coherent) as the excitation source for all experiments as shown in figure 3.1. The temperature sensitive probes are water-soluble, CdSe/ZnS core-shell quantum dots (Invitrogen) with a carboxyl termination. The QDs have a core diameter of about 6 nm with a peak emission wavelength of 606 nm and an overall hydrodynamic diameter of about 17 nm due to the water-soluble coating. The temperature independent reference dye is Rhodamine 110 (Sigma-Aldrich) with a peak emission wavelength of 520 nm. Solutions of both QDs and Rh110 were prepared in a 50 mM borate buffer with 8.4 pH. Flow experiments were carried out in 340 μm $\times$ 30 μm $\times$ 10 mm, rectangular poly-dimethyl siloxane (PDMS) (Sylgard 184 Silicone Elastomer, Dow Corning) micro-channels, fabricated by a soft lithography technique [117] and mounted on 170 μm thick borosilicate cover glass. Micro-channel dimensions were inferred from photoresist mold dimensions measured using a surface profiler (Dektak, Veeco). The fluid was driven by a syringe pump (Harvard Apparatus). The microscope stage and PDMS micro-channel temperature were maintained by Peltier heaters/coolers attached to copper blocks with embedded thermistors and controlled by two feedback temperature controllers (Lightwave). The copper blocks were coupled to either side of the channel along the flow direction with thermal grease and below the microscope stage. Several thermistors were embedded in the copper blocks within 1 mm of the PDMS to ensure that no temperature gradients existed in the system.
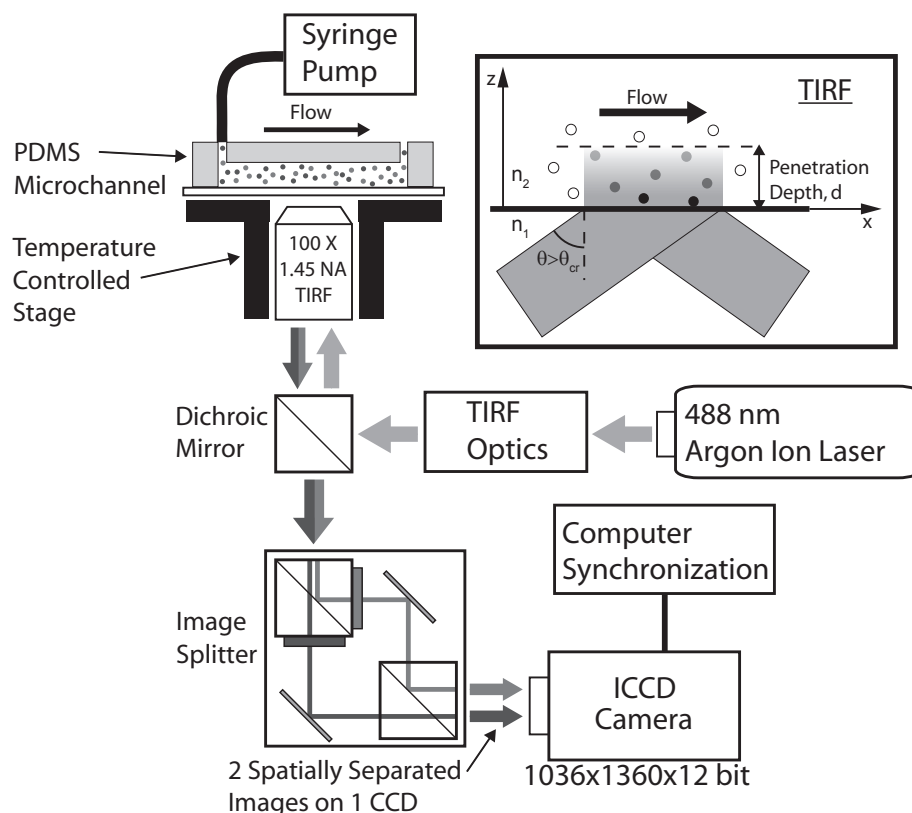
Figure 3.1: Schematic illustrating the experimental setup for simultaneous imaging of solutions of rhodamine 110 and single quantum dots within 200 nm of a liquid-solid interface using total internal reflection fluorescence (TIRF) microscopy. Bulk intensity measurements of dye without single molecule resolution were achieved by removing TIRF optics and replacing the objective with a lower magnification 10× objective.

Dual wavelength images produced by the fluorescence emission of the QDs and Rh110 were separated by wavelength using an image splitter (Cairn) with a 1× magnification and projected side by side onto a single intensified CCD (ICCD) camera (QImaging). The image splitter separates the image using a dichroic mirror with a cutoff wavelength of 565 nm (Chroma). The images are bandpass filtered before recombination and projection onto the ICCD focal plane. A single camera system was chosen for convenience, because the image produced by our objective-based TIRFM system is smaller than half the size of our CCD. A second camera would be expensive and unnecessary. The camera is capable of

1,360 × 1,036 pixels, 12-bit images with an effective pixel size of 1.01 μm at 10× and 101 nm at 100×.

Images were corrected for any slight distortion caused by the image splitter optics and for proper overlap by image registration though a polynomial transformation. A silicon reference grid (Electron Microscopy Sciences) or reference image (dilute 100 nm diameter polystyrene particles dried on slide) was captured with the ICCD camera coupled directly to the microscope (i.e. without the image splitter in place). The image splitter was then aligned and a split image of two different wavelengths was captured. Each split image was transformed to the reference image using a third-order polynomial transformation intrinsic to MATLAB with 100 points, which was stored for later correction of the experimental images. The correction was very minimal with an error of 0.25 pixels computed from the residuals. After image correction, the necessary ratiometric temperature analysis and particle tracking were performed as discussed in sections 7.2.2 and 3.2.3. All image processing and analysis was performed using MATLAB.

3.2.2 Single Quantum Dot Imaging Using TIRF Microscopy

The detection and tracking of single QDs in aqueous solutions for the purpose of velocimetry has been demonstrated previously [9, 10] using a total internal reflection fluorescence (TIRF) microscopy illumination technique [35], which is illustrated in figure 3.1. TIRF allows for extremely high signal-to-noise-ratio (SNR) and illumination within about the penetration depth d (100-200 nm) away from the fluid-solid interface. We use an objective-based TIRF system, which creates a total internal reflection at the interface of the glass coverslip and the aqueous buffer with refractive indexes of $n_1 = 1.520$ and $n_2 = 1.333$, respectively. An intensity distribution $J(z)$ with exponential decay normal to the interface exists in the

lower optical density medium (buffer) described by

$$J\left(z\right) = J_0 e^{-z/d},\tag{3.5}$$

where z is the optical axis. The penetration depth d and the wall intensity J_0 in the low density medium are described by

$$d = \frac{\lambda_0}{4\pi}\left[n_1^2\sin^2\theta - n_2^2\right]^{-1/2},\tag{3.6}$$

$$\frac{J_0}{J_i} = \frac{4\cos^2\theta}{1 - (n_2/n_1)^2}\tag{3.7}$$

where θ is the incident angle and J_i is the intensity incident on the interface for light polarized perpendicular to the plane of incidence [35]. The incident angle in our system was $\theta = 62.4^o$ for a penetration depth of about 200 nm for the 488 nm, perpendicular polarized Argon-ion laser. A high numerical aperture NA objective is required to achieve the large incident angle for total internal reflection. We use a Nikon PL Apo NA 1.45 100× TIRF oil immersion objective, which also gives high resolution and efficient light collection for single QD visualization.

Since the QD diameters are significantly below the wavelength of light, we image the diffraction-limited spot, which can be several hundred nanometers in diameter. QD concentrations of 1 nM or less were sufficient for good SNR and particle center detection. Single QDs were detected by thresholding the maximum pixel value of an image until a possible particle was found. Next, the sub-pixel x and y locations, peak intensity I and diameter were found through a two-dimensional, Gaussian least-squares fit to a 3 × 3 pixel array centered on the maximum intensity pixel. The error in Gaussian fitting to sub-wavelength particle images has been shown to be as small as 0.1 pixels for a SNR greater than five [54].

After identifying a particle location, the particle and surrounding pixels (typically a five pixel radius) were blacked-out to avoid re-identification, then the threshold was further decreased until the next particle was found. This process was repeated until a predetermined number of particles in the interrogation volume were detected. For a penetration depth of about 200 nm and an effective image area of 22 μm $\times$ 22 μm, 25 QDs were detected per image for a 1 nM concentration. This is below the expected number of QDs per interrogation volume to ensure good particle image quality (high SNR). By taking a set of the brightest particles, a sufficient number of detectable particles are present in the interrogation volume on average. This method was chosen over an absolute threshold value for consistency at all temperatures, since the decrease in particle image intensity with temperature could create a bias in thresholding. Displacement (velocity) distributions for the stream-wise and cross-stream directions of the rectangular micro-channels were computed from image pairs using a statistical particle tracking velocimetry (SPTV) algorithm [10].

3.2.3 Ratiometric Intensity Analysis

We chose a two-color, ratiometric thermometry system to allow for normalization of the non-uniform illumination by the Gaussian beam spot produced by our TIRFM method. In addition, although simultaneous acquisition of reference dye images is not necessary for traditional LIF, we also normalize single QD images in time. The possibility of temporal laser fluctuations adds an additional variation to the measured intensity of single QDs and effectively widens the QD intensity distributions. For the best sensitivity at the detector, the dye concentrations were chosen to provide approximately equal intensities on both the reference image and temperature sensitive image [24]. For single QD detection using TIRFM under 100$\times$ magnification, the concentrations were 20 nM and 1 nM for Rh110

Sample Image for T=30°C
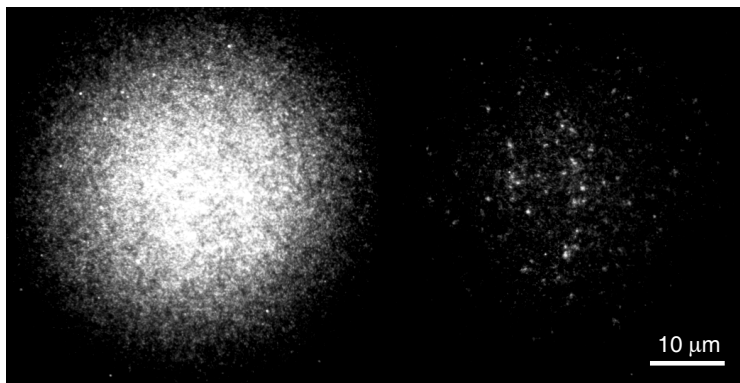
Figure 3.2: Sample split image of high concentration rhodamine 110 (left) and single quantum dots (right) imaged using total internal reflection fluorescence (TIRF) illumination at $T = 30$ ^{o}C with a penetration depth of 200 nm and an exposure time of $t_e = 1.5$ ms under $100\times$ magnification.

and QDs, respectively. A sample split wavelength image of single QDs and Rh110 is shown

in figure 3.2 for $T = 30.0$ ^{o}C. After correcting images for distortion as described in section

3.2.1, Rh110 reference dye images were averaged in time to alleviate the pixel-to-pixel noise

caused by the CCD and image intensifier. The average reference dye image was then scaled

by the mean image intensity in time, thus compensating for temporal fluctuations and

spatial intensity variations. Next, the fitted peak intensities (section 7.2.2) of individual

QDs were normalized by the corresponding single pixel from the Rh110 reference image

described above. Since the emission spectra of both fluorescent probes have a finite width

and optical filters are not perfect, some light from each fluorescent probe will inevitably leak

onto the detector region of the other, which is accounted for using the analysis described

by [24].

3.2.4 Bleaching and Photostability

Several measures were taken to minimize photobleaching of the fluorescent probes and verify that photostability was not a problem. The manufacturer of our commercially available QDs specifies a shelf-life of 6 months. Once diluted, however, the QDs degrade much more rapidly (1-2 days). All experiments were performed consistently within several hours of dilution in the same day. Experiments were carried out in flow with a small collimated beam spot, where the dye residence time in the illumination spot was less than one second. In the case of TIRF illumination, an extremely small fluid volume is probed by the evanescent field and the diffusion and convection of fluorophores into the imaging volume dominates over photbleaching. Time dependent intensity tests were conducted with solutions of QDs and Rh110 at room temperature. Bulk samples of both probes were exposed to flood illumination for over one hour in flow conditions similar to section 3.2.3 with minimal decrease in fluorescence emission. Additionally, temperature cycling from room temperature to the maximum and back to room temperature showed little hysteresis in the case of bulk QD solutions with a slightly more noticeable decrease for the lower concentration, single QD imaging experiments (figure 3.5). QDs also experience other, unique photo-stability issues. [112] discussed fluorescence decays of collection of colloidal QDs as they relate to single QD blinking phenomena. Simulations showed that under continuous light flux, collections of QDs decay by a power-law with decay times on the order of several minutes, and fluorescence recovers slowly after the illumination is terminated. We did not observe any similar effect in our tests, since QDs were exposed to illumination for a very short time in flow.

3.3 RESULTS

3.3.1 Verification of Bulk Thermo-optical Properties

A series of intensity measurements were performed to determine the spectral leakage of our filter system and to verify the thermo-optical properties of bulk solutions of QDs and Rh110 against those cited in literature. Here, we were only interested in measuring material properties and were not yet concerned with single QD intensities. For this reason, single particle detection was avoided by using a low magnification, 10× objective and flood illumination through the bulk of the sample volume with a relatively high concentration of QDs (42 nM) in aqueous buffer. Larger concentrations (1 μM to 3 μM) of Rh110 were necessary to maintain the same detector intensity signal due to the difference in quantum efficiency, the excitation efficiency of the absorption spectra and the optical filter transmission efficiency. Experiments were carried out using the system shown in figure 3.1 with the modifications mentioned above in a large PDMS cavity measuring about 3 mm × 3 mm × 1 cm with a low flow rate of 2 μL/min. The temperature was varied from 22 ^{o}C to 45 ^{o}C in 2.5 ^{o}C increments, waiting 5 to 10 minutes between data acquisitions to allow for temperature stabilization. The temperature was ramped up to the maximum and then down to room temperature to ensure that no hysteresis was present.

Each measurement point represents the intensity of the center portion of the illuminating beam spot averaged over 20 images taken at 10 Hz with an exposure time $t_e = 10$ ms. A linear fit for solutions of only QDs in buffer showed an intensity variation of -1.1% K^{-1}, which is in good agreement with the literature value of -1.1% K^{-1} to -1.3% K^{-1} for CdSe/ZnS core-shell QDs [32, 31]. No spectral leakage was observed from the QDs onto the Rh110 side of the detector. A similar experiment was performed for solutions of only Rh110
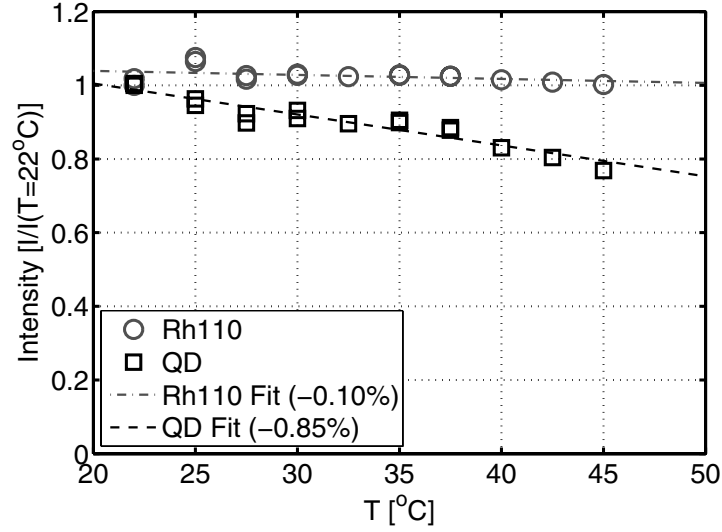
Figure 3.3: Intensity variation with temperature for bulk quantum dots and rhodamine 110 dye solutions under low magnification acquisitioned simultaneously with a split image system. A 10× objective with flood illumination ($\theta = 0$) was used to excite the solution to confirm the temperature dependence of fluorescence emission intensity with temperature. Each data point is the average intensity of the central beam spot over 20 images with an exposure time of $t_e = 10$ ms. The temperature was cycled from room temperature to the maximum and back to room temperature with minimal hysteresis. Linear fits to the intensity variation showed -0.10% K^{-1} ($R = 0.40$) and -0.85% K^{-1} ($R = 0.95$).

in buffer. The temperature dependence of Rh110 was -0.11% K^{-1}, which is also in good

agreement with the literature value of -0.13% K^{-1} [24]. Approximately 10% of the Rh110

intensity was observed on the QD detector section due to the wide emission spectrum of

Rh110. Finally, the temperature dependence of a solution consisting of both QDs and Rh110

was measured in a similar fashion and is shown in figure 3.3. The result showed very good

repeatability and minimal hysteresis ensuring that there are no unwanted temperature or

time-dependent effects present in the system. After appropriately subtracting the spectral

leakage, the sensitivity of the Rh110 remained unchanged, but the QDs decreased slightly

to -0.85% K^{-1}, which is most likely due to energy transfer between the species.

3.3.2   Fluid Properties from Single Quantum Dot Measurements

A solution of 1 nM QDs and 20 nM Rh110 in an aqueous, 50 mM borate buffer was used for simultaneous temperature, velocity and viscosity measurements of single QDs within 200 nm of the glass substrate in a PDMS micro-channel using TIRFM. The micro-channel cross-section was 340 μm $\times$ 30 μm $\times$ 10 mm with the overall cross-section of the PDMS structure measuring 5 mm $\times$ 5 mm $\times$ 40 mm. The solution was flowed at a rate of 2 μL/min through the channel to provide sufficient time for heat transfer. 450 image pairs were taken with an exposure time of 1.5 ms and an inter-frame time of 4 ms for statistical averaging at the five controlled micro-channel temperatures 22.5 ^{o}C, 30.0 ^{o}C, 39.0 ^{o}C, 46.0 ^{o}C and 23.0 ^{o}C in that order. The system temperature was allowed to stabilize for approximately 10 minutes between measurements and the first temperature (room temperature) is repeated at the end of the data set to ensure that no undesirable time-dependent phenomena have taken place (i.e. decrease in reference dye intensity, photo-bleaching). The images were analyzed for particle position and intensity using the methods described above section 7.2.2.

Ratiometric Temperature Sensing Using Single Quantum Dots

Intensity distributions of single QDs were collected for each temperature and characterized by their ensemble mean and standard deviation. Two sample intensity distributions are shown in figure 3.4 for $T = 30.0$ ^{o}C and $T = 39.0$ ^{o}C and demonstrate an obvious decrease in mean intensity with increasing temperature. The complex shape of the intensity distribution was due to several effects. The exponential decay of the evanescent field and concentration profile of particles in the wall-normal direction contribute to the overall shape of the distribution [42]. Gaussian fitting to the particle intensity profiles, the thresholding method and QD blinking events occurring on time scales below the exposure time add
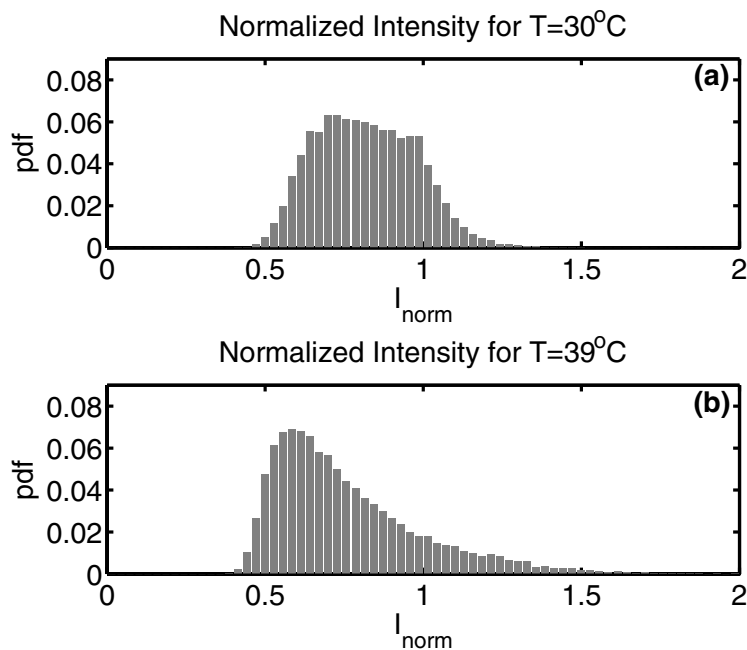
Figure 3.4: Normalized quantum dot intensity distributions at (a) $T = 30\ ^o$C and (b) $T = 39\ ^o$C for 450 image pairs each. There is an obvious decrease in mean intensity with increasing temperature.

additional variations and complexity to the shape of the intensity distribution. Although we currently do not have a complete, physical explanation for shape of the distributions, we believe that it is associated with saturation of the intensifier. Nevertheless, it does not significantly effect the behavior of the results.

Intensity distributions of single QDs were measured for applied temperatures cycled from room temperature to the maximum (46.0 ^{o}C), then back to room temperature to ensure repeatability. The mean normalized particle intensity was converted to temperature using the calibration from section 3.3.1. The results are shown in figure 3.5, where the error bar represents 99% confidence interval of the mean measured temperature. Since the variation associated with a single QD intensity is on the order of 10%, we must measure the ensemble-averaged intensity, which prevents instantaneous measurements of temperature
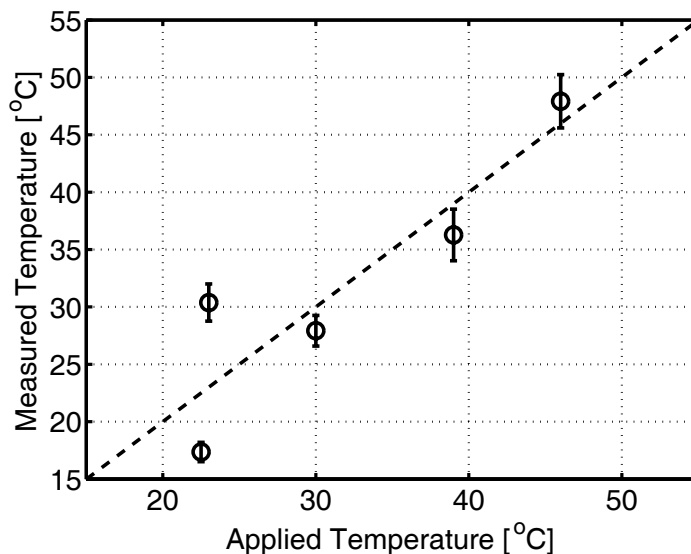
Figure 3.5: Measured temperature from mean single quantum dot intensity distributions, where the applied temperature was cycled from 22.5 ^{o}C to 46 ^{o}C and the final point was repeated at room temperature (23 ^{o}C). The error-bar represents 99% confidence interval of the normalized quantum dot intensity distribution for 450 image pairs each including over 2,000 samples each.

from single particles. The deviation of the mean measured temperature from the applied temperature was ± 4.9 ^{o}C. However, this large deviation is in part due to the final data point, which is a noticeable outlier from the rest of the data. The measured diffusivity in section 3.3.2 corroborates the possibility that the system was still elevated above room temperature. We also note that the slope of a linear fit to the single QD intensity data showed a decrease of -0.84% K^{-1} with increasing temperature, which is consistent with the temperature sensitivity found in section 3.2.3. This demonstrates that ensemble-averages of single QD intensities can be used to measure fluid temperatures optically within 200 nm of a liquid-solid interface.
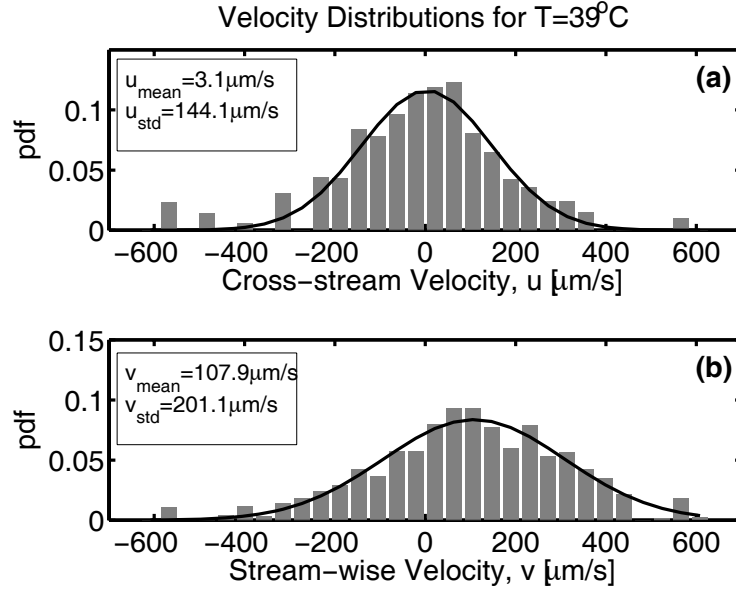
Figure 3.6: Measured velocity distributions for single, water-soluble quantum dots in the (a) cross-stream and (b) stream-wise directions in a 340 μm $\times$ 30 μm rectangular PDMS micro-channel within 200 nm of the wall using TIRF at $T = 39$ ^{o}C for a flow rate of $Q = 2$ μL/min over 450 image pairs. Here the standard deviation of the velocity corresponds to the Brownian motion of the quantum dots, while the error in the mean velocity measurement is significantly less when normalized by the number of samples (about ± 7 μm/s for the 95% confidence interval with over 2,000 samples).

Velocimetry Using Single Quantum Dots

After finding the sub-pixel particle locations as described in section 7.2.2, velocity distributions were computed from the individual particle displacements in the stream-wise and cross-stream directions for all temperatures. A sample velocity distribution is shown in figure 3.6 for $T = 39.0$ ^{o}C with a Gaussian fit. The mean of the distribution, u_{mean}, corresponds to the mean convective motion, while the standard deviation, u_{std}, is representative of the diffusion length, $s = u_{std}\Delta t$, due to the Brownian motion of the QDs and shear broadening in the stream-wise direction [42]. The mean velocities for all temperatures are shown in figure 3.7. The mean stream-wise velocity over all measured temperatures was 103.2 ± 7.1 μm/s, while the mean cross-stream velocity was 2.25 ± 6.0 μm/s. The standard
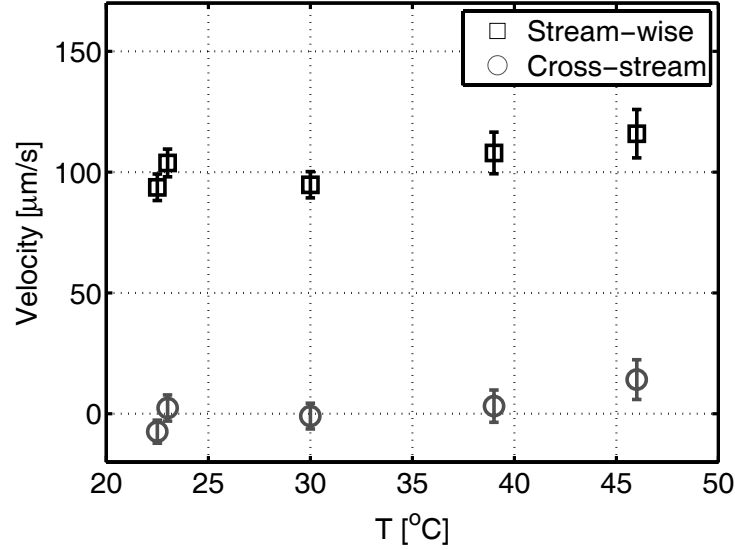
Figure 3.7: Mean velocity as a function of temperature for a constant flow rate of $Q = 2$ μL/min in a 340 μm $\times$ 30 μm rectangular PDMS micro-channel within 200 nm of the wall using TIRF for 450 image pairs. The error bar represents the 95% confidence interval with over 2,000 samples.

error of the ensemble-averaged velocity distribution for about $N = 2,000$ particle trackings was based on $\sigma = 2u_{std}/\sqrt{N}$ [10]. Again, here we measure the ensemble-averaged velocities, since the variation associated with a single QD displacement is extremely high due to the diffusivity of the particles. The ensemble-averaging prevents time resolved measurements with single QDs and currently, limits us to steady flows. The slight cross-stream velocity is consistent with a minor misalignment of the micro-channel and well within the error. An increase in the mean velocity was observed with temperature, which is most likely due to constriction of the micro-channel cross-section from thermal expansion of the PDMS at higher temperatures. Since the relatively soft PDMS micro-channel is constrained on three sides by the glass cover slip and copper blocks, thermal expansion of the bulk material could deform the channel cross-section enough to noticeably accelerated flow.

Characterizing Temperature and Viscosity through Brownian Motion

As outlined in section 3.1.1, particle displacements also carry some information about the fluid temperature and viscosity through their diffusion length, s. PIV Thermometry [27] measurements have been demonstrated previously by relating the PIV cross-correlation peak to temperature. However, we measure this relationship more directly through the standard deviation of the particle tracking displacement distribution (diffusion length) or alternatively, the diffusion coefficient D.

In the near-wall regions of micro-flows, hindered diffusion and shear broadening dominate particle displacement measurements [42]. Hindered diffusion arises from hydrodynamic interactions between the tracer particles and micro-channel walls, which suppresses the bulk diffusion coefficient [65, 66]. In the present study, we are only concerned with the wall-parallel directions, where the diffusion coefficients in the stream-wise and cross-stream directions are D_y and D_x, respectively. Since the hindered diffusion coefficients depend only on geometry, they exhibit the same $T/\mu(T)$ scaling as the theoretical Stokes-Einstein relation shown in equation (3.4). Additionally, shear broadening distorts the particle displacement distributions resulting in dispersion [39, 41]. Since shear broadening only effects the stream-wise particle displacements, accurate estimates of the diffusion coefficient are obtained from the cross-stream displacements.

Diffusion coefficients were calculated from the particle tracking data for each temperature from equation (3.3), and the results are plotted in figure 3.8 normalized by the appropriate diffusion coefficient at room temperature, D_0. D_x and D_y are normalized by the measured cross-stream diffusion coefficient $D_0 = D_x(T_0) = 30.0\ \mu\mathrm{m}^2/\mathrm{s}$, where $T_0 = 22.5\ ^o\mathrm{C}$. We can easily see the effects of shear broadening on the diffusion coefficient in the stream-wise direction. However, the cross-stream diffusion closely follows the $T/\mu(T)$ scaling, given
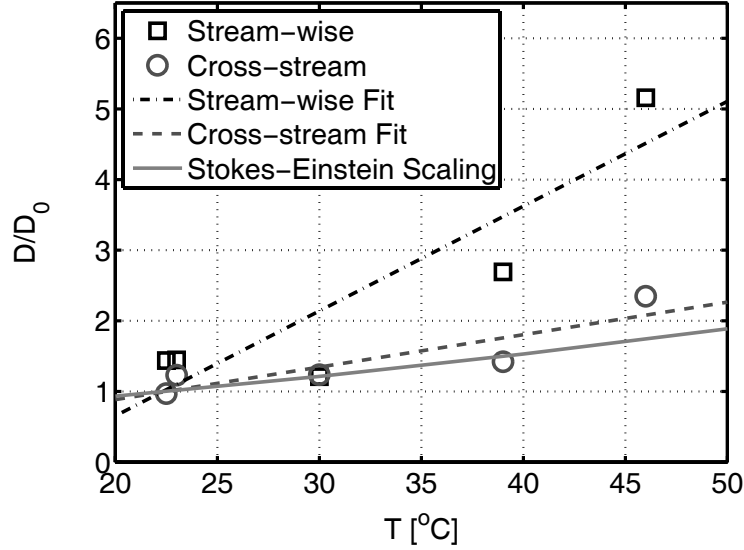
Figure 3.8: Scaled diffusion coefficients calculated from the stream-wise and cross-stream particle displacement distributions measured within 200 nm of the surface as a function of temperature compared to the Stokes-Einstein scaling of $T/\mu(T)$.

the viscosity of water as a function of temperature [118]. The slope of a linear fit through the measured cross-stream diffusion coefficients is 4.6% K^{-1}, compared to 3.2% K^{-1} for the Stokes-Einstein equation. Also, the diffusivity of the final data point at room temperature is consistent with the low intensity measured in section 3.3.2. Temperature measurements through diffusive particle displacements have a sensitivity of about four times that of temperature measurements through intensity changes. We also note that if the temperature can be measured accurately and independently, then it is possible to infer the fluid viscosity through the diffusivity from equations (3.3) and (3.4).

3.4 CONCLUSION

We have presented results from a series of experiments using ensemble-averages of single quantum dots as simultaneous temperature and velocity probes in steady, micro-scale flows.

The intensity variation with temperature of solutions of rhodamine 110 dye (Rh110) and quantum dots (QD) were characterized for use in a two-color, ratiometric temperature measurement system. A TIRF microscopy system was used to image Rh110 dye solutions and single QDs simultaneously within 200 nm of the liquid-solid interface of a micro-channel wall. By measuring both the position and intensity of single QDs flowing through PDMS micro-channels, the velocity and temperature of the solutions could be inferred. The near-wall velocity distributions were measured in the stream-wise and cross-stream directions from particle displacements using a statistical particle tracking velocimetry (SPTV) algorithm. The intensities of single QDs were normalized by simultaneously imaging a nearly temperature-independent reference dye (Rh110) to normalize temporal and spatial variations in the illumination intensity. Ensemble-averaged intensities from many single QDs were used to measure temperatures ranging from room temperature (22 ^{o}C) to 46 ^{o}C with an accuracy of ± 4.9 ^{o}C and a sensitivity of -0.84% K^{-1}. Ensemble-averaged measurements were used to suppress the high variance of a single intensity or displacement realization of a QD, preventing time resolved measurements.

Information about the fluid temperature and viscosity was also extracted from the ensemble-averaged statistics of Brownian particle displacements through the diffusion coefficient. The temperature sensitivity of the measured cross-stream diffusion coefficient was 4.6% K^{-1}, compared to 3.2% K^{-1} for the Stokes-Einstein equation scaling. If accurate information about either the solvent viscosity or temperature is known independently, then it is possible to extract information about the other quantity through diffusion measurements with QDs.

The sensitivity of the technique outlined here relies directly on the temperature sensitivity of the commercially available water-soluble CdSe/ZnS QDs used in the current

experiments. Modifications to the ZnS coating thickness have shown promise as a method to enhance the QD temperature sensitivity [31], and alternative materials, fluorophores or particles may provide improved sensitivity. The usefulness of this technique lies in the ability to make measurements in the very near-wall region of fluid-solid interfaces and in nano-flows (i.e. nano-channels) where other techniques may not be accessible and will be improved in the future by more sensitive materials.

ACKNOWLEDGMENT

Chapter 4

Direct measurement of slip velocities using three-dimensional total internal reflection velocimetry

P. Huang, J.S. Guasto and K.S. Breuer. *Journal of Fluid Mechanics*, Vol. 566, pp. 447-464, 2006.

The existence and magnitude of slip velocities between deionized water and a smooth glass surface is studied experimentally. Sub-micron fluorescent particles are suspended in water and imaged using Total Internal Reflection Velocimetry (TIRV). For water flowing over a hydrophilic surface, the measurements are in agreement with previous experiments and indicate that slip, if present, is minimal at low shear rates, but increases slightly as the shear rate increases. Surface hydrophobicity is observed to induce a small slip velocity, with the slip length reaching a maximum of 96 nm at a shear rate of 1800 s^{-1}. Issues associated with the experimental technique and the interpretation of results are also discussed.

4.1   INTRODUCTION

The century-old assumption of the no-slip boundary condition between a liquid and a solid has been challenged by recent experimental results and molecular dynamic simulations and has been the subject of many recent investigations exploring flows over both wetting and non-wetting surfaces. Although there is considerable disagreement regarding the existence of slip over a hydrophilic surface, it is generally believed that surface hydrophobicity aids slip, while the exact mechanism is not yet understood (for a review of this topic, see [119]). Experimental studies have reported a wide range of slip lengths, ranging from micrometers [120, 121, 122, 123], hundreds of nanometers [124, 125], to tens of nanometers or smaller (including no-slip) [126, 127, 128, 129, 130]. Molecular dynamics simulations, on the other hand, suggest small slip lengths, mostly less than 100 nm [131, 132, 133, 134, 135, 136].

The experiments have been conducted under various direct and indirect measurement techniques with varying accuracy and uncertainty. In indirect measurements, slip velocity is inferred from other flow quantities, such as the relationship between flow rate and pressure drop [126] or the measurement of the forces required to move a pair of crossed cylindrical surfaces separated by a thin film of the test fluid [127, 128, 129, 123]. In contrast, alternative techniques such as micro-particle image velocimetry (PIV) have resulted in direct measurements of near-surface fluid velocity using tracer particles [121, 130].

Although the direct measurements have a strong appeal, there are two major drawbacks inherent to conventional micro-PIV. The first is that the velocity is determined from the motion of a collection of particles in an interrogation area (IA) and, in order to obtain a reasonable estimate of the velocity, the IA must be measuring several hundred nanometers in size [121]. Hence the determination of phenomena which might measure a few nanometers is very difficult to resolve. A second problem is that the size of measurement volume along

the optical axis for flood-illuminated micro-PIV techniques is defined by the focal depth of the optical system, which is typically of the order of 0.5 to 1 micron [121, 130]. Although Joseph & Tabeling [130] reported a slip length measurement with 100-nm resolution, micro-PIV would still be insufficient to provide an affirmative conclusion if the true slip length is below 100 nm.

One attractive approach that solves both of these problems is the use of Total Internal Reflection Velocimetry (TIRV) [39] which uses total internal reflection of an incident laser pulse to generate a highly localized illumination of the surface flow, and relies on tracking the motion of single tracer particles rather than the collective particle motion that is used in PIV. Total internal reflection fluorescence microscopy (TIRFM) has long been used by biologists to study near-surface dynamics [137, 138, 139]. Zettner & Yoda [6] combined micro-PIV and TIRFM to study near-surface Couette flow while Pit *et al.* [124] measured slip velocity of hexadecane over a sapphire substrate using TIRFM and fluorescence recovery after photobleaching. We first reported on the TIRV technique in the context of slip velocities for near-wall microflows [39], but were unable to make a conclusive determination of the size or character of any slip lengths due to difficulties in the determination the location of tracer particles within the narrow evanescent illumination region.

The present manuscript reports on experiments in which the TIRV technique has been substantially improved to the point that quantitative statements can be made regarding the nature of slip velocities over hydrophilic and hydrophobic surfaces. By measuring the intensity of tracer particles' fluorescence, and in conjunction with a statistical model for the optical and hydrodynamic behaviour of small particles near a surface, we are able to track their motion within a narrow region above the solid surface and to compare that motion to the motion predicted for different levels of boundary slip.

4.2 THEORETICAL CONSIDERATIONS

4.2.1 Total Internal Reflection Microscopy

The evanescent field and its application to fluorescence microscopy has been thoroughly documented in literature [e.g. 140, 43, 36, 6, 141, 39]. In summary, an evanescent field can be created near a solid-liquid interface where total internal reflection occurs, as illustrated in figure 4.1. The field intensity, I, decays exponentially with distance, z, away from the two-medium interface by

$$I(z) = I_0 e^{-z/p}, \tag{4.1}$$

where I_0 is the intensity at the interface and p is known as the evanescent wave penetration depth. The penetration depth, which characterizes the length scale of the evanescent field, can be calculated from

$$p = \frac{\lambda_0}{4\pi} \left(n_1^2 \sin^2 \theta - n_2^2 \right)^{-\frac{1}{2}}, \tag{4.2}$$

where λ_0 is the wavelength of the incident light, θ is the beam incident angle and n_1 and n_2 are the indices of refraction of the solid and liquid, respectively.

4.2.2 Emission Intensity of Fluorescent Particles

For spherical tracer particles with a uniform volumetric fluorophore distribution in an evanescent field, Kihm *et al.* [43] calculated the particles' emission intensities as an exponential function of their distances to a substrate surface. Through experience we have found, however, that the intensity of fluorescence emission from a large number of nominally identical particles can vary due to a variety of factors, including statistical variations in illumination intensity, quantum efficiency of the imaging system and, most importantly, a distribution in the physical size of the particles. If we parameterize all of these variations
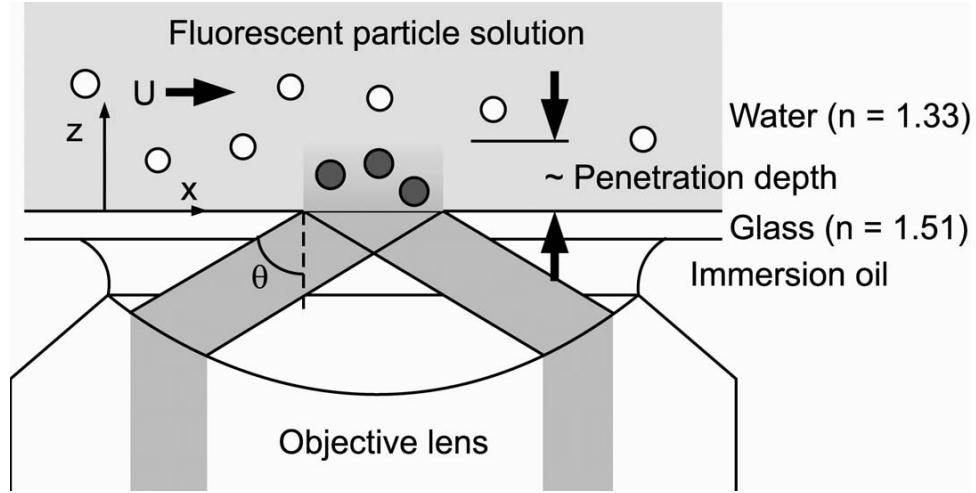
Figure 4.1: Objective-based total internal reflection fluorescence microscopy.

by an "effective emission radius", r, we can model the particle's probability density function (PDF) of its effective emission radius with a Gaussian distribution

$$P(r) = P_0 \exp\left[-\frac{\left(\frac{r}{a} - 1\right)^2}{\sigma_r^2}\right],$$ (4.3)

where a is the mean effective emission radius of the batch, σ_r is the characteristic variation (standard deviation) and P_0 is a normalization constant. Based on the calculation of Kihm *et al.* [43] and the assumption that emission intensity of a fluorescent particle is proportional to the number of fluorophores within its volume, the emission intensity, I^e, of a particle in an evanescent field is

$$I^e(r, h) = \left(\frac{r}{a}\right)^3 \left[I_0^e e^{-(h-a)/d}\right],$$ (4.4)

where h is the distance from the particle's centre to the substrate surface at which total internal reflection occurs, I_0^e is the emitted intensity of a single particle with $r = a$ located at $h = a$ (ie. touching the substrate surface), and d is an intensity decay length that need not be the same as the evanescent penetration depth. The intensity decay length can be

obtained experimentally by statistically measuring intensities of particles as a function of particles' distances away from the substrate. Combining (4.3) and (4.4), one gets the joint PDF of the emitted intensity and a particle's distance to the substrate as

$$P(I^e, h) = \alpha \exp\left\{-\frac{\left[\sqrt[3]{\left(\frac{I^e}{I_0^e}\right)e^{(h-a)/d}} - 1\right]^2}{\sigma_r^2}\right\}. \tag{4.5}$$

When an ensemble of tracer particles are imaged, they would certainly be located at a range of distances from the substrate surface. The lower limit of this imaging range is $h = a$, representing a particle touching the substrate surface. The upper limit of the imaging range is determined by the sensitivity of the recording medium, such as an intensified CCD camera used in this study. For a given imaging range of $h_1 < h < h_2$, the PDF of a tracer particle's intensity is given by

$$P(I^e, h_1 < h < h_2) = \int_{h_1}^{h_2} P(I^e, h)c(h) \, dh, \tag{4.6}$$

where $c(h)$ is the concentration profile of particles in the fluid. A sample plot of this distribution (4.6) is shown in figure 4.2 for a range of values of σ_r. For a low variation in effective emission radius (σ_r small), we see that the particles in the defined imaging range are sharply defined in intensity, with the brightest particles located at the surface ($I^e/I_0^e = 1$) and the faintest particles at the outer edge of the evanescent field ($I^e/I_0^e = 0.2$). However, as the variation in particle radius increases, the transitions become more blurred, and some larger particles close the wall contribute to the long tail at high observed intensities, while small particles close to the edge of the imaging range are represented by the smooth transition close to $I^e/I_0^e = 0$.
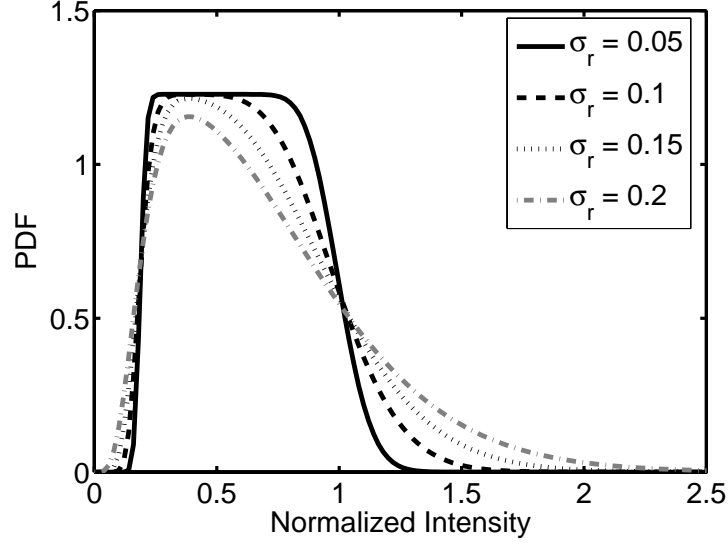
Figure 4.2: The emission intensity distribution of particles in a uniform concentration field. The normalized intensity in the horizontal axis is defined as I^e/I_0^e, and the calculation is performed with a normalized observation range of $0 < h/a < 3$ and a normalized intensity decay length of $d/a = 1.8$.

When performing image analysis, however, one need not analyse all imaged particles. Instead, using particle intensity as a guide, one can choose to identify and analyse only the particles within a certain desirable intensity range, ignoring particles that appear too bright or too dim. Equation (4.5) could also describe the particle position distribution within a normalized intensity range of $\alpha < I^e/I_0^e < \beta$ by

$$P\left(h, \alpha < I^e/I_0^e < \beta\right) = c(h) \int_\alpha^\beta P(I^e, h) \, d\left(\frac{I^e}{I_0^e}\right). \tag{4.7}$$

An example of this position distribution (4.7) is shown in figure 4.3 for a normalized intensity range of $0.5 < I^e/I_0^e < 1$. The most obvious feature of figure 4.3 is that the distribution is non-uniform with the majority of particles contributing to this range of intensities coming from close to the substrate surface (< 250 nm). In addition, one can observe that the
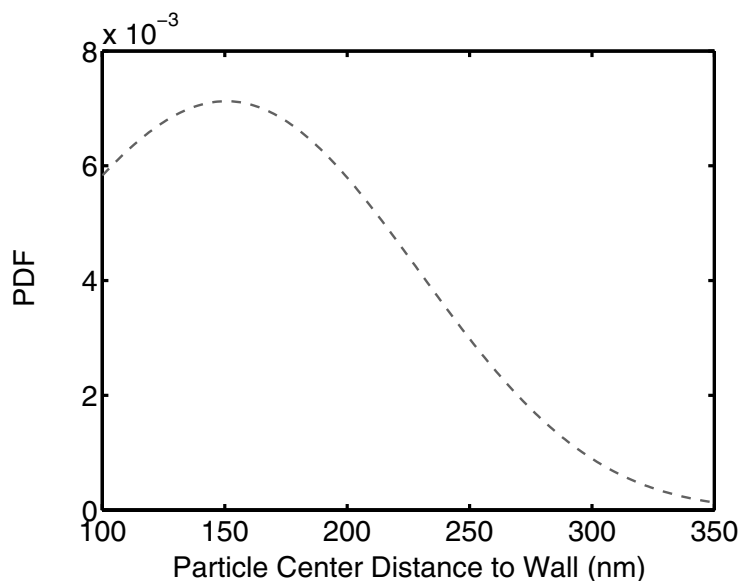
Figure 4.3: The predicted position distribution of particles with $0.5 < I^e/I^e_0 < 1$ in a uniform concentration field. In this prediction, $a = 100$ nm, $d = 181$ nm and $\sigma_r = 0.18$.

distribution has a long positive tail that gradually decays to zero at far away into the fluid bulk. Because of the large particle effective radius variation in this example, a large particle far away (for example, > 300 nm) can exhibit in the same the same fluorescence intensity as that of smaller particles close to the substrate surface. These observations reinforce the fact that a particle's intensity cannot be monotonically related to its distance to the solid surface, and attention should be given to any intensity-based quantitative analysis by recognizing the non-uniform position distribution and the contribution of particles far away from wall.

4.2.3 Near-Surface Shear Flow

Although we are interested in determining the velocity of a pure fluid near a solid surface, we actually measure the velocity of small spheres near the surface, and it is critical to recognize the differences between these two quantities. It is well known that shear and near-surface

hydrodynamic effects can cause a tracer particle to rotate and translate at a velocity lower than the local velocity of the fluid in the same shear plane [63, 66]. Goldman *et al.* [66] proposed that a particle's translational velocity, U, in a shear flow with local shear rate, S, is given by

$$\frac{U}{hS} \simeq 1 - \frac{5}{16}\left(\frac{h}{r}\right)^{-3}, \tag{4.8}$$

valid for large h/r, and

$$\frac{U}{hS} \simeq \frac{0.7431}{0.6376 - 0.2\ln\left(\frac{h}{r} - 1\right)}, \tag{4.9}$$

valid for small h/r. Although there exists no analytical approximation for intermediate values of h/r, Pierres *et al.* [142] proposed a cubic approximation to numerical values presented by Goldman *et al.* [66]:

$$\frac{U}{hS} \simeq \left(\frac{r}{h}\right)\exp\left\{0.68902 + 0.54756\left[\ln\left(\frac{h}{r} - 1\right)\right] + 0.072332\left[\ln\left(\frac{h}{r} - 1\right)\right]^2 \right.$$
$$\left. + 0.0037644\left[\ln\left(\frac{h}{r} - 1\right)\right]^3\right\}. \tag{4.10}$$

The apparent velocity, $\bar{U}$, of a large ensemble particles chosen from a normalized intensity range of $\alpha < I^e/I_0^e < \beta$ and located in an imaging range of $h_1 < h < h_2$ is given by the average of the local velocity integrated over the imaging range:

$$\bar{U} = \frac{1}{h_2 - h_1}\int_{h_1}^{h_2} U\left(h, a, S\left(h\right)\right) P(h, \alpha < I^e/I_0^e < \beta)\, dh. \tag{4.11}$$

This average apparent velocity, $\bar{U}$, can be compared to the mean velocity, of the pure fluid, $\bar{V}$, calculated for the same imaging range. The ratio of the two is shown in figure 4.4, from which we see that the average apparent velocity of particles is, not surprisingly, significantly lower than that of pure fluid velocity when the imaging range is very close to the substrate
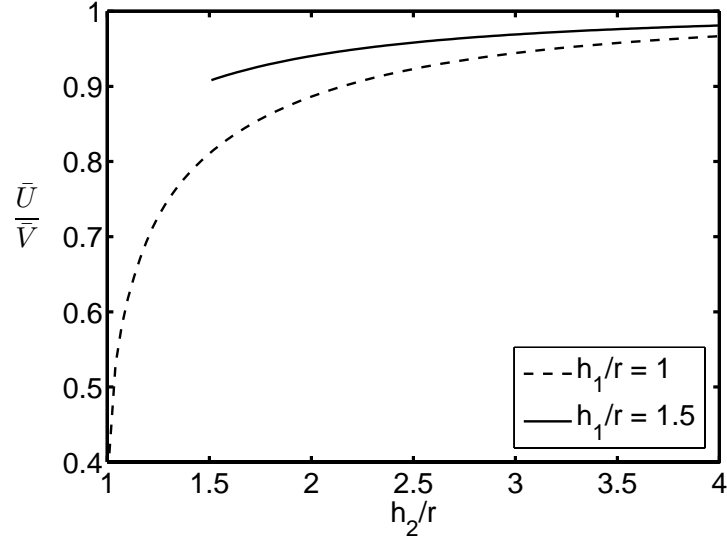
Figure 4.4: The ratio of statistical apparent velocity of particles and mean fluid velocity under no slip in an imaging range of $h_1 < h < h_2$, which is non-dimensionalized by particle radius. $\bar{V}$ is computed with linear fluid velocity profile, which is a good approximation near a surface. In the computation of $\bar{U}$, $c(h)$ is assumed to be uniform.

surface. This difference must be incorporated into the data analysis, and failure to recognize this effect can lead to misinterpretation of the measured data and underestimation of slip lengths.

It should be noted that (4.11) is based on a no-slip condition at the fluid/solid interface. If there exist a slip velocity, U_{slip}, at the solid boundary, the apparent velocity of the same ensemble of particles would be

$$\bar{U}_{app} = U_{slip} + \bar{U} = \delta S_w + \bar{U}, \qquad (4.12)$$

where the slip velocity is characterized as the product of the slip length, δ, and the wall shear rate, S_w.

4.3 EXPERIMENTAL PROCEDURES

4.3.1 Materials and Setup

A schematic of the image acquisition system is shown in figure 4.5. Fluorescent particles were illuminated with an objective-based TIRFM method, as detailed in [39]. A pair of 532-nm, 5-nsec laser pulses (Quantel Twins Q-Switched Double Pulse Nd:YAG Laser) were directed through a Nikon PL Apo NA 1.45 100X TIRF oil immersion objective at an angle that created total internal reflection at a glass-water interface, thus illuminating the near-surface region of water with an evanescent field (figure 4.1). Fluorescent images of near-surface particles were projected onto a Q-Imaging Intensified Retiga CCD camera (ICCD), capable of recording 1,360 pixels by 1,036 pixels 12-bit images. Under 100X magnification, each image pixel corresponds to 64.3 nm in the flow channel and the diffraction-limited spot size is 19.7 μm (calculated based on [108]). A TTL pulse generator (Berkeley Nucleonics Model 555) was used to synchronize laser pulses and image acquisitions. The energy of each illuminating laser pulse was recorded simultaneously with each image acquisition and this was used to adjust the resultant images and thus account for pulse-to-pulse variations in illumination intensity.

Test channels were fabricated using a polydimethylsiloxane (PDMS) (Dow Corning Sylgard 184) molding technique [143] and bonded onto polished glass wafers. The dimensions of the test channels were 50 ± 1 μm deep, 250 ± 1 μm wide and 15 mm long. To create hydrophilic microchannels, the pre-bonding PDMS surface was exposed to an oxygen plasma and immediately immersed in deionized-water after bonding to a glass wafer. Hydrophobic channels, on the other hand, were fabricated by bonding untreated PDMS channels onto octadecyltrichorosilane(OTS)-coated glass wafers. Detailed coating procedures can be found
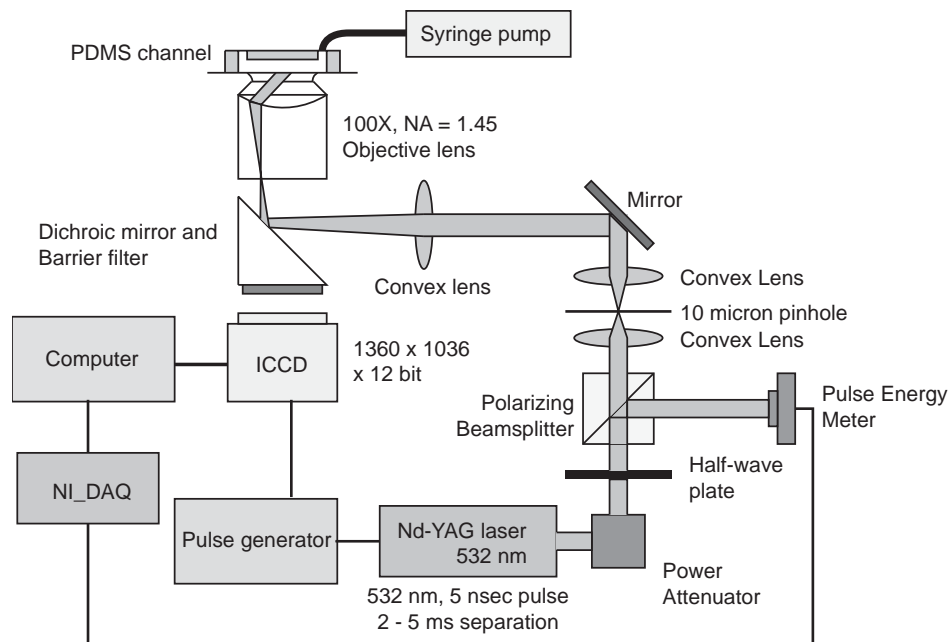
Figure 4.5: Image acquisition system.

in [39]. It has been reported that water has a contact angle of 120 degrees with a similarly prepared OTS-coating [121, 144]. The roughness of the test surface was measured using an atomic force microscope prior to bonding. The hydrophilic and hydrophobic surfaces had an RMS surface roughness of 0.47 nm and 0.35 nm respectively.

Monodisperse Fluorescent Polystyrene Microspheres (Duke Scientific) with diameters of 200 nm ($\pm$ 5%) suspended in purified water (Fluka) at 0.04% volume fraction were used as tracer particles in this experiment. These microspheres have a peak absorption wavelength of 542 nm and emit a red light at 612 nm. There are three reasons that 200-nm diameter particles were selected as probes in this experiment. First, smaller size fluorescent particles have much larger size variation, making relation of particle center distance from the solid wall and their fluorescent intensities less reliable. Secondly, smaller particles do not contain enough fluorophores to provide significant signals with a 5-nsec laser illumination. Lastly, 200-nm particles do not diffuse too far during the inter-frame time, with diffusion out of

imaging range being our major concern.

A Harvard Apparatus 22 syringe pump was used to maintain particle solution flow rates, ranging from 1 to 10 μL/min ($\pm 0.35\%$). To maintain steady pumping motions of the Harvard Apparatus stepper motor, we purposely introduced a large volume of air between the piston and the fluid in the syringe. This volume of air acted as a pressure shock absorber to damp out the oscillatory forcing of the syringe pump screw. In addition, a long tubing (> 1 m long) was used to connect the syringe and the channel inlet. Particle flow motion was observed to be very steady under this setup.

1200 images were captured at each flow rate, as well as in quiescent fluid. Once all necessary images of particle motion were captured, the test channel was filled with rhodamine-B solution. Images of the rhodamine-B solution were subsequently captured under the same evanescent illumination, and averaged to obtain an image characterizing the spatial distribution of the illuminating laser beam.

It has been suggested that nanobubbles and a gas bubble layer on hydrophobic surfaces could be alternative sources of apparent slip [119, 145, 146]. Prior to each experiment, the fluid was degassed by placing the solution in vacuum for at least 30 minutes. This procedure has been reported to significantly eliminate nanobubble formation [147].

It is intuitive to assume that one can infer the location of a particle in the evanescent illumination field based on the fluorescence intensity. Kihm *et al.* [43] used a ratiometric fluorescence intensity to track particle motions three-dimensionally. Although this is theoretically feasible, in practice, successful use of this technique requires precise knowledge of the illumination beam incident angle and a solution of Maxwell's equation for an evanescent field in a three media system (glass, water and polystyrene), which can be difficult to express explicitly. Thus, an experimental method was devised to obtain a ratiometric rela-

tion between particle emission intensity and its distance to the glass surface. We attached individual fluorescent particles to fine tips of glass micropipettes, which were translated perpendicularly to the glass substrate in the evanescent field with a 0.4-nm precision stage (MadCity Nano-OP25). At each distance to the surface, 30 images of the attached particles were captured. The pixel values of the imaged particles were then averaged, and subsequently fitted to a two-dimensional Gaussian function to find their centre intensities. The process was repeated several times with different particles. The particle intensities are shown in figure 4.6, along with a exponential fit to the measured data:

$$I_{peak} = Ae^{-\lambda(h-r)} + B, \tag{4.13}$$

where A, B and λ are constants determined by a least-squares fit. The fitted curve predicts an intensity decay depth of 181 nm, very close to the evanescent penetration depth that we would predict based on the imaging lens, wavelength and refractive indices of the system.

4.3.2   Velocimetry Analysis

The analysis of particle image pairs was performed using a custom particle-tracking program written in a MATLAB environment. Prior to velocimetry analysis, images of particles stuck on the glass substrate had to be removed from each image pair to prevent undesirable detection by the Particle Tracking Velocimetry (PTV) algorithm. Although the presence of these stuck particles could distort the velocity field, they generally had a very low density and were usually placed at the edge of an image and far away from where the velocimetry measurements were performed. For each image, the signals due to stuck particles and background noise were removed by subtracting a reference image formed from the rolling average of 10 previous and 10 subsequent image pairs. To account for laser pulse energy
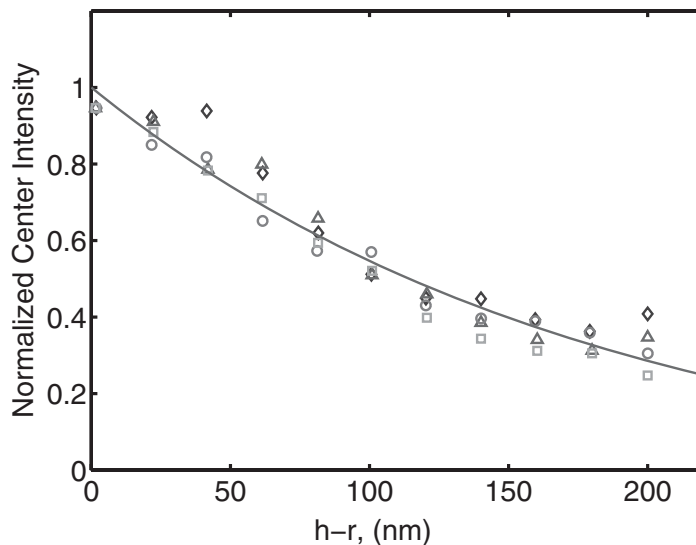
Figure 4.6: Fluorescent particle intensity as a function of its distance to the glass surface. The particles used here are 200 nm in diameter. The solid line is a least-square exponential fit to the data whose decay length, λ, is 181 nm.

fluctuation, every image was scaled by the measured laser illumination energy.

Velocimetry analysis started with finding the positions and peak intensities of all particles via threshold-identification and Gaussian fitting of the intensities of the pixels surrounding the peak. Subsequently each particle's displacement was obtained with a limited-range nearest-neighbor matching, and the displacement was decomposed into streamwise and cross-stream components (for details of the tracking algorithm, see [39]). The particle seeding density was low enough such that this tracking was unambiguous. Intensities of the "trackable" particles were converted to a normalized intensity ratio obtained by dividing the raw intensity counts by the average of all the stuck particles' initial intensity counts. Finally, particles within a desired normalized intensity range were selected for each flow rate and their mean streamwise velocity was defined as the apparent velocity of the ensemble. For the hindered diffusion analysis, the same analysis steps were followed except
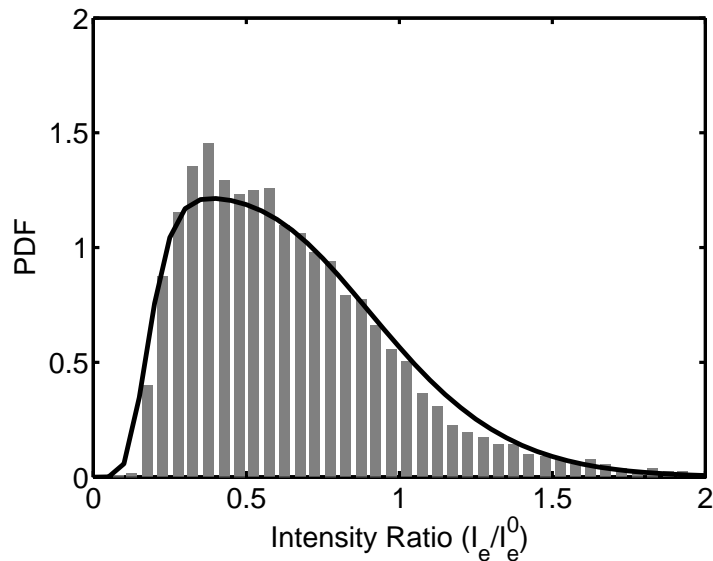
Figure 4.7: Observed fluorescent particle intensity distribution and its probability density function (PDF). The solid line represents the theoretical prediction (4.6) for an imaging range of 100 to 400 nm and a 15% intensity statistical variation with a uniform concentration distribution of particles.

that diffusion coefficients of particles in quiescent fluid were obtained from the variance of displacements instead of velocities.

4.4   RESULTS AND DISCUSSION

4.4.1   Validation of Intensity Calibration Curve

Figure 4.7 shows the distribution of particle intensities recorded during a typical data acquisition (in this case, in quiescent fluid). The accompanying solid line is the theoretical prediction (4.6), assuming an imaging range of 100 - 400 nm, and an effective emission radius variation of $\sigma_r = 0.15$. The good agreement between the observed and predicted intensity variation confirms our calibration results and the statistical theory of the observed particle intensities discussed earlier.

4.4.2 Hindered Diffusion

Near-surface tracer particles are known to exhibit anisotropic hindered diffusion due to hydrodynamic effects, and the hindered diffusion coefficient in the direction parallel to the substrate surface $D_\parallel$ is [65]

$$\frac{D_\parallel}{D_0} = 1 - \frac{9}{16}\left(\frac{h}{r}\right)^{-1} + \frac{1}{8}\left(\frac{h}{r}\right)^{-3} - \frac{45}{256}\left(\frac{h}{r}\right)^{-4} - \frac{1}{16}\left(\frac{h}{r}\right)^{-5} + O\left(\frac{h}{r}\right)^{-6}, \qquad (4.14)$$

where D_0 is the Stokes-Einstein diffusivity of a spherical particle in the fluid bulk. This "Method of Reflection" approximation is generally valid for $(h-r)/r > 1$. For $(h-r)/r < 1$, Goldman *et al.* [66] proposed an asymptotic solution,

$$\frac{D_\parallel}{D_0} = -\frac{2\left[\ln\left(\frac{h-r}{r}\right) - 0.9543\right]}{\left[\ln\left(\frac{h-r}{r}\right)\right]^2 - 4.325\ln\left(\frac{h-r}{r}\right) + 1.591}. \qquad (4.15)$$

The combination of our particle-tracking algorithm and the intensity calibration curve was applied to analyse near-surface particle Brownian motion parallel to the glass substrate. The results are compared to the Methods of Reflection calculation (4.14) and shown in figure 4.8. The experimental data shows reasonably good agreement with the theory, including the fall in the effective diffusion coefficient close to the surface. The results further improve our confidence in the overall experimental method and subsequent analysis.

4.4.3 Velocity Distributions of Particles

Figure 4.9 shows distributions of particle velocities at three different shear rates. Note that the streamwise velocity distributions widen as shear rate increases, and their asymmetric shapes show an increasing skewness as the shear rate increases. The increasing distribution width and skewness at high shear rates are both results of sampling particle displacements
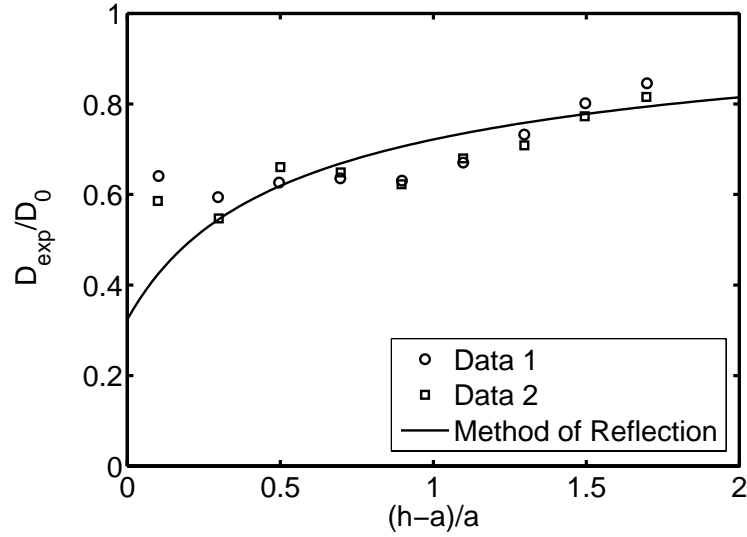
Figure 4.8: Ratio of hindered diffusion coefficients (D_{exp}) for Brownian motion parallel to a surface.

from an imaging range with finite thickness [39]. Physically, at higher shear rates, the finite-thickness imaging range contains particles that are translated by a wider range of local velocities, hence the increasing width of the apparent velocity distributions. In addition, because the particles are confined by the solid wall, they are more likely to move away from the wall and into a faster moving shear plane. Thus the distribution exhibits a more pronounced positive skewness at the higher shear rates.

The effect of shear with a finite-thickness imaging range can be characterized if the streamwise particle velocity in figure 4.9, V, is scaled by

$$\tilde{V} = \frac{V - \langle V \rangle}{\langle V \rangle}, \tag{4.16}$$

where $\tilde{V}$ is the scaled streamwise particle velocity and $\langle V \rangle$ is the mean value of each velocity distribution. The scaled velocity distributions are shown in figure 4.10. At each shear
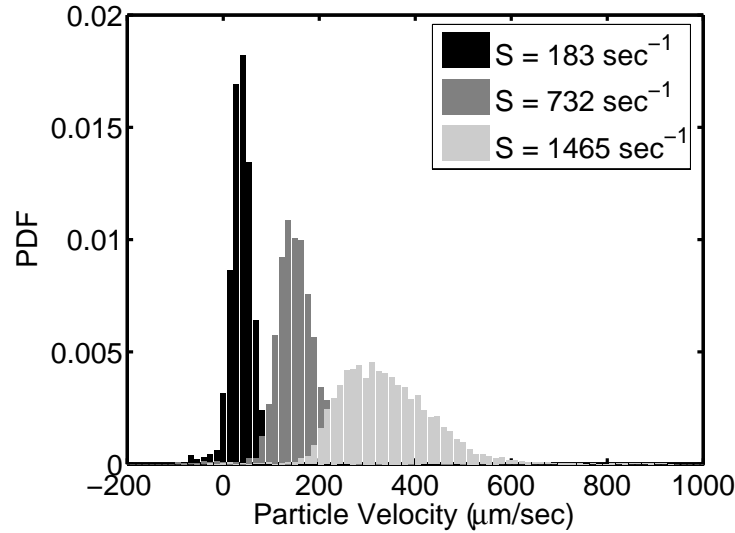
Figure 4.9: Distribution of observed particle streamwise velocities under various shear rates. Data include measurements of flow over a hydrophobic surface.

rate, the relatively contributions of velocities from shear flow and Brownian motion can be characterized by the Peclet number, Pe. Here the Peclet number is defined as the ratio of the shear-induced displacement, L, to the diffusive displacement, s, during the interframe time period, Δt,

$$Pe = \frac{L}{s} = \frac{\langle V \rangle \, \Delta t}{\sqrt{2D_0 \Delta t}}. \tag{4.17}$$

Because $\langle V \rangle$ is shear-dependent only, the shear-induced effects in all velocity distributions in figure 4.10 are scaled to equal magnitudes. It can be observed that small Peclet numbers are associated with greater distribution widths while the distributions collapse onto a single skewed distribution at high Peclet numbers. The explanation is the following: at low Peclet numbers the distributions widths scale inversely to shear, suggesting a diffusion dominance and thus the large widths of the velocity distributions are due to Brownian motion. As the Peclet number increases, the effect of shear flow on particle motion
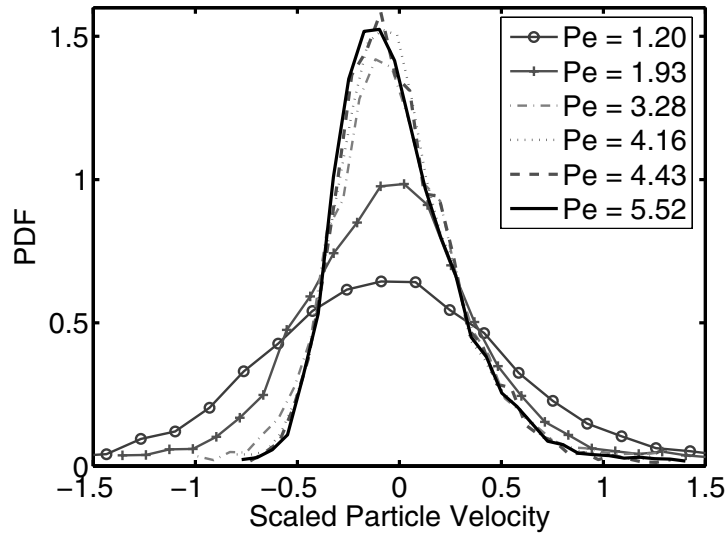
Figure 4.10: Distribution of observed particle streamwise velocities after scaling the velocities distributions in figure 4.9. The velocities are scaled according to (4.17). Pe of 1.20, 3.28 and 4.43 correspond to the shear rates of 183, 732 and 1465 $\sec^{-1}$ in figure 4.9, respectively.

increases and when $Pe > 3$, particle motions are completely shear-dominant, causing the distributions to overlap. It should be noted that the overlapping distributions have the same distribution width, asymmetric shape and the same positive tail, which are absent in small Peclet number cases. These observations confirm the explanation that in figure 4.9, the increasing distribution width and skewness at high shear rates are both effects of shear.

4.4.4 Measurements of Apparent Slip Velocities

For each flow case, the intensity distribution of all "trackable" particles were compared to the theoretical prediction (4.6) to identify the unknown parameters such as h_1, h_2 and σ_r through optimization, as demonstrated in section 4.4.1 and figure 4.7. With these parameters known, we calculated the theoretical apparent velocities of a particle ensemble, chosen from a normalized intensity range, by using equation (4.12) and varying the slip length

conditions. Subsequently, these velocities were compared to the experimental apparent velocities (mean values of the streamwise velocity distribution) of particles from the same normalized intensity range to extract experimental slip velocities and slip lengths.

Figures 4.11 and 4.12 show the experimental and theoretical apparent velocities as a function of wall shear rate over hydrophilic and hydrophobic surfaces, respectively. In both figures, the solid lines represent the theoretical apparent velocities assuming zero slip (equation (4.11)). The dashed and dotted lines are the expected apparent velocities if one were to assume a 50-nm and a 100-nm slip length, respectively (calculated using (4.12)). In the case of the hydrophilic surface (figure 4.11), the measured slip length ranges from 26 to 57 nm with a slightly increasing trend as wall shear rate increases. The data obtained for flow over the hydrophobic surface (figure 4.12), on the other hand, suggests a larger slip length ranging from 37 to 96 nm, with a more observable increasing trend of wall shear rate dependence at higher shear rates. A quantitative comparison of the two cases shows a slip length attributed to surface hydrophobicity ranging from -7 nm at low shear rates to 54 nm at the highest tested shear rate, with an average value of 16 nm in between (figure 4.13). The additional slip caused by surface hydrophobicity is in agreement with many experimental results [126, 127, 129, 130], but is in sharp disagreement with others [121, 125, 123].

There are three possible sources of measurement uncertainty in figure 4.11 and 4.12: determination of (a) the wall shear rate, (b) the apparent velocities of particle ensembles and (c) the imaging range. Because wall shear rates are calculated based on microchannel dimensions and flow rates which are controlled by the syringe pump, we estimate that the uncertainty in the wall shear rates is less than 3%. If there is significant slip at the wall, the shear rates could be slightly lowered than the reported values. However, the
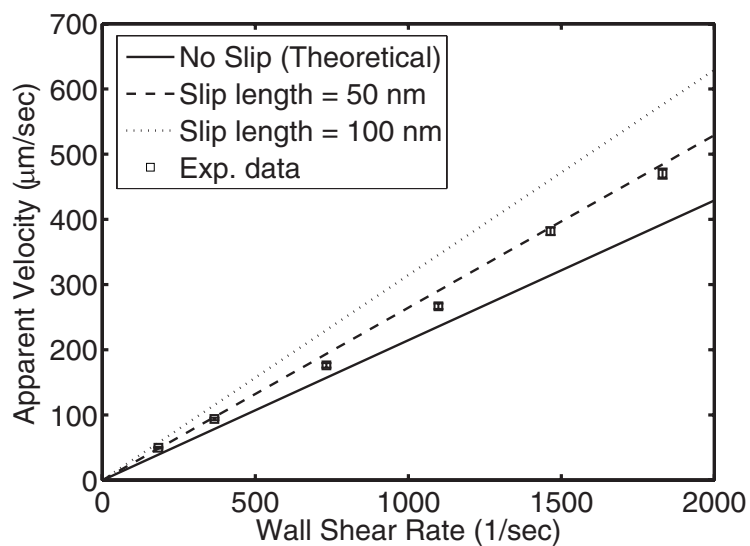
Figure 4.11: Experimental apparent velocity of particles in a shear flow over a hydrophilic surface $(0.21 < I^e/I_0^e < 0.78)$, and its comparison to slopes of expected apparent velocities if there exists a 0, 50 or 100-nm slip length. The error bar of each experimental data point represents a 95% confidence interval. In all cases the 95% confidence intervals are within $\pm 3\%$ of the reported mean velocity values.
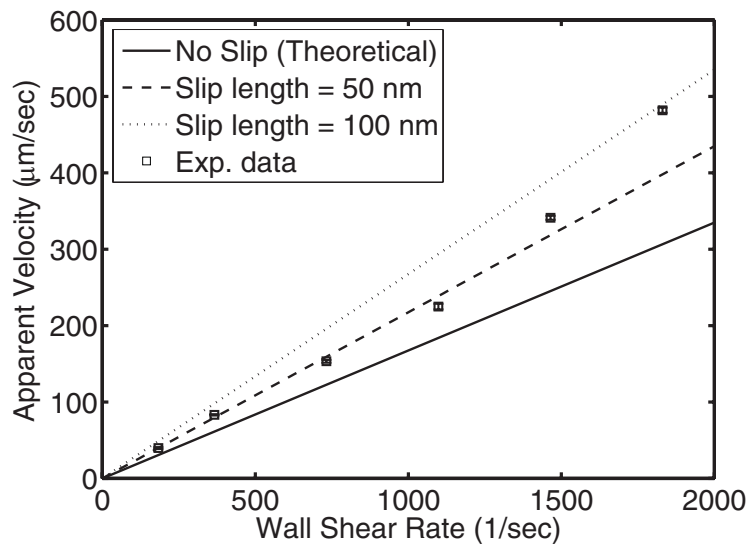
Figure 4.12: Experimental apparent velocity of particles in a shear flow over a hydrophobic surface $(0.5 < I^e/I_0^e < 1.0)$, and its comparison to slopes of expected apparent velocities if there exists a 0, 50 or 100-nm slip length. The error bar of each experimental data point represents a 95% confidence interval. In all cases the 95% confidence intervals are within $\pm3\%$ of the reported mean velocity values.
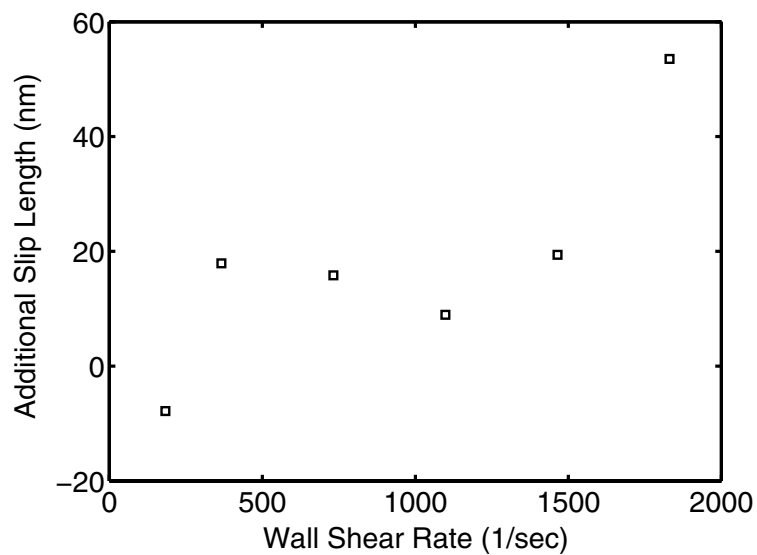
Figure 4.13: The additional slip length due to surface hydrophobicity.

largest observed slip length is less than 1% of the channel height, and thus the slip effect on wall shear rate calculation can be safely neglected. The determination of apparent velocities of particle ensembles also has extremely low uncertainly because central limit theorem constrains the statistical mean of a large sample (a few thousand trackings) to a very low uncertainty ($< \pm 3\%$ of the reported velocity values for 95% confidence intervals). In addition, with subpixel resolution of the particle centre detection, our PTV algorithm is able to track particle displacements with high accuracy (< 0.1 pixel, [54]). The largest source of uncertainty is the determination of the imaging range. The imaging range is determined statistically based on the particle intensity decay length obtained from figure 4.6 where intensity measurements were performed in increments of 20 nm, which could serve as the upper limit of imaging range uncertainty. However, it should be noted that, with an uncertainty of 20 nm taken into consideration, the largest measured slip length still will not exceed 150 nm – much smaller than other experimental studies which reported slip lengths greater than a few hundred nanometers.

One should note that the corrections due to shear-induced rotation (figures 4.11 and 4.12) do not account for the possibility of slip between the fluid and the tracer particle, and we are unaware of any work that extends the theory of Goldman *et al.* [66] to include the effect of surface slip. Physically, surface slip is unlikely to be an issue, because the tracer particles have relatively rough surfaces. Nevertheless, we can qualitatively estimate its effect. Slip between the fluid and the tracer particle will modify the particle velocity in two ways. Firstly, the reduced shear force will result in the particle velocity lagging the local fluid velocity. Secondly, however, slip will reduce the shear-induced rotation of the particle. Since these two mechanisms act in opposition to each other, we believe that, as a first approximation, we can ignore this effect.

Granick *et al.* [145] and Lauga *et al.* [119] both pointed out that large surface roughness can significantly decrease slip. The slip length we measured with sub-nanometer surface roughness, however, agrees well with the surface roughness dependency reported by Zhu & Granick [127]. It should also be noted that Joseph & Tabeling [130], with flow experiments conducted under similar surface roughness, hydrophobic coating and shear rates, reported slip length very close to the present results. It has also been suggested that electrokinetic effects could significantly affect velocimetry measurements of suspended particles close to a surface. Lauga [148] reported that a streaming potential can induce electrophoretic motion of particles if particle surfaces are charged, and applying this theory to the current conditions results in an "apparent" slip length of at most 18 nm.

Electrostatic interaction between tracer particles and surface could also affect accuracy of velocimetry measurements [119]. If the tracer particles and the substrate surface are similarly charged, electrostatic repulsion can create a depletion layer near the substrate surface that effectively shifts the imaging range. Because the slip length calculations in figure 4.11 and 4.12 are based on the assumption that particle concentration is uniform near surface, a depletion layer could be a source of "apparent slip" if it is not recognized. Lumma *et al.* [125] suggested that the depletion layer thickness can be as large as 0.9 μm for a pure water and glass combination. Such a thickness seems unreasonably large as it is much bigger than the evanescent field penetration depth and consequently few fluorescent particles would be observed. In contrast, Flicker *et al.* [149] experimentally measured the depletion layer thickness to be in the order of 10 to 30 nm. For our experimental setup, calculations suggest that, based on the overall particle seeding density, if the particles are uniformly distributed in the fluid one should be able to see around 19 particles in a 26 μm-by-26 μm image field. This is in close agreement with our experimentally-derived images,

and we can conclude that the depletion layer thickness must be much smaller than our imaging range and thus effects due to a depletion layer thickness of this magnitude would not be detectable with our current imaging technique. However, recognizing the possibility of such depletion layer's existence, we re-analysed the theoretical curves in figure 4.11 and 4.12 by assuming an imaging range farther away from the substrate surface. We found such a shift would result in higher theoretical apparent velocities of particle ensembles and therefore lower slip lengths for all shear rates, suggesting that our reported slip lengths are most likely the upper bound of the true slip length value.

The electrostatic and electrokinetic interactions are an interesting pair as their significance decreases with increasing ionic strength of the test fluid. Perhaps a more accurate direct measurement of the true surface slip can be obtained if aqueous solutions of moderately high ionic strengths were used.

4.5   CONCLUDING REMARKS

The results presented here represent direct measurements of local velocities in the near wall region of a fluid-solid boundary. Despite the relative simplicity of the experiment, several subtle issues need to be carefully addressed, including the spatial non-uniformity of the illumination region, the effects of the local shear on the dynamics of seeding particles, and the statistical variations in the effective visibility of the seeding particles. The current experiment confirms previous measurements in our own group [126] as well as some other recent measurements [127, 130] that there is minimal slip over hydrophilic surfaces, and that hydrophobic surfaces do appear to introduce a discernable, but small boundary slip.

Although the present technique does allow for measurement of particle motions very close to the solid surface, it does suffer from some limitations and there is room for improvement.

Most notably, the tracking in the wall-normal direction is currently limited to an accuracy of approximately 10% of the evanescent penetration depth (about 20 nm in the current case). If particles with a higher degree of monodispersity can be reliably found, and if the imaging system noise can be reduced (both of which are technical improvements on the immediate horizon), we believe that the technique can be used to track particles with an order of magnitude improvement in accuracy. However, even with the current levels of uncertainty, there is no possibility that the flow exhibits a slip length more than 150 nm (figure 4.12) over the range of shear rates tested.

While the debate of slip versus no-slip will likely continue in the foreseeable future, we believe that a consensus is forming from more recent experiments that the slip effect is not as extreme as some studies might have suggested. As many authors have pointed out, measurement and interpretation of slip data in the nanoscale can be very tricky because other physical phenomena, such as electrokinetics and nanobubbles, might lead to observations of an "apparent slip" caused by other complicating factors. All of these suggest that close attention must be to paid to documenting the experimental conditions, and that this might well reveal the reasons behind the range of reported apparent slip phenomena.

ACKNOWLEDGMENT

Chapter 5

Measurement bias in evanescent fields due to particle size variations and force interactions

J.S. Guasto and K.S. Breuer. *Measurement Science and Technology*, in review, 2008.

Total internal reflection fluorescence (TIRF) or evanescent wave microscopy has become a widely utilized tool in micro- and nano-fluidic studies for tracking the motions of small tracer particles (10 nm to 1 µm) near liquid-solid interfaces. Such measurements are used to measure particle displacements and to infer the near-wall fluid velocity. Several competing effects, including non-uniform particle size distribution, forces acting on the particles (electrostatic, van der Waals, etc.) and the optical detection of particle in the evanescent field, can bias the measurements, making it difficult to infer the particle concentration distribution and inferred fluid velocity. We present an analysis that considers all of these

phenomena, providing predictions for the observed light emission intensity of the particles and concentration distributions. Supporting measurements corroborate the theory well.

5.1 INTRODUCTION

The technique of total internal reflection fluorescence (TIRF) or evanescent wave microscopy has become widely popular in micro- and nano-scale studies of nanometer-sized colloidal particles near liquid-solid interfaces for particle tracking and velocimetry measurements [6, 39]. The high resolution and low signal-to-noise ratio of TIRF are due to the localized illumination, which decays exponentially with distance from the surface and a characteristic penetration length, $\delta \sim 200$ nm. The particle emission intensity may be used to infer distance from the interface [51, 43, 41], while tracking particles parallel to the interface yields an estimate of the velocity within the evanescent field. Applications have included the characterization of electro-osmotic flows [40], slip flows [41, 42], hindered diffusion [37, 43, 44] and quantum dot tracer particles [9, 10].

Recently, attention has been devoted to quantifying the velocity estimation error in total internal reflection velocimetry (TIRV) due to shear and diffusion [45, 46, 13]. This error depends on the time between successive images (inter-frame time), the exposure time and imaging depth. Here, we point out two other sources of error concerning the spatial distribution and optical detection of tracer particles. Forces exerted on particles, such as electrostatic interactions, and van der Waals forces [77, 37] (and in some cases gravitational or shear-induced forces) lead to a non-uniform particle concentration, which can bias the measured distribution of particle intensities. Similarly, particle size non-uniformity and the decaying intensity field further modify the measured particle intensity distribution. These effects are difficult to avoid, and raise the question as to how the experimentally *observed*
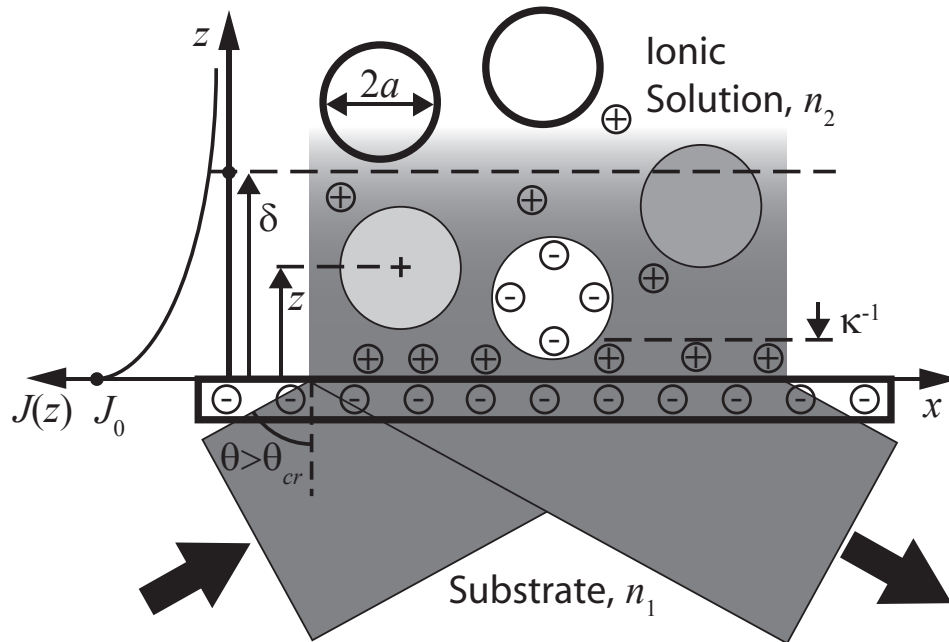
Figure 5.1: Typical geometry of total internal reflection fluorescence (TIRF) illumination, where a plane, monochromatic wave is incident on a dielectric interface at an angle greater than the critical angle, $\theta \geq \theta_{cr}$. The resulting evanescent field, $J(z)$ has a decay length, δ, on the order of 200 nm. Ionic solutions screen the electrostatic forces between charged particles and surfaces with a length scale characterized by the Debye length, κ^{-1}.

distribution of particle intensities is related to the *physical* distribution of particles. In the present letter, we characterize these distributions as functions of the size variation, electrostatic and van der Waals forces, and quantify the resulting mean velocity measurement bias for the case of a near-wall shear flow.

5.2   THEORETICAL CONSIDERATIONS

When an electromagnetic wave is incident upon a dielectric interface with indices n_1 and n_2, at an angle, θ, greater than the critical angle, $\theta_{cr} = \sin^{-1}(n_2/n_1)$, total internal reflection occurs (figure 5.1). An intensity field, $J(z)$, exists in the lower index medium, which

exponentially decays normal to the interface described by

$$J(z) = J_0 e^{-z/\delta}, \tag{5.1}$$

$$\delta = \frac{\lambda_0}{4\pi} \left[n_1^2 \sin^2 \theta - n_2^2 \right]^{-1/2}, \tag{5.2}$$

where z is the optical axis, J_0 is the intensity at the interface, δ is the penetration depth and λ_0 is the excitation wavelength [36]. We consider nanometer-sized tracer particles in the evanescent field with nominal radius, a_0, and a standard deviation specified as a fraction of the mean particle radius, $\sigma = S a_0$, where typically $0.03 \leq S \leq 0.20$. The particle radius distribution is thus given by

$$p(A) = \frac{1}{S\sqrt{2\pi}} \exp\left[-\frac{(A-1)^2}{2S^2} \right], \tag{5.3}$$

where $A = a/a_0$ is the dimensionless particle radius. The imaged intensities of particles are known to decay with the same characteristic length scale of the evanescent field, δ [51, 41], and we further assume that an individual particle's light emission intensity, I_p, is proportional to its volume [41]:

$$I(Z, A) = \frac{I_p(Z, A)}{I_p^0} = A^3 \exp\left[-\frac{Z-A}{\Delta} \right], \tag{5.4}$$

where $Z = z/a_0$ is the dimensionless distance from the wall to the particle center, I_p^0 is the light intensity emitted by a particle with radius a_0 touching the wall ($Z = 1$), I is the dimensionless particle emission intensity and $\Delta = \delta/a_0$ is the dimensionless evanescent decay length. We also note that quantum dots and single fluorescent molecules do not experience such intensity variations due to volumetric effects, since they are single fluo-

rophores. However, excitation efficiency and fluorescence intermittency create additional intensity variations, which must be taken into account.

The equilibrium concentration of colloidal particles in the wall-normal direction from a liquid-solid interface is given by the Boltzmann distribution

$$p\left(Z\right) = \frac{\exp\left[-U\left(Z\right)/k_B T\right]}{\int_{Z_1}^{Z_2} \exp\left[-U\left(Z\right)/k_B T\right] dZ} = p_0 \exp\left[-U\left(Z\right)/k_B T\right],$$ (5.5)

where p_0 is a normalization constant [37] from all particles in the range $Z_1 \leq Z \leq Z_2$ and U is the total potential energy of a particle. In the absence of any forces between particles and the surface, the potential is zero, leading to a uniform particle concentration distribution. For the present discussion of dilute, non-interacting, nanometer-sized particles, we consider two primary potential interactions: (i) electrostatic potential, U^{el}, and (ii) van der Waals potential, U^{vdw}, between particles and the surface resulting in the total potential energy, $U = U^{el} + U^{vdw}$.

The *electrostatic forces* between a charged particle and substrate in solution is moderated by ions, which screen the potential. The characteristic length scale of these forces is given by the Debye length,

$$\kappa^{-1} = \sqrt{\frac{\epsilon_f \epsilon_0 k_b T}{2ce^2}},$$ (5.6)

where ϵ_0 is the permittivity of free space, ϵ_f is the relative permittivity of the fluid, k_b is Boltzmann's constant, T is the absolute temperature, e is the elementary charge of an electron and c is the concentration of ions in solution [76]. The substrate exerts a repulsive force on particles of like charge quantified by the potential energy of the interaction:

$$\frac{U^{el}\left(Z\right)}{k_b T} = \hat{B}_{ps} e^{-K(Z-A)},$$ (5.7)

where $K^{-1} = \kappa^{-1}/a_0$ is the dimensionless Debye length. The magnitude of the electrostatic potential is given by

$$\hat{B}_{ps} = \frac{B_{ps}}{k_bT} = \frac{4\pi\epsilon_f\epsilon_0 a_0 A k_b T}{e^2} \left(\frac{\hat{\psi}_p + 4\gamma\Omega KA}{1 + \Omega KA}\right) \left[4\tanh\left(\frac{\hat{\psi}_s}{4}\right)\right], \tag{5.8}$$

where $\gamma = \tanh\left(\hat{\psi}_p/4\right)$, $\Omega = \left(\hat{\psi}_p - 4\gamma\right)/2\gamma^3$, $\hat{\psi}_p = \psi_p e/k_b T$ and $\hat{\psi}_s = \psi_s e/k_b T$ [77]. ψ_p and ψ_s represent the electric potentials of the particle and surface, respectively.

When considering interactions over length scales on the order of the evanescent field penetration depth ($\sim$200 nm), we must include contributions from attractive, short-ranged *van der Waals forces*. The potential energy associated with the van der Waals forces for a plane-sphere geometry is given by

$$\frac{U^{vdw}(Z)}{k_bT} = -\frac{\hat{A}_{ps}}{6}\left[\frac{A}{Z-A} + \frac{A}{Z+A} + \ln\left(\frac{Z-A}{Z+A}\right)\right], \tag{5.9}$$

where $\hat{A}_{ps} = A_{ps}/k_bT$ and A_{ps} is the Hamaker constant for the system [81].

In specific situations, other forces may also be relevant. Particle-particle interactions become important for high particle concentrations, but are generally negligible when particles are used as fluid tracers with small volume fractions ($< 0.1\%$). The gravitational potential energy for nearly density-matched, nanometer-sized particles is usually small when compared to the thermal energy ($U^g/k_bT \sim 10^{-5}$) and may also be neglected. Shear-induced migration effects require large particle Reynolds numbers, $Re_p > 1$ [150], which are not typical of TIRV measurements using nanometer-sized particles. Finally optical forces from the illuminating light can trap or push colloidal particles. In many experiments, this force is exploited to manipulate small objects (e.g. optical tweezers). However, when the particles are used as fluid tracers, illumination power is typically minimized in order to prevent

optical trapping effects, which are also not considered in the current discussion.

Considering the non-uniform distribution of particle radii given by equation (5.3), the Boltzmann distribution in equation (B.14) for the particle position should be a conditional probability of the particle height given the particle radius:

$$p\left(Z\right) \Rightarrow p\left(Z|A\right) = p_0 \exp\left[-U\left(Z, A\right)/k_B T\right]. \tag{5.10}$$

This result can be used, along with the appropriate definitions of the force potentials Equations (5.7) and (5.9), to determine the distribution of tracer particles in the direction normal to the interface. The joint probability, $p\left(Z, A\right)$, for a particle's size and location is given by the definition of conditional probability

$$p\left(Z|A\right) = \frac{p\left(Z, A\right)}{p\left(A\right)} \Rightarrow p\left(Z, A\right) = p\left(Z|A\right) p\left(A\right). \tag{5.11}$$

This distribution, illustrated in figure 5.2, is bounded below through the constraint that particles cannot penetrate the wall $(Z \geq A)$. An "observability" condition requiring that a particle must have an intensity greater than some threshold intensity, $I^* = I_p^*/I_p^0$, to be considered detectable and reliably distinct from noise $(I \geq I^*)$ provides the upper boundary. The particles must be large enough and not too far from the surface such that their emission intensity is above this threshold [41]. Combining this criterion with equation (5.4) defines this boundary of the joint probability density function (equation (5.10)):

$$Z = f\left(A\right) = A - \Delta \ln\left[\frac{I^*}{A^3}\right], \tag{5.12}$$

which is also shown in figure 5.2. The probability of finding a particle of any size at a given
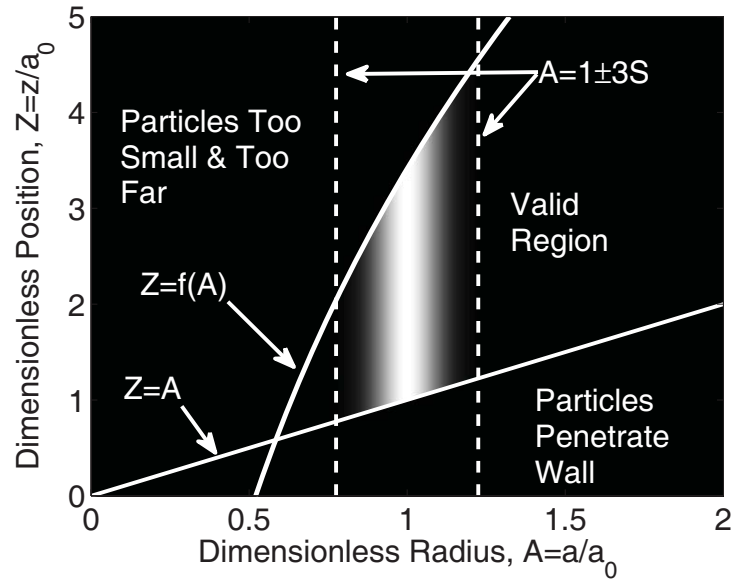
Figure 5.2: Joint probability density function of dimensionless particle size, $A = a/a_0$, and dimensionless distance from the surface, $Z = z/a_0$. Since particles contact the wall at $Z = A$, all particles are physically contained in the region $Z \geq A$. Only particles meeting the intensity criterion, $I \geq I^*$, are bright enough to be detected, which corresponds to particles in the region $Z \leq f(A)$. As a guide, the dashed lines for $A = 1 \pm 3S$ contain approximately 99% of the particles due to size variation.

distance from the wall, $p(Z)$, is obtained by integrating equation (5.11) over all optically

and physically accessible values of A (figure 5.2):

$$p(Z) = \frac{\int_{A=f^{-1}(Z)}^{Z} p(Z, A)\, dA}{\int_{Z=0}^{\infty} \int_{A=f^{-1}(Z)}^{Z} p(Z, A)\, dA dZ}, \tag{5.13}$$

where $A = f^{-1}(Z)$ is the inverse of equation (5.12).

In practice however, the particle concentration distribution is not directly measured. Instead, the concentration is inferred from the measured particle emission intensity distribution, $p(I)$, [37, 43, 41] formulated in a similar manner to the analysis above. The joint

probability distribution for the intensity and particle radius is

$$p\left(I, A\right) = p\left(Z\left(I, A\right), A\right) = p\left(Z\left(I, A\right) | A\right) p\left(A\right), \tag{5.14}$$

where $Z\left(I, A\right)$ is given by equation (5.4). The intensity distribution is computed by integrating over all particle radii for detectable particles, where the upper bound is $A \to \infty$, and the lower bound results from a particle of radius, A, contacting the wall at $Z = A$, or in terms of intensity:

$$I = A^3 = g\left(A\right), \tag{5.15}$$

or

$$A = g^{-1}\left(I\right) = I^{1/3}. \tag{5.16}$$

Integrating over all observable particles, which meet or exceed the threshold criterion, $I \geq I^*$, gives the normalized expected intensity distribution

$$p\left(I\right) = \frac{\int_{A=g^{-1}(I)}^{\infty} p\left(I, A\right) dA}{\int_{I=I^*}^{\infty} \int_{A=g^{-1}(I)}^{\infty} p\left(I, A\right) dAdI}. \tag{5.17}$$

5.3   RESULTS

5.3.1   Particle Position and Intensity Distributions

The particle concentration profile, $p\left(Z\right)$, and the particle emission intensity distribution, $p\left(I\right)$, were evaluated from equation (5.13) and equation (5.17), respectively, for the case of a typical imaging experiment using polystyrene particles ($a_0 = 100$ nm) over a glass substrate with a 150 nm penetration depth ($\Delta = 1.5$) and an intensity threshold of $I^* = 0.2$. The numerical integration was performed in MATLAB using a simple trapezoidal method.
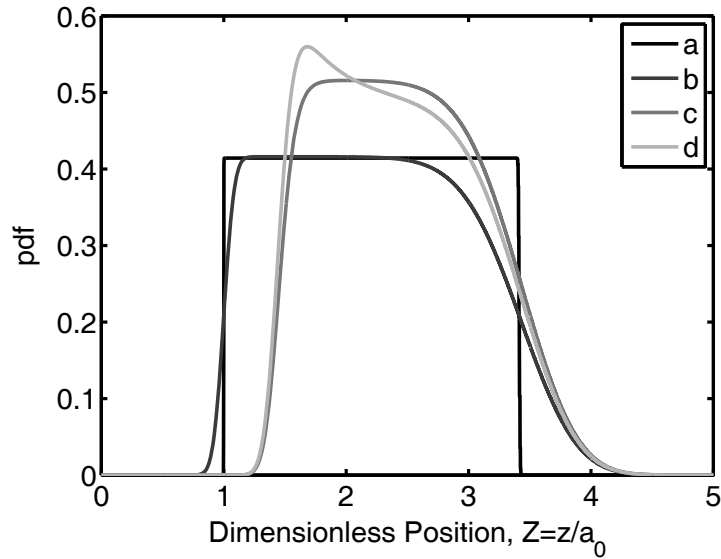
Figure 5.3: Probability density function (pdf) of dimensionless particle position, Z, for all detectable particles with dimensionless intensities $I \geq I^* = 0.2$ and a dimensionless penetration depth of $\Delta = 1.5$. (a) With no particle size variation, $S = 0$, and no potential interactions, the detectable particles are uniformly distributed. (b) Increased particle variation, $S = 0.068$, allows smaller particles to occupy the region $Z < 1$ and larger particles to be visible in the region $Z > 3.5$. (c) Electrostatic repulsion forces in an ionic solution, $K^{-1} = 0.06$, create a depletion layer near the wall. (d) Attractive van der Waals forces pull particles closer to the wall, creating a local maximum outside of the depletion layer.

For uniform tracer particles ($S = 0$) with no potential and no van der Waals interaction, the concentration profile is uniform and square as shown in figure 5.3a. As the particle radius variation increases ($S = 0.068$), smaller particles are visible near the wall ($0 \leq Z \leq 1$) and larger particles are visible at greater distances from the interface leading to the diffuse edges in the concentration distribution (figure 5.3b). As the Debye screening length increases ($K^{-1} = 0.06$), particles are pushed away from the wall forming a depletion layer (figure 5.3c). Finally, the inclusion of the attractive van der Waals interaction pulls the distribution back toward the wall, and results in a local maximum in the concentration immediately outside of the depletion layer (figure 5.3d).
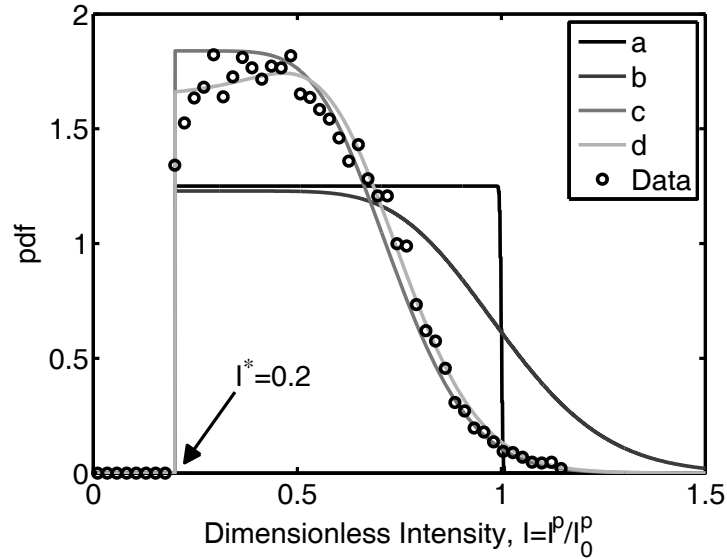
Figure 5.4: Probability density function (pdf) of dimensionless particle emission intensity, I, for particles with intensities $I \geq I^* = 0.2$ and dimensionless penetration depth $\Delta = 1.5$. (a) With no particle size variation, $S = 0$, and no potential interactions the uniformly distributed particles yield a uniform intensity distribution. (b) Particle size variations, $S = 0.068$, allow larger, brighter particles to be seen in the region $I > 1$. (c) Electrostatic forces, $K^{-1} = 0.06$, push the particles into regions of lower excitation intensity, which lowers the overall intensity distribution. (d) Attractive van der Waals forces pull particles into regions of higher intensity, creating a local maximum in the intensity distribution. An experimentally measured intensity distribution ($\circ$) for 200 nm diameter particles in an aqueous solution ($K^{-1} \approx 0.06$) yielded a particle size variation of $S = 0.068$ and a threshold intensity of $I^* = 0.19$.

The measured intensity distributions corresponding to these four concentration distributions is shown in figure 5.4a-d. For a uniform particle radius distribution with no forces, the particle emission intensity distribution is square (figure 5.4a). As the size variation increases, larger particles with $A > 1$ contribute to particle intensities with $I > 1$, but a sharp step increase persists for lower intensities due to the discrete threshold, $I^* = 0.2$, (figure 5.4b). In general, particles close to the wall and/or large particles contribute to high intensity values, while smaller particles and/or particles farther away populate the probability density function at lower values of I. Including the electrostatic force lowers

the average intensity of the ensemble due to the reduced number of particles close to the interface (figure 5.4c). As expected, including the van der Waals potential moderates the effect of the electrostatic repulsion, creating a local maximum in the intensity distribution (figure 5.4d).

Data from an experimentally-measured intensity distribution is also presented in figure 5.4. Polystyrene particles with a mean radius of $a_0 = 100$ nm and a variation of $S = 0.05$ (Duke Scientific, R200) were suspended in a 2.5 mM aqueous salt solution ($K^{-1} \approx 0.06$). The measured penetration depth was $\Delta = 1.47$. The data was fit to the theoretical model in equation (5.17), allowing the particle radius variation, S, and the threshold intensity I^* to vary as fitting parameters. Values of $S = 0.068$ and $I^* = 0.19$ were found to minimize the fitting error, and the corresponding concentration distribution is shown in figure 5.3d. The slight discrepancy between the measured and quoted particle radius variation is assumed to result from variations in the uniformity of the intensified CCD camera and the particle detection algorithm.

5.3.2   Errors in near-wall velocimetry

Particle tracking in the evanescent field is often used to infer near-wall fluid velocity, which is obtained by ensemble-averaging particle displacements through the evanescent field. The fluid velocity changes very rapidly in the wall-normal direction to the interface. As a result, the mean inferred fluid velocity is sensitive to the particle concentration distribution. To assess the errors associated with this deviation, we compare the average measured velocity of a distribution of non-uniform particles, $\langle V \rangle$, to the known mean fluid velocity, $\langle V_0 \rangle$, inside a finite imaging depth, H, where the angled brackets denote the ensemble average. For simplicity, we consider a shear flow with constant shear rate $\dot{\Gamma}$ and no-slip at the wall,

$V(Z) = \dot{\Gamma}Z$. The apparent relative velocity is

$$\frac{\langle V \rangle}{\langle V_0 \rangle} = \frac{\int_0^\infty V(Z) p(Z) \, dZ}{\int_0^\infty V(Z) p(Z)|_{S,U=0} dZ} = \frac{\dot{\Gamma} \int_0^\infty Z p(Z) \, dZ}{\dot{\Gamma} \int_1^H Z p(Z)|_{S,U=0} dZ} = 2 \frac{\int_0^\infty Z p(Z) \, dZ}{H+1}, \qquad (5.18)$$

which is simply a ratio of the first moments of the concentration distributions. The known velocity, $\langle V_0 \rangle$, results from the average value of a uniform distribution

$$\langle V \rangle = \int_0^\infty V(Z) p(Z) \, dZ = \int_{Z_1}^{Z_2} \dot{\Gamma} Z \frac{1}{Z_2 - Z_1} dZ = \frac{\dot{\Gamma}}{2} (Z_2 + Z_1), \qquad (5.19)$$

with the bounds $Z_1 = 1$ and $Z_2 = H$ where H is the distance of the farthest visible particles from the interface with $S = 0$ and no electrostatic or van der Waals potential interaction. For the case of no potential interaction, the apparent velocity increases with particle size variation, S (figure 5.5). This is due to a the contribution of larger particles now visible from beyond the original imaging depth (and hence moving faster), which overestimates the mean velocity. As we have already seen (figure 5.3) increasing the electrostatic interaction creates a depletion layer by pushing particles away from the wall and further biases the velocity distribution toward even higher values. Allowing for attractive van der Waals interactions has a moderate compensating effect by pulling particles closer to the wall and lowering the apparent velocity.

5.4   CONCLUDING REMARKS

TIRF has proven a powerful technique in measuring colloidal particle motions near liquid-solid interfaces. However, poly-dispersed particle radii and forces on particles create non-uniform near-wall particle concentration distributions and uncertainty in measuring fluid
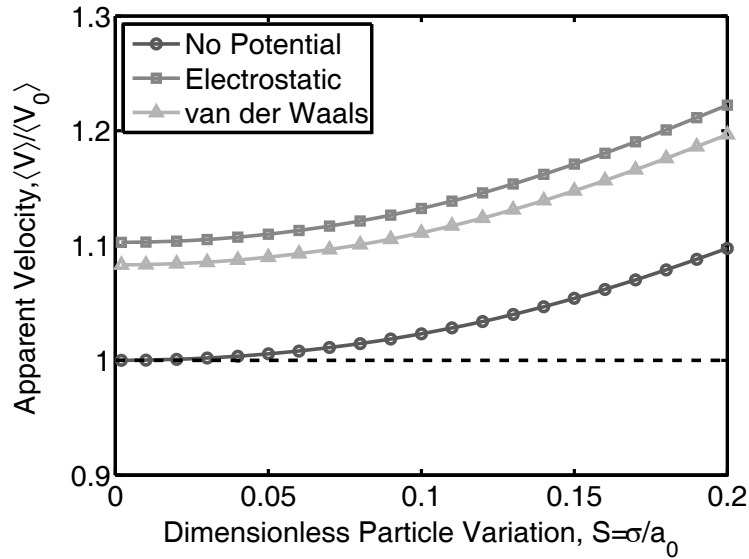
Figure 5.5: Apparent, relative ensemble-averaged particle velocities for all detectable particles with intensities $I \geq I^* = 0.2$ and a dimensionless penetration depth $\Delta = 1.5$. With no electrostatic or van der Waals potential interaction, the apparent velocity increases with particle size variation, S, due to large particles that become visible beyond the original imaging depth. Including electrostatic interactions ($K^{-1} = 0.06$) creates a depletion layer by pushing particles farther from the wall, biasing the average to regions of higher velocity. Attractive van der Waals interactions mediate this effect pulling particles closer to the wall into regions of lower average velocity.

velocities. Through a simple analysis, we have quantified a significant source of measurement bias associated with these effects. A Boltzmann distribution describes the equilibrium distribution of nanometer-sized, colloidal particles in the wall-normal direction of a microchannel. Electrostatic forces produce a significant tracer particle depletion layer near the liquid-solid interface, moderated slightly by the effect of van der Waals forces. The exponential decay of the evanescent wave illumination technique combined with inherent tracer particle radius variations produces a gradual decay of detectable particles away from the wall, which is unlike the sharp-sided, uniform distribution often assumed. The expected intensity distributions associated with ensembles of detectable particles were also character-

ized and showed good agreement with experiment. In the context of velocity measurements in a near-wall shear flow, the ensemble-averaged particle velocities over the imaging depth showed a relative error on the order of 10% overestimation compared to the mean fluid velocity due to mis-weighting of the local fluid velocity profile. Although this phenomena is well described through the combination of several theories, the associated error is generally overlooked.

ACKNOWLEDGMENT

The authors would like to thank Professor Peter Huang for his detailed discussions and insight on TIRF.

Chapter 6

Hindered Brownian motion and depletion layer of particles in shear flow and their implications for near-wall velocimetry

The behavior of spherical particles in a near-wall shear flow is explored using Langevin simulations, focusing on the effects of their anisotropic hindered Brownian motions and a near-wall depletion layer due to electrostatic and van der Waals forces. The results are discussed in the context of particle velocity distributions that would be obtained in near-wall velocimetry experiments. It is observed that the shear force dominates over Brownian motion for Peclet numbers larger than three, and the asymmetric shape of apparent velocity

distributions are attributed to the presence of the wall breaking the geometric symmetry. Strength of shear inside the depth of observation, hindered mobility of the particles and their tendency to undergo a biased Brownian motion away from the wall also contribute to the skewness. The accuracy of near-wall velocimetry measurements is also examined. It is concluded that hindered Brownian motion normal to the wall is a major cause of measurement bias for a long time interval between two successive image acquisitions, while the shear-induced hindered mobility of particles causes a more significant measurement bias if the time interval between image acquisitions is short. Further complicating the measurement accuracy is the existence of a near-wall particle depletion layer, whose presence can also lead to an over-estimation of the actual fluid velocity. Nevertheless, the simulation results suggest a method to overcome the bias and infer the correct fluid velocity from the apparent particle velocity distributions.

6.1   INTRODUCTION

Colloidal particle-based image velocimetry is a widely accepted experimental technique for measuring fluid velocity profiles and other physical quantities. Its accuracy heavily relies on the assumption that tracer particles will accurately conform to local fluid velocities. In the past decade, particle image velocimetry (PIV) has been extended to the micro-[5] and nano-scale [6, 39, 41, 10] where size of tracer particles has also decreased from microns to nanometers. At these physical length scales, Brownian motion of tracer particles can be quite significant, thus violating the assumption of particles traveling at velocities equal to that of the surrounding fluids. Consequently, conducting an accurate velocimetry experiment requires a good understanding and a careful treatment of Brownian motion via either a thorough error [5] or probabilistic analysis [48], an ensemble correlation averaging

technique [151], a statistical analysis of the particle ensemble's displacement [39, 41] or a method of statistical tracking [10].

In the vicinity of a solid wall, a colloidal particle will undergo an anisotropic "hindered" motion due to the increase of its hydrodynamic drag near the surface. This reduced mobility has been reported both theoretically [63, 64, 65, 66] and experimentally [69, 70, 71, 72, 75]. In most cases, such a spatially dependent hindered mobility leads to difficulties in determining measurement uncertainties, although a few researchers have managed to turn the disadvantages into merits by proposing usage of the hindered Brownian motion to reconstruct near-wall shear flow velocity profile [152] and to probe the no-slip boundary condition [153].

There are two equally appropriate approaches to study the ensemble behavior of hindered near-wall particle motions [154]. One is the Fokker-Planck approach, which solves the momentum-space partial differential equations to obtain a time evolution of spatial configuration function of the particle ensemble. Recently, Sadr *et al.* has taken this approach to study the effect of single-dimensional near-wall hindered diffusion on measurement bias in velocimetry [45]. The other approach is a Langevin simulation, which is to simulate the motion of each particle in a large ensemble through a stochastic differential equation. In this approach, both deterministic (such as fluid flow and sedimentation) and stochastic (such as Brownian motion) processes contribute to particle displacements. The overall simulation then yields a spatial distribution of the particle ensemble after each time step. Details provided by this method are not only intuitive in understanding ensemble behavior, but also bear a close resemblance to physical velocimetry experiments. The usefulness of Langevin simulations has been demonstrated in studying the impact of hindered Brownian diffusion on the accuracy of nano-PIV [141], on the colloidal particle deposition in a microchannel

flow [155], and on the accuracy of potential energy profiles determined via total internal reflection microscopy [156].

Using the Fokker-Planck approach, Sadr *et al.* focused on how hindered Brownian motions normal to the wall could cause bias on accuracy of near-wall velocimetry measurements [45]. They proposed that particle diffusion into and out of the depth of observation is the main cause of measurement inaccuracy and there exists a relationship between particle diffusion, time between image acquisitions and the accuracy of velocity measurements. Furthermore, they offered a scaling similarity, which allows the velocimetry inaccuracies to be corrected during result analysis. While Pouya *et al.* [13] had presented experimental results that are in qualitative agreement with the simulation findings of Sadr *et al.*, these researchers did not consider the effect of fluid shear in their analyses and therefore had overlooked the significant contribution of particle hindered mobility in streamwise direction to velocimetry inaccuracy. Under certain shear flow conditions, it is expected that shear effect would dominate over the effect of hindered diffusion and becomes the primary source of velocimetry measurement bias.

Further complicating the matter is the potential existence of a near-wall depletion layer of particles due to electrostatic and van der Waals interactions between particles and the wall [37, 48]. While it is certainly convenient in velocimetry data analysis to assume that tracer particles are uniformly distributed in the absence of a depletion layer, one can easily imagine that the ensemble-averaged velocities of near-wall particles can be greatly skewed if a significant portion of the observation depth encompasses the depletion layer. Thus from the perspective of velocimetry accuracy, it is critical to understand how the presence of a particle depletion layer leads to measurement bias.

In contrast to Sadr *et al.*, we had chosen to investigate velocimetry measurement inac-

curacy through a Langevin simulation study, which enabled us to consider all sources of bias simultaneously. Experimental studies were then conducted to support our conclusions. Furthermore, we examined how the combined effects of hindered diffusion and fluid shear contribute to the skewed near-wall apparent velocity distributions first reported by Jin *et al.* in their total internal reflection velocimetry (TIRV) experiment [39]. In this paper, the theories of near-wall particle dynamics are presented first and followed by a detailed description of the simulation algorithm and experimental procedures. We then discuss the results and their implications, and conclude with a summary and our thoughts on minimizing inaccuracies of near-wall velocimetry measurements.

6.2 THEORIES AND COMPUTATIONS

6.2.1 The Langevin Equation

In a Langevin simulation, particle displacements are computed based on a stochastic equation [154]. For a particle in a shear flow as shown in figure 6.1, its displacement between simulation time step i and step $i + 1$ with a step size δt is,

$$x_{i+1} - x_i = v\delta t + \frac{dD_x}{dx}\delta t + \frac{D_x}{k_B\Theta}F_x\delta t + N\left(0, \sqrt{2D_x\delta t}\right), \tag{6.1a}$$

$$z_{i+1} - z_i = \frac{dD_z}{dz}\delta t + \frac{D_z}{k_B\Theta}F_z\delta t + N\left(0, \sqrt{2D_z\delta t}\right), \tag{6.1b}$$

where (x, z) is the particle's center position, k_B is the Boltzmann constant and Θ is the fluid temperature. D_x and D_z are the diffusion coefficients in the directions parallel and normal to the solid surface, respectively. In the fluid bulk, both D_x and D_z would be equal to the Stokes-Einstein diffusivity, D_0. As it has been mentioned earlier, near-wall diffusion is
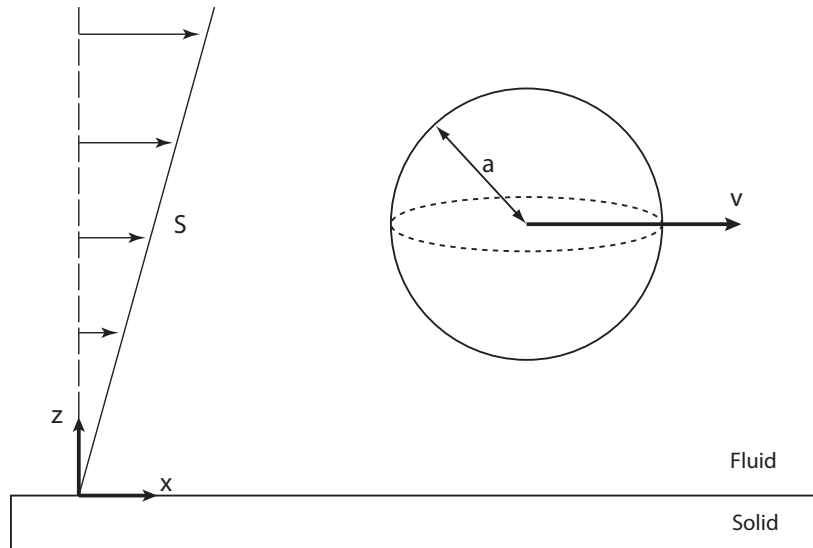
Figure 6.1: A schematic of the simulation geometry. A colloidal particle of radius a is freely suspended in a fluid but near a solid wall. The fluid is undergoing a linear shear flow of shear rate S, and thus the particle translates with a velocity V due to both fluid flow and its Brownian motion. A no-slip boundary condition is assumed at the fluid/solid wall interface. Even though existence of slip has been reported [41], its presence would not alter the simulation results and is thus neglected.

anisotropic and hindered, and thus $D_x < D_0$ and $D_z < D_0$. It should be noted that because D_x is only a function of z [65], $dD_x/dx = 0$ in equation (6.1a). The z-dependency of D_x and D_z is discussed in subsequent sections. F_x and F_z represent external forces acting on the particle in the x- and z-directions, respectively, and $N\left(0, \sqrt{2D\delta t}\right)$ denotes the stochastic displacement of Brownian motion randomly sampled from a normal distribution with a zero mean and a standard deviation $\sqrt{2D\delta t}$. In the current simulation scheme there exists no force in the x-direction and $F_x = 0$. In the z-direction, however, density mismatch between tracer particles and the fluid can lead to either sedimentation or flotation of the particles. For particles with density greater than the suspending fluid, such as polystyrene particles

(relative density 1.05) in water, the gravitation sinking force acting on the particles, F_g, is

$$F_g = \frac{4\pi}{3} a^3 \Delta \rho g, \tag{6.2}$$

where $\Delta \rho$ is the density difference between the tracer particles and the suspending fluid, and g is the gravitational acceleration. Other external forces acting on the particles may also include electrostatic repulsion and van der Waals force between particles and the solid boundary surface, and can be calculated from the DLVO theory [77].

The equations of motion (6.1a) and (6.1b) are non-dimensionalized by choosing the particle radius, a, as the length scale and the time required for an isolated particle to diffuse a distance of one radius, a^2/D_0, as the time scale. Therefore equations (6.1a) and (6.1b) become

$$X_{i+1} = X_i + F(Z_i) \cdot Pe \cdot Z_i \cdot \delta T + N\left(0, \sqrt{2\beta_x(Z_i)\,\delta T}\right) \tag{6.3a}$$

and

$$Z_{i+1} = Z_i + \left.\frac{d\beta_z}{dZ}\right|_{Z_i} \delta T + (G+H) \cdot \beta_z(Z_i)\,\delta T + N\left(0, \sqrt{2\beta_z(Z_i)\,\delta T}\right) \tag{6.3b}$$

where $X \equiv x/a$, $Z \equiv z/a$, and $T \equiv D_0 t/a^2$ are the non-dimensional x, z and t, respectively. The advection and diffusion terms are given by

$$F(Z) \equiv \frac{v}{zS}, \quad \beta_x(Z) \equiv \frac{D_x(z)}{D_0}, \quad \beta_z(Z) \equiv \frac{D_z(z)}{D_0},$$

where we have also introduced the fluid shear rate, S. Finally, the flow conditions are governed by a Peclet number, Pe and a sedimentation coefficient, G, and a particle-wall

a (μm)	G	S (s^{-1})			
		10^0	10^1	10^2	10^3
0.1	-5.042×10^{-5}	0.0046	0.0463	0.4630	4.630
1.0	-0.5042	4.630	46.30	463.0	4630

Table 6.1: Sample values of the Peclet number, Pe, and sedimentation coefficient, G, for polystyrene particles in aqueous solution ($\Delta\rho = 50$ kg/m^3).

interaction coefficient, H, for electrostatic and van der Waals forces, F_{pw}:

$$Pe \equiv \frac{Sa^2}{D_0}, \quad G \equiv \frac{4\pi a^4 g \Delta\rho}{3k_B\Theta}, \quad H \equiv \frac{F_{pw}a}{k_B\Theta}.$$

The Peclet number represents the strength of shear compared with that of diffusion, while the sedimentation coefficient characterizes the gravitational pull on the particles. Representative values of Pe and G are shown in table 6.1. Because most near-wall velocimetry measurements utilize sub-micron tracer particles, all results presented in this paper fall under the regime of $G \ll 1$ where the gravitational pull is much less significant than thermal energy-driven Brownian motion. The magnitude of H, on the other hand, can lead a depletion layer of particles and thus is taken into consideration and discussed in a later section.

Finally, for image-based velocimetry measurements, another important control parameter is the time between consecutive image acquisitions, Δt, from which the fluid velocity is estimated. Some sample values of non-dimensional time between consecutive image acquisition, $\Delta T = \Delta t D_0/a^2$, for 1-$\mu$m and 100-nm particles are shown in table 6.2.

a (μm)	Δt (ms)			
	0.1	1	10	100
0.1	0.022	0.22	2.2	22
1.0	0.000022	0.00022	0.0022	0.022

Table 6.2: Representative values of the non-dimensional time between consecutive image acquisition, ΔT.

6.2.2 Effects of Shear on Particle Velocities

It is well known that shear and near-surface hydrodynamic effects can cause a tracer particle to rotate and translate at a velocity lower than the local fluid velocity in the same shear plane [63, 66]. Goldman *et al.* [66] proposed that the translational velocity, v, of a particle with radius a in a linear shear flow of a local shear rate S is given by

$$\frac{v}{zS} \equiv F(Z) \simeq 1 - \frac{5}{16}(Z)^{-3},$$ (6.4)

which is valid for large Z, and

$$\frac{v}{zS} \equiv F(Z) \simeq \frac{0.7431}{0.6376 - 0.2\ln(Z-1)}$$ (6.5)

for small Z. Although there exists no analytical approximation for intermediate values of Z, Pierres *et al.* [142] proposed a cubic approximation to numerical values presented by Goldman *et al.* in [66]:

$$\frac{v}{zS} \equiv F(Z) \simeq \left(\frac{1}{Z}\right) \exp\{0.68902 + 0.54756\left[\ln(Z-1)\right]$$

$$+0.072332\left[\ln(Z-1)\right]^2 + 0.0037644\left[\ln(Z-1)\right]^3\}.$$ (6.6)

Because a particle's translational velocity depends on the shear rate and the distance to the wall, it needs to be updated in equation (6.1a) at every time step of the simulation.

It has also been suggested that shear-induced lift can be a source of particle migration away from the wall [73]. However, based on the theory presented by Cherukat & McLaughlin [74], the shear-induced lift is insignificant for micro- and nano-particles in a low shear flow regime, and thus will be neglected [75].

6.2.3   Hindered Brownian Motion

Near-wall tracer particles are known to exhibit anisotropic, hindered Brownian motion due to hydrodynamic effects, and their hindered diffusion coefficient in the direction parallel to the solid surface, D_x, is [65]

$$\frac{D_x}{D_0} \equiv \beta_x\left(Z\right) = 1 - \frac{9}{16}\left(Z\right)^{-1} + \frac{1}{8}\left(Z\right)^{-3} - \frac{45}{256}\left(Z\right)^{-4} - \frac{1}{16}\left(Z\right)^{-5} + O\left(Z\right)^{-6}, \qquad (6.7)$$

where D_0 is the Stokes-Einstein diffusivity of an isolated spherical particle in the fluid bulk. This "Method of Reflection" approximation is more accurate for $Z > 2$. For $Z < 2$, Goldman $et\ al.$ [66] proposed an asymptotic solution,

$$\frac{D_x}{D_0} \equiv \beta_x\left(Z\right) = -\frac{2\left[\ln\left(Z - 1\right) - 0.9543\right]}{\left[\ln\left(Z - 1\right)\right]^2 - 4.325\ln\left(Z - 1\right) + 1.591}. \qquad (6.8)$$

In the direction normal to the wall, the modified diffusion constant, D_z, is such that [64]

$$\frac{D_z}{D_0} \equiv \beta_z\left(Z\right) = \left\{\frac{4}{3}\sinh\alpha\sum_{n=1}^{\infty}\frac{n\left(n + 1\right)}{\left(2n - 1\right)\left(2n + 3\right)}\right.$$
$$\left.\left[\frac{2\sinh\left(2n + 1\right)\alpha + \left(2n + 1\right)\sinh 2\alpha}{4\sinh^2\left(n + \frac{1}{2}\right)\alpha - \left(2n + 1\right)^2\sinh^2\alpha} - 1\right]\right\}^{-1}, \qquad (6.9)$$

where $\alpha = \cosh^{-1}(Z)$. Bevan & Prieve [69] reported that the equation

$$\beta_z(Z) = \frac{6(Z-1)^2 + 2(Z-1)}{6(Z-1)^2 + 9(Z-1) + 2} \tag{6.10}$$

well approximates equation (6.9) and is much less computationally intensive than the infinite series. Like the particle translational velocity, the dependence of these hindered diffusion coefficients on Z requires them to be updated at every time step of the simulation.

6.2.4 Electrostatic and van der Waals Forces

The electrostatic repulsion, F_{el}, and the van der Waals force, F_{vdw}, acting on a suspended particle due to the presence of the wall can be characterized by the DLVO theory [77]. In dimensional terms,

$$F_{el} = 4\pi\epsilon\epsilon_0 a \left(\frac{k_B\Theta}{e}\right)^2 \left(\frac{\hat{\zeta}_p + 4\gamma\Omega\kappa a}{1 + \Omega\kappa a}\right) \left[4\tanh\left(\frac{\hat{\zeta}_w}{4}\right)\right] \kappa e^{-\kappa(z-a)} \equiv B_{pw}\kappa e^{-\kappa(z-a)}, \tag{6.11}$$

where $\hat{\zeta}_p = e\zeta_p/k_B\Theta$, $\hat{\zeta}_w = e\zeta_w/k_B\Theta$, $\gamma = \tanh\left(\hat{\zeta}_p/4\right)$ and $\Omega = \left(\hat{\zeta}_p - 4\gamma\right)/2\gamma^3$. Specifically, ϵ is the dielectric constant of the suspending medium, ϵ_0 is the vacuum electrostatic permeability, e is the elementary charge, κ is the inverse of the wall Debye length, and ζ_p and ζ_w are the ζ-potentials of the particle and the wall, respectively. The van der Waals force, on the other hand, takes the form of

$$F_{vdw} = \frac{A_{pw}}{6}\left[-\frac{a}{(z-a)^2} - \frac{a}{(z+a)^2} + \frac{1}{z-a} - \frac{1}{z+a}\right], \tag{6.12}$$

where A_{pw} is the Hammaker's constant for a spherical particle near a flat wall. With $F_{pw} = F_{el} + F_{vdw}$, one can characterize the particle-wall interaction using the constant H,

$$H = \frac{B_{pw}}{k_B\Theta}Ke^{-K(Z-1)} + \frac{A_{pw}}{6k_b\Theta}\left[-\frac{1}{(Z-1)^2} - \frac{1}{(Z+1)^2} + \frac{1}{Z-1} - \frac{1}{Z+1}\right], \qquad (6.13)$$

where $K = \kappa a$. Again since H depends on the value of Z, the quantity H needs to be updated at each time step of the simulation.

6.2.5 Implementation of Simulation

Since the experiments are conducted using dilute suspensions, the Langevin simulations were conducted under an assumption of no particle-particle hydrodynamic interactions. At the beginning of each simulation, a particle was situated at $X = 0$ and placed within a pre-determined range of $1 < Z < 10$. The physical distribution of the particles, however, depends on the magnitude of particle-wall electrostatic and van der Waals interactions. In the absence of such interactions, the particle is randomly placed within the pre-determined range. However, in the event that particle-wall interactions were important, the initial position of the particle was randomly sampled from a Boltzmann distribution based on the DLVO potential.

The simulation then progressed for a total of $\Delta T/\delta T$ steps as prescribed by equations (6.3a) and (6.3b), with F, H and β's updated and the position (X, Z) of the particle recorded after each time step. Because the solid wall was located at $Z = 0$, the smallest Z value a particle could have was $Z = 1$, where the particle would be in contact with the wall. A boundary condition was needed in the event that a particle attempted to enter the solid wall during a simulation step. Peters & Barenbrug [157, 158] had studied the efficiencies of different boundary conditions for Langevin simulations. Here we chose a simple and yet

effective specular reflection to prevent a particle from entering the wall. With the time step taken small enough, the use of the boundary condition was seldom triggered and less than 0.001% of the simulated displacements required applications of the boundary condition.

The single particle simulation was then repeated 10^5 times to obtain a large ensemble. It was also repeated for various values of Pe to study its effect. The random number generator, which controls initial particle positions, was seeded identically for all simulation trials to ensure that the results were a consequence of physical parameters only.

Finally, it is important to mention the selection of the size of the computational time step, δT, which has two physical constraints [154]. First, the time step must be much greater than the particle relaxation time, $mD_0/k_B\Theta$, where m is mass of one particle. In nondimensional terms it is equivalent to

$$\delta T \gg \frac{mD_0^2}{k_B\Theta a^2} \sim O\left(10^{-6}\right) \tag{6.14}$$

for $a > 100$ nm. Secondly, numerical accuracy requires that the time step must be short enough such that the diffusion coefficients and their gradients are essentially constant during the time step (that is, $\delta T \ll 1$). Therefore δT was chosen to be 10^{-4}, which satisfies both constraints and was numerically efficient.

6.3 EXPERIMENTAL PROCEDURES

6.3.1 Materials and Optical System

A schematic of the experimental setup is shown in figure 6.2. Flow experiments were carried out in 197 μm $\times$ 40 μm $\times$ 10 mm, rectangular poly-dimethyl siloxane (PDMS) (Sylgard 184 Silicone Elastomer, Dow Corning) micro-channels fabricated by a soft lithography technique
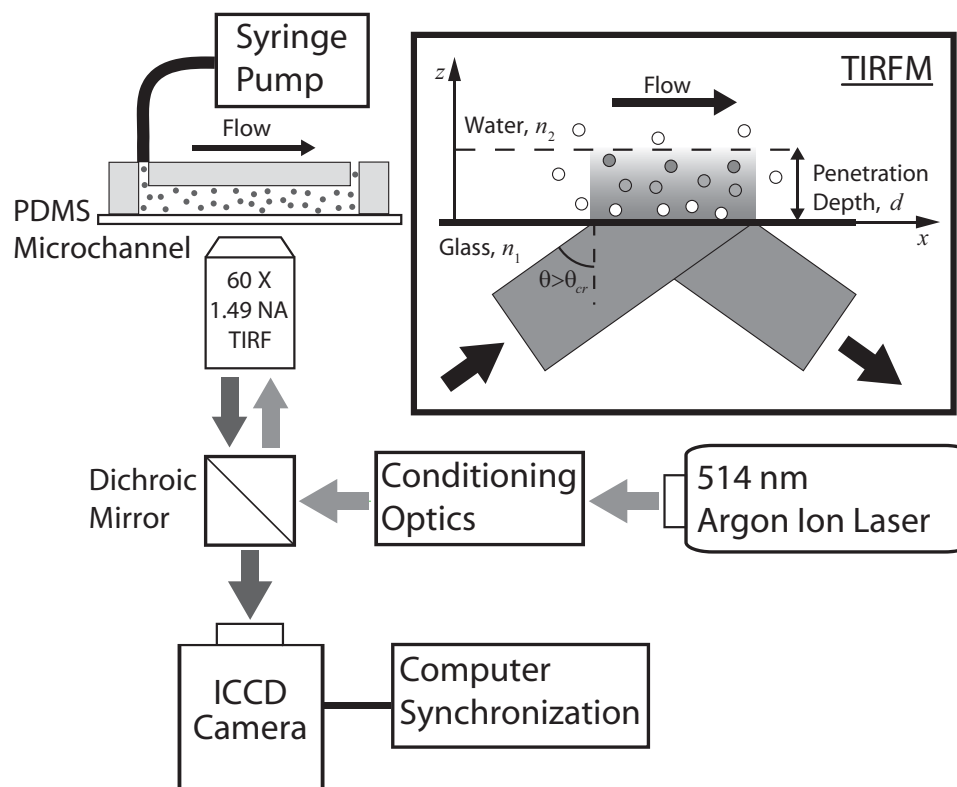
Figure 6.2: This schematic illustrates the optical system used for objective-based total internal reflection fluorescence microscopy (TIRFM). A total internal reflection is created at the glass-water interface of a PDMS microchannel with a penetration depth of about 150 nm. The flow is driven by a syringe pump, and fluorescence emission from tracer particles is imaged using an intensified CCD (ICCD) camera.

[117] and mounted on 170 μm thick borosilicate cover glass. The working fluid was pure water (Fluka) with 2.5 mM sodium chloride to reduce the Debye length to approximately 6.1 nm, and thus, reduce the near-wall depletion layer of particles. A low volume fraction (0.01%) of aqueous, polystyrene, fluorescent particles (Duke Scientific) were used as tracers. The particles had a mean radius, a_0, of 100 nm $\pm$ 5% and an emission wavelength, λ_{em}, of 612 nm. The flow was driven by a syringe pump (Harvard Apparatus) at a constant flow rate of 1.5 μL/min $\pm$ 0.0035% for all experiments.

Near-wall tracer particle images were captured using an objective-based total internal reflection fluorescence microscopy (TIRFM) imaging system [36]. The system was built around a Nikon Eclipse TE2000-U inverted fluorescence microscope with the 514 nm line of an Argon-ion CW laser (Coherent) as the excitation source with a penetration depth of 150 nm. Objective-based TIRFM requires a high numerical aperture objective to achieve an incident angle greater than the critical angle of the fluid-solid interface of the microchannel. For this purpose, we used a CFI Apochromat TIRF 60$\times$ oil immersion objective with a numerical aperture of 1.49. Fluorescence images of the particles were captured with an intensified CCD (ICCD) camera (QImaging). The camera is capable of 1360$\times$1036 pixels, 12-bit images with an effective pixel size of 161.3 nm at 60$\times$ and a minimum inter-frame time, Δt, of about 1 ms due to the decay of the phosphor screen.

6.3.2 Particle Tracking

Image pairs were taken at 5 Hz with an exposure time of 50 μs and inter-image acquisition times varying from about 3 ms to 43 ms. The polystyrene particle diameters are below their emission wavelength, so the diffraction-limited spot was imaged, which was several hundred nanometers in diameter. Particles were detected by intensity thresholding the maximum

pixel value of an image until a possible particle was found. Next, the sub-pixel x and y locations and peak intensity I were identified by least-squares fitting a two-dimensional, Gaussian profile to a 3x3 pixel array centered on the maximum intensity pixel [41]. The error in locating a sub-wavelength particle center through Gaussian fitting has been shown to be as small as 0.1 pixels for a SNR greater than five [54]. After identifying a particle, the particle and surrounding image region were blacked-out to avoid re-identification, then the threshold was lowered until a predefined minimum threshold was reached. This procedure was performed for both images of an image pair, then particles were matched through a nearest neighbor search with window shifting to capture large displacements for long inter-frame times. The low particle concentration helped to minimize misidentification. Once matched, particle displacements (and velocities) were computed for all particles in the 1100 image pairs per trial. Additionally, the the experimental depth of observation was determined by comparing distributions of measured particle intensities to the expected distributions, based on DLVO theory, penetration depth and particle size variation [48]. With a constant flow rate (constant velocity) and a fixed exposure time, t_e, (50 μs), 1100 image pairs were captured at each inter-frame time, Δt, (3.1, 4.2, 5.6, 7.5, 10.1, 13.5, 18.1, 24.3, 32.5 and 43.6 ms) resulting in 6000 to 12000 particle trackings per data set. The tracked particle displacements were decomposed onto a new basis, which lies along the mean measured flow direction to eliminate effects from misalignment of the microchannel to the camera's CCD array.
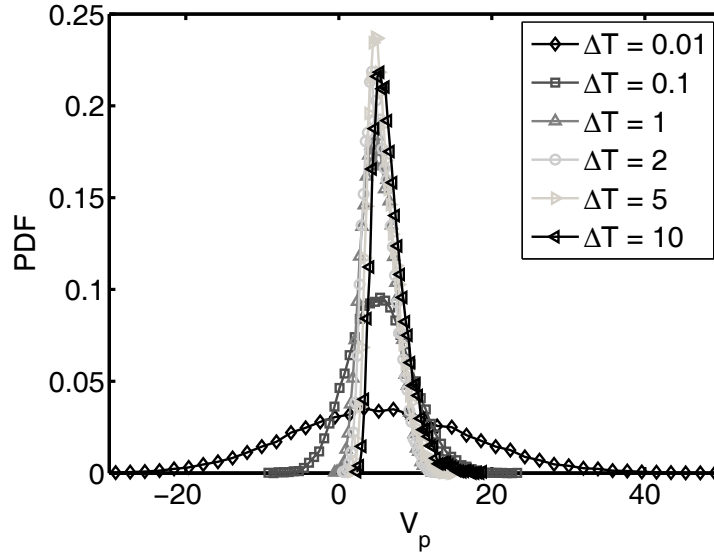
Figure 6.3: Time evolution of the simulated streamwise apparent velocity distribution. All apparent velocity probability density functions (PDF's) are obtained at $Pe = 3$ and with particles within the observation depth of $1 < Z < 3$ at $T = 0$. Note that the apparent velocity distribution narrows and skews with increasing inter-acquisition time, ΔT.

6.4 RESULTS AND DISCUSSIONS

6.4.1 Time Dependence of Apparent Velocity Distribution

The time evolution of apparent particle velocity distributions, V_p, was examined and shown in figures 6.3 (Langevin simulation) and 6.4 (experiment). For a fixed Pe, it is observed that Brownian motion is dominant at small ΔT, leading to apparent velocity distributions that are significantly wider than that of at large ΔT. As ΔT increases, the apparent velocity distribution narrows due to increased shear dominance. Such change can be explained by the fact diffusive velocity distribution width scales with $\Delta T^{-1/2}$,

$$\Delta X \sim \sqrt{\Delta T} \quad \Rightarrow \quad V = \frac{\Delta X}{\Delta T} \sim \frac{1}{\sqrt{\Delta T}}, \quad (6.15)$$
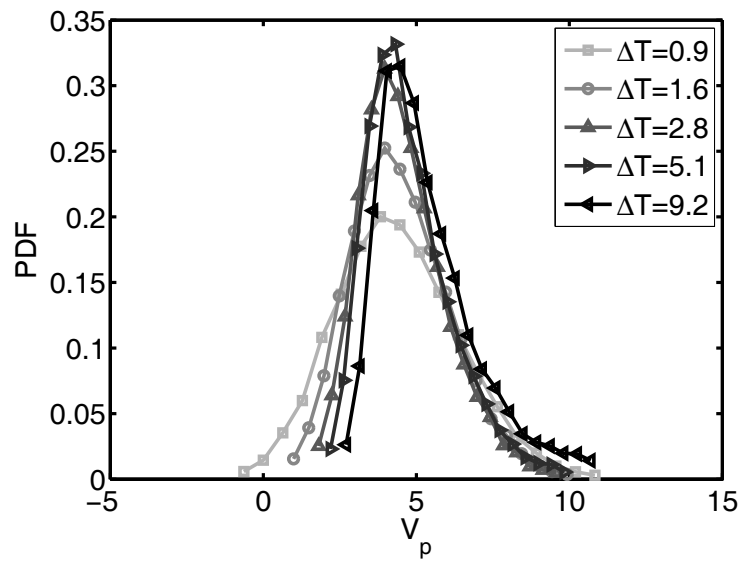
Figure 6.4: Time evolution of streamwise apparent velocity distribution in an actual experimental measurement. All apparent velocity PDF's are obtained at identical flow condition ($Pe = 2.4$), but with different time between image acquisitions for each data set. Note that the apparent velocity distribution narrows and skews with increasing inter-acquisition time, ΔT.

while the shear-induced flow velocity distribution width scales linearly with ΔT. Thus Brownian motion accounts for a large fraction of the measured apparent velocity at short inter-acquisition time, while the majority of the measured velocity is due to the shear flow at large ΔT. This explains the narrowing of the apparent velocity distributions in both figures 6.3 and 6.4 as ΔT increases. Clearly, if the apparent velocity distributions evolve as a function of inter-acquisition time, it would be of interest to see if the accuracy of particle-based velocimetry depends on the length of inter-acquisition time as well.

6.4.2 Velocimetry Measurement Bias Due to Hindered Brownian Motion and Hydrodynamic Mobility

The objective of velocimetry is to infer fluid velocities from the measured particle translational velocities, V_p. In practice, this is achieved by computing an average velocity of all particles within a desirable depth of observation $Z_1 < Z < Z_2$ to estimate the fluid velocity either by finding the maximal correlation value (as used in PIV) or through direct calculation (as used in particle tracking velocimetry, PTV). We denote this statistical mean velocity of the particle ensemble as $\langle V_p \rangle$. Because the current Langevin simulation emulates a PTV experiment, $\langle V_p \rangle$ is computed by

$$\langle V_p \rangle = \frac{\langle \Delta X \rangle}{\Delta T} \tag{6.16}$$

where $\langle \Delta X \rangle$ is the mean displacement of all particles that are present inside the depth of observation at the times of successive image acquisitions. In other words, $\langle V_p \rangle$ is the mean values of the apparent velocity distributions shown in figures 6.3 and 6.4. Mathematically, the particles' Z-positions must satisfy the requirements that $Z_1 < Z\,(T = 0) < Z_2$ and $Z_1 < Z\,(T = \Delta T) < Z_2$ in order to be imaged at both image acquisitions of the image pair.

The average velocity of all fluid planes within the same depth of observation is,

$$\langle V_f \rangle = \frac{1}{Z_2 - Z_1} \int_{Z_1}^{Z_2} V_f dZ, \tag{6.17}$$

where V_f is the fluid velocity profile. For a linear shear flow, $V_f = Pe \cdot Z$ and thus

$$\langle V_f \rangle = \frac{Pe}{2} (Z_1 + Z_2), \tag{6.18}$$

or the fluid velocity of the shear plane at the center of the depth of observation. $\langle V_p \rangle / \langle V_f \rangle$ can be interpreted as a measure of velocimetry accuracy, with $\langle V_p \rangle / \langle V_f \rangle = 1$ being the perfect agreement. The first velocimetry scenario being considered is that of a measurement conducted with uniform particle distribution, where the particle ensembles do not experience any external forces in the direction normal to the wall (ie. $G = 0$, $H = 0$). The time dependency of the velocimetry accuracy for an observation depth of $1 < Z < 3$ in this idealized scenario is shown in figure 6.5. It can be observed that all $\langle V_p \rangle / \langle V_f \rangle$ ratios exhibit the form of a concave-up function of ΔT, with a minimum occurring at approximately $\Delta T = 1$. Figure 6.5 also shows that the measurement accuracy is independent of Peclet number, eliminating shear rate as a potential source of bias. When velocimetry measurement accuracy is compared across different depths of observations $1 < Z < W$, as shown in figure 6.6, a similar shape of concave-up curves is observed. However, the curves do not fall on top of each other, suggesting that velocimetry accuracy does depend on the thickness of the observation depth.

Sadr *et al.* [45] had previously suggested that the velocimetry measurement inaccuracy shown in figure 6.6 is the result of particles diffusing in and out the depth of observation between successive image acquisitions (or during ΔT). They explained that for small ΔT
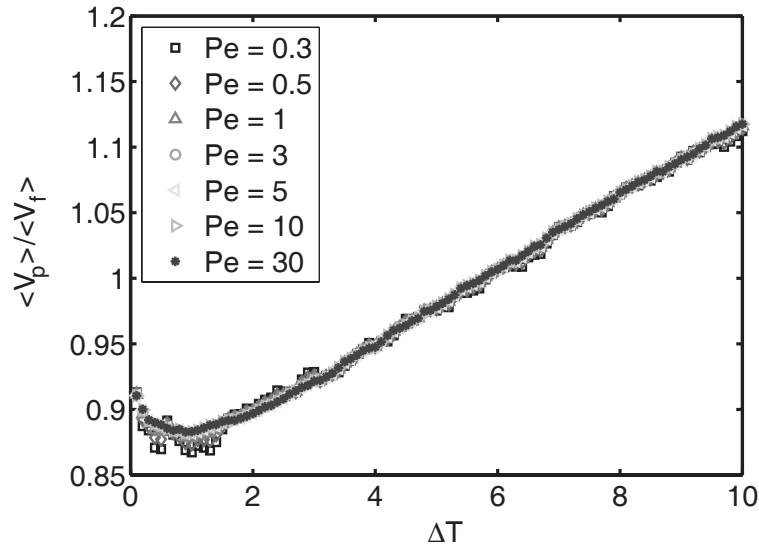
Figure 6.5: Time evolution of velocimetry measurement accuracy, $\langle V_p \rangle / \langle V_f \rangle$, at various Pe for a depth of observation of $1 < Z < 3$. Note that data of all Pe show a minimum velocity ratio at approximately $\Delta T = 1$.

imaged tracer particles are more likely sample the lower velocity planes, and thus the averaged apparent velocity of the particle ensemble is lower than the true fluid velocity. On the other hand at large ΔT there is a higher probability that particles can sample velocity planes farther away from the surface and still manage to return to the depth of observation at the time of second image acquisition. Such excursions bias the observed particle displacements, leading to erroneously large values of the particle translational velocity and thus over-estimating the fluid velocity. Sadr *et al.* further suggested that by re-scaling ΔT with $(W + 0.8)^2$, the curves of $\langle V_p \rangle / U_c$ ratios would collapse onto each other and they offer an empirical fit that can estimate measurement accuracy within 7% for all ΔT. To compare their finding with the current Langevin simulation results, the velocimetry accuracy (figure 6.6) is plotted using the proposed alternative time scale of Sadr *et al.* and compared with the empirical fit of Sadr *et al.* In figure 6.6 it can be observed that for large values of
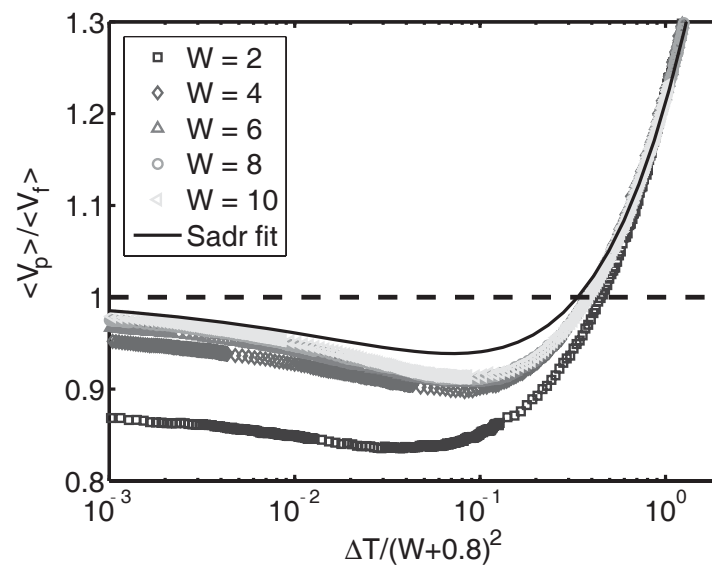
Figure 6.6: The time evolution of velocimetry measurement accuracy scaled with $1/(W + 0.8)^2$ as suggested by Sadr *et al.* [45] The empirical fit proposed by Sadr *et al.* is also shown for comparison. The depth of observation is defined as $1 < Z < W$. Note that the fit of Sadr *et al.* predicts the measurement accuracy very well for large values of $\Delta T/(W + 0.8)^2$ as the curves for all values of W collapse onto each other, while the prediction is much less accurate at $\Delta T/(W + 0.8)^2 \lesssim 5$. All data series have $Pe = 30$.

$\Delta T/\left(W+0.8\right)^{2}$ the velocimetry accuracy curves collapse onto each other and the empirical fit of Sadr et $al.$ predicts the velocimetry accuracy very well, while the curves still diverge at lower values of $\Delta T/\left(W+0.8\right)^{2}$ and the fit of Sadr et $al.$ over-estimates the velocimetry accuracy. Because Sadr et $al.$ examined only the effect of hindered particle Brownian motion on velocimetry accuracy, the closeness of their empirical fit to our simulation data curves at large $\Delta T/\left(W+0.8\right)^{2}$ implies that under this range of time scale hindered Brownian motion is the main source of velocimetry bias. On the other hand, the over-estimation of their empirical fit on the measurement accuracy at small $\Delta T/\left(W+0.8\right)^{2}$ suggests that under this time scale the bias is not solely dominated by hindered Brownian motion, and shear-induced hindered mobility of the particles also contributes significantly. In figure 6.6 one can observe that the deviation between our simulation results and the fit of Sadr et $al.$ for $\Delta T/\left(W+0.8\right)^{2}\lesssim 5$ grows larger as W becomes smaller. Such a trend suggests the role of shear-induced hindered mobility on velocimetry measurement bias becomes more prominent when the depth of observation is set closer to the solid wall.

Our simulation result also offers an algorithm using which the true fluid velocity can be estimated more accurately than by using the correction curve that Sadr et $al.$ proposed. First, the velocimetry bias can be estimated by

$$\frac{\langle V_{p}\rangle}{\langle V_{f}\rangle}=\left(\frac{\langle V_{p}\rangle}{\langle V_{ps}\rangle}\right)\left(\frac{\langle V_{ps}\rangle}{\langle V_{f}\rangle}\right)\tag{6.19}$$

where $\langle V_{ps}\rangle$ is the mean velocity of a uniformly distributed particle ensemble inside a depth of observation $Z_{1}<Z<Z_{2}$, if particles do not experience Brownian motion and only the shear effects on the particles are considered. Mathematically, in a linear shear flow $\langle V_{ps}\rangle$

can be computed by

$$\langle V_{ps} \rangle = \frac{Pe}{Z_2 - Z_1} \int_{Z_1}^{Z_2} F(Z) \cdot Z dZ \qquad (6.20)$$

where $F(Z)$ is the shear-induced hindered particle mobility as described in section 6.2. Therefore,

$$\left(\frac{\langle V_{ps} \rangle}{\langle V_f \rangle} \right) = \frac{Pe}{\langle V_f \rangle (Z_2 - Z_1)} \int_{Z_1}^{Z_2} F(Z) \cdot Z dZ, \qquad (6.21)$$

which can be easily calculated using equations (6.4), (6.5), (6.6) and (6.18) for the desired range of Z. The values of $\langle V_p \rangle / \langle V_{ps} \rangle$, on the other hand, can be obtained empirically from the current Langevin simulation. The values of $\langle V_p \rangle / \langle V_{ps} \rangle$ is found to exhibit a time-scale similarity, as demonstrated by all curves of $\langle V_p \rangle / \langle V_{ps} \rangle$ for various depths of observation collapsing closely onto each other when plotted against T/W^2 in figure 6.7. The curves of $\langle V_p \rangle / \langle V_{ps} \rangle$ can be closely fitted by an empirical equation form first suggested by Sadr *et al.* [45],

$$\frac{\langle V_p \rangle}{\langle V_{ps} \rangle} \approx A + (1 - A) \exp\left(-B \sqrt{\frac{T}{W^2}} \right) + C \sqrt{\frac{T}{W^2}}. \qquad (6.22)$$

By fitting equation (6.22) to the values of $\langle V_p \rangle / \langle V_{ps} \rangle$ for $1 < Z < 2$ using a least square of residual method, we found that A = 0.43, B = 1.85 and C = 0.63, and the resulting fit predicts the $\langle V_p \rangle / \langle V_{ps} \rangle$ values of all depths of observation to within 3%. Thus by combining equations (6.19), (6.21) and (6.22), an appropriate correction factor to $\langle V_p \rangle$ can be obtained to estimate the true fluid velocity with a less than 3% inaccuracy.

6.4.3 Velocimetry Measurement Bias Due to the Presence of a DLVO Interaction

The accuracy of particle-based velocimetry measurements can be compromised if there exists a neglected biased sampling of fluid velocities by the particle ensemble. Specifically, one
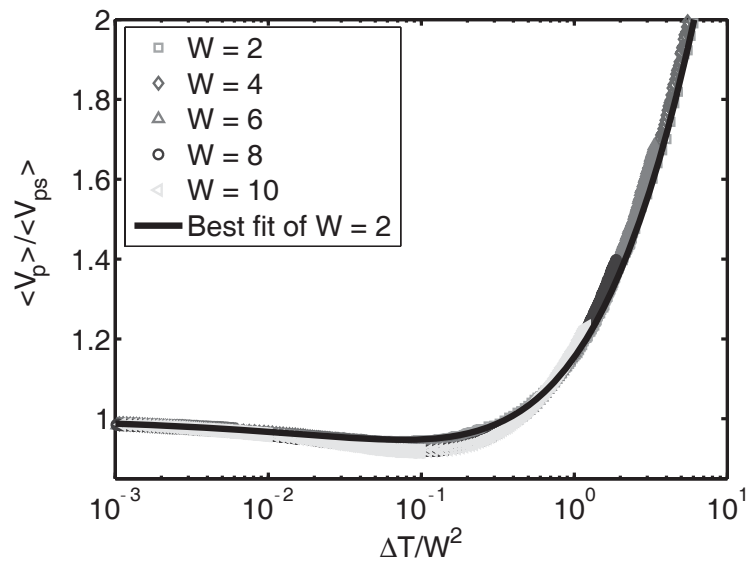
Figure 6.7: Time evolution of velocimetry accuracy for $Pe = 30$ due to hindered Brownian motion only. Because $\langle V_{ps} \rangle$ takes the shear-induced effect into consideration, $\langle V_p \rangle / \langle V_{ps} \rangle$ represents the measurement inaccuracy resulted from hindered Brownian motion of particles. The measurement accuracy curves for all observation ranges of $1 < Z < W$ show a scaling similarity under a time scale of $\Delta T / W^2$. A least-square residual fit of equation (6.22) to the data of $W = 2$, denoted "Best fit of $W = 2$", is found to predict $\langle V_p \rangle / \langle V_{ps} \rangle$ to within 3% of the actual values for all W.
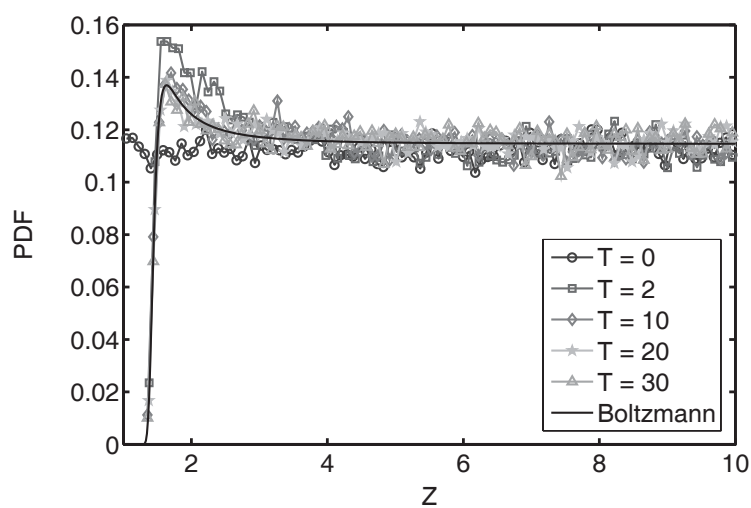
Figure 6.8: Spatial distribution of particles at $K = 16.33$, which is equivalent to a 100 nm-radius polystyrene particle (density 1050 kg/m^3) suspended in water of 2.5 mM ionic concentration with a Debye length of 6.1 nm. The particles are initially uniformly distributed in the volume ($1 < Z < 10$) at $T = 0$ and allowed to translate only within this volume, due to Brownian motion, electrostatic repulsion and van der Waals force between the particles and the wall. Note that the spatial distribution of the particles settles into the Boltzmann distribution after a transient period ($\Delta T \approx 10$).

can easily assume that particles are uniformly distributed within the observation depth and completes the data analysis under such an assumption, while not being aware of the potential sampling bias existing in the system. A common bias of this sort in almost all aqueous fluids is the electrostatic and van der Waals force interactions between particles and the wall as described in section 6.2.4. To demonstrate that our Langevin simulation can accurately capture such particle-wall interactions (ie. $H \neq 0$) based on the DLVO theory, a uniform particle concentration distribution in the wall-normal direction sampled after various times ΔT are shown in figure 6.8. It can be observed that the spatial distribution of a particle ensemble that start out uniformly evolves with time and eventually settles into a steady, non-uniform spatial distribution after a transient period, with the final spatial distribution agreeing to the Boltzmann distribution prediction based on the DLVO theory [159]. This suggests that the DLVO-Boltzmann distribution is the steady-state concentration profile of a particle ensemble experiencing electrostatic and van der Waals interaction with the wall.

The DLVO-Boltzmann distribution suggests a depletion layer of particles very near wall (approximately $Z < 1.5$ for the presented case in figure 6.8), which can be expected to also affect velocimetry accuracy. A full Langevin simulation incorporating DLVO interactions ($H \neq 0$) were conducted to investigate its effect. In this simulation, particles are initially seeded according to the DLVO-Boltzmann distribution shown in figure 6.8 by assuming that the particle ensemble has reached the spatially steady state. The rest of the simulation steps follow that of section 6.2, with particles experiencing hindered Brownian motion, electrostatic and van der Waals forces at each time step. The simulation was conducted using Debye length and Peclet number identical to that of the experimental conditions described in section 6.3.1 for comparison. The experimental and simulation results are compared and shown in figures 6.9 and 6.10. In figure 6.9, the velocimetry accuracy parameter,
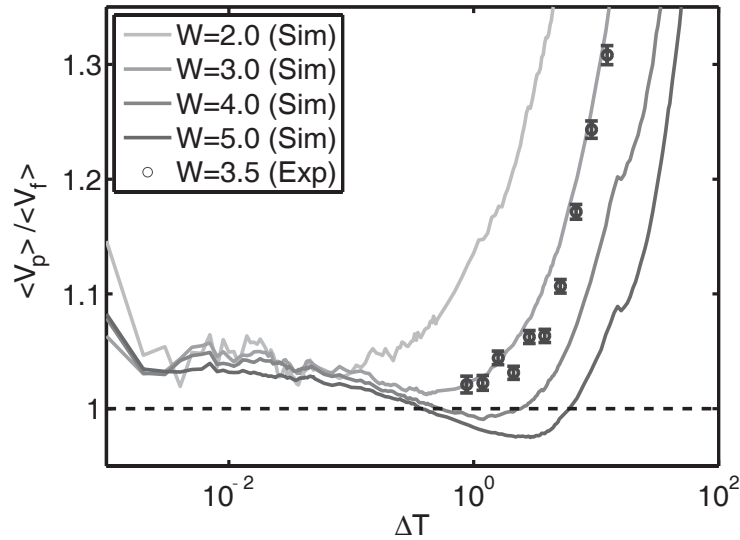
Figure 6.9: Time evolution of velocimetry accuracy, $\langle V_p \rangle / \langle V_f \rangle$, with particles experiencing hindered Brownian motion, DLVO particle-wall interactions and shear flow. The depth of observation is defined as $1 < Z < W$. Note that the experimental depth of observation is $1 < Z < 3.5$. All data series, including simulations and experiments, have $Pe = 2.4$.

$\langle V_p \rangle / \langle V_f \rangle$, is plotted against the time between image acquisitions, ΔT. Also observed in this case is that the velocimetry accuracy starts out at a constant level, decreases to a local minimum, and then increases with increasing ΔT. A major distinction in the presence of DLVO interaction, however, is that the ratio of $\langle V_p \rangle / \langle V_f \rangle$ is larger than unity for small ΔT. In fact, for depth of observation very close to the wall (ie. small W), the ratio of $\langle V_p \rangle / \langle V_f \rangle$ stay above unity for all ΔT, suggesting that such near-wall particle velocimetry measurements will always over-estimate the actual fluid velocity within this region. Such an observation can be explained by the existence of the near-wall particle depletion layer, whose presence leads to bias sampling of near-wall velocities and under-representation of the low fluid velocities near-wall in the velocity distribution statistics.

To further understand the effects of hindered Brownian motion, the presence of the wall,
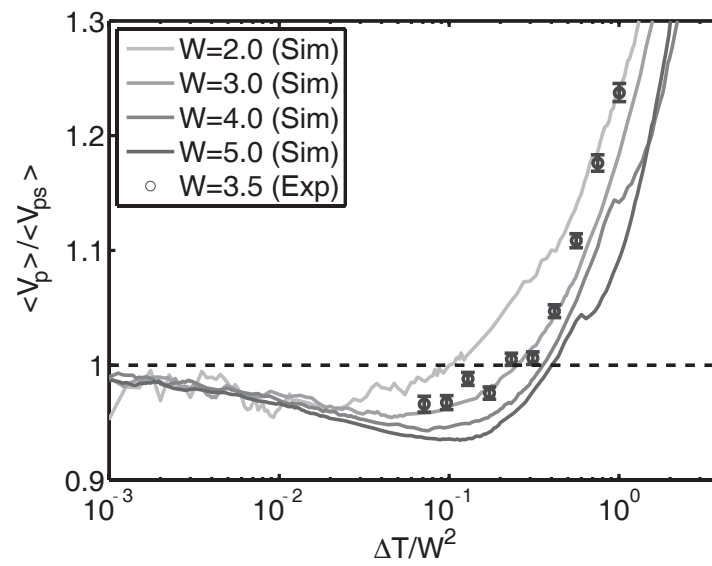
Figure 6.10: Time evolution of velocimetry accuracy with a rescaled nondimensional time $\Delta T/W^2$ and the shear-induced effect on particles taken into consideration by $\langle V_p \rangle / \langle V_{ps} \rangle$ as discussed in section 6.4.2 and equation (6.20). The measurement accuracy curves for all observation ranges of $1 < Z < W$ again show a scaling similarity, particularly for $\Delta T/W^2 < 0.02$. All data series have $Pe = 2.4$.

and the electrostatic and van der Waals forces, the shear effect on particles and the spatial distribution of the particle ensemble are taken into consideration by plotting $\langle V_p \rangle / \langle V_{ps} \rangle$ against a rescaled nondimensional time $\Delta T / W^2$ in figure 6.10. Here again we observe scaling similarity for all curves, particularly for $\Delta T / W^2 < 0.02$. In constrast to figure 6.9, the values within this region of rescaled nondimensional time remain less than unity. Such an observation suggests that proper consideration of near-wall particle depletion layer during data analysis can reduce over-estimation of fluid velocity. For $\Delta T / W^2 > 0.02$, however, the curves for different W values do not collapse as completely as the curves in figure 6.7 do. This is most likely due to the different ratios of depletion layer thickness, ϕ, to the depth of observation for different curves. As the values of W increases, the ratio of ϕ / W starts to converge and thus the curves of $\langle V_p \rangle / \langle V_{ps} \rangle$ begin to fall closer and close to each other. Undoubtedly, the method to obtain a better fluid velocity estimate described in section 6.4.2, namely equation (6.19), can still be applied to improve velocimetry accuracy by using the values of $\langle V_p \rangle / \langle V_{ps} \rangle$ obtained from curves such as those shown in figure 6.10, and by incorporating the DLVO-Boltzmann distribution of the particles, $C(Z)$, to modify equation (6.21),

$$\left(\frac{\langle V_{ps} \rangle}{\langle V_f \rangle} \right) = \frac{Pe}{\langle V_f \rangle (Z_2 - Z_1)} \int_{Z_1}^{Z_2} F(Z) \cdot C(Z) \cdot Z dZ. \tag{6.23}$$

6.4.4 Apparent Velocity Distributions

Another advantage of a two-dimensional Langevin simulation is the ability to investigate the effects of shear and random (Brownian) motion on apparent velocity distributions. The apparent velocity of a particle is defined by its displacement, ΔX, during the time between successive image acquistion, ΔT. Shown in figure 6.11 is the distribution of non-
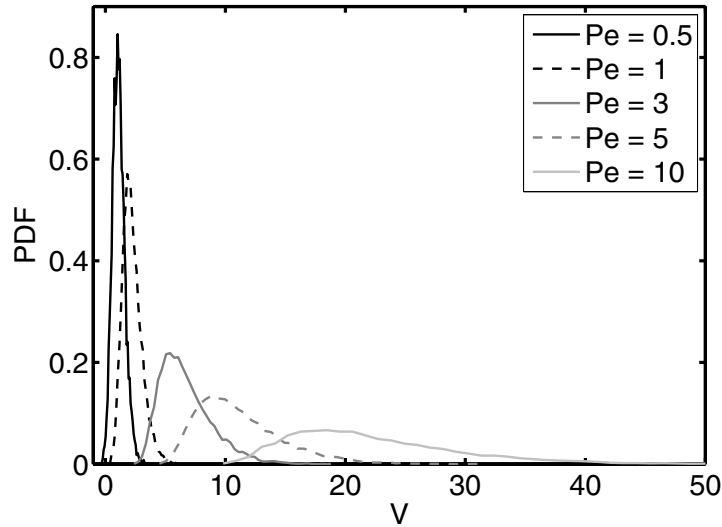
Figure 6.11: Apparent velocity distribution of particles remaining in the observation range $1 < Z < 3$ after $\Delta T = 10$. Larger Pe leads to an apparent velocity distribution with larger mean, width, and skewness.

dimensional apparent velocity, $V = \Delta X / \Delta T$, for ensembles of particles subject to different Peclet numbers, Pe. One can observe that the apparent velocity PDF's widen and skew as the shear rate increases, in good agreement with the experimentally measured PDF's reported by Jin *et al.* [39] and Huang *et al.* [41].

Upon further analysis, it is observed that, by scaling with the ensemble average velocity $\langle V_p \rangle$, the apparent velocity PDF's collapse onto a single distribution for $Pe > 3$, as shown in figure 6.12. The collapsed PDF's for $Pe > 3$ have a smaller distribution width but a more pronounced skewness, while the re-scaled distributions of $Pe < 3$ are wider but more symmetric. The explanation for such a scaling characteristic is that at low Pe, the displacements of the particle ensemble in the direction parallel to the flow is dominated by diffusion, leading to a wider re-scaled distribution. At high Pe, on the other hand, the combination of fluid shear and a finite thickness for a depth of observation give rise to the
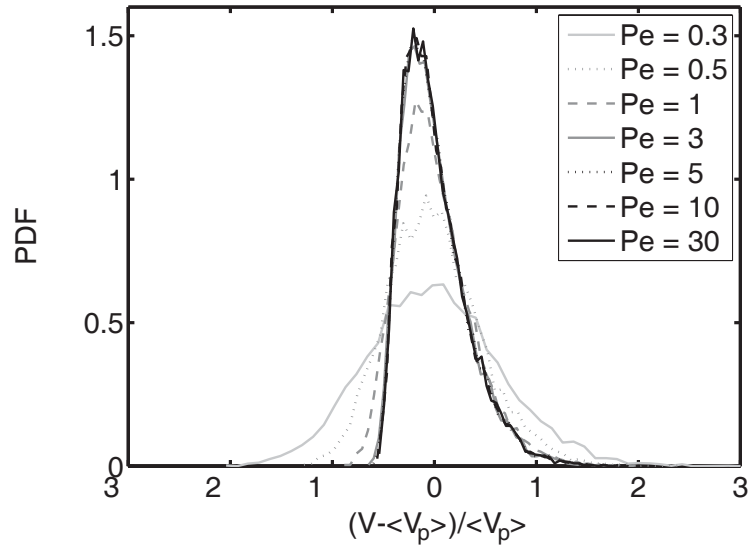
Figure 6.12: Re-scaled apparent velocity distribution of particles remaining in the observation range $1 < Z < 3$ after $\Delta T = 10$. $\langle V_p \rangle$ is the mean value of each apparent velocity PDF. The re-scaled PDF's collapse onto each other at $Pe > 3$. In general, larger Pe has a narrower but more skewed distribution.

increased skewness and broader distribution width. The fact that only at $Pe > 3$ both skewness and distribution width are scalable by the ensemble average velocity $\langle V_p \rangle$, and thus the shear rate, further supports this explanation. The same shear-dominance effect at $Pe > 3$ has been reported experimentally by Huang *et al.* [41], and the agreement of current Langevin simulation further validates the presented physical reasoning.

The sources of apparent velocity distribution skewness are the hindered Brownian motion of the particles and more importantly, the presence of the wall. One can observe in figure 6.13 that the apparent velocity PDF's of depths of observation farther away from the wall are wider and less skewed than those obtained from imaging ranges closer to the wall. When an observation depth is set to be far way from the wall, the targeted particle ensemble is equally likely to sample fluid velocities that are above and below the observation range, leading to a more symmetric apparent velocity distributions. However, for particle ensembles that are
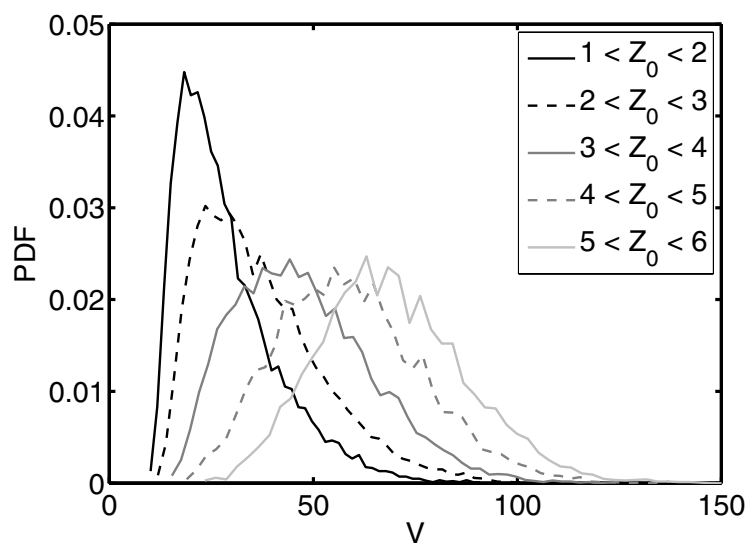
Figure 6.13: Apparent velocity distribution of particles at various depths of observation. All apparent velocity distributions are obtained at $\Delta T = 10$ and $Pe = 10$. Particles that start off farther away from the surface move faster because they are carried by fluids at higher velocity planes, and their distributions are more symmetric due to less influence of the wall and hindered Brownian motion.

close to the wall, such symmetric sampling is broken as the particles are unable to enter the wall and therefore are more likely to sample velocities at shear planes above the depth of observation. As a result, the apparent velocity PDF has an asymmetric shape with a long positive tail coming from the bias in sampling higher shear planes. Also contributing to the skewness are the hindered Brownian motion and the shear-induced hindered mobility of particles in the near-wall region, while far away from the wall, their effects are less experienced.

The skewness of apparent velocity distributions could further lead to undesirable velocimetry inaccuracy, particularly in the case of PIV. PIV obtains an ensemble-averaged displacement by searching for the optimal cross-correlation between successive image acquisitions. Statistically, the ensemble displacement of PIV thus represents the particle displacement that occurs most frequently, or the mode of particle displacement. This is in contrast to using the statistical average, or the mean of the particle displacements to calculate the ensemble velocity usually accomplished in PTV. Because the apparent velocity distributions of the near-wall regions have long positive tails, as demonstrated in figure 6.13, their statistical mean values will always be greater than the values of the distribution modes. Referring back to figure 6.6, at $\Delta T / (W + 0.8)^2 \lesssim 5$, PIV would under-estimate the true fluid velocity more than PTV would as in this region the obtained $\langle V_p \rangle / \langle V_f \rangle$ is less than one, and thus PTV would be more accurate than PIV under this time scale. At $\Delta T / (W + 0.8)^2 > 5$, on the other hand, PTV would over-estimate the true fluid velocity than PIV, suggesting that PIV might be the more accurate for this time scale. However, such an improvement in measurement accuracy could be offset by the fact PIV ignores particle drop-ins and drop-outs between image acquisitions, and could become a significant source of bias at large ΔT. Such reasoning suggests that PTV is probably a more accurate

method for near-wall velocity measurements under most circumstances.

6.5   CONCLUDING REMARKS

Langevin simulation offers an attractive approach to the study of near-wall particle dynamics. We demonstrate that hindered Brownian motion due to hydrodynamic interactions with the wall and reduced translational velocity due to shear-induced rotation of a colloidal particle in a shear flow can be accurately captured with results that confirm previously obtained experimental data. In the direction parallel to the wall, colloidal particle motion is dominated by shear when Peclet number is greater than 3, with the presence of the wall breaking the system symmetry and contributing to changes in the velocity distribution width and its skewness. Furthremore, the accuracy of velocimetry is also examined for the cases of highly idealized uniformly distributed and the more realistic non-uniformly distributed particle ensembles. In both cases, the simulation result offers a method to obtain a better estimate of the true fluid velocity through a combination of empirically obtained velocimetry accuracy curves and theoretical calculation of hindered mobility of near-wall particles.

Finally, we note that correlation-based methods, such as Particle Image Velocimetry (PIV) will have a difficult time achieving accurate results. Particle Tracking Velocimetry (PTV) approaches will tend to be more successful, although they require low seeding densities in order to achieve reliable particle-particle matching and thus might be more time consuming. An approach that allows for high particle seeding densities while still obtaining an ensemble velocity distribution is the Statistical Particle Tracking Velocimetry (SPTV) [10] which is ideal for this class of flows. Apparent velocities obtained from SPTV measurements can be corrected using the algorithm outlined in the results and discussion section

to minimize diffusion and wall-induced measurement bias.

ACKNOWLEDGMENT

Chapter 7

High-speed quantum dot tracking using evanescent wave illumination

Total internal reflection velocimetry (TIRV) is applied to measure the dynamics of 17 nm diameter, colloidal quantum dot (QD) tracer particles within 200 nm of a microchannel wall at shear rates in excess of 20,000 s^{-1}. QDs are quickly developing into viable tracer particles for measuring microscale fluid dynamics. However, the low emission intensities of QDs usually require long exposure and inter-frame times, which limit velocity resolution and compromise accuracy (due to their fast diffusion as a consequence of a small diameter). In this study, a two-stage, high-speed image intensifier and camera were integrated into an evanescent wave microscopy imaging system to provide the necessary temporal resolution to image the fast diffusion dynamics of QDs in real time (up to 10,000 fps), which allowed individual particles to be tracked continuously for extended periods of time. In addition to

examining the trajectories of individual particles, ensemble-averaged tracking measurements reveal near-wall velocity distributions in high-speed microchannel flows (Re ∼ 10), where velocities on the order of 5 mm/s are measured within 200 nm of the microchannel wall. This data provides a robust confirmation of recent results demonstrating diffusion-induced bias error for near-wall velocimetry.

7.1 INTRODUCTION

Micro-scale fluid diagnostics have made tremendous progress over the past several years, such that microscale Particle Image Velocimetry (μPIV) with micron depth resolution is commonplace. These μPIV techniques typically use flood illumination (either from a pulsed laser, continuous wave (CW) laser or a broadband source), fluorescent tracer particles and an epiflourescent microscope or similar optical system. While these approaches are extremely valuable, their optical axis resolution is limited to the order of microns, primarily by two constraints. First, this illumination technique relies on the depth of field of the imaging objective to define the two-dimensional measurement plane (approximately 1 micron [151]). Secondly, imaging small tracer particles in μPIV is limited by the signal-to-noise ratio and Brownian motion of the particles. For extremely small tracer particles, an exposure time, t_e, of up to several milliseconds is required to reliably image the particles and therefore a minimum inter-frame time (the time between two successive images), Δt, is established as being at least 3 times (preferably 10 times) the exposure time. This inter-frame time limitation effectively defines a maximum measurable velocity so that particle displacements are not excessively large, which can degrade particle tracking accuracy.

In recent years, there have been a number achievements that have extended the limits of micron-scale velocimetry. Evanescent wave microscopy, or Total Internal Reflection

Fluorescence (TIRF) microscopy when imaging fluorescence, allows for confinement of the illumination light within about 100 nm of a dielectric interface [36]. The evanescent wave is typically created by reflecting excitation light off of a dielectric interface at an angle greater than the critical angle (for example, the glass-water interface at the wall of a microchannel). Near-wall flow measurements using this TIRF microscopy have been demonstrated by several researchers and have enabled detailed measurements of the mechanics near fluid-solid interfaces [6, 39, 9, 116, 41]. However, even with such localization of the excitation light, relatively large tracer particles ($\sim$ 100 nm diamter) are required to provide enough light emission for imaging purposes. These tracer particles span nearly the entire imaging depth, where complex dynamics take place in the high-shear region near the wall. In this respect, it is beneficial to probe the flow with smaller tracer particles that have less hydrodynamic interaction with the local flow structure and solid substrate.

In the search for smaller tracer particles, quantum dots (QDs) have attracted increasing attention. QDs are single fluorophores, with fluorescence lifetimes and quantum efficiencies similar to conventional fluorophores, but with significantly higher resistance to photo-bleaching [15]. They exhibit several qualities beneficial to nano-scale velocimetry including small diameters ranging from 5 nm to 25 nm, a narrow and finely tunable emission wavelength, and selectable surface coatings for solubility in either organic or inorganic solvents. However, single QDs have a significantly lower emission intensity as compared to much larger polystyrene particles containing several thousand fluorophores. The first practical demonstrations using QDs in aqueous solutions for velocimetry purposes used either extremely dilute solutions [9] or statistical velocimetry algorithms [10] to negotiate the necessarily long exposure times and high diffusivities.

In the present work, we extend our previous studies using QDs as tracer particles with

TIRF microscopy to explore the limits of high-speed, near-wall velocimetry. We present a system that enables single QD imaging at frame rates as high as 10 kHz, exposure times as low as 90 μs and with in-plane spatial resolution of 35 nm. In the current manuscript, we demonstrate these capabilities and confirm several results reported by our own group, as well as other researchers, concerning fluid velocity measurement bias associated with varying inter-frame time and tracking particle motion [141, 45, 13, 46].

7.2 EXPERIMENTAL METHODS

7.2.1 Quantum Dots and Microfluidics

The key experimental details have been discussed earlier [39, 41, 10], but are reviewed here briefly here for convenience. Rectangular poly-dimethyl siloxane (PDMS) (Sylgard 184 Silicone Elastomer, Dow Corning) microchannels with a 260 μm $\times$ 40 μm cross-section were fabricated using soft lithography techniques [117] and mounted on 170 μm thick borosilicate cover glass. The dimensions were inferred from photoresist mold dimensions measured using a surface profiler (Dektak, Veeco). A microchannel was mounted on an inverted microscope (Nikon Eclipse TE2000-U) and the flow was driven using a syringe pump (Harvard Apparatus) as shown in figure 7.1. The microscope is equipped with epiflourescence filters and an oil immersion objective lens (Nikon TIRF 100$\times$, 1.45 NA). The tracer particles are water-soluble, CdSe/ZnS core-shell quantum dots with a carboxyl termination (Invitrogen). The QDs have a core diameter of about 6 nm with an overall hydrodynamic diameter of about 17 nm due to the water-soluble coating and a peak emission wavelength of 606 nm. All experiments were performed using a 50 mM borate buffer with a 0.1 to 1.0 nM QD concentration. The QDs have a broad excitation spectrum, and for these experiments, the 514
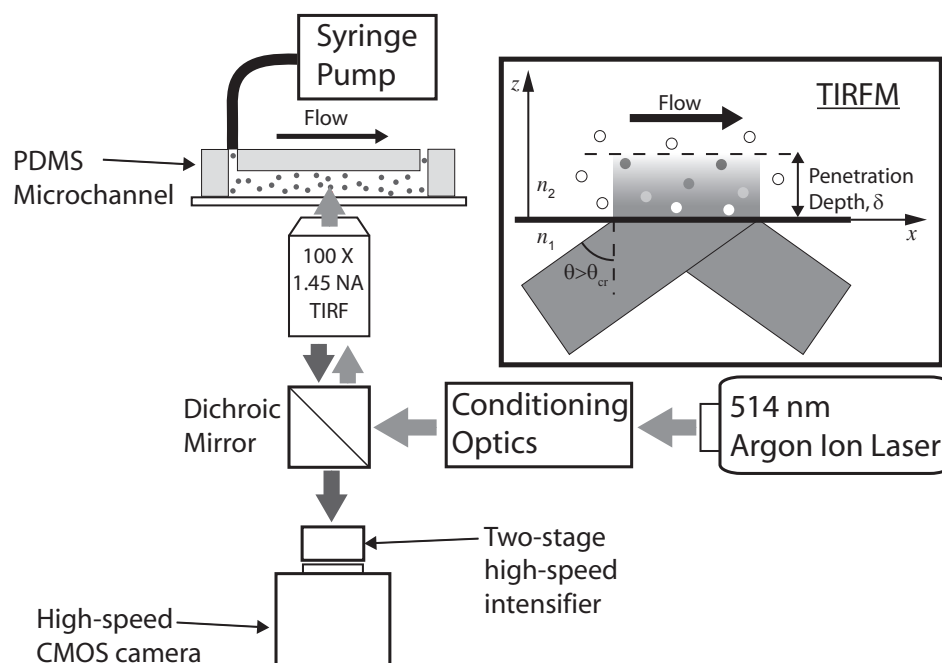
Figure 7.1: Schematic of the experimental setup and high-speed TIRF imaging system.

nm line of an Argon-ion CW laser (Coherent) was used as the excitation source. Exposure times, t_e, for all data presented here were between 200 to 300 μs (the minimum achieved exposure time was 90 μs, not shown).

7.2.2 Single Quantum Dot Imaging Using TIRF Microscopy

The detection and tracking of single QDs in aqueous solutions for the purpose of velocimetry has been demonstrated previously [9, 10, 12] using a Total Internal Reflection Fluorescence (TIRF) microscopy technique [35, 36] (Figure 7.1). TIRF allows for extremely high signal-to-noise-ratio (SNR) and illumination within about the penetration depth, δ, (100-200 nm) away from the fluid-solid interface. We use an objective-based TIRF system, which creates a total internal reflection at the interface of the glass cover slip and the aqueous buffer with refractive indexes of $n_1 = 1.52$ and $n_2 = 1.33$, respectively. An intensity distribution

with exponential decay normal to the interface exists in the lower optical density medium (buffer). For our system, the penetration depth, δ, was about 200 nm corresponding to an incident angle of $\theta = 62.6^o$.

A high-speed, two-stage image intensifier (Hammamatsu) was employed to amplify the low intensity QD images emerging from the microscope camera port, which were then projected onto a high-speed CMOS camera sensor (Photron APX-RS, 17 μm pixels). Image intensifiers of this type have an inherently low resolution (35 lp/mm). Thus, the image from the microscope was magnified 1.5× before the intensifier, then de-magnified using a 2× relay lens from the intensifier to the camera. The total system magnification was 75× with a effective 512×512 pixel field of view and a magnified pixel size of 227 nm. The camera is capable of 3,000 frames per second (fps) at full frame (1024×1024 pixels). However, the TIRF illumination spot takes up only a fraction of the field of view (256×256 pixels). Thus, the camera could acquire images at >10,000 fps using a smaller region of interest, and typical data sets consisted of 20,000 images.

Since the quantum dots are significantly smaller than the wavelength of light, we image only a diffraction-limited spot, typically measuring about 5 pixels. Single QDs were detected by intensity thresholding the local maxima of an image. The sub-pixel center locations, x and y, peak intensity, I, and radius, b, of each potential particle were found through a two-dimensional, Gaussian least-squares fit to a 3×3 pixel array centered on the maximum intensity pixel [55]. The error in Gaussian fitting to sub-wavelength particle images has been shown to be as small as 0.1 pixels for a SNR greater than five [54]. A significant amount of single pixel and blooming noise from the intensifier can be rejected based on the fitted diameters of potential particles, which will appear to be about one pixel or less ($b \leq 1$ pixel). The single QDs were then tracked using nearest-neighbor matching with window
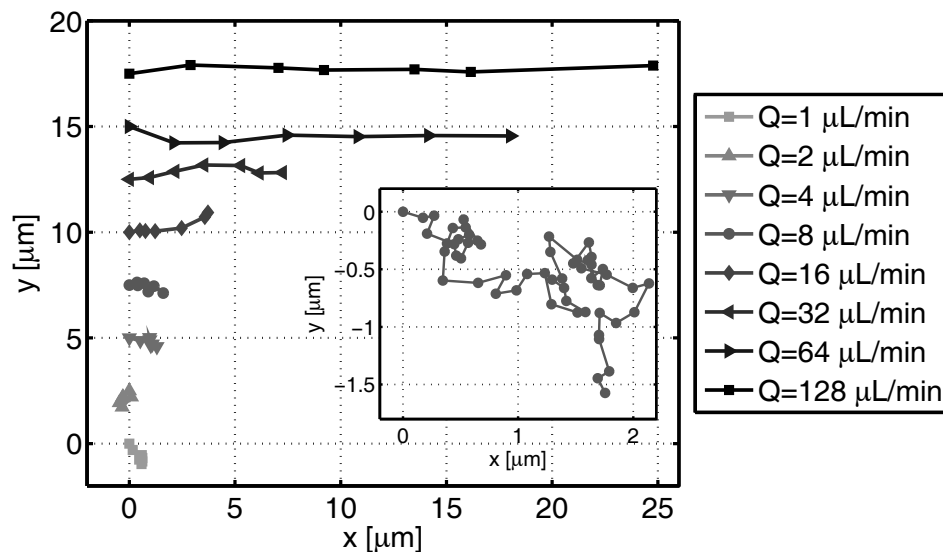
Figure 7.2: Individual QD trajectories at several flow rates imaged at 1,000 fps and tracked for 7 frames. As the flow rate (and Peclet number) increases, the random walks stretch and the relative contribution of Brownian motion diminishes. The inset shows a detailed random walk for a single quantum dot diffusing within the evanescent field with a mean flow rate of 4 μL/min. The frame rate was 4,000 fps, and in this particular case, the particle was tracked for about 14 ms or 56 frames.

shifting to capture large displacements when necessary.

7.3 RESULTS AND DISCUSSION

7.3.1 Time-resolved QD Tracking

A unique capability of this system is the ability to track single QD trajectories in real time for an extended number of frames. An example of this is illustrated in the inset of figure 7.2, which shows a single QD trajectory in a 4 μL/min flow tracked for 14 ms at 4,000 fps (56 frames) within the evanescent field. Similar, measurements were made for a series of flow rates ranging from 1 to 128 μL/min. Sample particle trajectories from these results are also shown in figure 7.2, where the particles were imaged at 1,000 fps, and all trajectories are
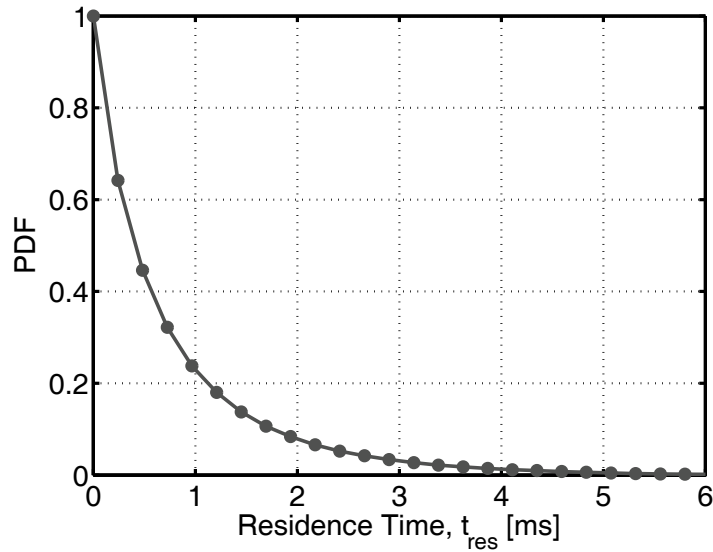
Figure 7.3: A probability distribution function (PDF) of the residence times for QDs in the evanescent field. We see that 80% of the QDs have left the observation range within 1 ms of their initial detection.

7 frames long. As the flow rate increases, the random walks begin to stretch in the flow (stream-wise) direction. This is somewhat similar to a random walk with drift, however the wall-normal velocity gradient further complicates this process resulting in dispersion.

The fast imaging speed helps to ensure that we are tracking the same QD over multiple frames. Of course, QDs diffuse in the wall-normal direction perpendicular to the interface and out of the evanescent field, as well as parallel to the interface. Additionally, fluorescence intermittency (blinking) will cause the QD fluorescence emission to cease for an indeterminate amount of time [18]. Thus, there is a finite length of time during which one can track any given QD. The fraction of particles that drop-out of the imaging zone (either physically or optically) is shown in figure 7.3. We see that almost 80% of the QDs initially identified in an image have migrated out of the evanescent field after 1 ms, which is in good agreement predictions based on diffusion alone (discussed in section 7.3.2). This is not to say that they

are lost to tracking algorithms, since there is a good probability that they will re-enter the observation range shortly afterwards.

7.3.2   Ensemble-averaged Particle Dynamics

Cross-stream Motion

In addition to single particle dynamics, much insight is gained from various statistical quantities of the ensemble particle dynamics. As expected particle displacements in the cross-stream direction (perpendicular to the flow), Δy, demonstrate purely diffusive behavior. The probability density functions (pdfs) of cross-stream displacement for several inter-frame times, Δt, acquired at 4,000 fps are shown in figure 7.4. It is important to note that the inter-frame time was varied by re-sampling a single, high-speed image sequence by skipping frames. Thus, the same set of particles was used to produce each distribution shown. The mean-squared particle displacement, $\langle \Delta y^2 \rangle = \sigma_y^2$, scales linearly with the inter-frame time, Δt, which reaffirms that the motion in the cross-stream direction is purely diffusive (shown in the inset of figure 7.4). Additionally, we note that no dispersion was observed for particle displacements in the cross-stream direction for all observed flow rates (not shown).

The cross-stream diffusion coefficient, D_y, computed from a linear fit of the mean-squared displacements was found to be 37.9 $\mu\text{m}^2/\text{s}$ ($R = 0.996$). According to theory, the standard deviation (width) of the displacement distribution, σ_y, should grow as $\sqrt{2D\Delta t}$ in one dimension, where D is the diffusion coefficient. Ignoring the effects of hindered diffusion for small particles over a relatively large imaging range, the characteristic time to diffuse one diameter is $t_c \approx a^2/D \sim 8$ μs for a nominal hydrodynamic radius of $a = 8.5$ nm (quoted by the manufacturer). Finally, the characteristic residence time for a particle to remain
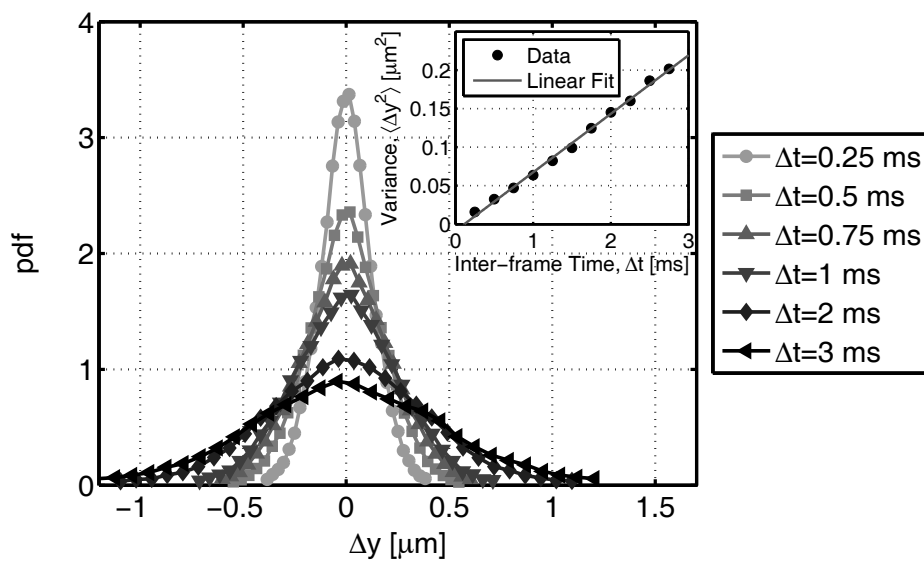
Figure 7.4: QD displacement, Δy, distributions at a fixed flow rate (4 μL/min) in the cross-stream direction perpendicular to the flow taken at 4,000 fps. As the inter-frame time, Δt, increases, the displacement distributions broaden due to Brownian motion. The inset shows that the mean-squared displacement, $\langle \Delta y^2 \rangle = \sigma_y^2$, scales linearly with the inter-frame time, Δt.
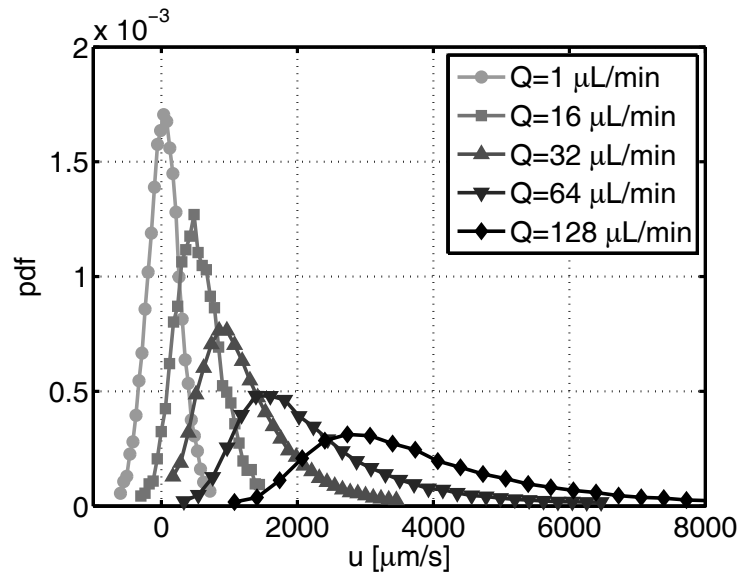
Figure 7.5: Distribution of streamwise velocities, u, for various flow rates. The inter-frame time for all cases is $\Delta t = 1$ ms at 1,000 fps. As the flow rate increases, the distributions shift to the right due to increasing mean velocity, broaden due to dispersion and skew due to the presence of the wall.

within the $\delta \sim 200$ nm observation depth is just $t_{res} = \delta^2/D \sim 1$ ms. This scaling is in good agreement with the residence times measured in section 7.3.1.

Stream-wise Motion

In the stream-wise direction parallel to the flow, it is advantageous to characterize the particle dynamics by velocity statistics rather than particle displacements. Figure 7.5 shows the stream-wise velocity distributions for a variety of flow rates, obtained with a fixed inter-frame time of $\Delta t = 1$ ms (1,000 fps). We see that the distributions shift to the right reflecting the increasing mean velocity, as well as broaden. The broadening and marked increase in the skewness as the flow rate increases are purely due to dispersion effects. These characteristics were first noted by Jin et al [39] and have subsequently been explained as consequences of (i) the finite thickness of the TIRF illumination depth, which generates

a "shear broadening" dispersion effect, and (ii) the presence of the wall which introduces a positive bias to the particle displacements (which preferentially follow diffusive paths through high-velocity regions of the flow in the time between image acquisitions) [45, 46]. High-speed imaging of the QDs enabled by this experimental configuration illustrates these features of the distribution very clearly and emphasizes the capabilities of this new system with extremely robust statistics. The shape of the velocity distribution is also dependent on the wall-normal concentration of tracer particles [41, 47, 46, 48], which may be non-uniform due to electrostatic, van der Waals, and other near-wall forces [37]. We note that optical forces due to electric field gradients in the excitation field are negligible for such small particles at low excitation power, where the potential energy of the trapping force is $\sim 10^{-6} k_b T$ [55]. Hydrodynamic effects causing hindered diffusion are also small due to the size of the tracers relative to the observation depth. In any case, the maximum velocities measured are, by microfluidic standards, large, with near-wall velocities of more than 4 mm/s (within 200 nm of the surface) and some of the highest reported for QDs to date. This represents flow measurements with a local shear rate of approximately 20,000 s^{-1}. Assuming that there is no significant deformation of the channel, mean velocities at the highest flow rate are over 20 cm/s, and the channel Reynolds number, Re, is on the order of 10.

Recently, much interest has centered around the dependence of ensemble-averaged particle velocity on inter-frame time due to the effects mentioned above [45, 46, 13]. Figure 7.6 shows typical particle velocity distributions in the flow direction for a series of increasing inter-frame times, Δt, at a fixed flow rate ($Q = 4$ μL/s). Again, this data was obtained from a single, high-speed image sequence acquired at 4,000 fps by re-sampling the sequence at different intervals to vary the inter-frame time. This has two distinct advantages: (i) all
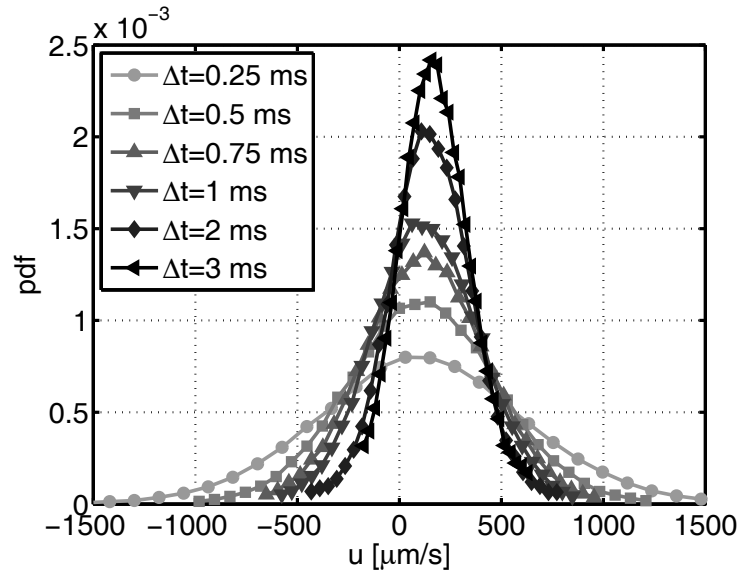
Figure 7.6: QD velocity distributions for a fixed flow rate, Q, (4 μL/min) and increasing inter-frame time, Δt. The distributions narrow with increasing interframe time and skew due to the velocity bias introduced by the presence of the wall.

of the data was conveniently acquired with a single data set and (ii) the observed effects can only be due to inter-frame time, since the same set of particles is used for all trials. The standard deviation of the displacement distribution grows with the scaling $\sigma_x \sim \Delta t^{1/2}$ (excluding dispersion). Since the velocity is computed through a simple derivative, $u = \Delta x/\Delta t$, the velocity distribution is expected to narrow with the scaling $\sigma_u = \sigma_x/\Delta t \sim \Delta t^{-1/2}$. This is confirmed in figure 7.6. Additionally, a careful inspection of the distributions reveals an increasing positive skewness, κ_u, toward the downstream direction of the micro-channel as compared to the cross-stream skewness, κ_v, with increasing inter-frame time. These details along with several other statistical parameters are given in table 7.1.

The bias in the velocity measurement associated with changes in the inter-frame time is highlighted by the results presented in figure 7.7, which shows the mean velocity, $\bar{u}$, and most probable velocity (maximum of the pdf), u^*, plotted as a function of the inter-frame

Inter-frame Time	Mean	Most Probable	Standard Deviation	Standard Deviation	Skewness	Skewness
Δt	$\bar{u}$	u^*	σ_u	σ_v	κ_u	κ_v
ms	μm/s	μm/s	μm/s	μm/s		
0.25	110.6	92.3	515.6	506.2	0.039	-0.002
0.50	118.3	115.6	363.7	359.8	0.029	-0.007
0.75	127.3	120.3	293.1	289.3	0.041	0.000
1.00	132.0	120.4	257.6	252.2	0.024	0.003
1.25	138.2	126.9	234.2	229.3	0.017	-0.010
1.50	144.4	130.7	215.2	209.9	0.043	0.002
1.75	150.8	139.6	207.7	201.6	0.053	-0.006
2.00	156.3	145.3	202.5	190.4	0.071	-0.002
2.25	161.4	150.4	190.4	177.8	0.083	-0.006
2.50	171.2	154.6	181.8	172.7	0.230	-0.002
2.75	179.5	158.7	172.5	163.3	0.299	-0.002

Table 7.1: Velocity distribution statistics for QDs imaged at 4,000 fps with $Q = 4$ μL/min sampled at various inter-frame times, Δt.

time, Δt. We see that the apparent velocity increases monotonically as the inter-frame time increases. As Δt decreases, the estimation of the true fluid velocity does appear to become more precise in the sense that the rate of change of the estimation decreases. However, it has been shown via both Langevin and Fokker-Plank simulations that the estimation is only accurate as $\Delta t \to 0$, and that while large values of Δt lead to extremely large errors, intermediate values can actually under-predict the true value of the local fluid velocity [141, 45, 13, 46]. In the present case, the small size of the QDs (and hence their high diffusivity) means that the biases are not negligible, even at very short inter-frame times of $\Delta t = \mathcal{O}(1ms)$.

7.4 CONCLUDING REMARKS

We have demonstrated the capabilities of a sensitive, high-speed imaging system with the ability to image single quantum dots in real time and with large velocities within about
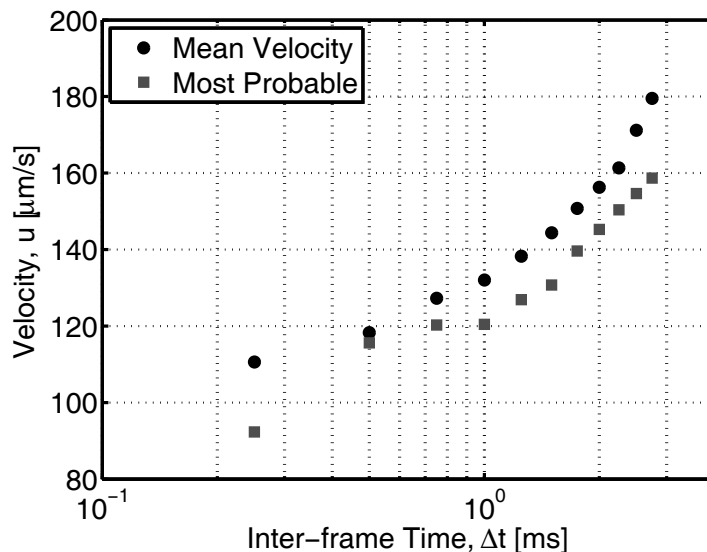
Figure 7.7: Streamwise velocity (determined from both the mean and the most probably values of the velocity distribution) as a function of the inter-frame time, Δt. The high diffusivity of the QDs results in extremely large velocity estimation errors, even for values of Δt that would be normally considered small in microfluidic experiments.

200 nm of a microchannel wall. A two-stage image intensifier and high-speed CMOS camera combined with the sensitivity and high spatial resolution of evanescent wave (TIRF) microscopy enabled this system to capture the trajectories of single quantum dot random walks for well over 50 consecutive frames at 4,000 fps (with a limiting frame rate of about 10 kHz). In addition to single particle dynamics, ensemble-averaging of particle displacement allows for robust measurements of large mean velocities (over 4 mm/s) within the evanescent field. Long image sequences with uniform frame rates allowed for convenient, robust re-sampling of the images to probe dispersion and velocity measurement effects due to varying inter-frame times. This provided additional confirmation of the diffusion-induced bias error reported by several other researchers [45, 13, 46]. In addition, the real-time tracking of single tracer particles will enable detailed studies of diffusion, dispersion, chaotic advection,

and even fluid instabilities at the micron and nanometer scale. At the present time, we have not used the tracer intensity to infer distance from the wall, although this is possible, and has been used previously with larger tracer particles to perform three-dimensional velocimetry, [41, 47]. We will certainly explore this in the near future.

ACKNOWLEDGMENT

Chapter 8

Evanescent wave imaging of particle adhesion dynamics near solid surfaces

J.S. Guasto, B.J. Schmidt, M.B. Lawrence and K.S. Breuer.
In preparation for *Biophysical Journal*, 2008.

Inflammatory responses are initiated by leukocyte (white blood cell) adhesion to blood vessel walls. This process is mediated by adhesion proteins (ligands) on the leukocyte (PSGL-1) that interact with receptors bound to the arterial wall (P-selectin), which can tether the cell within about 100 nm of the wall. The kinetics of this interaction are force dependent and vary with several factors, including the protein adsorption density, the fluid shear rate, the cell size and the distance between the cell and the surface. We present a microfluidic diagnostic system to investigate this process, specifically, particle tethering dynamics and the binding interaction between P-selectin and PSGL-1. An aqueous buffer solution containing

fluorescent, 6 µm polystyrene particles conjugated with P-selectin is driven through a microchannel, where the lower wall is conjugated with PSGL-1. The three-dimensional particle trajectories are observed in real time within about 200 nm of the substrate using total internal reflection fluorescence (TIRF) microscopy. From the particle dynamics, reaction rates and bond forces can be measured.

8.1   INTRODUCTION

The primary function of leukocytes (white blood cells) is to initiate an inflammatory response against harmful stimuli in the body. This process begins with capture and adhesion of leukocytes to vascular endothelial cells, and their subsequent rolling along blood vessel walls to investigate for infection and disease. When stimulated by the presence of chemoattractants, the leukocyte will arrest and transmigrate through the vessel wall, then go to the origin of the stimulus. Otherwise, the cell eventually releases back into the blood stream for further investigation (see figure 8.1). This process is extremely complex, and is mediated by a wide variety of proteins, anitbodies and other chemical interactions. One family of receptor proteins, known as selectins, on the vessel walls along with their complimentary ligands on the leukocytes are responsible for the reversible binding reactions that tether the cells to the wall and mediate rolling. Of particular interest are P-selectin and P-selectin Glycoprotein Ligand-1 (PSGL-1), which form some of the longest tethers estimated at about 92 nm in length [160].

Given the importance of this process, it is beneficial to understand the dynamics of tethered cells and the reaction rates of the protein binding. Numerical simulation has been a popular avenue for studying cell adhesion dynamics to account for deformation of leukocytes in flow and stretching microvilli [161, 162]. Additionally, many researchers have provided
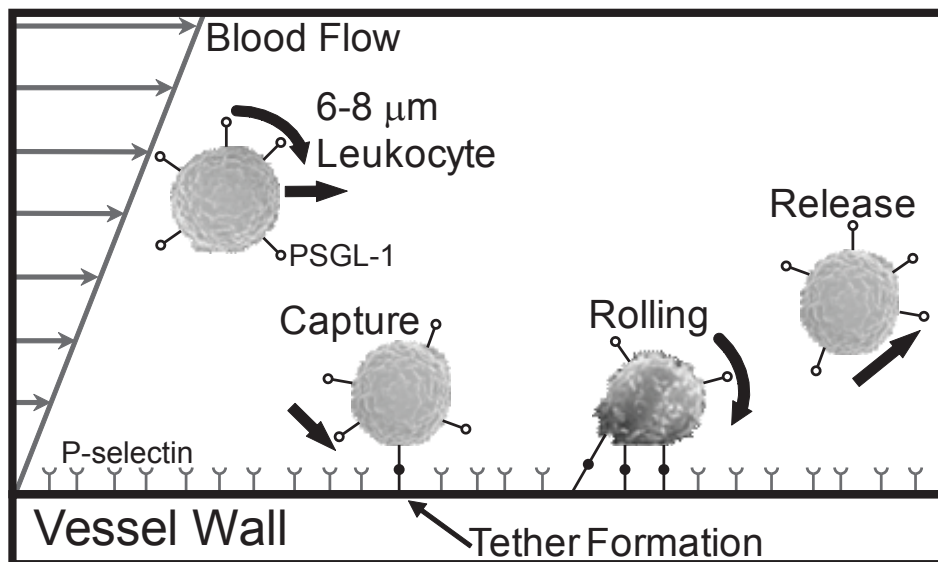
Figure 8.1: Schematic depicting the leukocyte adhesion process. Leukocytes that are convected along in the blood stream rotate due to local fluid shear. When a leukocyte contacts the vascular endothelial cells lining the blood vessel walls, there is a finite probability that a bond (or tether) will form between the receptor (P-selectin) and ligand (PSGL-1). When a tether forms, the cells will begin to roll along the wall of the vessel forming and breaking additional bonds stochastically. If the leukocyte does not arrest and transmigrate through the wall, then it will eventually release back into the blood stream.

experimental measurements and estimates for affinity and dissociation constants, on- and off-rate constants for reaction kinetics and more recently, force dependent rate constants of specific selectin-ligand interactions [163]. Past studies have included optical tweezer measurements [164], atomic force microscopy (AFM) [165] and flow chambers [166, 167, 168]. The latter is widely used due to simplicity and the ability to replicate hydrodynamic conditions found in nature. Additionally, the discovery of flow enhanced cell adhesion [169] motivates the use of flow chambers to vary the hydrodynamic drag on particles through shear rate in ways that the other methods cannot, despite the fact that it is an inherently two-dimensional technique. Here, we demonstrate the use of a three-dimensional, near-wall measurement technique incorporated into a flow chamber system to measure particle/cell dynamics and tethering events.
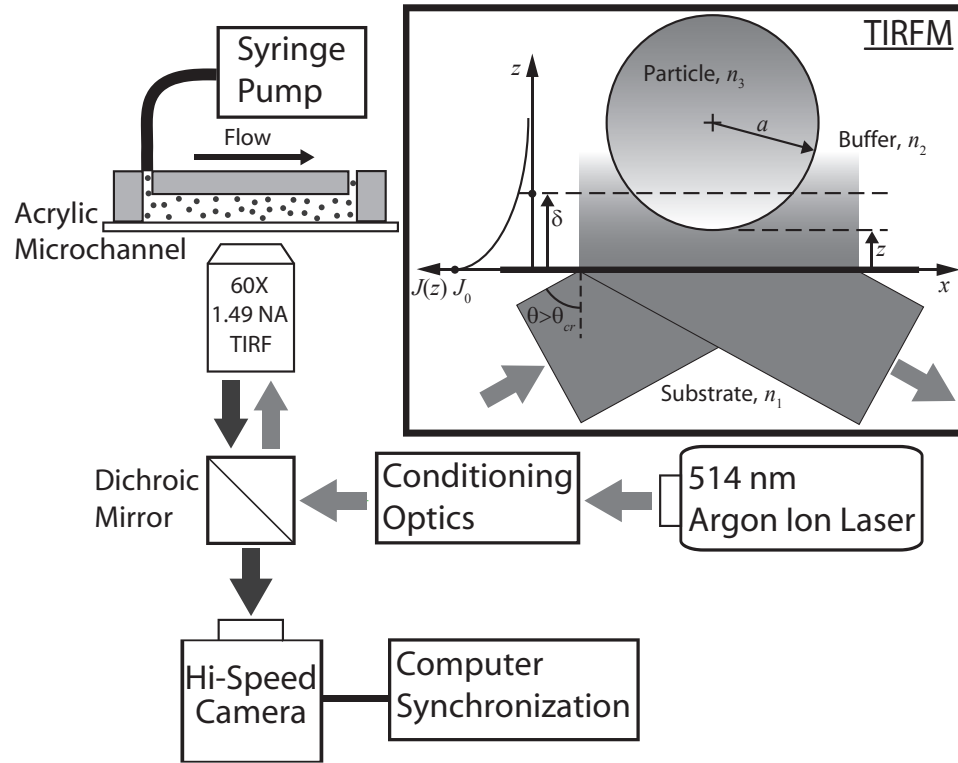
Figure 8.2: Schematic of the experimental setup and TIRF imaging system built around an inverted microscope for measuring near-wall colloidal particle motion.

The highly sensitive imaging method that we use to make these measurements is known as evanescent wave illumination, or in combination with fluorescence microscopy, is referred to as total internal reflection fluorescence (TIRF) microscopy. When an electromagnetic wave is incident upon a dielectric interface with indices n_1 and n_2, at an angle, θ, greater than the critical angle, $\theta_{cr} = \sin^{-1}(n_2/n_1)$, total internal reflection occurs (figure 8.2). An intensity field, $J(z)$, exists in the lower index medium, which exponentially decays normal to the interface described by

$$J(z) = J_0 e^{-z/d}, \tag{8.1}$$

$$d = \frac{\lambda_0}{4\pi} \left[n_1^2 \sin^2\theta - n_2^2 \right]^{-1/2}, \tag{8.2}$$

where z is the optical axis, J_0 is the intensity at the interface, d is the penetration depth and λ_0 is the excitation wavelength [36]. The localized illumination combined with fluorescence detection results in extremely high signal-to-noise-ratio images within about 200 nm of the interface. Furthermore, the emission intensities of particles decrease monotonically away from the interface, and this can be used to map a particle's intensity to distance [51, 43, 41]. Recently, applications of particle tracking within the evanescent field have included the characterization of electro-osmotic flows [40], slip flows [41, 42], hindered diffusion [37, 43, 44] and quantum dot tracer particles [9, 10].

In this study, we take advantage of the well developed flow chamber techniques for specific protein binding measurements and combine it with the three-dimensional sensitivity of TIRF microscopy. In what follows, we describe the microfluidic system and optical measurement technique. The details of particle image calibration and three-dimensional tracking are outlined. Finally, we present results from tracking a single particle in the presence of adhesion proteins to describe capture, rolling and release events, and we make recommendations for future work.

8.2   EXPERIMENTAL METHODS

8.2.1   Microfluidics and Protein Adsorption

An acrylic microchannel (GlycoTech Parallel Plate Flow Chamber) with a 5 mm wide and 254 μm high cross-section was vacuum sealed via a rubber gasket to a 170 μm thick cover glass, which serves as the lower wall of the microchannel and the adhesion surface. The flow was driven by a syringe pump (Harvard Apparatus) at a flow rates up to 1.0 mL/min $\pm$ 0.0035% corresponding to wall shear rates of up to 310 s^{-1}, which are physiologically

typical. Fluorescent (red), polystyrene particles (Spherotech) with a mean radius, a, of 3 μm were conjugated with P-selectin. PSGL-1 was adsorbed to the glass substrate at a concentration between 0.1-10 μg/mL. The substrate was subsequently blocked with casein and incubated overnight in a 1% Tween buffer, which helps to prevent non-specific binding events. Flow assays were performed in an aqueous buffered solution (HBSS) with 1% Tween and 2 mM calcium chloride.

8.2.2 Particle Imaging and Tracking

A schematic of the experimental setup is shown in figure 8.2. Near-wall tracer particle images were captured using an objective-based TIRF microscopy imaging system. The system was built around a Nikon Eclipse TE2000-U inverted fluorescence microscope with the 514 nm line of an Argon-ion CW laser (Coherent) as the excitation source and an evanescent wave penetration depth, d, of about 200 nm. Objective-based TIRFM requires a high numerical aperture, NA, objective to achieve an incident angle greater than the critical angle of the fluid-solid interface of the microchannel. For this purpose, we used a CFI Apochromat TIRF 60× 1.49 NA oil immersion objective. Fluorescence images of the particles were captured with a high-speed camera (Photron, Ultima APX-RS) capable of 3,000 fps with 10-bit, full resolution (1,024 × 1,024) and a pixel size of 17 μm. Frame rates of 250-500 fps were sufficient to capture the particle dynamics with exposure times, t_e, ranging from 0.5-1.0 ms and an effective pixel size of 283 nm at 60×.

The emission intensities of small tracer particles with diameters well below the diffraction limit are known to closely follow the local evanescent field intensity [43, 41]. The 6 μm diameter particles used in this study are far above this limit, and frustration of the evanescent field [170] by the dielectric particle can excite fluorophores well beyond the evanescent
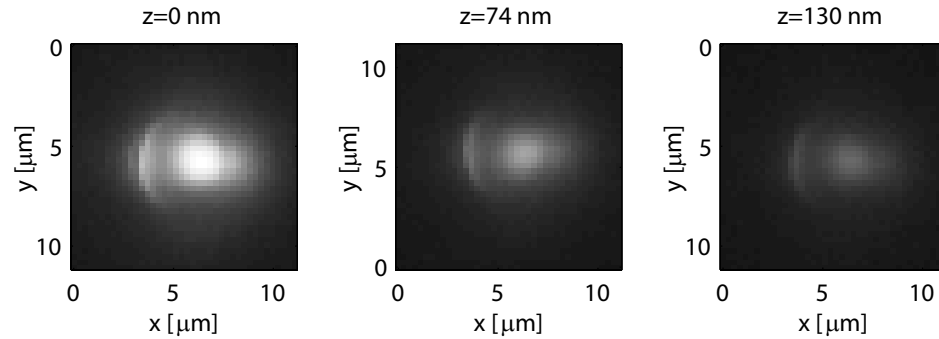
Figure 8.3: Characteristic images of a 6 μm particle at varying distance from a glass-buffer interface created by frustration of the evanescent wave by the fluorescent, dielectric particle.

field, several microns from the interface. This effect produces radially asymmetric particle images, which also decrease in intensity with distance from the wall, as shown in figure 8.3. To quantify the particle fluorescence intensity as a function of distance from the interface, a single 6 μm diameter particle was attached to the tip of an opaque micropipette connected to a one-dimensional nano-precision stage (Mad City Labs). The particle was traversed perpendicular to the coated glass-buffer interface into and then out of the evanescent field in steps of 20 nm ± 1 nm, while imaging the particle intensity. The form of the integrated particle intensity, I, was assumed to also vary exponentially with distance from the surface given by

$$I\left(z\right) = A + I_0 e^{-z/\delta},\tag{8.3}$$

where A is a constant background intensity and I_0 is the particle intensity when touching the wall. A fit of equation (8.3) (shown in figure 8.4) yielded a decay length of $\delta = 204$ nm, which is nearly identical to the evanescent field penetration depth measured independently. Each point represents the mean over 50 images and the intensity variance is due to both thermal motion of the particle and stage noise. These finding are supported by similar
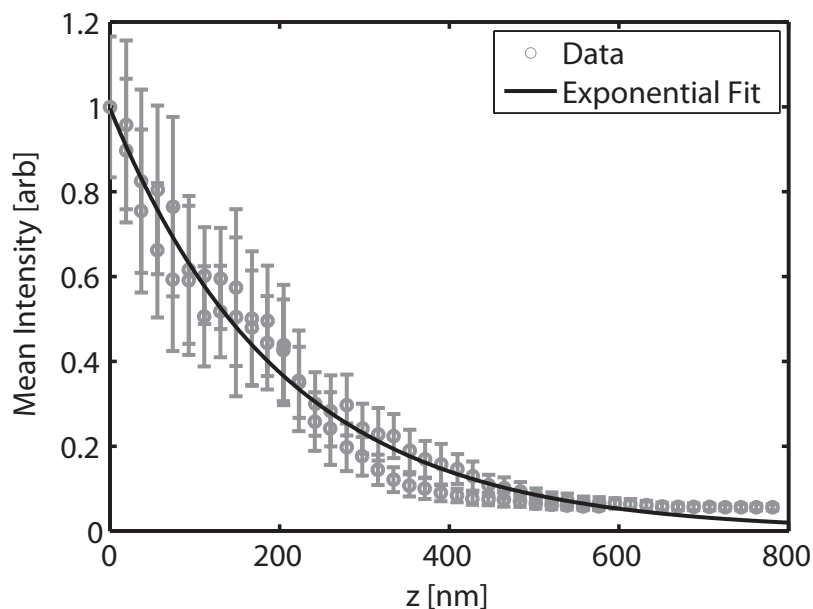
Figure 8.4: Mean, integrated fluorescence emission intensity from a single 6 μm diameter particle as a function of distance from the glass-buffer interface. The particle was held on the tip of an opaque micropipette controlled by a nano-precision stage.

experimental and computational results for the scattering intensity of similar-sized particles in an evanescent field [51, 75], where the scattering intensity decay was also found to follow the exponential decay of the evanescent field.

Particle locations were coarsely identified by intensity thresholding and matched to new positions in subsequent images by a nearest neighbor search. Given the oddly shaped, asymmetric particle images, a cross-correlation tracking algorithm was then used to refine the particle locations [54]. Gaussian fitting to the peak of the correlation map yielded an accuracy of about 0.1 pixels (28.3 nm) in the wall parallel directions, x and y. The local pixel intensity was integrated over each particle and normalized by the Gaussian shape of the illuminating beam as measured by an aqueous solution of Rhodamine B dye. Finally, the relative particle position in the wall-normal direction, z, was computed by inverting equation (8.3), where I_0 is given by the largest intensity of a given particle along it's trajectory (i.e.

closest position to the wall). The resolution in the wall-normal direction is estimated to be on the order of 10 nm by comparison to the intensity variation due to particle diffusion, laser fluctuation and camera noise. Additional uncertainty can result from non-uniformity in the cover slip, non-uniformity in surface coating thickness and illumination light intensity variation over the field of view.

8.3 RESULTS

8.3.1 Wall-parallel Particle Motion

Particle trajectories were tracked in the wall-parallel directions, x and y, using the correlation-based algorithm described in section 8.2.2. Here we present results for a single particle. As is typical in flow chamber based assays, tethering can be detected by arresting events in the particle's in-plane motion. Figure 8.5a shows a segment of such a trajectory, where the plateaus signal that the particle is arrested. The instantaneous particle displacements (figure 8.5b) show much more detail of this process. There are distinctly different features amongst the various binding events as indicated by the position fluctuations in the plateaus. This likely indicates the strength of an arresting event due to variations in the number of tethers that combat the Brownian motion. Although we have demonstrated this technique for a single particle here, from statistical averaging of such measurements, reaction rate constants for off-times can be computed by binning the lengths of the arresting times [163]. Furthermore, a histogram of the particle displacements shows a strongly bimodal distribution (figure 8.6), where the system transitions stochastically between the free and tethered states. There is also evidence of a third, intermediate mode that may indicate a steady rolling velocity around $\Delta x = 100$ nm.
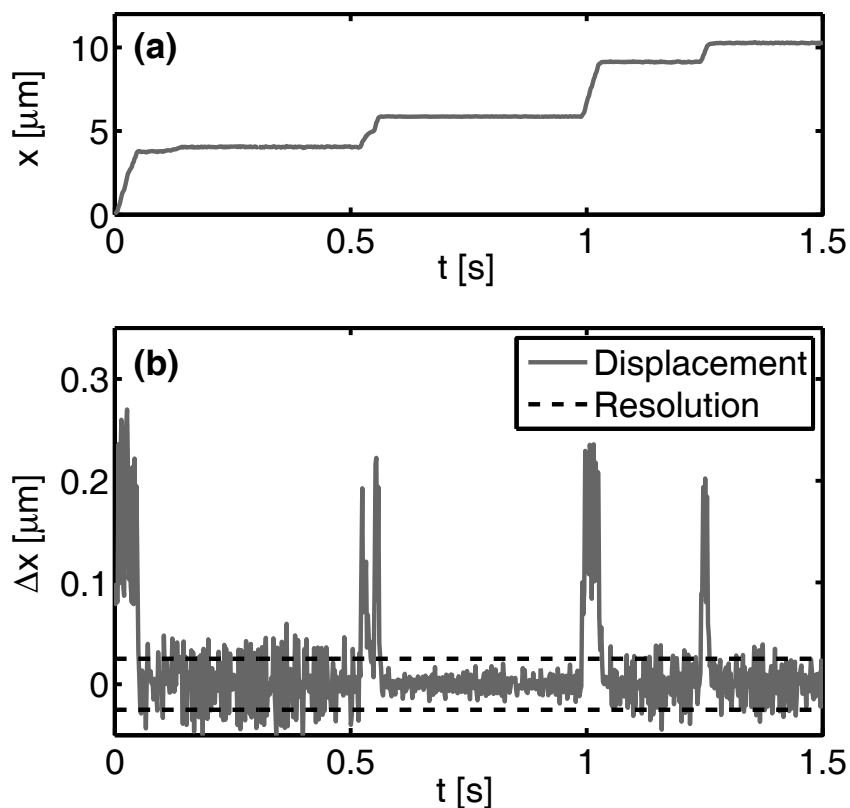
Figure 8.5: Time trace of the wall-parallel motion in the flow direction for a single parti-
cle, illustrating the tethering dynamics near the substrate: (a) particle trajectory and (b)
particle displacement

8.3.2   Wall-normal Particle Motion

Particle motion in the wall-normal direction, z, tends to be more complex than the wall

parallel case as shown for a segment of a single particle trajectory in figure 8.7. Tethering

events are clearly visible in the wall-normal trajectory by sharp transitions between plateau

regions, especially in comparison to figure 8.5. The plateaus correspond to times when

the particle is temporarily arrested by a tether. As in the wall parallel trajectory, each

plateau has a different variance due to Brownian fluctuations, which likely corresponds to

the number of tethers arresting the particle. The statistical variation of the particle's height
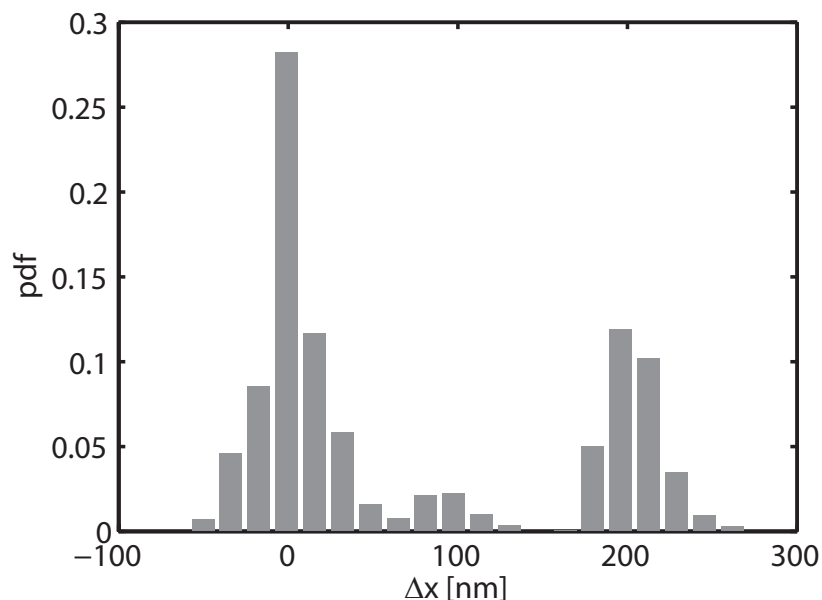
Figure 8.6: A histogram of the wall-parallel particle displacements for the trajectory of a typical particle. The bimodal nature of the histogram demonstrates the fraction of time that the particle is tethered versus free.

during tethering events contains additional information about the tether stiffness, which may also be examined. The dashed line in figure 8.7 corresponds to the longest possible bond length of about 92 nm. Since the particle motion is within this range, tethered particles in shear are likely bending tethers toward the wall. Finally, the general trend of decreasing particle distance to the surface with time (or more appropriately x-position) is due to variation of the illumination light intensity across the beam spot. This effect was diminished by rescaling the particle intensity by the local mean evanescent field intensity. However, the frustration of light into the particle further complicates the particle intensity normalization, and thus our simple intensity calibration does not completely compensate for this variation. Improvements to the calibration method should alleviate this problem.
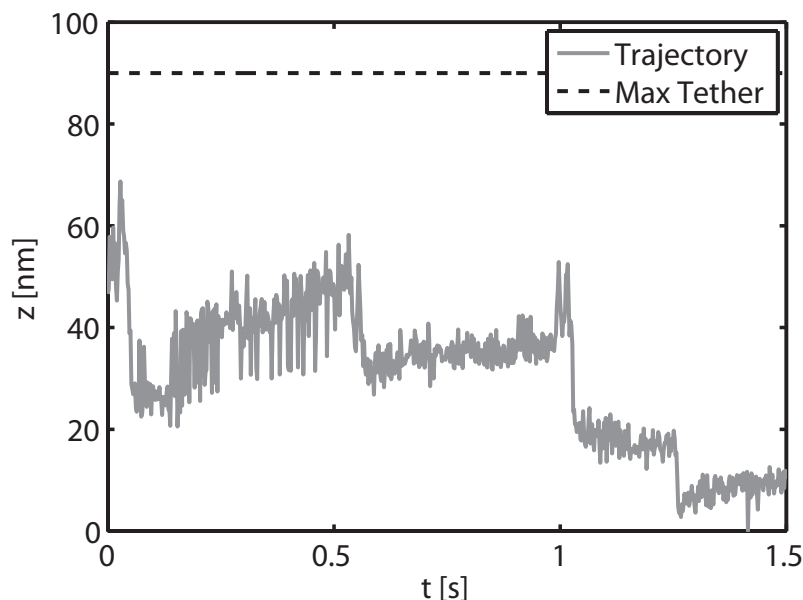
Figure 8.7: Time trace of the vertical position for a single particle, where the transitions between tethered and free states are clearly detectable by jumps in the wall-normal position, z, (interpreted from the particle intensity) as compared to the horizontal displacements. The dashed line shows the typical maximum bond length of about 92 nm for the P-selectin/PSGL-1 system.

8.4 CONCLUDING REMARKS

We have presented results demonstrating the use of a three-dimensional total internal reflection fluorescence (TIRF) imaging technique applied to measure the adhesion dynamics of particles in flow chambers. The adhesion and rolling of leukocytes along the vascular endothelium perform an important function for initiating immune system responses. It is of great importance to understand the dynamics of this process from both a fluid mechanics and chemical kinetics point of view. We have shown that, like much smaller diffraction limited fluorescent particles, larger 6 μm particles also follow the monotonically decreasing intensity of the evanescent field. With this information, we have demonstrated that it is possible to accurately measure the three-dimensional displacements of such particles in real

time. Although we have focussed on the trajectory of a single particle to demonstrate this technique, by applying statistical analyses to the observed fluctuations and trajectories of many particle realizations, information about force-dependent tethering on- and off-rates may be decoded.

ACKNOWLEDGMENT

Chapter 9

Visualization and tracking of electrospray droplet emissions using fluorescence and holographic techniques

A.N. Zorzos, J.S. Guasto and K.S. Breuer. In preparation for *Journal of Colloid and Interface Science*, 2008.

We report results on the optical characterization of electrospray droplets emitted from a Taylor cone. Individual droplets are imaged and tracked using fluorescence microscopy with a statistical particle tracking velocimetry (SPTV) algorithm. Droplet diameters were measured between 1.5 to 2.5 µm for flow rates ranging from 15 to 25 nL/s. Droplet velocities over 40 m/s were observed from the analysis of double-exposure, fluorescence images. The tip stream instability and evolution of the spray divergence were observed for droplet emission

frequencies over 3.5 MHz. Additionally, we demonstrate the use of holographic microscopy to examine three-dimensional electrospray droplet structures and measure droplet diameters.

9.1   INTRODUCTION

Electrospray atomization produces mono-disperse droplets from charged liquid at high velocities and has applications in space propulsion [86, 87, 88, 89], mass spectrometry [90], aerosol science [91], and combustion technology [92]. To produce an electrospray, a Taylor cone is formed in an electric field by the free surface of conducting fluid contained at the end of a capillary tube. A liquid jet emanates from the apex of the Taylor cone, eventually necking into droplets due to surface tension. The like-charged droplets exert a Coulombic repulsive force, causing the linear droplet stream to diverge into a spray. Cloupeau and Prunet-Foch have classified various operating modes of electrosprays [93, 94], but in this study, we are only concerned with the stable cone-jet mode [95, 96].

Several studies have been conducted to characterize different aspects of both the Taylor cone and its emissions. Ganan-Calvo studied droplet size and velocity dependence on axial and radial position [97]. Later, they examined emission current and droplet size for various fluids and conductivities using phase Doppler anemometry (PDA) and developed scaling laws [98]. Cloupeau and Prunet-Foch used a laser granulometer to measure droplet diameter and emission frequency [96]. Tang and Gomez also used a PDA to study droplet size, axial velocity, droplet concentration and field strengths. Additionally, they quantified the relative importance of the external field and the Coulomb interaction among the charged droplets [99]. Gamero-Castano and Hruby used time-of-flight and energy analysis techniques to measure the voltage difference, velocity, and natural wavelength for varicose breakup of the jet [86]. However, their study was inconclusive in determining if the droplet diameter scaling

with flow rate is of the Ganan-Calvo form [98] or Fernandez de la Mora [100]. Fernandez de la Mora presented results on the current and droplet size emitted from highly conducting Taylor cones, and put forth scaling laws for both current and droplet size relative to flow rate [101]. de Juan and Fernandez de la Mora investigated droplet charge and diameter using a differential mobility analyzer (DMA) [100] and showed that the diameter distribution of the primary droplets has a full width at half maximum between 20 and 30 percent of the mean.

We are interested in the size distribution, structure and dynamic behavior of the emitted droplets in relation to flow rate. The study presented here is unique, since we utilize fluorescence microscopy as the primary droplet detection method and develop digital in-line holographic microscopy for three-dimensional measurements of electrospray size and structure. Image processing techniques were used to directly extract droplet size and velocity from images of droplets. We analyze the dynamic behavior and evolution of the droplets in space, as well as their size, and compare our results with existing theoretical and experimental findings.

Holographic image reconstruction has been used to measure the position, size and motion of micron-sized particles suspended in both fluids and solids [102, 103, 104]. In in-line holographic microscopy, coherent laser light is scattered by an object (electrospray droplets), which interferes with the unperturbed laser light (reference beam) creating a hologram, $I_h(x,y)$, on a CCD detector. The field, $f(x,y;z_i)$, at any plane, z_i, is mathematically reconstructed through a convolution of the hologram intensity with a spherical wave diffraction kernel, $h(x,y;z_i)$,

$$f(x,y;z_i) = I_h(x,y) \otimes h(x,y;z_i). \tag{9.1}$$

The spherical wave diffraction kernel is described by

$$h\left(x, y; z_i\right) = \frac{\exp\left[jk\left(x^2 + y^2 + z_i^2\right)^{1/2}\right]}{\left(x^2 + y^2 + z_i^2\right)^{1/2}},$$ (9.2)

where k is the propagation constant given by $k = 2\pi/\lambda$ and λ is the wavelength of the illuminating light [104]. In practice, the convolution is computed in Fourier space using the two-dimensional fast Fourier transform (FFT). The intensity distribution at the z_i plane is then given by

$$I_p\left(x, y; z_i\right) = f\left(x, y; z_i\right) f\left(x, y; z_i\right)^*,$$ (9.3)

where $*$ denotes the complex conjugate. Once the intensity volume is reconstructed, particles are located by searching for dark regions within the volume.

9.2 MATERIALS AND METHODS

Electrosprays were generated using a tapered, silica capillary (New Objective) as an emitter, which was distal coated, with inner and outer diameters of 100 μm and 360 μm, respectively. The working fluid was isopropanol doped with 0.013% rhodamine B by mass for fluorescence imaging purposes, which had a measured conductivity of 2 μS/cm. The fluid was contained in a pressurized reservoir that provided flow rates on the order of nanoliters per second. Flow rates were measured by tracking the position of a gas bubble in the capillary tube through time as shown in figure 9.1. A square, metal wire screen was used as the extractor with a mesh spacing of 703 μm and wire diameter of 355 μm. The extractor was 1 cm square and orthogonally oriented to the emitter at 1.5 cm downstream. A voltage difference of $\sim$4.2 kV was maintained between the emitter and grounded extractor to generate the high electric field necessary to form a Taylor cone. The external electric field between the emitter and

extractor was estimated using COMSOL. All experiments were performed at atmospheric pressure and ambient temperature. The flow rate due to evaporation from the capillary was measured independently and determined to be negligible compared to the electrospray flow rate.

Fluorescence imaging of single droplets was accomplished using a 532 nm Twin Nd:Yag laser (Quantel) capable of delivering two 5 ns, 150 mJ laser pulses with arbitrary time separation. The beam was attenuated by two orders of magnitude and focussed to a ∼150 μm diffraction limited spot in the spray also shown in figure 9.1. Fluorescence images were collected using a 50X, 0.55 NA objective with an intensified CCD (ICCD) camera capable of recording 1360×1036 pixel 12-bit images and a long pass filtered over 575 nm for the rhodamine fluorescence. For in-line holography, the collimated laser beam is further attenuated and directed through the electrospray directly into an identical CCD camera with no intensifier.

For accurate droplet size measurements, it is necessary to account for distortion due to the diffraction limit. The diffraction limited spot size of a an imaging system is given by [171, 150]

$$d_s = 2.44(M + 1)f^{\#}\lambda, \tag{9.4}$$

where M is the objective magnification, $f^{\#}$ is the f-number, and λ is the fluorescence emission wavelength, ∼575 nm. For our system, the diffraction limited spot size was ∼400 nm. The measured droplet diameter, d_e, is given by [150]

$$d_e^2 = d_s^2 + M^2 d_p^2, \tag{9.5}$$

where d_p is the actual droplet diameter. For droplets on the order of 2 μm in diameter, the
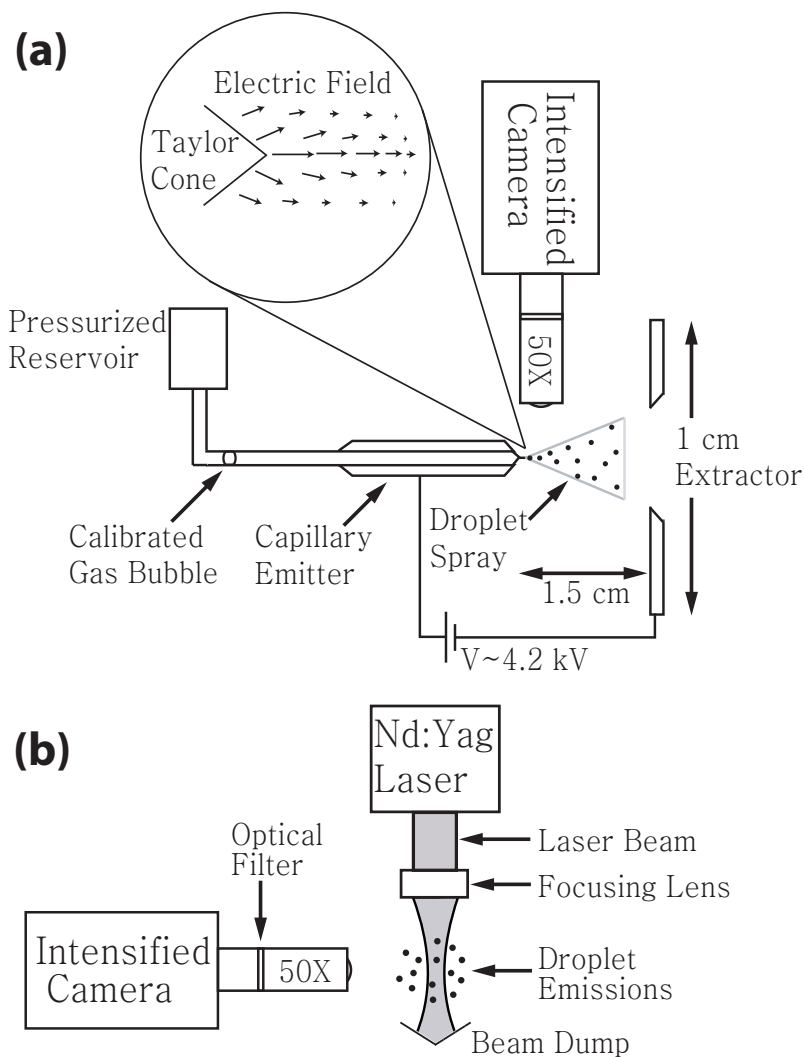
Figure 9.1: (a) Schematic of the electrospray generation system. Nanoliter per second flow rates were measured by tracking a gas bubble in the capillary tube. The voltage difference between the emitter and extractor was ∼4.2 kV, and the external electric field was estimated using COMSOL. (b) Fluorescence microscopy imaging system. The fluid was doped with rhodamine B and excited using a double pulsed Nd:Yag with 532 nm emission wavelength and 150 mJ, 5 ns pulses. The beam was focussed to a 150 μm spot in the spray and fluorescence images were collected using a 50X objective with an intensified CCD (ICCD) camera. For in-line holography, the collimated laser beam is directed through the electrospray directly into the camera.

95 μm

Figure 9.2: A single-exposure fluorescence image of the electrospray droplets.

error in particle size measurement introduced by the diffraction limit is less than 5%.

9.3   RESULTS AND DISCUSSION

9.3.1   Droplet Size

A single, 5 ns laser pulse during the ICCD camera exposure produces a single-exposure image as shown in figure 9.2. The droplet locations are determined by intensity thresholding the image and fitting a 2-D Gaussian function to the intensity profile. A probability density function (PDF) of the measured droplet diameter at a flow rate of 20 nL/s is shown in figure 9.3. The following analysis explains the skewed nature of this distribution and provides an argument for characterizing it by a Rician distribution.

Given the relatively large capillary number ($Ca \sim 5$) of the liquid jet, let us assume that the cross-sectional jet shape can vary independently in the horizontal and vertical dimensions, X and Y respectively. If X and Y are Gaussian random variables with mean R and standard deviation σ, the PDF of interest is $Z = \left(X^2 + Y^2\right)^{\frac{1}{2}}$. The cumulative
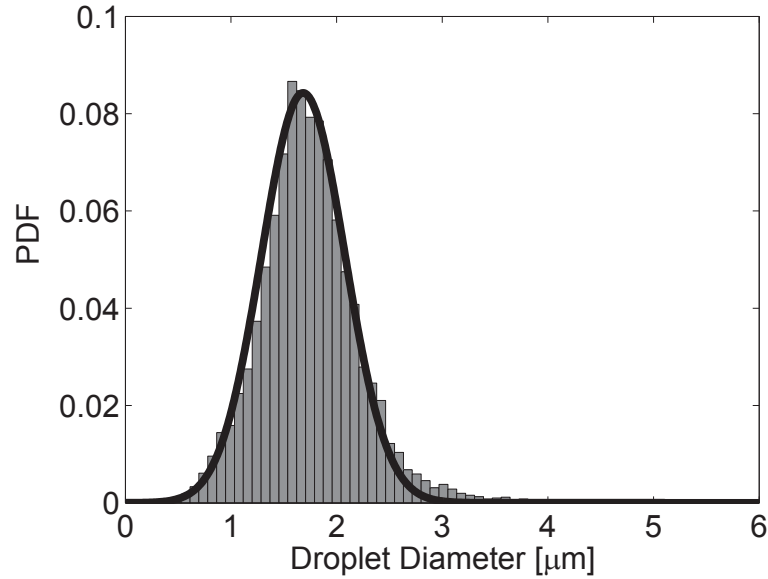
Figure 9.3: Measured droplet diameter distribution (PDF) at 20.0 nL/s demonstrates characteristics of a Rician distribution

distribution function of Z is given by

$$F(z) = \frac{1}{2\pi\sigma^2} \int\!\!\int_{(x^2+y^2)^{\frac{1}{2}} \leq z} \exp\left[-\frac{1}{2}\left(\left[\frac{x-R}{\sigma}\right]^2 + \left[\frac{y-R}{\sigma}\right]^2\right)\right] dx\,dy. \qquad (9.6)$$

Under transformation to polar coordinates, this becomes

$$F(z) = \frac{e^{-\frac{R^2}{\sigma^2}}}{\sigma^2} \int_0^z re^{-\frac{1}{2}\left[\frac{r}{\sigma}\right]^2} I_0\left(\frac{zR\sqrt{2}}{\sigma^2}\right) dr. \qquad (9.7)$$

I_0 is a zero-order, modified Bessel function of the first kind, and is given by

$$I_0 = \frac{1}{2\pi} \int_0^{2\pi} e^{x\cos\theta} d\theta. \qquad (9.8)$$

It is well established that the ratio of droplet diameter to jet diameter is $g \approx 1.9$ [99]. Differentiating equation (9.7) with respect to z and accounting for the aforementioned

ratio, g, the droplet diameter distribution is

$$f(z) = \frac{gz}{\sigma^2} \exp\left[-\frac{1}{2}\left(\frac{2R^2 + g^2 z^2}{\sigma^2}\right)\right] I_0 \left(\frac{gzR\sqrt{2}}{\sigma^2}\right). \tag{9.9}$$

This equation is nearly a Rician distribution [172], with the exception of the $\sqrt{2}$ in I_0 as well as the factor of g throughout. A least-squares fit of equation (9.9) to the measured droplet diameter distribution yields $g = 1.908$, which is in good agreement with the literature, and is shown in figure 9.3.

Figure 9.4 shows average droplet size for a range of flow rates plotted against the scaling laws of both Fernandez de la Mora [100] and Ganan-Calvo [98], given by

$$d = G(\varepsilon)\left[\frac{\varepsilon\varepsilon_0 Q}{K}\right]^{\frac{1}{3}}, \tag{9.10}$$

and

$$\frac{d}{d_0} = A\left[\frac{Q}{Q_0}\right]^{\frac{1}{2}} - B, \tag{9.11}$$

respectively, where d is the droplet diameter, ε is the dielectric constant of the liquid, ε_0 is the vacuum permittivity, G is a constant dependent on the dielectric constant of the liquid, Q is the flow rate, K is the liquid conductivity, d_0 is a scaling parameter for droplet diameter and Q_0 is a scaling parameter for flow rate. A and B in equation (9.11) are free parameters that Ganan-Calvo fit to experimental findings, instead of the theoretical derivation of

$$\frac{d}{d_0} \sim \left[\frac{Q}{Q_0}\right]^{\frac{1}{2}}. \tag{9.12}$$

The liquid used satisfies the scaling law conditions presented in [98], namely that equation (9.11) only applies to liquids with sufficiently low viscosity and conductivity. Ganan-Calvo
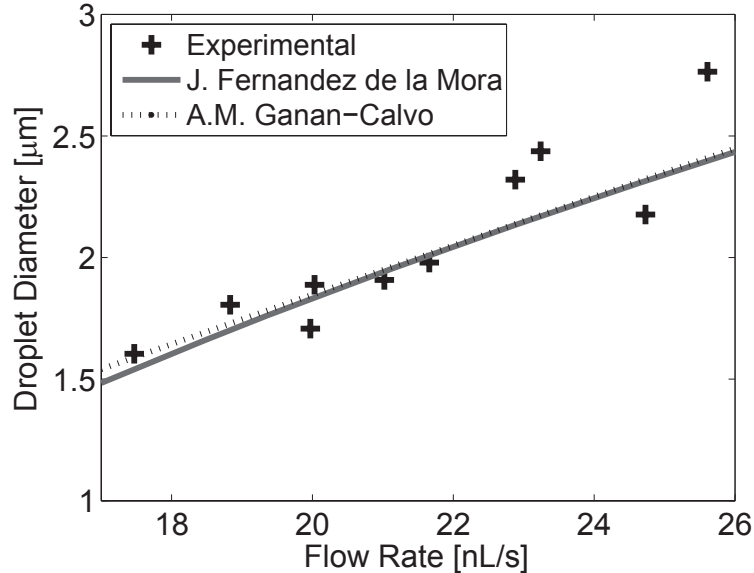
Figure 9.4: Average droplet size for various flow rates plotted against the scaling laws of both Fernandez de la Mora [100] and Ganan-Calvo [98].

[98] found experimentally that $A = 1.2$ and $B = 0.3$. A fit to the Ganan-Calvo scaling law for our results gave $A = 19.1$ and $B = 4.7$ (figure 9.4). However, given the narrow range of flow rates and freedom in choosing A and B, no definitive conclusion was made in comparing the Fernandez de la Mora and Ganan-Calvo scaling laws. The constant, G, in the former scaling law was found to be 1.26.

9.3.2 Droplet Trajectories

Particle image velocimetry (PIV) and particle tracking velocimetry (PTV) [150] are well established optical velocity measurement techniques. These methods, at their simplest level, estimate the motion of fluid by tracking the position of particles in time as estimated from a sequence of images or multiple exposures on a single image. Due to the extremely high velocities and small length scales, we take advantage of double-exposure images to track droplets. Two consecutive laser pulses are used to illuminate the electrospray droplets,

95 μm
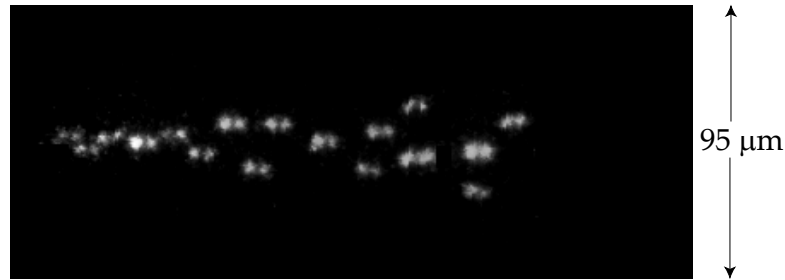
Figure 9.5: A double exposure image, produced by exciting fluorescent droplets with two consecutive pulses separated by 150 ns during one camera frame exposure.

while exposing a single frame of the ICCD camera as shown in figure 9.5. The result is two

superimposed droplet images on a single frame. By matching the particles and computing

their displacements, we can compute their trajectories and velocities at an instant in time.

A laser pulse delay time of 150 ns provided sufficient separation between droplet images to

resolve their displacements. However, when the spacing between different droplets is small,

it is difficult (if not impossible) to deterministically match particle image pairs correctly.

To avoid problems associated with mismatched droplet pairs, we instead rely on a proba-

bilistic tracking method based on the statistical particle tracking velocimetry (SPTV) tech-

nique in [10]. The premise is to compute all possible displacements between detected droplet

positions, which includes physical droplet displacements and spurious, mismatched droplet

trackings. When examining the ensemble of all displacements, the mismatched droplet po-

sitions are uncorrelated, and thus can be removed from the ensemble statistically. In [10],

the particles are uniformly distributed throughout the entire field of view. Therefore, the

unphysical trackings yield a random, uniform distribution, which is easily subtracted from

the ensemble. In the present work, the detected droplets are non-uniformly distributed due

to the droplet stream and its divergence. Therefore, our uncorrelated droplet trackings yield

a complex, non-uniform distribution as shown in figure 9.6 for the horizontal and vertical droplet velocity. Note that we have also included the distributions computed from single exposure images. Although they do not yield information about particle velocities, they do tell us something about the shape of the diverging spray. Qualitatively, the peak of the double exposure distribution corresponds to the mean velocity and the width to the standard deviation. In the single exposure distributions, the peak corresponds to the mean droplet spacing and the peak width of the vertical displacements to the spray divergence.

To quantify the complex velocity distributions produced by this tracking method, we simulate droplet positions and displacements using a simple Monte-Carlo method based on parameters such as the mean particle spacing, mean velocity and divergence angle with relative uncertainties. Next, the simulated droplet positions are tracked using the same algorithm above to produce simulated velocity distributions as shown in figure 9.6. The parameterized shapes of the simulated distributions are then optimized to the experimental distributions by varying the Monte-Carlo simulation parameters.

The steps used to simulate the emissions are as follows: (1) generate droplets with a predefined spacing, (2) define a divergence angle, (3) generate uncertainty in the droplet horizontal and vertical positions, (4) generate displaced droplets according to the mean velocity, and (5) generate uncertainty in the displaced droplet positions. To optimize the simulated velocity distribution to the experimental distribution, we first parameter-ize them. Specifically, we use the double-exposure horizontal distribution peak position and height, the single-exposure horizontal distribution peak position and height, the single- and double-exposure horizontal distribution tail slope, the single- and double-exposure horizon-tal distribution height at zero displacement, and the single- and double-exposure vertical distribution height at zero displacement. This allows for quantitative evaluation of the dif-
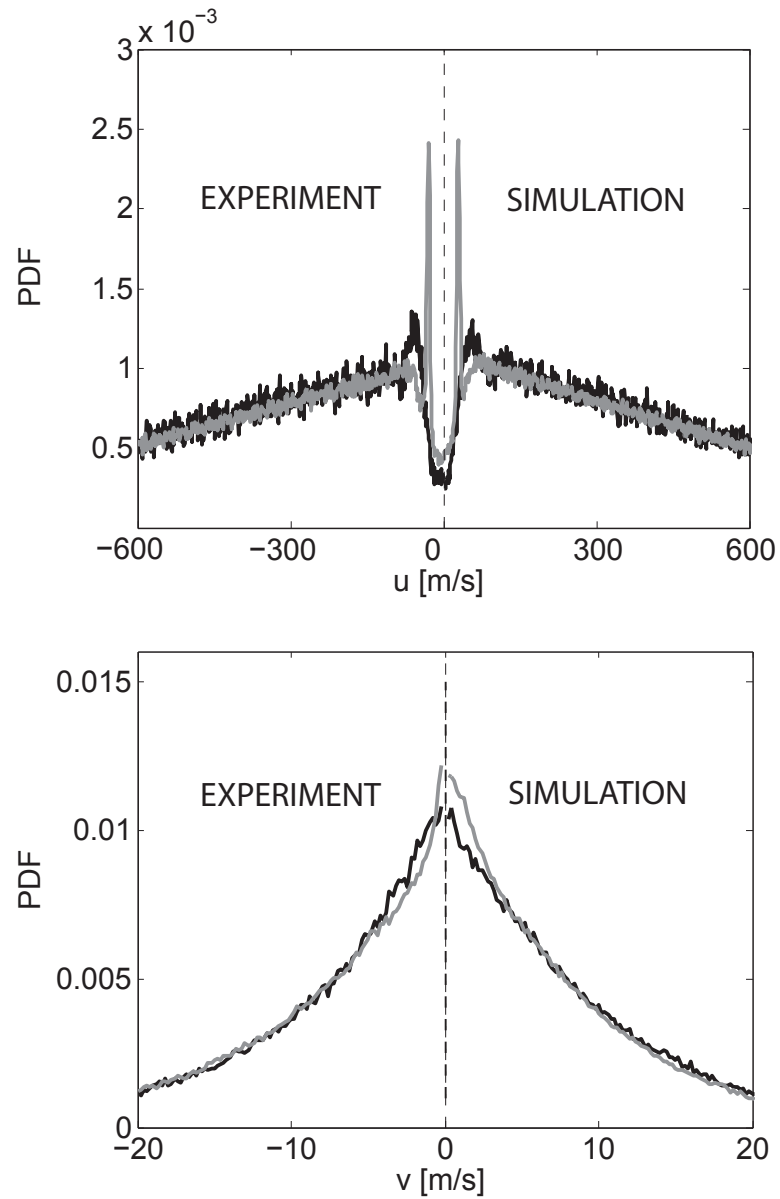
Figure 9.6: Ensemble velocity distributions for the horizontal and vertical components of droplet motion with both single- and double-exposure images. Experimental results are shown on the left and simulation results on the right. Since the distributions are symmetric, there is no loss of generality.

ference between the simulated distribution and the experimental. Using a custom written optimization code, we adjust the set of simulation parameters to minimize this difference for both the horizontal and vertical components as shown in figure 9.6. The optimization parameters in this case were a droplet spacing of 9.0 ± 3.5 μm, a horizontal velocity of 36.7 ± 3.3 m/s, a divergence angle of 0.06 radians, and a vertical velocity deviation of 4.3 m/s.

Divergence Angle

Droplet dynamics were measured as a function of distance from the Taylor cone apex. The mean divergence angle was computed through the method described above for image segments along the electrospray propagation direction. The evolution of the droplet divergence angle is depicted graphically in figure 9.7 plotted over a composite of 500 superimposed images at a flow rate of $\sim$20 nL/s. This analysis was performed for three different flow rates (20.0, 22.9 and 24.7 nL/s) shown in figure 9.8. There is a decrease in divergence angle with higher flow rates and an increase in divergence angle with distance for all flow rates. The initial droplet divergence instability occurs farther from the cone apex at higher flow rates. The Coulombic repulsive forces between the like-charged droplets cause outward acceleration, and hence, the divergence angle increases.

Droplet Velocity

Using a similar analysis to section 9.3.2, the mean horizontal droplet velocity was also measured as a function of flow rate and distance from the Taylor cone apex, which is shown in figure 9.9. The horizontal velocity increases with flow rate and decreases along the propagation direction at a fixed flow rate. If this decrease in velocity were due to aerodynamic drag, we would expect such an effect over $\sim$10 cm, not 200 μm. But, as
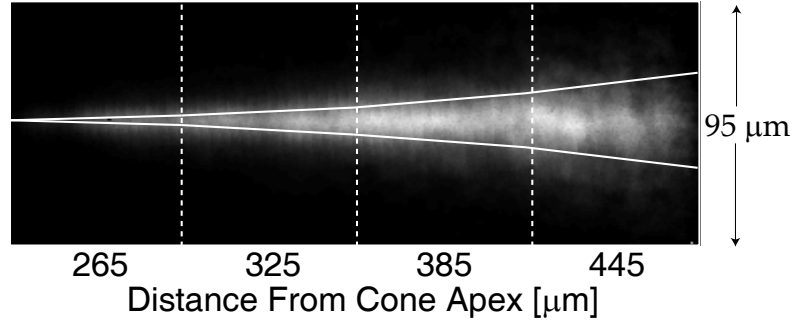
Figure 9.7: A composite image generated by superimposing 500 single-exposure images at a flow rate of 20.0 nL/s. The measured evolution of the divergence angle (solid lines) fits well with the composite image.

the divergence increases, more droplets are located away from the centerline, where the velocities are known to be lower [99].

Since the droplet trajectories are axisymmetric, the mean vertical velocity is zero, so we quantify the vertical velocity by the absolute deviation from zero. Figure 9.10 shows the velocity for varying flow rates and distances from the cone apex. As one would expect, the vertical velocity deviation is highly correlated to the behavior of the divergence angle. The vertical velocity deviation increases with decreasing flow rate and increases with distance from the Taylor cone apex.

Emission Frequency

Given the droplet spacing and horizontal velocity, the emission frequency was directly calculated from

$$D \cdot f = u, \tag{9.13}$$

where D is the droplet spacing, f the emission frequency and u is the horizontal velocity. The breakup (emission) frequency is related to the droplet radius through the scaling
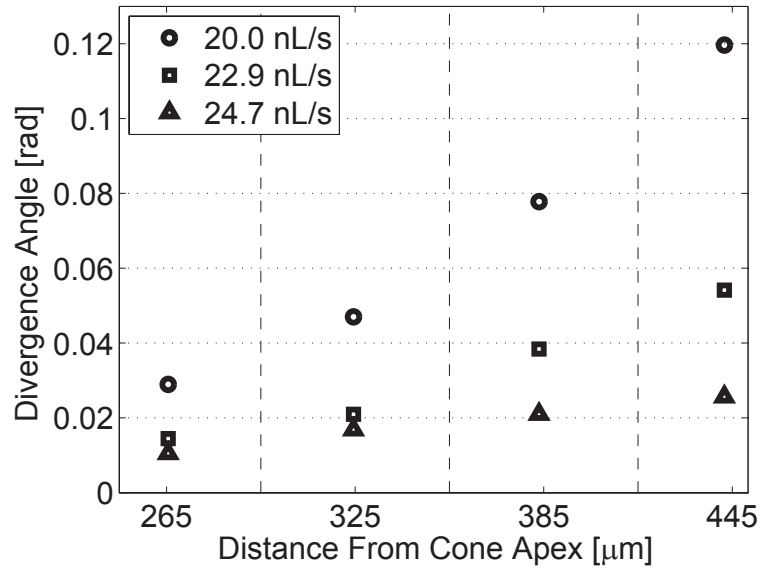
Figure 9.8: Evolution of the divergence angle with distance from the Taylor cone apex for three flow rates.

argument

$$f = \left[\frac{\gamma}{\rho r^3} \right]^{\frac{1}{2}}, \tag{9.14}$$

where γ is the surface tension, ρ is the liquid density and r is the droplet radius [88]. Equation (9.14), in combination with the Fernandez de la Mora scaling law (equation (9.10)), yields the predicted emission frequency as a function of flow rate

$$f = \left[\frac{8\gamma K}{\rho G(\varepsilon)^3 \epsilon \epsilon_0 Q} \right]^{\frac{1}{2}}. \tag{9.15}$$

The experimentally measured emission frequency shows good agreement with equation (9.15) as shown in figure 9.11.
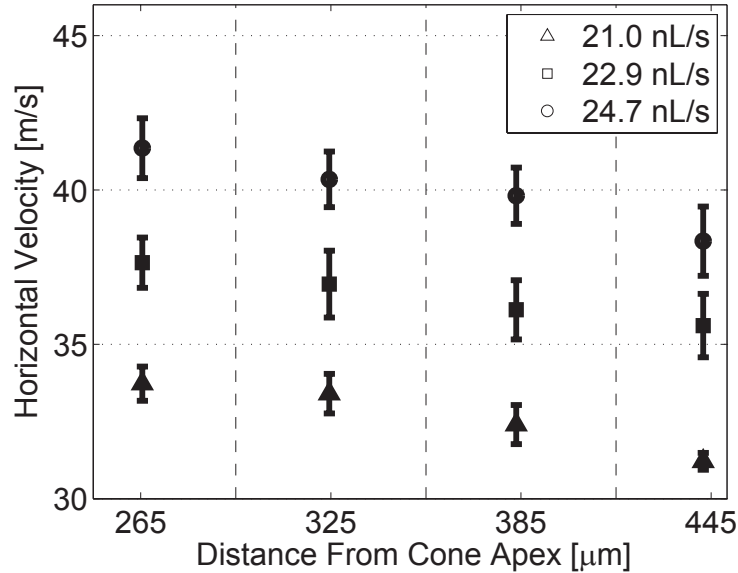
Figure 9.9: Horizontal droplet velocity as a function of distance from the cone apex for three different flow rates, where the error bars represent the standard deviation of the velocity distribution.

9.3.3 Holographic Electrospray Imaging

During this study, we also demonstrated the use of in-line holographic microscopy [102, 103, 104] for the purpose of three-dimensional electrospray droplet characterization. In contrast to the fluorescence studies, droplets were imaged with the CCD camera aligned on the optical axis of the laser and no fluorescence filter. The camera and objective lens were de-focussed from the electrospray by about 75 μm to form an in-line hologram on the CCD. The three-dimensional volume intensity distribution was reconstructed plane-by-plane in the z direction from 60 μm to 90 μm according to equations (9.1-9.3) with a resolution equal to the effective pixel size (0.15 μm). An example hologram reconstruction is shown in figure 9.12 for the linear droplet regime of the electrospray just after jet breakup. The upper image is the original hologram taken at 75 μm out of focus, while the lower image is the mathematical reconstruction at 75 μm from the hologram plane. The electrospray
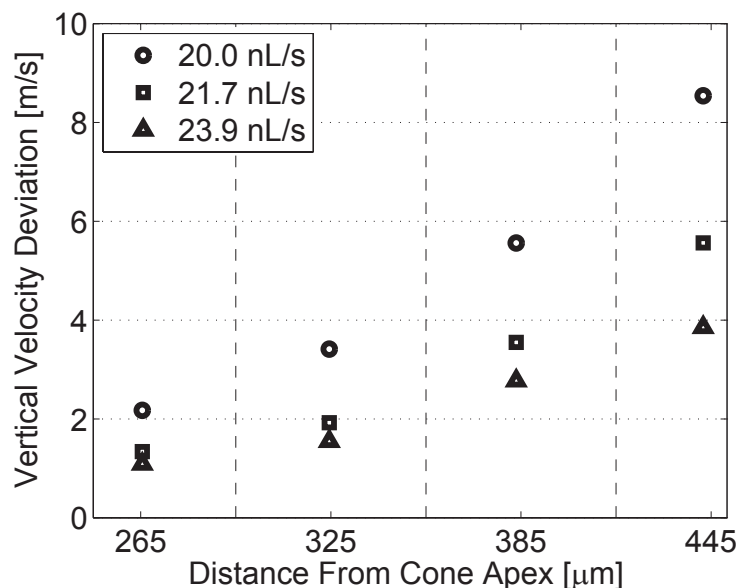
Figure 9.10: Vertical velocity deviation for droplets at varying distances from the cone apex and for different flow rates.

droplets are easily visible as dark spots, where the diameter of the spot is representative of the droplet diameter.

After volumetric reconstruction, particles were identified by thresholding the intensity minima. The sub-pixel droplet center location and diameter were determined by fitting a circular aperture to the image gradient of the in-focus reconstruction in the x-y plane. Further resolution is obtained in locating the particle center along the optical axis, z, by fitting a parabola to the intensity and taking the minimum location. 500 particle diameters were measured with a mean particle diameter of 1.79 ± 0.4 μm.

A sample of the measured three-dimensional droplet structure is shown in figure 9.13, where features like the droplet divergence and satellite droplets were clearly visible. We have demonstrated that holographic reconstruction is a valuable tool for electrospray diagnostics and accurately determines the size and location of droplets in three dimensions from a single hologram. Future work will include tracking the three-dimensional displacements of
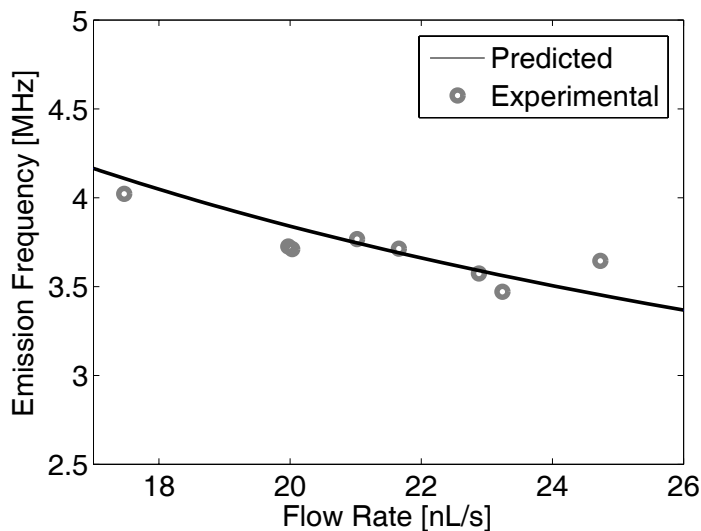
Figure 9.11: Measured emission frequency plotted against the predicted frequency derived using dimensional analysis and the scaling law of Fernandez de la Mora [100].

the droplets to construct a full velocity field of the electrospray.

9.4 CONCLUSIONS

We have demonstrated the ability to image and track individual droplets emitted from a Taylor cone using fluorescence microscopy and in-line holographic microscopy. Droplet size measurements correlated well with the scaling laws of both Fernandez de la Mora [100] and Ganan-Calvo [98]. Droplet size distributions were measured and shown to be nearly Rician and of the form in equation (9.9). Double-exposure images were used to measure the evolution of droplet dynamics with respect to flow rate and downstream position. The onset and subsequent growth of the instability in the linear droplet stream occurs farther from the cone apex at higher flow rates. The divergence angle and vertical velocity deviation increased as a function of distance from the cone apex, which is likely explained by
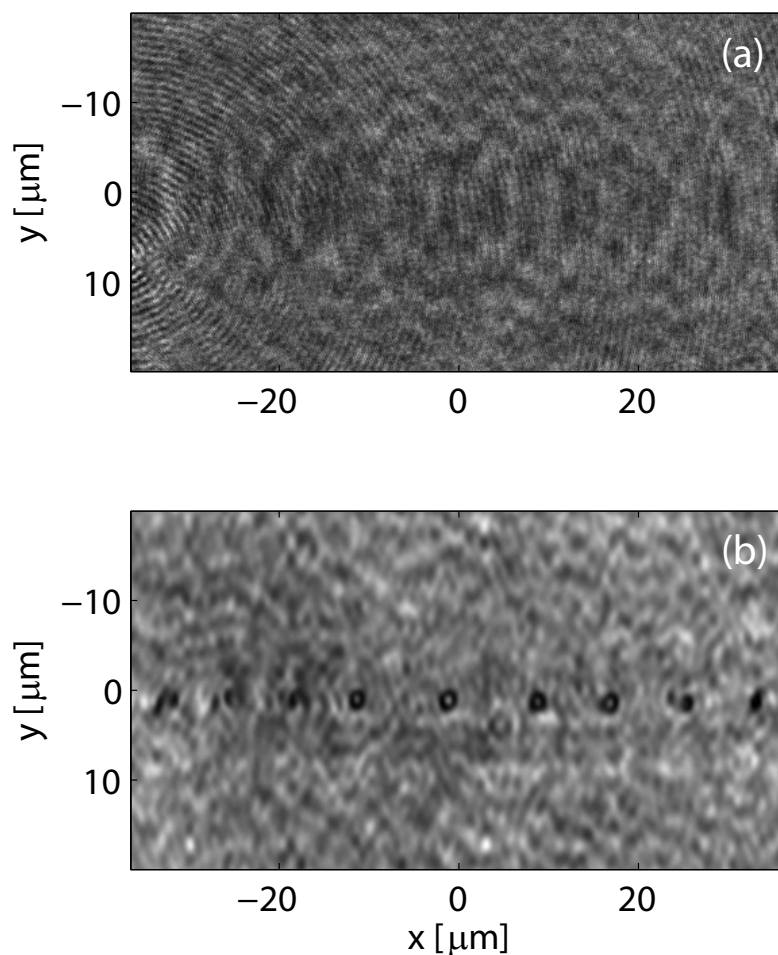
Figure 9.12: Sample holographic reconstruction where (a) is the original hologram image at 75 μm out of focus and (b) is the mathematical image reconstruction at 75 μm from the hologram plane.

the Coulombic repulsive forces between the like-charged droplets. The horizontal velocity decreased as a function of distance from the cone apex, which we conclude is due to the divergence of the spray [99], not aerodynamic drag. The droplet emission frequency of the electrospray was related to flow rate, equation (9.15), using dimensional analysis and scaling [100] and shows good agreement with our experimental results.

Since the measured horizontal velocity in our experiments increased with flow rate, we can argue in favor of the Fernandez de la Mora scaling law [100]. Let the mean jet or droplet
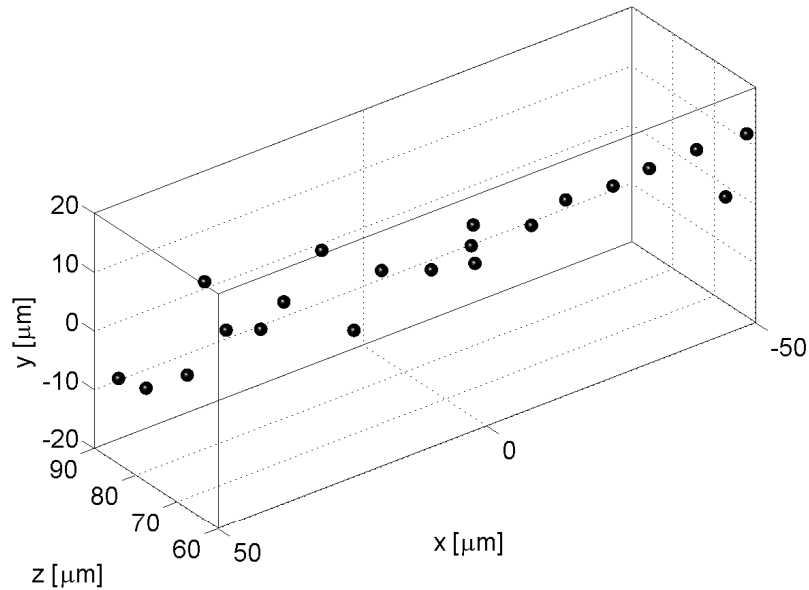
Figure 9.13: Isometric, three-dimensional view of droplets detected near the divergence region of an electrospray using in-line holographic reconstruction. The droplets are traveling in the positive x-direction.

velocity be $v^* = 4Q/\pi d^2$. If we substitute the Fernandez de la Mora scaling law [100], we find that the mean velocity scales as $v^* \propto Q^{\frac{1}{3}}$. However, the scaling law of Ganan-Calvo [98] yields $v^* \propto constant$, which is unphysical. Again, v^* is not an absolute velocity and ignores the external electric field, but we present it to explain the horizontal droplet velocity dependence on flow rate.

Finally, we have demonstrated the use of in-line holographic microscopy for the purpose of three-dimensional electrospray droplet characterization. The volumetric intensity distribution of the droplet region of the electrospray was mathematically reconstructed from a single holographic image. Particle locations were identified in three dimensions and their measured diameters were in good agreement with results from fluorescence imaging. From these measurements, the three-dimensional droplet structure was resolved. Future work will include the application of holography to displacement measurements of the droplets to

construct a three-dimensional velocity field of the electrospray.

ACKNOWLEDGMENT

Chapter 10

Conclusion

Over the past ten years, the fabrication of small scale fluid devices and application of microscopy techniques to fluid mechanics and colloidal dynamics has enabled the detailed investigation of capillary and low Reynolds number flows. As the device dimension shrinks, bulk properties of the fluid medium become less important and understanding interfacial and near-wall fluid-solid interactions become vital. We have examined several different aspects of near-wall colloidal physics and fluid mechanics, their application and associated measurement techniques. Over the past five years, quantum dots (QDs) have emerged as viable fluorescent tracer particles in near-wall flow physics studies for measuring fluid velocity and temperature. The technique of total internal reflection fluorescence (TIRF) microscopy is an invaluable resource for investigating near-wall colloidal dynamics and interfacial phenomena. Throughout this manuscript, we have developed new experimental techniques associated with TIRF microscopy, proposed and examined various sources of error and demonstrated new measurement applications for measuring slip velocities and the three-dimensional motion of large particles for leukocyte dynamics investigations. Finally, we explored the application of various microscale diagnostic techniques to electrospray

droplet dynamics, in particular fluorescence microscopy and holographic microscopy.

Although QDs have some drawbacks as flow tracers (high diffusivity, low intensity, blinking), their potential as micro- and nano-scale probes far outweighs any problematic features. QDs are among the most robust nanometer-sized particles that have been applied to micro-scale diagnostics to date. We presented one of the first studies of near-wall velocity measurements, velocity fields and diffusion dynamics using QDs along with novel measurement techniques to alleviate several of the aforementioned problems with QD tracers. Furthermore, we demonstrated their application as temperature probes in micro-scale thermal-fluid systems by simultaneously measuring temperature (through both intensity and diffusion) and velocity. Most recently, unparalleled temporal and velocity resolution has been achieved by measuring time-resolved QD dynamics with the integration of high-speed intensified imaging into a TIRF system. As the technology and materials evolve, improvements will be made in quantum efficiency, brightness, temperature sensitivity [31] and reduction of blinking [111] in QDs. With the recent progress in time-resolved QD tracking, three-dimensional QD tracking will soon be realized by applying existing TIRF techniques [41, 47]. To date, the significantly smaller size of QDs has not been fully exploited, and their applications in nanofluidics [3] have yet to be realized.

Evanescent wave microscopy has already yielded a number of contributions to the fields of micro- and nano-scale fluid and mass transport, including investigation of the no-slip boundary condition, applications to electrokinetic flows, verification of hindered diffusion, etc. We have examined several applications of TIRF including the quantification of slip velocities in aqueous flows. In addition to enabling the application of extremely small particles (QDs), TIRF was also applied to accurately measure nanometer scale displacements of significantly larger particles (6 μm) for studying the adhesion dynamics of leukocytes in blood

flow. We have also scrutinized the accuracy of these TIRF techniques and proposed and implemented solutions. In doing so, we uncovered interesting effects concerning the fundamental dynamics of colloidal particles in shear flows near solid surfaces through statistically studying their motion. As the application of TIRF continues to spread throughout the engineering, fluid mechanics and colloidal physics communities, a wealth of new experimental data and experiences are certain to provide improvements to these techniques. Brighter, more stable fluorescent nanoparticles (QDs), higher numerical aperture objectives and high sensitivity, low noise camera systems will provide unparalleled accuracy and resolution. Combining particle detection and manipulation using evanescent fields [84] is also a possibility, and integration of evanescent wave optics into on-chip platforms for lab-on-a-chip microfluidics applications will soon follow.

Like evanescent wave imaging, electrospray's are also a well-established technology. However, we have demonstrated that the application of newer, more accurate diagnostic techniques will bring about a deeper understanding of the complex underlying physics. We have demonstrated two such techniques including standard fluorescence microscopy and in-line holographic microscopy. Thus far, fluorescence microscopy has been able to measure two-dimensional droplet dynamics. In-line holographic microscopy, although somewhat computationally expensive, can easily extract three-dimensional droplet spray structure. Further improvements will allow for time-resolved three-dimensional trajectories of electrospray droplets to help understand charged droplet instabilities.

The dynamics of colloidal particles near solid surfaces represents an important branch micro-scale science. Colloids play an important role as diagnostic tools in micro-scale fluid mechanics, and understanding their behavior will improve measurement accuracy and bring about new applications. As microfabrication techniques improve, the nominal dimensions

of microfludic devices continue to decrease down to nanometer scales, where wall effects are increasingly important. Although evanescent wave microscopy is a well-established technique, it's application to micro-scale fluid mechanics and nanoparticle colloidal dynamics is relatively new. There is much room for improvement of these applications and vast new areas for the expansion of the technology including the measurement of three-dimensional dynamics of particles, molecules and polymers in nanochannels [3, 173] and over micro-patterned substrates. This will allow us to approach the molecular scale and examine the breakdown of the continuum limit.

Appendix A

Near-wall particle hydrodynamics

A.1 HINDERED BROWNIAN MOTION

The Brownian motion of small particles due to molecular fluctuations is generally well understood [60]. The random, thermal forcing of the particles is damped by the hydrodynamic drag resulting from the surrounding solvent molecules, and the particle's motion can be described as a diffusion process [61]:

$$\frac{\partial p\left(\vec{r}, t\right)}{\partial t} = \nabla \cdot \left(D\left(\vec{r}\right) \nabla p\left(\vec{r}, t\right)\right),$$
(A.1)

where p is the probability of finding a particle at a given location, $\vec{r}$, at time, t, and D is the diffusion coefficient. For an isolated, spherical particle that is significantly larger than the surrounding solvent molecules, the diffusion coefficient is constant and isotropic, and it is described by the Stokes-Einstein relation [62]

$$D_0 = \frac{k_b T}{\xi} = \frac{k_b T}{6\pi\mu a},$$
(A.2)

where k_b is Boltzmann's constant, T is the absolute temperature, ξ is the drag coefficient, μ is the dynamic viscosity of the solvent and a is the particle radius. In this case, the solution to equation A.1 subject to the condition $p(\vec{r}, t = t_0) = \delta(\vec{r} - \vec{r}_0)$ becomes

$$p(\vec{r}, t) = \frac{1}{8\left(\pi D_0 \Delta t\right)^{3/2}} \exp\left[-\frac{|\vec{r} - \vec{r}_0|^2}{4 D_0 \Delta t}\right], \tag{A.3}$$

where $\Delta t = t - t_0$ [174].

When an isolated particle in a quiescent fluid is in the vicinity of a solid boundary, its Brownian motion is hindered anisotropically due to an increase in hydrodynamic drag. Several theoretical studies have accurately captured this effect for various regimes of particle wall separation distance [63, 64, 65, 66]. The hindered diffusion coefficient in the wall-parallel direction, D_x, is described by

$$\frac{D_x}{D_0} = 1 - \frac{9}{16}\left(\frac{z}{a}\right)^{-1} + \frac{1}{8}\left(\frac{z}{a}\right)^{-3} - \frac{45}{256}\left(\frac{z}{a}\right)^{-4} - \frac{1}{16}\left(\frac{z}{a}\right)^{-5} + O\left(\frac{z}{a}\right)^{-6}, \tag{A.4}$$

where z is the particle center distance to the wall. This is a direct result from the drag force on a moving particle near a stationary wall in a quiescent fluid calculated by the "method of reflections," which is accurate far from the wall, $z/a > 2$ [67]. A better approximation for small particle-wall separation distances results from an asymptotic solution for the drag force based on lubrication theory for $z/a < 2$ [65]. Under these assumptions, the corresponding, normalized diffusion coefficient is

$$\frac{D_x}{D_0} = -\frac{2\left[\ln\left(\frac{z}{a} - 1\right) - 0.9543\right]}{\left[\ln\left(\frac{z}{a} - 1\right)\right]^2 - 4.325\ln\left(\frac{z}{a} - 1\right) + 1.591}. \tag{A.5}$$

The relative hindered diffusion coefficient for a particle diffusing in the wall-normal direction,

D_z, is described by

$$\frac{D_z}{D_0} = \left\{ \frac{4}{3} \sinh \alpha \sum_{n=1}^{\infty} \frac{n\,(n+1)}{(2n-1)\,(2n+3)} \right. $$
$$\left. \left[\frac{2 \sinh (2n+1)\,\alpha + (2n+1) \sinh 2\alpha}{4 \sinh^2 \left(n + \frac{1}{2}\right) \alpha - (2n+1)^2 \sinh^2 \alpha} - 1 \right] \right\}^{-1}, \tag{A.6}$$

where $\alpha = \cosh^{-1}(z/a)$. This results from an exact solution of the force experience by a particle for motions perpendicular to a stationary wall in a quiescent fluid [64]. The wall-parallel and wall-normal hindered diffusivities described in equations (A.4-A.6) are plotted in figure A.1. We also note that equation (A.6) has been shown to be well-approximated by

$$\frac{D_z}{D_0} = \frac{6 \left(\frac{z}{a} - 1\right)^2 + 2 \left(\frac{z}{a} - 1\right)}{6 \left(\frac{z}{a} - 1\right)^2 + 9 \left(\frac{z}{a} - 1\right) + 2}, \tag{A.7}$$

which is convenient for fast computation [69]. These theoretical results have been verified over different length scales by various researchers including several evanescent wave illumination studies [68, 37, 69, 70, 71, 72, 44]. Deviations from the bulk diffusivity become noticeable for particle-wall separation distances of order one. For instance, the wall-parallel diffusivity drops to one half of its bulk value when $z/a \approx 1.2$, while the wall-normal diffusivity drops to one half at $z/a \approx 2.1$.

A.2 NEAR-WALL SHEAR EFFECTS

The motion of an incompressible fluid obeys the continuity condition (conservation of mass)

$$\nabla \cdot \vec{u} = 0, \tag{A.8}$$
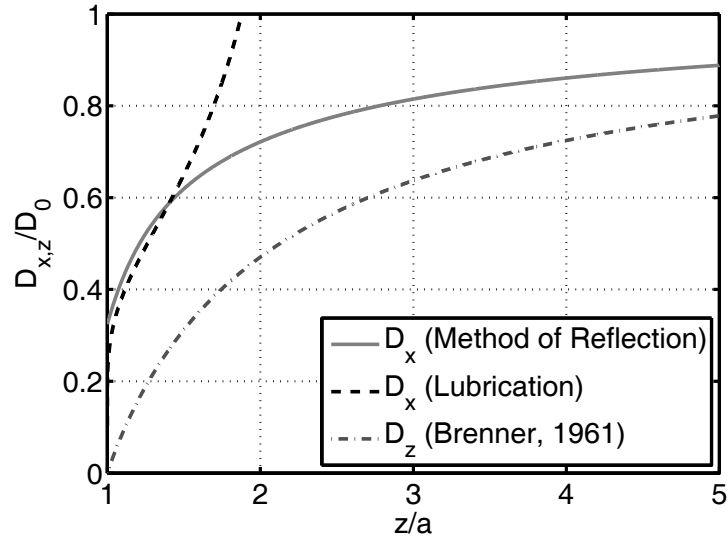
Figure A.1: Hindered diffusion coefficients in the wall-parallel, D_x, and wall-normal, D_z, directions for a neutrally buoyant spherical particle near a solid boundary.

where the velocity field, $\vec{u}$, is divergence free. The Navier-Stokes equation governs the motion of a viscous fluid and in the case of an incompressible fluid is

$$\rho \left(\frac{\partial \vec{u}}{\partial t} + \vec{u} \cdot \nabla \vec{u} \right) = -\nabla P + \mu \nabla^2 \vec{u}, \tag{A.9}$$

where ρ is the fluid density and P is the dynamic pressure. For the small Reynolds numbers ($Re \ll 1$) typical of microfluidic devices, equation A.9 greatly reduces in complexity to Stokes' equation [175]:

$$\nabla P = \mu \nabla^2 \vec{u}. \tag{A.10}$$

Most microfabrication techniques produce microchannels with approximately rectangular cross-sections. Thus, a useful result from equation A.10 is the solution for the velocity profile in a rectangular duct with height, d, and width, w, subject to the no-slip boundary

condition ($\vec{u} = 0$) at the walls. The laminar, unidirectional flow occurs in the pressure gradient direction with velocity, u_x, described below [174]:

$$u_x(y, z) = \frac{1}{2\mu}\left(-\frac{\partial P}{\partial x}\right)\left[\frac{d^2}{4} - z^2 + \frac{8}{d}\sum_{n=1}^{\infty}\frac{(-1)^n\cos(mz)\cosh(my)}{m^3\cosh(mw/2)}\right], \quad \text{(A.11)}$$

$$m = \frac{\pi(2n-1)}{d},$$

where the pressure gradient and volumetric flow rate, Q, are related by

$$Q = \frac{wd^3}{12\mu}\left(-\frac{\partial P}{\partial x}\right)\left[1 - \frac{192d}{\pi^5 w}\sum_{n=1,3,5,\dots}^{\infty}\frac{1}{n^5}\frac{1-\exp(-n\pi w/d)}{1+\exp(-n\pi w/d)}\right]. \quad \text{(A.12)}$$

It is well known that rigid particles tend to rotate in shear, and in the special case of a sphere near a planar wall, additional hydrodynamic drag slows the particle's translational velocity below that of the local fluid velocity [63, 66]. For wide microchannels ($w \gg d$) in the very near-wall region ($h \ll d$), the nearly parabolic velocity profile can be approximated by a linear shear flow

$$u \approx zS, \quad \text{(A.13)}$$

where S is the shear rate. The wall-parallel drag force experienced by a neutrally buoyant, free particle with radius, a, in a shear flow results in a translational velocity, v, estimated by the "method of reflections" [67], which is valid for large z/a [66]. The velocity normalized by the local fluid velocity at the particle's center is

$$\frac{v}{zS} \simeq 1 - \frac{5}{16}\left(\frac{z}{a}\right)^{-3}. \quad \text{(A.14)}$$

For small particle-wall separation distances (small z/a), an asymptotic solution based on
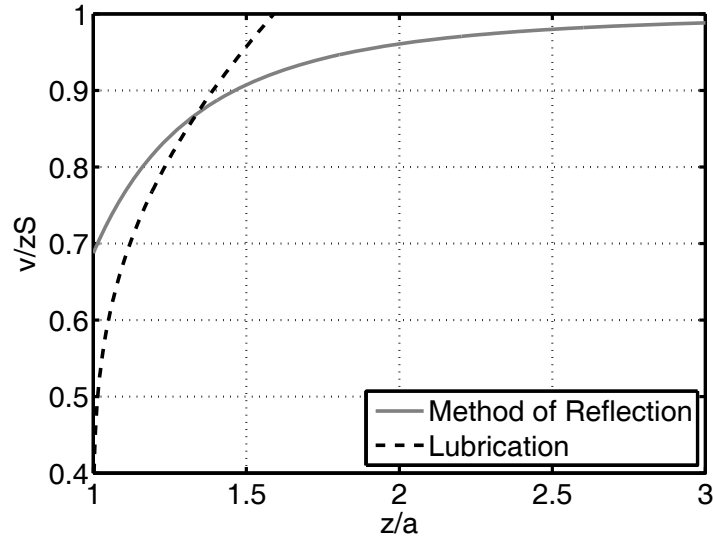
Figure A.2: Particle velocity normalized by the local fluid velocity in a near-wall shear flow given by the "method of reflection" and lubrication approximation solutions from Goldman *et al.*, 1967b.

lubrication theory is again employed, resulting in the translational particle velocity

$$\frac{v}{zS} \simeq \frac{0.7431}{0.6376 - 0.2\ln\left(\frac{z}{a} - 1\right)}, \tag{A.15}$$

which is also normalized by the unperturbed fluid velocity at the particle's center [66]. The "method of reflections" solution and asymptotic lubrication solution from equations (A.14-A.15) are shown in figure A.2. Additionally, Pierres *et al.* used a cubic approximation [142] to segment the solutions for intermediate values of z/a:

$$\begin{aligned}
\frac{v}{zS} \simeq \left(\frac{z}{a}\right)^{-1} \exp\Big\{ &0.68902 + 0.54756\left[\ln\left(\frac{z}{a} - 1\right)\right] \\
&+0.072332\left[\ln\left(\frac{z}{a} - 1\right)\right]^2 + 0.0037644\left[\ln\left(\frac{z}{a} - 1\right)\right]^3 \Big\}.
\end{aligned} \tag{A.16}$$

Particle rotation also induces a lifting force, which tends to make the particles migrate away

from the wall [73]. The magnitude of this force depends upon the Reynolds number near the wall, where the velocity scale is based on the shear rate and particle distance from the wall, and the particle Reynolds number with the velocity scale being the relative velocity of the particle to the local fluid velocity [74]. For nano-particles within several radii away from the wall at moderate shear rates in microchannels, these lifting forces are negligible [75].

Appendix B

The Boltzmann distribution for

near-wall colloidal particles

B.1 PARTICLE POTENTIAL

Electrostatic forces arise from the Coulombic interactions between charged bodies. When immersed in an ionic solution, these forces are moderated by the formation of an ionic double layer on their surfaces, which screen the charge. The characteristic length scale of these forces is given by the Debye length,

$$\kappa^{-1} = \sqrt{\frac{\epsilon_f \epsilon_0 k_b T}{2ce^2}}, \tag{B.1}$$

where ϵ_0 is the permittivity of free space, ϵ_f is the relative permittivity of the fluid, e is the elementary charge of an electron and c is the concentration of ions in solution [76]. In the case of a plane-sphere geometry for like-charged objects, the substrate exerts a repulsive

force on particles quantified by the potential energy of the interaction:

$$U^{el}(z) = B_{ps}e^{-\kappa(z-a)}. \tag{B.2}$$

The magnitude of the electrostatic potential is given by

$$B_{ps} = 4\pi\epsilon_f\epsilon_0 a \left(\frac{k_bT}{e}\right)^2 \left(\frac{\hat{\psi}_p + 4\gamma\Omega\kappa a}{1 + \Omega\kappa a}\right) \left[4\tanh\left(\frac{\hat{\psi}_s}{4}\right)\right], \tag{B.3}$$

where $\gamma = \tanh\left(\hat{\psi}_p/4\right)$, $\Omega = \left(\hat{\psi}_p - 4\gamma\right)/2\gamma^3$, $\hat{\psi}_p = \psi_p e/k_bT$ and $\hat{\psi}_s = \psi_s e/k_bT$ [77]. ψ_p and ψ_s represent the electric potentials of the particle and substrate, respectively.

Contributions from attractive, short-ranged van der Waals forces, which originate from multipole dispersion interactions [79], should also be considered when the particle-wall separation is on the order of 10 nm. The potential due to van der Waals interactions for a plane-sphere geometry is given by

$$U^{vdw}(z) = -\frac{A_{ps}}{6}\left[\frac{a}{z-a} + \frac{a}{z+a} + \ln\left(\frac{z-a}{z+a}\right)\right], \tag{B.4}$$

where A_{ps} is the Hamaker constant [80, 81]. The gravitational potential can also be important for large or severely density mismatched particles. The gravitational potential of a buoyant particle in a fluid is given by

$$U^g(z) = \frac{4}{3}\pi a^3 \left(\rho_s - \rho_f\right) g\left(z - a\right), \tag{B.5}$$

where ρ_s and ρ_f are the densities of the sphere and fluid, respectively, and g is the acceleration due to gravity.

Finally, optical forces due to electric field gradients from the illuminating light can trap

or push colloidal particles [82]. Below, we present an order of magnitude estimation for the potential of a dielectric particle in an evanescent field. Following Novotny and Hecht [55], the force on a dipole is given by

$$\vec{F} = (\vec{\mu} \cdot \nabla) \vec{E} = \left(\alpha \vec{E} \cdot \nabla \right) \vec{E} = \alpha \nabla |\vec{E}|^2. \tag{B.6}$$

The dipole moment, $\vec{\mu}$, polarizability, α, and electric field magnitude are given by the following:

$$\vec{\mu} = \alpha \vec{E}, \tag{B.7}$$

$$\alpha = 4\pi\epsilon_0 a_0^3 \frac{n_p^2 - n_0^2}{n_p^2 + 2n_0^2}, \tag{B.8}$$

$$I(z) = I_0 e^{-z/\delta} = \frac{1}{2} c\epsilon_0 n_0 |\vec{E}|^2, \tag{B.9}$$

where n_0 is the index of the surrounding medium, n_p is the index of the particle and c is the speed of light in a vacuum. Combining the above expressions, we can write an approximation to the potential of a particle near an interface due to an evanescent field:

$$U^{opt} \approx -\alpha |\vec{E}|^2 = -\frac{8\pi a_0^3}{cn_0} \frac{n_p^2 - n_0^2}{n_p^2 + 2n_0^2} I_0 e^{-z/\delta}, \tag{B.10}$$

which is an attractive force. However, more detailed analyses should be conducted to determine the forces on strongly absorbing particles, which can be repulsive (for example the semiconductor materials found in quantum dots).

B.2 NEAR-WALL PARTICLE CONCENTRATION

The equilibrium distribution for a suspension of non-interacting, Brownian particles in an external potential has been shown to be given by a Boltzmann distribution [176]. For a brief description, we follow Doi and Edwards (1986) and consider a one-dimensional distribution below. Fick's law of diffusion describes the flux, j, of material

$$j(z,t) = -D\frac{\partial p(z,t)}{\partial z}, \tag{B.11}$$

where D is the diffusion coefficient and p is the probability of finding a particle (concentration) at a location, z, in the wall-normal coordinate at time, t. In the presence of an external potential, $U(z)$, particles experience an additional force

$$F_z = -\frac{\partial U}{\partial z}. \tag{B.12}$$

Fick's law (equation B.11) is modified to reflect the additional flux induced by this force

$$j(z,t) = -D\frac{\partial p}{\partial z} - \frac{p}{\xi}\frac{\partial U}{\partial z}, \tag{B.13}$$

where, as in appendix A, the drag coefficient, ξ, is related to the diffusion coefficient, $D = k_b T/\xi$. In the steady state, the net flux vanishes, $j \to 0$, and the solution of equation B.13 leads to the Boltzmann distribution

$$p(z) = \frac{\exp\left[-U(z)/k_b T\right]}{\int_{z_1}^{z_2} \exp\left[-U(z)/k_b T\right] dz} = p_0 e^{-U/k_b T}, \tag{B.14}$$
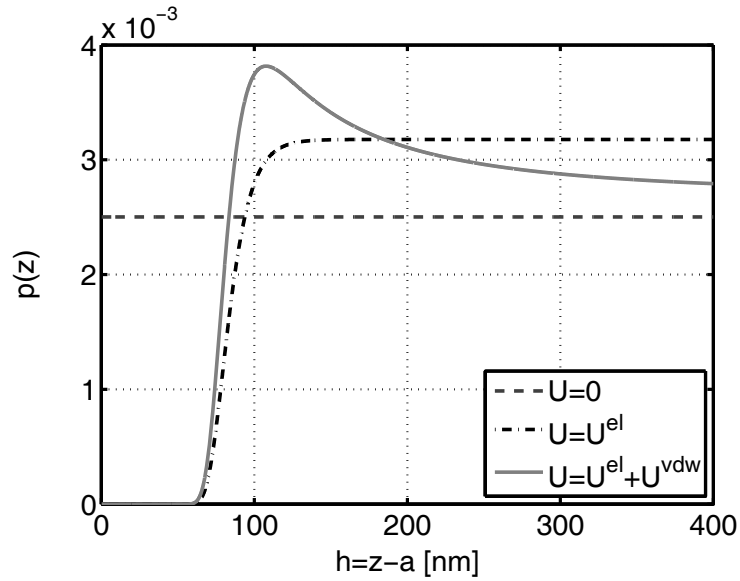
Figure B.1: Equilibrium, near-wall particle concentration for a 500 nm diameter polystyrene particle in water near a glass substrate with a 10 nm Debye length.

where p_0 is a normalization constant [37] from all particles in the range $z_1 \leq z \leq z_2$ and U is the total potential energy given by the sum of all potentials experienced by the particle (electrostatic, van der Waals, etc.). An example illustrating the non-uniform particle concentrations in the near-wall region is shown in figure B.1 for a 500 nm diameter polystyrene particle in water near a glass substrate with a 10 nm Debye length. In this case, electrostatic and van der Waals forces dominate, clearly forming a depletion layer within about 100 nm of the wall.

Appendix C

Nanoparticle fluorescence intensity

In Total Internal Reflection Fluorescence (TIRF) microscopy, many researchers have exploited the monotonic decay of the evanescent field to map the intensity of fluorescent dye molecules or particles to their distance from the fluid-solid interface [43, 41, 47]. When applying this technique to an ensemble of nanometer-sized particles that are typically used in fluid mechanics and colloid dynamics measurements, one must consider the non-uniformity of the particles and the variation of emission intensity with particle size. All commercially available polystyrene and latex nano-particles are manufactured with a finite size distribution, where the mean particle radius, a_0, can vary by up to 20%. Several researchers have attempted to compensate for this variation statistically, when making ensemble-averaged measurements of fluorescent nano-particles with TIRF [41, 48]. Most manufacturers impregnate the volume of the polymer particles with fluorescent dye, thus it is often assumed that the light intensity emitted by a particle is proportional to its volume. For instance, Huang *et al.* proposed that the intensity of a given particle, I^p, of radius, a, at a distance, z, from the interface is

$$I^p(z, a) = I_0^p \left(\frac{a}{a_0} \right)^3 \exp\left[-\frac{z}{\delta} \right], \qquad \text{(C.1)}$$

where I_0^p is the intensity of a mean radius particle and δ is the penetration depth of the evanescent field [41].

Below, we quote results from Chew (1988) for dipole radiation inside dielectric spheres [58] to support the claim that particle intensity is proportional to volume and demonstrate the limits of this assumption for larger particles. Consider a dielectric sphere of radius, a, permittivity, ϵ_1, permeability, μ_1, and index of refraction, $n_1 = \sqrt{\mu_1 \epsilon_1}$, inside of a second, infinite dielectric medium with ϵ_2, μ_2, and n_2. The radiation from an emitting dipole with free space wavelength, λ_0, will have momentum vectors, $k_{1,2} = 2\pi n_{1,2}/\lambda_0$, and subsequently, $\rho_{1,2} = k_{1,2}a$. The power emitted by a dipole is proportional to the dipole transition rate, $R^{\perp,\parallel}$, for perpendicular and parallel polarizations. These relations are provided in Chew (1988) normalized by the transition rates for dipoles contained in an infinite medium 1, $R^{\perp,\parallel}/R_0^{\perp,\parallel}$. For a distribution of dipoles, $c(\vec{r})$, located within the sphere, the volume averaged emission is

$$\left\langle \frac{R^{\perp,\parallel}}{R_0^{\perp,\parallel}} \right\rangle = \frac{\int \left(R^{\perp,\parallel}/R_0^{\perp,\parallel} \right) c(\vec{r}) \, d^3\vec{r}}{\int c(\vec{r}) \, d^3\vec{r}} \tag{C.2}$$

Finally, the volume averaged emission for randomly oriented dipoles, R/R_0, with a uniform concentration distribution, $c(\vec{r}) = c_0$, is

$$\left\langle \frac{R}{R_0} \right\rangle \equiv \frac{1}{3} \left\langle \frac{R^{\perp}}{R_0^{\perp}} + 2\frac{R^{\parallel}}{R_0^{\parallel}} \right\rangle = 2H \sum_{n=1}^{\infty} \left[\frac{J_n}{|D_n|^2} + \frac{GK_n}{|D_n'|^2} \right], \tag{C.3}$$

where

$$H = \sqrt{\frac{\mu_1 \epsilon_1 \epsilon_2}{\mu_2}} \left(\frac{9\epsilon_1}{4\rho_1^5}\right),$$

$$G = \frac{\mu_1 \mu_2}{\epsilon_1 \epsilon_2},$$

$$K_n = \frac{\rho_1^3}{2} \left[j_n^2(\rho_1) - j_{n+1}(\rho_1) j_{n-1}(\rho_1)\right],$$

$$J_n = K_{n-1} - n\rho_1 j_n^2(\rho_1),$$

$$D_n = \epsilon_1 j_n(\rho_1) \left[\rho_2 h_n^{(1)}(\rho_2)\right]' - \epsilon_2 h_n^{(1)}(\rho_2) \left[\rho_1 j_n(\rho_1)\right]',$$

$$D_n' = \mu_1 j_n(\rho_1) \left[\rho_2 h_n^{(1)}(\rho_2)\right]' - \mu_2 h_n^{(1)}(\rho_2) \left[\rho_1 j_n(\rho_1)\right]'.$$

Spherical Bessel functions of the first kind are denoted by j_n, and spherical Hankel functions of the first kind are denoted by $h_n^{(1)}$. The terms D_n and D_n' are the same denominators of the Mie scattering coefficients [57]. In the Rayleigh limit ($ka \ll 1$), the transition rates become independent of polarization and simplify greatly to

$$\left\langle \frac{R}{R_0} \right\rangle = \frac{9}{(\epsilon_1/\epsilon_2 + 2)^2} \sqrt{\frac{\epsilon_2 \mu_2^3}{\epsilon_1 \mu_1^3}}. \tag{C.4}$$

Figure C.1 shows the normalized mean emission rates (power) for both the Rayleigh limit and the full solution proposed by Chew (1988) [58] as a function of the particle radius, a, for a polystyrene particle ($n_1 = 1.59$) immersed in water ($n_2 = 1.33$) with an emission wavelength $\lambda_0 = 600$ nm. For particles with radius $a \leq 200$ nm, the Rayleigh limit is a good approximation to the full solution.

The total power, $\dot{E}$, emitted by a particle is the volume averaged emission rate, $\langle R/R_0 \rangle$,

Figure C.1: Volume averaged emission rate for uniformly distributed, randomly oriented radiating dipoles with emission wavelength, $\lambda_0 = 600$ nm, within a polystyrene sphere ($n_1 = 1.59$) immersed in water ($n_2 = 1.33$).

scaled by the volume of a given particle

$$\dot{E} = \frac{4}{3}\pi a^3 \left\langle \frac{R}{R_0} \right\rangle. \tag{C.5}$$

The total power emitted by a particle is shown in figure C.2 normalized by the emission

of a particle with radius $a = 500$ nm. Since all particle radii considered here are sub-

wavelength ($a < \lambda_0$) with the obvious exception of chapter 8, the Rayleigh limit is a descent

approximation. For particles with radii $a \lesssim 125$ nm, the Rayleigh approximation follows

the full solution quite closely as seen in the inset of figure C.2. Thus, the total power scales

with the particle volume for sub-wavelength particle at or near the Rayleigh limit, which

partially vindicates the approximation made in equation C.1. In the future, one should also

verify the uniformity of excitation in both the plane wave and evanescent wave excitation
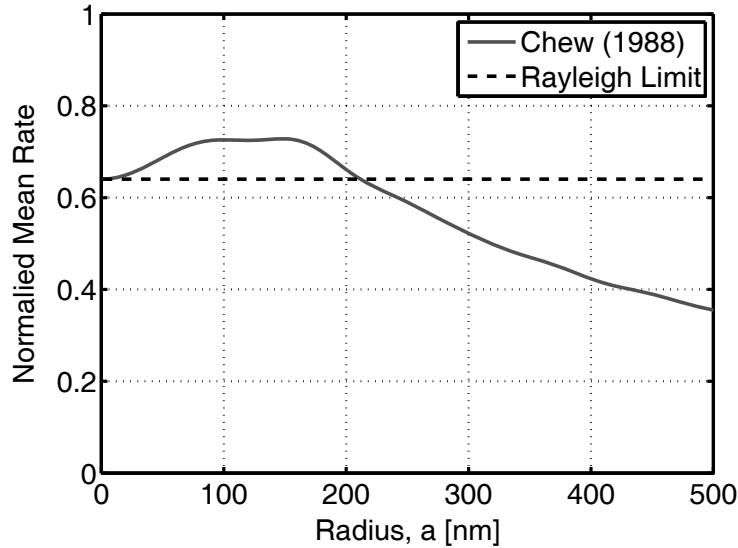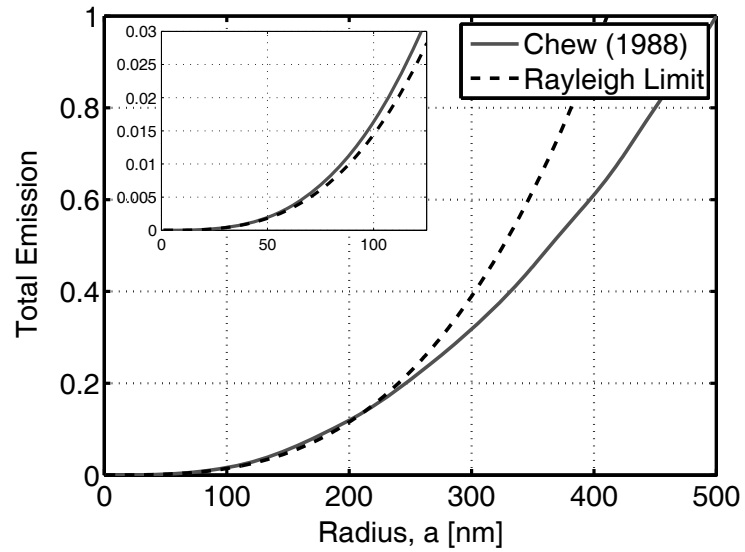
Figure C.2: Total emission (power) for uniformly distributed, randomly oriented radiating dipoles with emission wavelength, $\lambda_0 = 600$ nm, within a polystyrene sphere ($n_1 = 1.59$) immersed in water ($n_2 = 1.33$). For particles approaching the Rayleigh limit with radii, $a \leq 125$ nm, the emitted power scales with the particle volume.

cases to fully validate equation C.1.

Appendix D

TIRF Microscopy Alignment

Procedure

Objective-based evanescent wave (TIRF) microscopy systems are becoming much more common in experimental micro-scale mechanics. With proper alignment and conditioning of the incident beam, extremely clean images can be produced with good control over the excitation field. Here, we discuss general methodologies for alignment and beam conditioning as well as supply the relevant details to reconstruct a proven system with an inverted microscope. The procedure, which follows, is valid for both pulsed and continuous wave (CW) lasers. Caution should always be exercised when work with high powered laser. Proper eye protection should be warn at all times and power should be kept to a minimum during alignment to prevent injury or damage to equipment.

We use a Coherent Innova CW Argon Ion laser capable of several hundred milliwatts of output power in both the green (514 nm) and blue (488 nm). The microscope is a Nikon TE2000-U with two epifluorescence filter turrets. The lower turret accommodates the mercury lamp, and the upper turret can be accessed from the rear of the microscope
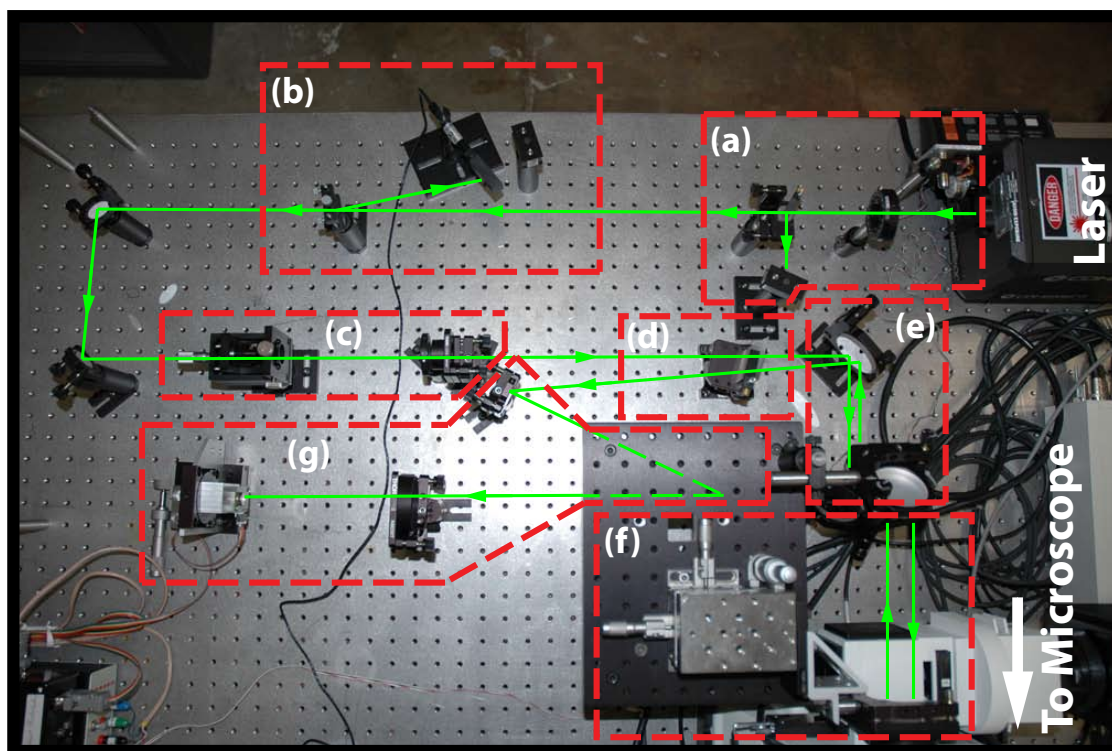
Figure D.1: Schematic of the beam conditioning and manipulation optics for an objective-based evanescent wave (TIRF) microscopy system. The components are broken down into several subsystems: (a) power control, (b) power meter, (c) spatial filter, (d) shifting prism, (e) periscope, (f) incident beam angle control and (g) reflected beam monitor.

(through free space). The components of the conditioning and alignment optics are shown in figure D.1, which are categorized in several subsystems: power control, power meter, spatial filter, shifting prism, periscope, incident beam angle control and reflected beam monitor. Not all of these systems are necessary for TIRF imaging (optional elements are somewhat obvious), but each system should be aligned in turn working from the laser to the microscope. We will discuss each system and its purpose.

The laser should always be operated near maximum power for the best thermal stability. As a safety mechanism and control, a mechanical chopper is placed directly in front of the laser aperture (figure D.1a). It is used as a beam stop for warm-up and can be controlled

electronically for periodic modulation of the beam if desired. Next, the already vertically polarized laser passes through a half-wave plate to rotate the polarization to an arbitrary angle. The wave plate in combination with the polarizing beam splitter that follows allow one to continuously vary the intensity to the evanescent wave microscopy system, while maintaining maximum operating power at the laser. By rotating the polarization, the vertical component is allowed to propagate along its original path through the beam splitter, while dumping the horizontally polarized light (excess power) to a beam stop toward the interior of the optical table. Next, the useful component of the beam is split again for power measurement (figure D.1b). With a fairly sensitive meter, a few hundred microwatts is sufficient for accurate measurement without being wasteful of the excitation power.

Two mirrors are now used redirect the beam back toward the microscope and align the beam conveniently along the optical table bolt pattern using two irises (not shown). After referencing the beam to the table, a spatial filter is implemented to obtain the TEM00 mode and expand the laser beam diameter (figure D.1c). The spatial filter movement containing an objective lens ($f = 8$ mm) and pinhole ($\sim$20 μm) is the aligned to the beam as shown in figure D.2a. When properly aligned, the spatial filter movement should produce a diverging, concentric ring pattern that is symmetric and bright (figure D.2b), while maintaining alignment to the original trajectory along the optical table. To collimate and expand the beam, a lens ($f \approx 20$ cm) is placed roughly one focal length away from the pinhole, where the focal length of the lens and divergence angle of the beam determine the final beam diameter, which should be about one centimeter in our case. Now, place an adjustable iris between the spatial filter movement and the collimating lens. Be sure to place it close to the collimating lens, but leave sufficient space for further adjustment of the lens. Align the iris to block all of the rings from the diverging beam by placing the edges
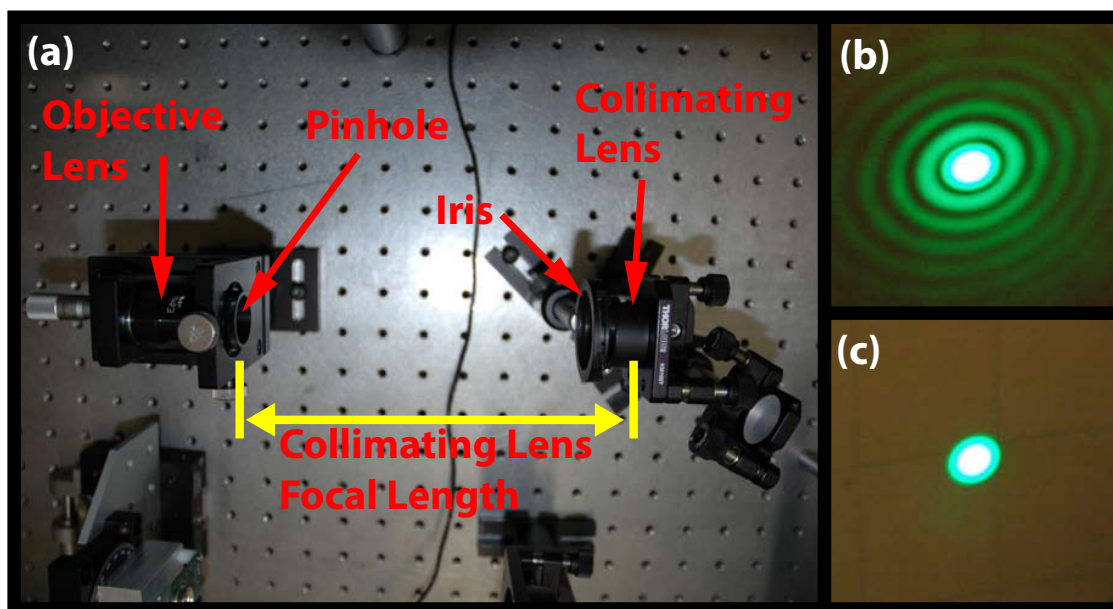
Figure D.2: Spatial filter schematic and resulting laser beam modes: (a) spatial filter components and orientation, (b) concentric rings produced by diffraction through the spatial filter pinhole and (c) resulting Gaussian beam spot produced by clipping the concentric rings with an iris.

of the iris in the first minimum of the concentric ring pattern. You should now be left with a very "clean," Gaussian beam spot as shown in figure D.2c. Finally, fine tune the position of the collimating lens such that the beam is collimated and again maintains the original trajectory along the bolt pattern of the optical table. One can determine if the beam is collimated by measuring the beam diameter just after the collimating lens, the projecting the beam on a wall several meters away and ensuring that the diameter is indeed the same.

The shifting prism (figure D.1d) is actually one of the final elements to be placed in the beam path and is optional. For now, we need to proceed with aligning the beam to the microscope's optical axis. First, place the epifluorescence filter set to be used with the TIRF system in the upper turret of the microscope. In the nosepiece of the microscope,

you should have an empty slot, a mirror fixed atop another empty slot with the reflective side facing down into the microscope, the TIRF objective ($100\times$, 1.45 NA or $60\times$, 1.49 NA in our case) and a low magnification objective ($\sim 10\times$, air). The TIRF objective should be focused to the correct operating height by placing a sample of dried particles on the microscope. After focusing, remove the sample and do not change the focus. Next, place a mark on the ceiling directly along the optical axis of the microscope. As an alternative, a semi-transparent optical element (diffuser glass) with a cross-hair can be fitted to the open hole of the nosepiece. For now, set the nosepiece to the empty slot.

The large, five centimeter diameter periscope mirrors (figure D.1e) should be placed at the rear of the microscope such that the beam enters the microscope, reflects off of the dichroic mirror and aligns to the ceiling. Large mirrors are used for the periscope to capture the reflected beam, since the incident and reflected beams will no longer travel on the same axis, once the system is shifted into TIRF mode. Right now, however, we want to align the laser system's optical axis to the microscope's optical axis. From this position, rotate the nosepiece to the up-side-down mirror position. You should see the reflected beam exit the rear of the microscope. Use only one of the periscope mirrors to align the incident and reflected beam paths at the rear of the microscope. Rotate the nosepiece back to the open position and use the opposite mirror to align the incident beam to the ceiling. Repeat this process until no further adjustment is needed and the optical axes will be co-linear. The shifting prism (figure D.1d), which is simply a rectangular solid piece of glass, is now inserted between the collimating lens of the spatial filter and the periscope. Rotate the prism until the beam hits the aligned position on the ceiling and verify that its reflection is also aligned (if not further adjustment of the shifting prism is necessary).

The incident beam angle control (figure D.1f), which consists of a large, five centimeter

lens ($f \approx 30$ cm) on a two dimensional rotation stage attached to a micron precision three-dimensional translation stage, should be placed between the periscope and microscope at approximately one focal distance away from the objective's back focal plane (BFP) as shown in figure D.3a. Again, the large lens is used to accommodate the shifted reflection of the incident beam in TIRF mode. By placing an iris on the lens, one can align the lens to the existing beam path. Use the rotation mount to align the beam to the ceiling (with an open slot in the nose piece), then translate the lens in two dimensions to align the beam to the iris (do not translate along the optical axis). Repeat this operation until no further adjustments are necessary. Rotate the nosepiece to the low magnification objective and repeat the alignment of the lens (low magnification objective alignment is optional). Rotate the nosepiece to the high magnification TIRF objective, place a clean slide on the stage and verify that the objective is still in focus (this is *extremely* important). Repeat the alignment of the beam angle control lens once more. At this point, the optical axes are once again co-linear. The final remaining step is to collimate the beam emerging from the objective lens by ensuring that the focal plane of the beam angle control lens and the objective's BFP coincide. Adjust the translational control of the three dimensional stage along the optical axis of the beam to minimize the spot projected on the ceiling, which should appear Gaussian and symmetric.

The incident angle can be controlled and calibrated by translating the beam shifting lens perpendicular to the optical axis (figure D.3b) and measuring the angle of the beam emerging from the objective and extrapolating the incident angle as a function of the translation stage position through a least-squares fit [75]. Once this relationship is obtained, a sample drop of fluid containing particles is placed on the slide and the beam angle is adjusted until TIRF is achieve (again, remember to wear proper eye protection here). Compare the predicted
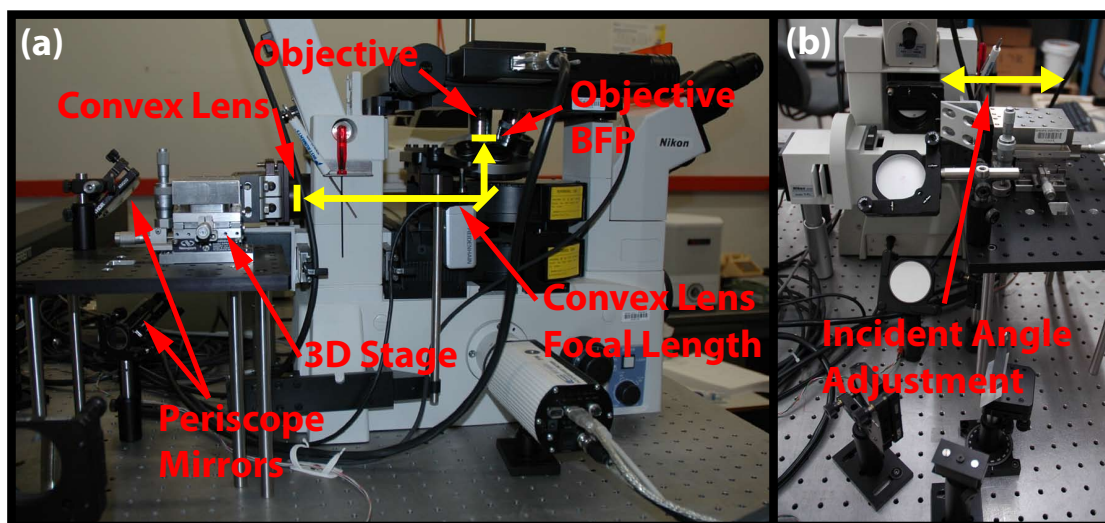
Figure D.3: Schematic of the periscope and beam angle control lens orientation in relation to the microscope: (a) by focusing the beam onto the back focal plane (BFP) of the objective, a collimated beam emerges from the microscope objective and (b) the proper translational adjustment direction for manipulating the incident angle into TIRF mode.

TIRF angle to the experimentally determined angle to verify the calibration. Last, the shifting prism can be rotated to center the TIRF spot in the field of view. Although this final adjustment is optional, if is performed, the incident angle should be re-calibrated.

The final (and optional) system for the evanescent wave microscopy system is the reflected beam monitoring system (figure D.1g), which can be used to detect changes in the refractive index of the liquid phase above the cover slip substrate and also, vertical deflections of the cover slip. The reflected beam is picked-off of its typical trajectory using two kinematic mirrors and centered along a bolt pattern of the optical table. A quadrant-photodiode is aligned to the beam using a two- or three-dimensional translation stage. A concave or convex lens can be inserted to increase the beam diameter, and thus increase the sensitivity of the photodiode. As mentioned above, translations of the beam at the photodiode, result from vertical displacements of the dielectric interface or relative changes

in index of the interface.

Bibliography

[1] T. P. Bigioni, X.-M. Lin, T. T. Nguyen, E. I. Corwin, T. A. Witten, and H. M. Jaeger, Kinetically driven self assembly of highly ordered nanoparticlemonolayers, Nature Materials **5**, 265 (2005).

[2] O. V. Salata, Applications of nanoparticles in biology and medicine, Journal of Nanobiotechnology **2** (2004).

[3] S. Pennathur and J. G. Santiago, Electrokinetic transport in nanochannels. 2. experiments, Analytical Chemistry **77**, 6782 (2005).

[4] R. J. Adrian, Particle imaging techniques for experimental fluid mechanics, Annual Review of Fluid Mechanics **23**, 261 (1991).

[5] J. Santiago, S. Wereley, C. Meinhart, D. Beebe, and R. Adrian, A particle image velocimetry system for microfluidics, Experiments in Fluids **25**, 316 (1998).

[6] C. M. Zettner and M. Yoda, Particle velocity field measurements in a near-wall flow using evanescent wave illumination, Experiments in Fluids **34**, 115 (2003).

[7] T. Schmidt, G. J. Schutz, W. Baumgartner, H. J. Gruber, and H. Schindler, Imaging of single molecule diffusion, in *Proceedings of the National Academy of Sciences USA*, volume 93, pp. 2926–2929, 1996.

[8] A. R. Bausch and D. A. Weitz, Tracking the dynamics of single quantum dots: Beating the optical resolution twice, Journal of Nanoparticle Research **4**, 477 (2002).

[9] S. Pouya, M. Koochesfahani, P. Snee, M. Bawendi, and D. Nocera, Single quantum dot (qd) imaging of fluid flow near surfaces, Experiments in Fluids **39**, 784 (2005).

[10] J. S. Guasto, P. Huang, and K. S. Breuer, Statistical particle tracking velocimetry using molecular and quantum dot tracer particles, Experiments in Fluids **41**, 869 (2006).

[11] P. E. Freudenthal, M. Pommer, C. D. Meinhart, and B. D. Piorek, Quantum nanospheres for sub-micron particle image velocimetry, Experiments in Fluids **43**, 525 (2007).

[12] J. S. Guasto and K. S. Breuer, Simultaneous, ensemble-averaged measurement of near-wall temperature and velocity in steady micro-flows using single quantum dot tracking, Experiments in Fluids **45**, 157 (2008).

[13] S. Pouya, M. M. Koochesfahani, A. B. Greytak, M. Bawendi, and D. G. Nocera, Experimental evidence of diffusion-induced bias error in near-wall velocimetry using quantum dot measurements, Experiments in Fluids **44**, 1035 (2008).

[14] D. Lasne, A. Maali, Y. Amarouchene, L. Cognet, B. Lounis, and H. Kellay, Velocity profiles of water flowing past solid glass surfaces using fluorescent nanoparticles and molecules as velocity probes, Physical Review Letters **100**, 214502 (2008).

[15] M. Bruchez, M. Moronne, P. Gin, S. Weiss, and A. P. Alivisatos, Semiconductor nanocrystals as fluorescent biological labels, Science **281**, 2013 (1998).

[16] M. W. Burke, *Image Acquisition*, chapter 5, Chapman and Hall, first edition, (1996).

[17] N. T. Ouellette, H. Xu, and E. Bodenschatz, A quantitative study of three-dimensional lagrangian particle tracking algorithms, Experiments in Fluids **40**, 301 (2006).

[18] M. Nirmal, B. O. Dabbousi, M. G. Bawendi, J. J. Macklin, J. K. Trautman, T. D. Harris, and L. E. Brus, Fluorescence intermittency in single cadmium selenide nanocrystals, Nature **383**, 802 (1996).

[19] J. Liu, M. Enzelberger, and S. Quake, A nanoliter rotary device for polymerase chain reaction, Electrophoresis **23**, 1531 (2002).

[20] K. Sun, A. Yamaguchi, Y. Ishida, S. Matsuo, and H. Misawa, A heater-integrated transparent microchannel chip for continuous-flow pcr, Sensors and Actuators B **84**, 283 (2004).

[21] J. R. Thome, Boiling in microchannels: a review of experiment and theory, International Journal of Heat and Fluid Flow **25**, 128 (2004).

[22] I. Hassan, Thermal-fluid mems devices: A decade of progress and challenges ahead, Journal of Heat Transfer **128**, 1221 (2006).

[23] J. Sakakibara, K. Hishida, and M. Maeda, Measurements of thermally stratified pipe flow using image-processing techniques, Experiments in Fluids **16**, 82 (1993).

[24] J. Sakakibara and R. J. Adrian, Whole field measurement of temperature in water using two-color laser induced fluorescence, Experiments in Fluids **26**, 7 (1999).

[25] M. Olsen and R. Adrian, Brownian motion and correlation in particle image velocimetry, Optics and Laser Technology **32**, 621 (2000).

[26] V. Hohreiter, S. Wereley, M. Olsen, and J. Chung, Cross-correlation analysis for temperature measurement, Measurement science and technology **13**, 1072 (2002).

[27] K. S. Breuer, editor, *Microscale Diagnostic Techniques*, chapter 2, Springer, (2005).

[28] D. Ross, M. Gaitan, and L. E. Locascio, Temperature measurement in microfluidic systems using a temperature-dependent fluorescence dye, Analytical Chemistry **73**, 4117 (2001).

[29] H. Kim, K. Kihm, and J. Allen, Examination of ratiometric laser induced fluorescence thermometry for microscale spatial measurement resolution, International Journal of Heat and Mass Transfer **46**, 3967 (2003).

[30] V. K. Natrajan and K. T. Christensen, A two-color fluorescent thermometry technique for microfluidic devices, 46th AIAA Aerospace Sciences Meeting (2008).

[31] T.-C. Liu, Z.-L. Huang, H.-Q. Wang, J.-H. Wang, X.-Q. Li, Y.-D. Zhao, and Q. ming Luo, Temperature-dependent photluminescence of water-soluble quantum dots for a bioprobe, Analytica Chimica Acta **559**, 120 (2006).

[32] G. W. Walker, V. C. Sundar, C. M. Rudzinski, A. W. Wun, M. G. Bawendi, and D. G. Nocera, Quantum-dot optical temperature probes, Applied Physics Letters **83**, 3555 (2003).

[33] M. Koochesfahani, Personal communication, 2005.

[34] U. Banin, M. Bruchez, A. Alivisatos, T. Ha, S. Weiss, and D. Chemla, Evidence for a thermal contribution to emission intermittency in single cdse/cds core/shell nanocrystals, Journal of Chemical Physics **110**, 1195 (1999).

[35] D. Axelrod, T. P. Burghardt, and N. L. Thompson, Total internal reflection fluorescence, Annual Review of Biophysics and Bioengineering **13**, 247 (1984).

[36] D. Axelrod, Total internal reflection fluorescence microscopy in cell biology, Traffic **2**, 764 (2001).

[37] D. C. Prieve, Measurement of colloidal forces with tirm, Advances in Colloid and Interface Science **82**, 93 (1999).

[38] S. G. Bike, Measureing colloidal forces using evanescent wave scattering, Colloid and Interface Science **5**, 144 (2000).

[39] S. Jin, P. Huang, J. Park, J. Y. Yoo, and K. S. Breuer, Near-surface velocimetry using evanescent wave illumination, Experiments in Fluids **37**, 825 (2004).

[40] R. Sadr, M. Yoda, Z. Zheng, and A. T. Conlisk, An eperimental study of electro-osmotic flow in rectangular microchannels, Journal of Fluid Mechanics **506**, 357 (2004).

[41] P. Huang, J. S. Guasto, and K. S. Breuer, Direct measurement of slip velocities using three-dimensional total internal reflection velocimetry, Journal of Fluid Mechanics **566**, 447 (2006).

[42] P. Huang and K. S. Breuer, Direct measurement of slip length in electrolyte solutions, Physics of Fluids **19**, 028104/3 (2007).

[43] K. D. Kihm, A. Banerjee, C. K. Choi, and T. Takagi, Near-wall hindered Brownian diffusion of nanoparticles examined by three-dimensional ratiometric total internal reflection fluorescence microscopy (3-d r-tirfm), Experiments in Fluids **37**, 811 (2004).

[44] P. Huang and K. S. Breuer, Direct measurement of anisotropic near-wall hindered diffusion using total internal reflection velocimetry, Physical Review E **76**, 046307 (2007).

[45] R. Sadr, C. Hohenengger, H. Li, P. J. Mucha, and M. Yoda, Diffusion-induced bias in near-wall velocimetry, Journal of Fluid Mechanics **577**, 443 (2007).

[46] P. Huang, J. S. Guasto, and K. S. Breuer, Simulation and experimental measurement of particle motion in shear flow and its implication for near-wall particle velocimetry, In preparation (2008).

[47] H. F. Li and M. Yoda, Multilayer nano-particle image velocimetry (MnPIV) imn microscale Poiseuille flows, Measurement Science and Technology **19**, 075402 (2008).

[48] J. S. Guasto and K. S. Breuer, Measurement bias in evanescent fields due to particle size variations and force interactions, Measurement Science and Technology, In Review (2008).

[49] S. Kasap, *Optoelectronics and Photonics: Principles and Practices*, chapter 1, pp. 1–49, Prentice Hall, (2001).

[50] S. Inoue and K. R. Spring, *Video Microscopy: The Fundamentals*, Plenum Press, second edition, (1997).

[51] D. C. Prieve and J. Y. Walz, Scattering of an evanescent surface wave by a microscopic dielectric sphere, Applied Optics **32**, 1629 (1993).

[52] H. Li, R. Sadr, and M. Yoda, Multilayer nano-particle image velocimetry, Experiments in Fluids **41**, 185 (2006).

[53] J. C. Crocker and D. G. Grier, Methods of digital video microscopy for colloidal studies, Journal of Colloid and Interface Science **179**, 298 (1996).

[54] M. K. Cheezum, W. F. Walker, and W. H. Guilford, Quantitative comparison of algorithms for tracking single fluorescent particles, Biophysical Journal **81**, 2378 (2001).

[55] L. Novotny and B. Hecht, *Principles of Nano-Optics*, Cambridge University Press, (2006).

[56] V. Breedveld, D. van den Ende, and A. T. A. Acrivos, The measurement of the shear-induced particle and fluid tracer diffusivities in concentrated suspensions by a novel method, Journal of Fluid Mechanics **375**, 297 (1998).

[57] H. Chew, P. J. McNulty, and M. Kerker, Model for Raman and fluorescent scattering by molecule embedded in small particles, Physical Review A **13**, 396 (1976).

[58] H. Chew, Radiation and lifetimes of atoms inside dielectri partilces, Physical Review A **38**, 3410 (1988).

[59] H. Schniepp and V. Sandoghdar, Spontaneous emission of europium ions embedded in deielectric nanospheres, Physicsl Review Letters **89**, 257403 (2002).

[60] R. Brown, A brief account of microscopical observations made in the months of june, july and august, 1827, on the particles contained in the pollen of plants; and on the general existence of active molecules in organic and inorganic bodies., Philosophical Magazine **4**, 161 (1828).

[61] A. Einstein, ber die von der molekularkinetischen theorie der wrme geforderte bewegung von in ruhenden flssigkeiten suspendierten teilchen, Annalen der Physik **17**, 549 (1905).

[62] E. L. Cussler, *Diffusion: Mass Transfer in Fluid Systems*, Cambridge University Press, (1997).

[63] M. Chaoui and F. Feuillebois, Creeping flow around a sphere in a shear flow close to a wall, Quarterly Journal of Mechanics and Applied Mathematics **56**, 381 (2003).

[64] H. Brenner, The slow motion of a sphere through a viscous fluid towards a plane wall, Chemical Engineering Science **16**, 242 (1961).

[65] A. J. Goldman, R. G. Cox, and H. Brenner, Slow viscous motion of a sphere parallel to a plane wall - i: motion through a quiescent fluid, Chemical Engineering Science **22**, 637 (1967).

[66] A. J. Goldman, R. G. Cox, and H. Brenner, Slow viscous motion of a sphere parallel to a plane wall - ii: Couette flow, Chemical Engineering Science **22**, 653 (1967).

[67] J. Happel and H. Brenner, *Low Reynolds Number Hydrodynamics: With Special Applications to Particulate Media*, Springer, (1983).

[68] N. A. Frej and D. C. Prieve, Hindered diffusion of a single sphere very near a wall in a nonuniform force field, Journal of Chemical Physics **98**, 7552 (1993).

[69] M. A. Bevan and D. C. Prieve, Hindered diffusion of colloidal particles very near to a wall: revisited, Journal of Chemical Physics **113**, 1228 (2000).

[70] B. Lin, J. Yu, and S. A. Rice, Direct measurements of constrained Brownian motion of an isolated sphere between two walls, Physical Review E **62**, 3909 (2000).

[71] R. J. Oetama and J. Y. Walz, Simultaneous investigation of sedimentation and diffusion of a single colloidal particle near an interfce, The Journal of Chemical Physics **124**, 164713 (2006).

[72] A. Banerjee and K. D. Kihm, Experimental verification of near-wall hindered diffusion for the Brownian motion of nanoparticles using evanescent wave microscopy, Physical Review E **72**, 042101 (2005).

[73] M. R. King and D. T. L. Jr., Measurement of the inertial lift on a moving sphere in contact with a plane wall in a shear flow, Physics of Fluids **9**, 1248 (1997).

[74] P. Cherukat and J. B. McLaughlin, The inertial lift on a rigid sphere in a linear shear flow field near a flat wall, Journal of Fluid Mechanics **263**, 1 (1994).

[75] P. Huang, *Near-surface slip flow and hindered colloidal diffusion at the nano-scale*, PhD thesis, Brown University, 2006.

[76] R. A. L. Jones, *Soft Condensed Matter*, Oxford University Press, (2004).

[77] M. R. Oberholzer, N. J. Wagner, and A. M. Lenhoff, Grand canonical Brownian dynamics simulation of colloidal adsorption, Journal of Chemical Physics **107**, 9157 (1997).

[78] D. C. Prieve and N. A. Frej, Total internal reflection microscopy: a tool for measuring colloidal forces, Langmuir **6**, 396 (1990).

[79] J. N. Israelachvili and D. Tabor, The measurement of van der Waals dispersion forces in the range 1.5 to 130 nm, Proceeding of the Royal Society of London A **331**, 19 (1972).

[80] H. C. Hamaker, The Londonvan der Waals attraction between spherical particles, Physica (Amsterdam) **4**, 1058 (1937).

[81] V. A. Parsegian, *Van Der Waals Forces: A Handbook for Biologists, Chemists, Engineers and Physicists*, Cambridge University Press, (2006).

[82] A. Ashkin, J. M. Dziedzic, J. E. Bjorkholm, and S. Chu, Observation of a single-beam gradient force optical trap for dielectric particles, Optics Letters **11**, 288 (1986).

[83] A. Ashkin, Optical trapping and manipulation of neutral particles using lasers, Proceedings of the National Academy of Sciences of the United States of America **94**, 4853 (1997).

[84] B. S. Schmidt, A. H. J. Yang, D. Erickson, and M. Lipson, Optofluidic trapping and transport on solid core waveguides within a microfluidic device, Optics Express **15**, 14322 (2007).

[85] G. I. Taylor, Disintegration of water drops in an electric field, Proceedings of the Royal Society of London. Series A **280**, 383 (1964).

[86] M. Gamero-Castano and V. Hruby, Electrospray as a source of nanoparticles for efficient colloid thrusters, Journal of Propulsion and Power **17**, 977 (2002).

[87] A. Jones and K. Thong, The production of charged monodisperse fuel droplets by electrical dispersion, J. Phys. D: Appl. Phys. **4**, 1159 (1971).

[88] P. Lozano, *Studies on the Ion-Droplet Mixed Regime in Colloid Thrusters*, PhD thesis, Massachusetts Institute of Technology, 2003.

[89] P. Lozano, M. Martinez-Sanchez, and J. M. Lopez-Uridales, Electrospray emission from nonwetting flat dielectric surfaces, Journal of Colloid and Interface Science **276**, 392 (2004).

[90] J. Fenn, M. Mann, C. Meng, S. Wong, and C. Whitehouse, Electrospray ionization for mass spectrometry of large biomolecules, Science **246**, 64 (1989).

[91] J. F. de la Mora, J. Navascues, F. Fernandez, and J. Rosell-Llompart, Generation of submicron monodisperse aerosols by electrosprays, Journal of Aerosol Science **21**, S673 (1990).

[92] A. Gomez and G. Chen, Charge-induced secondary atomization in diffusion flames of electrostatic sprays, Combustion Science Technology **96**, 47 (1994).

[93] M. Cloupeau and B. Prunet-Foch, Electrostatic spraying of liquids: Main functioning modes, Journal of Electrostatics **25**, 165 (1990).

[94] M. Cloupeau and B. Prunet-Foch, Electrohydrodynamic spraying functioning modes: A critical review, Journal of Aerosol Science **25**, 1021 (1994).

[95] M. Cloupeau, Recipes for use of ehd spraying in cone-jet mode and notes on corona discharge effects, Journal of Aerosol Science **25**, 1143 (1994).

[96] M. Cloupeau and B. Prunet-Foch, Electrostatic spraying of liquids in cone-jet mode, Journal of Electrostatics **22**, 135 (1989).

[97] A. M. Ganan-Calvo, J. Lasheras, J. Davila, and A. Barrero, The electrostatic spray emitted from an electrified conical meniscus, Journal of Aerosol Science **25**, 1121 (1994).

[98] A. Ganan-Calvo, J. Davila, and A. Barrero, Current and droplet size in the electrospraying of liquids. scaling laws, Journal of Aerosol Science **28**, 249 (1997).

[99] K. Tang and A. Gomez, On the structure of an electrostatic spray of monodisperse droplets, Physics of Fluids **6**, 2317 (1994).

[100] L. de Juan and J. F. de la Mora, Charge and size distributions of electrospray drops, Journal of Colloid and Interface Science **186**, 280 (1996).

[101] J. F. de la Mora and I. Loscertales, The current emitted by highly conducting taylor cones, Journal of Fluid Mechanics **260**, 155 (1994).

[102] S. Murata and N. Yasuda, Potential of digital holography in particle measurement, Optics and Laser Technology **32**, 567 (2000).

[103] W. Xu, M. N. Jericho, I. A. Meinertzhagen, and H. J. Kreuzer, Digital in-line holography of microspheres, Applied Optics **41**, 5367 (2002).

[104] J. Sheng, E. Malkiel, and J. Katz, Digital holographic microscope for measuring three -dimensional particle distributions and motions, Applied Optics **45**, 3893 (2006).

[105] J. H. Milgram and W. Li, Computational reconstruction of images from holograms, Applied Optics **41**, 853 (2002).

[106] J. Sheng, E. Malkiel, J. Katz, J. Adolf, R. Belas, and A. Place, Digital holographic microscopy reveals prey-induced changes in swimming behavior of predatory dinoflagellates, Proceedings of the National Academy of Sciences **104**, 17512 (2007).

[107] J. W. Goodman, *Introduction to Fourier Optics*, chapter 9, pp. 297–397, Roberts and Company, (2005).

[108] C. D. Meinhart and S. T. Wereley, The theory of diffraction-limited resolution in microparticles image velocimetry, Measurement Science and Technology **14**, 1047 (2003).

[109] M. Kendall and A. Stuart, *The Advanced Theory of Statistics*, volume 1, chapter 10, Macmillan, fourth edition, (1977).

[110] K. T. Shimizu, R. G. Neuhauser, C. A. Leatherdale, S. A. Empedocles, W. K. Woo, and M. G. Bawendi, Blinking statistics in single semiconductor nanocrystal quantum dots, Physical Review B **63**, 1 (2001).

[111] S. Hohng and T. Ha, Near-complete supression of quantum dot blinking in ambient conditions, Journal of the American Chemical Society **126**, 1324 (2004).

[112] I. Chung and M. G. Bawendi, Relationship between single quantum dot intermittency and fluorescence decays from collections of dots, Physical Review B **70**, 2897 (2004).

[113] T.-H. Lin and G. D. Phillies, Probe diffusion in poly(acrylic acid)-water. effect of probe size, Macromolecules **17**, 1686 (1984).

[114] Y. Cheng, R. K. Prud'homme, and J. L. Thomas, Diffusion of mesoscopic probes in aqueous polymer solutions measured by fluorescence recovery after photobleaching, Macromolecules **35**, 8111 (2002).

[115] M. L. Sheely, Glycerol viscosity tables, Industrial and Engineering Chemistry **24**, 1060 (1932).

[116] R. Sadr, M. Yoda, P. Gnanaprakasam, and A. T. Conlisk, Velocity measurements inside the diffusie electric couble layer in electro-osmotic flow, Applied Physics Letters **89**, 044103 (2006).

[117] Y. Xia and G. M. Whitesides, Soft lithography, Annual Review in Material Science **28**, 153 (1998).

[118] R. C. Weast, editor, *CRC Handbook of Chemistry and Physics*, The Chemical Rubber Company, (1971).

[119] E. Lauga, M. P. Brenner, and H. A. Stone, in *Handbook of Experimental Fluid Dynamics*, edited by J. F. anc C. Tropea and A. Yarin, Springer, New York, 2006, chapter 15.

[120] E. Schnell, Slippage of water over nonwettable surfaces, Journal of Applied Physics **27**, 1149 (1956).

[121] D. C. Tretheway and C. D. Meinhart, Apparent fluid slip at hydrophobic microchannel walls, Physics of Fluids **14**, L9 (2002).

[122] K. Watanabe, Yanuar, and H. Mizunuma, Slip of newtonian fluids at solid boundary, JSME International Journal **41**, 525 (1998).

[123] Y. Zhu and S. Granick, Rate-dependent slip of newtonian liquid at smooth surfaces, Physical Review Letters **87**, 096105 (2001).

[124] R. Pit, H. Hervet, and L. Leger, Direct experimental evidence of slip in hexadecane: solid interface, Physical Review Letters **85**, 980 (2000).

[125] D. Lumma, A. Best, A. Gansen, F. Feuillebois, J. O. Radler, and O. I. Vinogradova, Flow profile near a wall measured by double-focus fluorescence cross-correlation, Physical Review E **67**, 056313 (2003).

[126] C.-H. Choi, J. A. Westin, and K. S. Breuer, Apparent slip flows in hydrophilic and hydrophobic microchannels, Physics of Fluids **15**, 2897 (2003).

[127] Y. Zhu and S. Granick, Limites of the hydrodynamic no-slip boundary condition, Physical Review Letters **88**, 106102 (2002).

[128] C. Neto, V. S. J. Craig, and D. R. M. Williams, Evidence of shear-dependent boundary slip in newtonian liquids, The European Physical Journal E **12**, S71 (2003).

[129] C. Cottin-Bizonne, B. Cross, A. Steinberger, and E. Charlaiz, Boundary slip on smooth hydrophobic surfaces: intrinsic effects and possible artifacts, Physical Review Letters **94**, 056102 (2005).

[130] P. Joseph and P. Tabeling, Direct measurement of the apparent slip length, Physical Review E **71**, 035303(R) (2005).

[131] P. A. Thompson and S. M. Troian, A general boundary condition for liquid flow at solid surfaces, Nature **389**, 360 (1997).

[132] J.-L. Barrat and L. Bocquet, Large slip effect at a nonwetting fluid-solid interface, Physical Review Letters **82**, 4671 (1999).

[133] M. Cieplak, J. Koplik, and J. R. Banavar, Boundary conditions at a fluid-solid surface, Physical Review Letters **86**, 803 (2001).

[134] T. M. Galea and P. Attard, Molecular dynamics study of the effect of atomic roughness on the slip length at the fluid-solid boundary during shear flow, Langmuir **20**, 3477 (2004).

[135] G. Nagayama and P. Cheng, Effects of interface wettability on microscale flow by molecular dynamics simulation, International Journal of Heat and Mass Transfer **47**, 501 (2004).

[136] C. Cottin-Bizonne, J.-L. Barrat, L. Bocquet, and E. Charlaiz, Low-friction flows of liquid at nanopattened interfaces, Nature Materials **2**, 237 (2005).

[137] N. L. Thompson and B. C. Langerholm, Total internal reflection fluorescence: applications in cellular biophysics, Current Opinion in Biotechnology **8**, 58 (1997).

[138] J. S. Burmeister, L. A. Olivier, W. M. Reichert, and G. A. Truskey, Application of total internal reflection fluorescence microscopy to study cell adhesion to biomaterials, Biomaterials **19**, 307 (1998).

[139] D. Toomre and D. J. Manstein, Lighting up the cell surface with evanescent wave microscopy, Trends in Cell Biology **11**, 298 (2001).

[140] M. Hosoda, K. Sakai, and K. Takagi, Measurement of anisotropic Brownian motion near an interface by evanescent light-scattering spectroscopy, Physical Review E **58**, 6275 (1998).

[141] R. Sadr, H. Li, and M. Yoda, Impact of hindered Brownian diffusion on the accuracy of particle-image velocimetry using evanescent-wave illumination, Experiments in Fluids **38**, 90 (2005).

[142] A. Pierres, A.-M. Benoliel, C. Zhu, and P. Bongrand, Diffusion of microspheres in shear flow near a wall: use to measure binding rates between attached molecules, Biophysical Journal **81**, 25 (2001).

[143] D. C. Duffy, J. C. McDonald, O. J. A. Schueller, and G. M. Whitesides, Rapid prototyping of microfluidic systems in poly(dimethylsiloxane), Analytical Chemistry **70**, 4974 (1998).

[144] C.-H. Choi, K. J. A. Westin, and K. S. Breuer, To slip or not to slip - water flows in hydrophilic and hydrophobic microchannels, in *Proceedings of IMECE 2002*, pp. IMECE2002–33707, 2002.

[145] S. Granick, Y. Zhu, and H. Lee, Slippery questions about complex fluids flowing past solids, Nature Materials **2**, 221 (2003).

[146] E. Lauga and M. P. Brenner, Dynamic mechanisms for apparent slip on hydrophobic surfaces, Physical Review E **70**, 026311 (2004).

[147] X. H. Zhang, X. D. Zhang, S. T. Lou, Z. X. Zhang, J. L. Sun, and J. Hu, Degassing and temperature effects on the formation of nanobubbles at the mica/water interface, Langmuir **20**, 3813 (2004).

[148] E. Lauga, Apparent slip due to the motion of suspended particles in flows of electrolyte solutions, Langmuir **20**, 8924 (2004).

[149] S. G. Flicker, J. L. Tipa, and S. G. Bike, Quantifying double-layer repulsion between a colloidal sphere and a glass plate using total internal reflection microscopy, Journal of Colloid and Interface Science **158**, 317 (1993).

[150] S. Wereley and C. Meinhart, *Microscale Diagnostic Techniques*, Springer, (2005).

[151] S. T. Wereley and C. D. Meinhart, in *Microscale Diagnostic Techniques*, edited by K. Breuer, Springer, 2005, pp. 51–112.

[152] C. Hohenegger and P. J. Mucha, Statistical reconstruction of velocity profiles for nanoparticle image velocimetry, Journal of Applied Mathematics **68**, 239 (2007).

[153] E. Lauga and T. M. Squires, Brownian motion near a partial-slip boundary: A local probe of the no-slip condition, Physics of Fluids **17**, 103102 (2005).

[154] D. L. Ermak and J. McCammon, Brownian dynamics with hydrodynamic interactions, Journal of Chemical Physics **69**, 1352 (1978).

[155] H. N. Unni and C. Yang, Brownian dynamics simulation and experimental study of colloidal particle deposition in a microchannel flow, Journal of Colloid and Interface Science **291**, 28 (2005).

[156] D. S. Sholl, M. K. Fenwick, E. Atman, and D. C. Prieve, Brownian dynamics simulation of the motion of a rigid sphere in a viscous fluid very near a wall, Journal of Chemical Physics **113**, 9268 (2000).

[157] E. A. J. F. Peters and T. M. A. O. M. Barenbrug, Efficient Brownian dynamics

simulation of particles near wall. i. reflecting and absorbing walls, Physical Review E **66**, 056701 (2002).

[158] E. A. J. F. Peters and T. M. A. O. M. Barenbrug, Efficient Brownian dynamics simulation of particles near wall. i. sticky walls, Physical Review E **66**, 056702 (2002).

[159] R. A. L. Jones, *Soft Condensed Matter*, Oxford University Press, Oxford, England, (2002).

[160] E. Y. H. Park, M. J. Smith, E. S. Stropp, K. R. Snapp, J. A. DiVietro, W. F. Walker, D. W. Schmidtke, S. L. Diamond, and M. B. Lawrence, Comparison of psgl-1 microbead and neutrophil rolling: microvillus eleongation stabilizes p-selectin bond clusters, Biophysical Journal **82**, 1835 (2002).

[161] K. E. Caputo and D. A. Hammer, Effect of microvillus deformability on leukocyte adhesion using adhesive dynamics simulations, Biophysical Journal **89**, 187 (2005).

[162] S. Jadhav, C. D. Eggleton, and K. Konstantopoulos, A 3-d computational model predicts that cell deformation affects selectin-mediated leukocyte rolling, Biophysical Journal **88**, 96 (2005).

[163] P. Robert, A.-M. Benoliel, and P. Bondgrand, What is the biological relevance of the specific bond properties revealed by single-molecule studies?, Journal of Molecular Recognition **20**, 432 (2007).

[164] L. J. Rinko, M. B. Lawrence, and W. H. Guilford, The molecular mechanics of p- and l-selectin lectin domains binding to psgl-1, Biophysical Journal **86**, 544 (2004).

[165] J. Fritz, A. G. Katopodis, F. Kolbinger, and D. Anselmetti, Force-mediated kinetics of

single p-selectin/ligand complexes observed by atomic force microscopy, Proceedings of the Nationl Academy of Science **95**, 12283 (1998).

[166] M. J. Smith, E. L. Berg, and M. B. Lawrence, A direct comparison of selectin-mediated transient, adhesion events using high temporal resolution, Biophysical Journal **77**, 3371 (1999).

[167] C. D. Paschall, W. H. Guilford, and M. B. Lawrence, Enhancement of l-selectin, but not p-selectin, bond formation frequency by convective flow, Biophysical Journal **94**, 1034 (2008).

[168] B. J. Schmidt, P. Huang, K. S. Breuer, and M. B. Lawrence, Catch strip assay for the relative assessment of two-dimensional protein association kinetics, Analytical Chemistry **80**, 944 (2008).

[169] C. Zhu, T. Yago, J. Lou, V. I. Zarnitsyna, and R. P. McEver, Mechanisms for flow enhanced cell adhesion, Annals of Biomedical Engineering **36**, 604 (2008).

[170] S. Zhu, A. W. Yu, D. Hawley, and R. Roy, Frustrated total internal reflection: a demonstration and review, American Journal of Physics **57**, 601 (1986).

[171] C. Meinhart and S. Wereley, The theory of diffraction-limited resolution in microparticle image velocimetry, Measurement Science and Technology **14**, 1047 (2003).

[172] H. Stark and J. W. Woods, *Probability and Random Processes with Applications to Signal Processing*, Prentice Hall, 3 edition, (2002).

[173] J. Han, S. W. Turner, and H. G. Craighead, Entropic trapping and escape of long DNA molecules at submicron size constriction, Physical Review Letters **83**, 1688 (1999).

[174] D. A. McQuarrie, *Statistical Mechanics*, chapter 17, pp. 379–401, University Science Books, (2000).

[175] W. M. Dean, *Analysis of Transport Phenomena*, Oxford University Press, (1998).

[176] M. Doi and S. F. Edwards, *The Theory of Polymer Dynamics*, chapter 2, pp. 46–50, Oxford University Press, (1986).